

ADDING TO THE CODEBOOK: REGULATION OF LOCAL CHROMATIN

ARCHITECTURE IN *NEUROSPORA CRASSA*

by

AILEEN R. FERRARO

(Under the Direction of Zachary A. Lewis)

ABSTRACT

Local chromatin architecture is an important feature of nuclear organization of eukaryotic genomes. This local chromatin environment is established, maintained, and interpreted in a number of ways including post-translation modifications to histones, binding of DNA by regulatory proteins, and rearrangement of nucleosomes. This work uses the model filamentous fungus *Neurospora crassa* to understand fundamental mechanisms regulating local chromatin architecture in eukaryotes. The findings presented here demonstrate mechanisms for the control of both accessible and inaccessible chromatin and provides a possible unifying mechanism for epigenetic compensation in eukaryotes when the normal local chromatin environment is disrupted. Further, this work presents evidence of possible evolutionary conservation of features of local chromatin architecture and mechanisms of transcriptional silencing in eukaryotes.

INDEX WORDS: Fungal genetics; *Neurospora crassa*; Genomics; Chromatin accessibility; Histone modifications

ADDING TO THE CODEBOOK: REGULATION OF LOCAL CHROMATIN  
ARCHITECTURE IN *NEUROSPORA CRASSA*

by

AILEEN R. FERRARO

B.S., Southern Connecticut State University, 2014

A Dissertation Submitted to the Graduate Faculty of The University of Georgia in Partial  
Fulfillment of the Requirements for the Degree

DOCTOR OF PHILOSOPHY

ATHENS, GEORGIA

2020

© 2020

Aileen R. Ferraro

All Rights Reserved

ADDING TO THE CODEBOOK: REGULATION OF LOCAL CHROMATIN  
ARCHITECTURE IN *NEUROSPORA CRASSA*

by

AILEEN R. FERRARO

Major Professor:	Zachary A. Lewis
Committee:	Vincent J. Starai
	Robert J. Schmitz
	Chang-Hyun Khang

Electronic Version Approved:

Ron Walcott  
Interim Dean of the Graduate School  
The University of Georgia  
August 2020



## DEDICATION

For my parents, Linda and Roger, who has always believed in me and pushed me to achieve what they knew I was capable of. To the Ferraro women who have always supported me: Maureen Ferraro-Davis, Maria Ferraro, Isabelle Ferraro, Kathryn Davis, and Irene Ferraro. And to Sharon Ferraro (1963 - 1993).

## ACKNOWLEDGEMENTS

I would like to acknowledge Elizabeth Lewis Roberts for her continued support and encouragement, without which I would not be where I am. I would also like to acknowledge Hervé Agaisse, Isabelle Derre, Ying Han, and Carole Kuehl, who furthered my scientific development. I would like to acknowledge the MoMy class of 2019 for welcoming me into medical mycology. Lastly, I would like to acknowledge Jennifer Kurasz, Nathan Glueck, Emily Carpinone, Justin Duma, Abigail Courtney, Alysha Higgs, Andy Murray, and Curtis Jenkins for keeping me sane for the past five years.

## TABLE OF CONTENTS

	Page
ACKNOWLEDGEMENTS .....	v
CHAPTER	
1 INTRODUCTION AND LITERATURE REVIEW .....	1
Purpose of this study .....	1
Chromatin architecture dynamics in <i>Neurospora</i> .....	1
Function and control of chromatin domains .....	3
References .....	10
Figures .....	18
2 CHROMATIN ACCESSIBILITY PROFILING IN <i>NEUROSPORA</i> <i>CRASSA</i> REVEALS A ROLE FOR H3K36ME3 IN LIMITING CHROMATIN ACCESSIBILITY .....	22
Abstract .....	23
Introduction .....	23
Materials and Methods .....	27
Results .....	30
Discussion .....	41
References .....	45
Tables .....	51
Figures .....	53

3	THE HISTONE DEACETYLASE HDA-1 IS IMPORTANT FOR NORMAL PATTERNS OF H3K27ME3 IN <i>NEUROSPORA</i> .....	67
	Abstract.....	68
	Introduction.....	68
	Materials and Methods.....	71
	Results.....	72
	Discussion.....	76
	References.....	78
	Tables.....	79
	Figures.....	81
4	H3K36ME3 EPIGENETICALLY COMPENSATES FOR THE LOSS OF HETEROCHROMATIN IN <i>NEUROSPORA</i> .....	93
	Introduction.....	93
	Materials and Methods.....	95
	Results.....	96
	Discussion.....	100
	References.....	102
	Tables.....	103
	Figures.....	105
5	DISCUSSION.....	111
	<i>Neurospora</i> provides evidence of fundamental mechanisms of regulation of accessible chromatin.....	112

HDA-1 provides a unifying mechanism for maintenance of heterochromatin domains.....	114
A new role for H3K36me3 .....	115
References.....	116

## APPENDICES

A CHIP-SEQ ANALYSIS IN <i>NEUROSPORA CRASSA</i> .....	117
B DECTIN-1 TARGETED ANTIFUNGAL LIPOSOMES EXHIBIT ENHANCED EFFICACY .....	133
C TRANSCRIPTION FACTOR ZNF2 COORDINATES WITH THE CHROMATIN REMODELING SWI/SNF COMPLEX TO REGULATE DIFFERENTIATION IN <i>CRYPTOCOCCUS NEOFORMANS</i> .....	175
D ISWI IS REQUIRED FOR NORMAL H3K27ME3 IN <i>NEUROSPORA CRASSA</i> .....	240

## CHAPTER 1

### INTRODUCTION AND LITERATURE REVIEW

#### **Purpose of this study**

The work here is focused on addressing three key aspects of local chromatin architecture in *Neurospora*: (1) characterization of accessible chromatin and defining molecular features associated with and responsible for forming open or closed chromatin structures in *Neurospora*, (2) identification of a regulatory relationship between a histone deacetylase (HDA-1) and key repressive chromatin modifications methylation of lysine 9 on histone H3 (H3K9me3) and methylation of lysine 27 on histone H3 (H3K27me3), and (3) a role for H3K36me3 in epigenetic compensation for the loss of H3K9me3 in *Neurospora*. All together, these studies characterize control of local chromatin architecture of both active and repressive domains in *Neurospora*.

#### **Chromatin architecture dynamics in *Neurospora***

##### *Measuring chromatin accessibility*

Local chromatin architecture can be measured by how accessible DNA is in a given region. DNA can be occupied by nucleosomes, transcription factors, or other DNA-binding proteins such as RNA polymerase II (1–3) . Chromatin is considered accessible when the DNA is unoccupied by nucleosomes or regulatory proteins and is therefore “available” to a given enzyme used in an accessibility assay. For example, early chromatin accessibility profiling assays measured regions where unoccupied DNA could be digested by DNaseI, and these DNaseI hypersensitivity experiments identified

regulatory regions such as gene promoters and enhancers (4, 5) . Micrococcal nuclease digestion (MNase) assays have proven useful for identifying sites of nucleosome occupancy in the genome and has been used for nucleosome phasing studies and determination of nucleosome-depleted regions throughout the genome (2). Importantly, these studies have helped to identify the role of nucleosome remodelers and regulatory DNA-binding proteins in regulating nucleosome dynamics at promoter regions (2, 6, 7).

More recently, assay for transposase accessible chromatin followed by sequencing (ATAC-seq) has been developed as a robust and sensitive assay to identify and characterize accessible chromatin (8–10)). ATAC-seq utilizes a promiscuous Tn5 pre-loaded with Illumina sequencing adaptors to fragment the genome and isolate unoccupied DNA. The nature of this assay allows for high-resolution profiling of chromatin accessibility and allows for profiling of both transcription factor and nucleosome dynamics throughout the genome (8, 11) ).

There has been much work in *Neurospora* exploring chromatin dynamics in circadian rhythm. For example, MNase-seq studies have identified a role for components of the White Collar Complex (WCC) in modulating nucleosome occupancy at light-responsive genes in *Neurospora*. Importantly, this study demonstrated a role for transcription factor white-collar 2 (WC-2) in modulating nucleosome occupancy at promoters of light-response genes (12) .

#### *Regulation of accessible chromatin*

Accessible chromatin is generally found at regulatory regions throughout the genome, i.e. active gene promoters and enhancers. Notably, gene bodies and promoters of repressed genes are generally inaccessible. These accessible regions can be bound by

transcription factors or transcriptional machinery. These regions are also generally enriched for histone modifications associated with transcriptional activation, namely acetylation of lysine 27 on histone H3 (H3K27ac) and methylation of lysine 4 on histone H3 (H3K4me)(1, 13, 14) . Additionally, production of small, abortive RNAs have been identified flanking accessible chromatin regions. While initially believed to be unique to higher eukaryotes, these small RNAs have been identified in *Nematostella* and *Neurospora*, indicating that these may in fact be evolutionarily conserved features of accessible promoters and regulatory regions in eukaryotes(15).

Accessibility of these regions are regulated by transcription factor binding and subsequent rearrangement of nucleosomes. This rearrangement can be a result of simply competition between nucleosomes and transcription factors for unoccupied DNA (16–18). Conversely, nucleosomes can be actively rearranged by transcription factors and ATP-depending nucleosome remodelers. For example, transcription factors can bind to a promoter region, which then triggers recruitment of nucleosome remodelers which can evict or reposition nucleosomes. This newly accessible chromatin can then be occupied by RNA polymerase II, resulting in transcription (Fig. 1.2). It is unclear whether the act of transcription itself plays a role in regulating chromatin accessibility. While small abortive transcripts appear to be evolutionarily conserved, there has not yet been direct evidence of these transcripts regulating accessibility of chromatin.

### **Function and control of chromatin domains**

DNA-protein interactions regulate key cellular functions such as gene transcription, cell-cycle progression, and DNA repair. In eukaryotes, DNA-protein interactions are the fundamental organizational units of chromatin, which drives



organization of the genome within the nucleus into distinct domains: densely packed, transcriptionally repressed heterochromatin and loosely packed, transcriptionally active euchromatin (19, 20)). This organization is fundamentally established by interactions between DNA and an octamer of core histone proteins (two each of H2A, H2B, H3, and H4) to form a nucleosome (21) ). Histones contain a globular domain, which provide a platform for approximately 150 base pairs of DNA to wrap around the core histones (20). Histones also contain flexible tails which extend out of the nucleosome (22, 23)). These tails can be reversibly modified post-translationally by histone methyltransferases or demethylases, histone acetyltransferases or deacetylases, or other post-translational modification machinery (Fig. 1.1) (24, 25) .

These modifications can provide a means of establishing a secondary genetic code, coined the “histone code” by Strahl and Allis in 2001 (13). This “histone code” can be interpreted by chromatin readers and therefore signal recruitment of downstream regulatory proteins or preclude binding of these proteins. These two mechanisms of regulation are not necessarily mutually exclusive, and there is evidence of “crosstalk” between histone modifications (26–28), adding a layer of complexity to both control of these modifications and interpretation of modifications by chromatin readers.

While chromatin dynamics and histone modifications have been implicated in myriad cellular processes, perhaps their most fundamental role lies in the regulation of gene transcription. Indeed, decades of work has demonstrated a role for histone modifications in transcriptional activation or repression (1, 3, 13, 29). Much of this early work, however, has been done in yeasts, which lack repressive chromatin pathways found in higher eukaryotes (29–31). Additionally, many components of heterochromatin

pathways are essential in higher eukaryotes, making it difficult to study their role in these organisms. The model filamentous fungus *Neurospora crassa*, however, shares features of heterochromatin with higher eukaryotes that are missing from other simple model fungi, including *S. cerevisiae*, *S. pombe*, and *Aspergillus* (32). Studies in *Neurospora* have provided insight into fundamental mechanisms of chromatin dynamics and is used here as a model to further understand regulation and control of both active and repressive chromatin domains.

Two key histone modifications are associated with distinct repressive heterochromatin domains: H3K9me3 (constitutive heterochromatin) and H3K27me3 (facultative heterochromatin). These domains are established in different parts of the genome, have different qualities, and perform different functions, as described below.

#### *Constitutive heterochromatin*

Work in the fission yeast *Schizosaccharomyces pombe* first demonstrated that trimethylation of lysine 9 on the tail of histone H3 (H3K9me3) leads to a condensed chromatin state, establishment of constitutive heterochromatin, and subsequent transcriptional silencing (33–35). Additionally, H3K9me3 is a critical component of centromere formation in many eukaryotes, and is associated with silencing transposable elements which, if transcribed, could be detrimental to the cell (29, 33, 36, 37).

Work in the model filamentous fungus *Neurospora crassa* has been critical to understanding fundamental mechanisms controlling heterochromatin control and function (Fig. 1.3). Constitutive heterochromatin in *N. crassa* occupies repeat-rich regions of the genome, namely transposable element relics and centromeres. Constitutive heterochromatin consists of DNA methylation, H3K9me3, and hypoacetylation of histone

H3. Heterochromatin is nucleated at cytosine residues at A:T-rich DNA. The methyltransferase complex DCDC (DIM-5; DIM-7; DIM-9; CUL4; DDB1) is recruited by unknown mechanisms to these regions, and H3K9me3 is catalyzed by the histone methyltransferase DIM-5. This H3K9me3 is recognized by the chromodomain H3K9me3 reader HP1 and DNA methyltransferase DIM-2. This is followed by the histone deacetylase complex HCHC (HP1, CDP-2, HDA-1, CHAP). Histone deacetylation and DNA methylation then promotes further H3K9me3 by DCDC, ultimately resulting in a repressive chromatin domain (38–41).

#### *Facultative heterochromatin*

Facultative heterochromatin is defined by methylated lysine 27 on histone H3 (H3K27me) (42, 43). This chromatin mark is established by Polycomb group (PcG) proteins, of which there are two major PcG complexes: Polycomb repressive complex 1 (PRC1) and Polycomb repressive complex 2 (PRC2). PRC2 in *Drosophila* is composed of four core subunits: the histone methyltransferase Enhancer of zeste (Ez), the Zinc-finger protein Suppressor of zeste (SuZ12), the histone binding protein p55, and the WD40 protein Extra Sex Combs (ESC) (44). PRC2 is responsible for catalyzing H3K27me at repressive domains, and is conserved among plants, animals, and some fungi (32).

PRC1 is composed of Polycomb (PC), Polyhomeotic (PH), Posterior sex combs (PSC), and Sex Combs Extra/dRING (SCE/dRing) (44). Its role in facultative heterochromatin seems to vary between organisms, but ubiquitination of lysines 118/119 on histone H2A (H2AK118/119ub1) seems to be a hallmark function of PRC1 (45). Additionally, PRC1 directly interacts with H3K27me3 and has been shown to inhibit

chromatin remodelers and thus mediate chromatin accessibility (46, 47). PRC1 is conserved in animals (43). *Arabidopsis* has a functional homolog to PC and multiple homologs of PSC and SCE/dRING which mediate H2A ubiquitination (48, 49). PRC1, however, seems to have been lost in fungi, and no functional homologs have been identified (32).

Polycomb group proteins were first discovered in *Drosophila melanogaster*, where H3K27me3 was shown to be critical for conditional gene silencing during *Drosophila* development (44, 50)). For example, disruption of the Polycomb pathway leads to malformed body segmentation in *Drosophila* embryos (51, 52)). Later work in mammals revealed a critical role in embryonic development (53–56), and there is a large body of work identifying the role of H3K27me3 in embryonic development and cellular differentiation (57–59)). In plants, H3K27me3 is important for control of flower development, diurnal response, and cold response (60–63)).

Targeting of Polycomb group (PcG) proteins differs in higher eukaryotes. For example, in *Drosophila* there is strong evidence of Polycomb Response Elements (PREs), which are short DNA sequences that act to recruit PRC2 for H3K27me3 deposition (64, 65)). PcG appears to be targeted to CpG islands in humans (66, 67). *Arabidopsis* seems to share *Drosophila* targeting, as PREs have recently been identified in these organisms (68, 69).

PcG proteins have been lost in some fungi. In fungi containing Polycomb-group proteins, H3K27me3 has been shown to regulate transcription of secondary metabolism biosynthesis clusters, providing a role for H3K27me3 in response to environmental cues in these organisms (32, 70, 71). Key work has been done in *N. crassa* to understand

fundamental mechanisms of control of H3K27me3 establishment. *N. crassa* possesses PRC2 yet lacks PRC1 (32). *Neurospora* PRC2 consists of four core subunits: the methyltransferase SET-7, Suz-12, ESC homolog EED, and CAC-3, which is a component of a number of complexes in *Neurospora*, including nucleosome assembly complex CAF (32) PRC2 is non-essential in fungi studied (Fig. 1.4) (32, 70, 71). This trimmed down facultative heterochromatin pathway allows for genetic studies of the PRC2 pathway and H3K27me3 that would not be possible in higher eukaryotes. *N. crassa* studies have demonstrated that H3K27me3 is localized to the telomeric and subtelomeric regions of the genome and is enriched over relatively large blocks of genes and promoters (32) . Further, deletion of the PRC2 catalytic subunit SET-7 results in loss of H3K27me3 and upregulation of normally silent genes marked by H3K27me3 (32). Other subunits of *N. crassa* PRC2 are necessary for proper H3K27me3 deposition. For example, CAC-3 is necessary for telomeric H3K27me3, while EED is necessary for all H3K27me3 (32) ).

Studies aimed at understanding mechanisms of H3K27me3 establishment in *N. crassa* have identified at least two distinct pathways for H3K27me3 deposition by PRC2: subtelomeric and internal. Subtelomeric H3K27me3 has been shown to require sequence-specific factors of recruitment, namely telomeric repeat sequences (72). Additionally, new PRC2 accessory proteins have recently been identified in establishing telomeric H3K27me3, although the mechanism by which they contribute to H3K27me3 establishment has not been identified (73). Normal H3K27me3 establishment has been shown to require another histone modification, di-methylation of lysine 36 on histone H3 (H3K36me2) (74).

In higher eukaryotes and the filamentous fungi *Neurospora crassa* and *Fusarium fujikoroii*, but not in model yeasts *Saccharomyces cerevisiae* or *Schizosaccharomyces pombe*, H3K36 is di-methylated by the histone methyltransferase ASH-1 (74, 75). This H3K36me is deposited independent of transcription, and in *Neurospora* it acts a repressive chromatin mark, and it plays an important role in priming chromatin for H3K27me<sub>2/3</sub> (74, 75). In higher eukaryotes, H3K36me<sub>2</sub> recruits the DNA methyltransferase DNMT3A and contributes to intergenic DNA methylation (76–78). There is no evidence of this in *Neurospora*, as there is no methylation at these regions in *Neurospora* methylome studies. This stark difference between *Neurospora* and humans presents a new role of H3K36me in eukaryotes.

#### *Interactions between heterochromatin domains*

While constitutive and facultative heterochromatin are both repressive domains, they are not interchangeable. These regions are mutually exclusive in normal cells, with constitutive heterochromatin occupying repeat-rich, A:T-rich DNA and H3K27me<sub>2/3</sub> being confined to repressed genes (38). Loss of constitutive heterochromatin can lead to invasion of facultative heterochromatin with negative consequences for the cell. This is seen in glioblastoma in humans, where disruption of DNA methylation leads to loss of H3K27me<sub>3</sub> at native loci and re-distribution into heterochromatin domains (22, 79–81). Critical work in *Neurospora* has identified that this is a conserved phenotype. Loss of H3K9me<sub>3</sub>, but not DNA methylation, in *Neurospora* leads to redistribution of H3K27me<sub>3</sub> into constitutive heterochromatin domains and loss of H3K27me<sub>3</sub> from facultative heterochromatin domains. This redistribution of H3K27me<sub>3</sub> leads to genotoxic stress and increased sensitivity to DNA-damaging agents (82). Later work

identified that this is mimicked in the H3K9me3 reader HP1 (83). Importantly, mass spectrometry experiments in cells lacking HP1 show that H3K27me2 and H3K9me3 co-exist on the same nucleosome (83). These previous studies reveal a role in H3K9me3 and HP1 in protecting constitutive heterochromatin by excluding PRC2, yet the underlying mechanism remains unclear. The studies presented here attempt to address mechanisms of maintaining exclusivity of these two repressive chromatin domains via histone deacetylase activity, as well as mechanisms of preserving a repressive chromatin environment in the absence of constitutive and facultative heterochromatin machinery.

## References

1. Heintzman ND, Stuart RK, Hon G, Fu Y, Ching CW, Hawkins RD, Barrera LO, Van Calcar S, Qu C, Ching KA, Wang W, Weng Z, Green RD, Crawford GE, Ren B. 2007. Distinct and predictive chromatin signatures of transcriptional promoters and enhancers in the human genome. *Nat Genet*.
2. Ponts N, Harris EY, Prudhomme J, Wick I, Eckhardt-Ludka C, Hicks GR, Hardiman G, Lonardi S, Le Roch KG. 2010. Nucleosome landscape and control of transcription in the human malaria parasite. *Genome Res*.
3. Feil R, Fraga MF. 2012. Epigenetics and the environment: Emerging patterns and implications. *Nat Rev Genet*.
4. McCall K, Bender W. 1996. Probes of chromatin accessibility in the *Drosophila* bithorax complex respond differently to Polycomb-mediated repression. *EMBO J* 15:569–580.
5. Bargaje R, Alam MP, Patowary A, Sarkar M, Ali T, Gupta S, Garg M, Singh M, Purkanti R, Scaria V, Sivasubbu S, Brahmachari V, Beena Pillai. 2012. Proximity of H2A.Z containing nucleosome to the transcription start site influences gene expression levels in the mammalian liver and brain. *Nucleic Acids Res*.
6. Luger K. 2006. Dynamic nucleosomes. *Chromosome Res* 14:5–16.
7. Pathak R, Singh P, Ananthakrishnan S, Adamczyk S, Schimmel O, Govind CK. 2018. Acetylation-dependent recruitment of the FACT complex and its role in regulating pol II occupancy genome-wide in *saccharomyces cerevisiae*. *Genetics* 209:743–756.

8. Greenleaf WJ, Denny S, Schwartz K, Schep A, Buenrostro J, Sherlock G. 2015. High-resolution nucleosome positioning from ATAC-seq chromatin accessibility data. *ArrayExpress Arch.*
9. Lu Z, Hofmeister BT, Vollmers C, DuBois RM, Schmitz RJ. 2017. Combining ATAC-seq with nuclei sorting for discovery of cis-regulatory regions in plant genomes. *Nucleic Acids Res* 2016/12/03. 45:e41.
10. Satpathy AT, Saligrama N, Buenrostro JD, Wei Y, Wu B, Rubin AJ, Granja JM, Lareau CA, Li R, Qi Y, Parker KR, Mumbach MR, Serratelli WS, Gennert DG, Schep AN, Corces MR, Khodadoust MS, Kim YH, Khavari PA, Greenleaf WJ, Davis MM, Chang HY. 2018. Transcript-indexed ATAC-seq for precision immune profiling. *Nat Med* 2018/04/25. 24:580–590.
11. Schep AN, Buenrostro JD, Denny SK, Schwartz K, Sherlock G, Greenleaf WJ. 2015. Structured nucleosome fingerprints enable high-resolution mapping of chromatin architecture within regulatory regions. *Genome Res.*
12. Sancar C, Ha N, Yilmaz R, Tesorero R, Fisher T, Brunner M, Sancar G. 2015. Combinatorial Control of Light Induced Chromatin Remodeling and Gene Activation in *Neurospora*. *PLoS Genet.*
13. Strahl BD, Allis CD. 2000. The language of covalent histone modifications. *Nature. Nature.*
14. Gatta R, Mantovani R. 2010. Single nucleosome ChIPs identify an extensive switch of acetyl marks on cell cycle promoters. *Cell Cycle* 9:2149–2159.
15. Duttke SH, Chang MW, Heinz S, Benner C. 2019. Identification and dynamic quantification of regulatory elements using total RNA. *Genome Res* 29:1836–1846.
16. Zaret KS, Carroll JS. 2011. Pioneer transcription factors: Establishing competence for gene expression. *Genes Dev.*
17. Soufi A, Garcia MF, Jaroszewicz A, Osman N, Pellegrini M, Zaret KS. 2015. Pioneer transcription factors target partial DNA motifs on nucleosomes to initiate reprogramming. *Cell.*
18. Meers MP, Janssens DH, Henikoff S. 2019. Pioneer Factor-Nucleosome Binding Events during Differentiation Are Motif Encoded. *Mol Cell.*
19. Comings DE. 1972. The Structure and Function of Chromatin BT - Advances in Human Genetics, p. 237–431. *In* Harris, H, Hirschhorn, K (eds.), *Advances in human genetics*. Springer US.



20. Widom J. 1998. Structure, dynamics, and function of chromatin in vitro. *Annu Rev Biophys Biomol Struct.* *Annu Rev Biophys Biomol Struct.*
21. Richmond TJ, Finch JT, Rushton B, Rhodes D, Klug A. 1984. Structure of the nucleosome core particle at 7 resolution. *Nature* 311:532–537.
22. Peters AHFM, Kubicek S, Mechtler K, O’Sullivan RJ, Derijck AAHA, Perez-Burgos L, Kohlmaier A, Opravil S, Tachibana M, Shinkai Y, Martens JHA, Jenuwein T. 2003. Partitioning and Plasticity of Repressive Histone Methylation States in Mammalian Chromatin. *Mol Cell.*
23. Zheng C, Lu X, Hansen JC, Hayes JJ. 2005. Salt-dependent intra- and internucleosomal interactions of the H3 tail domain in a model oligonucleosomal array. *J Biol Chem* 280:33552–33557.
24. ALLFREY VG, FAULKNER R, MIRSKY AE. 1964. ACETYLATION AND METHYLATION OF HISTONES AND THEIR POSSIBLE ROLE IN THE. *Proc Natl Acad Sci United States* 51:786–794.
25. Kouzarides T. 2007. Chromatin Modifications and Their Function. *Cell.* *Cell.*
26. Guan X, Rastogi N, Parthun MR, Freitas MA. 2013. Discovery of Histone Modification Crosstalk Networks by Stable Isotope Labeling of Amino Acids in Cell Culture Mass Spectrometry (SILAC MS)\* □ S.
27. Jung I, Park J, Choi C, Kim D. 2015. Identification of novel trans-crosstalk between histone modifications via genome-wide analysis of maximal deletion effect. *Genes and Genomics* 37:693–701.
28. Wojcik F, Dann GP, Beh LY, Debelouchina GT, Hofmann R, Muir TW. 2018. Functional crosstalk between histone H2B ubiquitylation and H2A modifications and variants. *Nat Commun* 9:1394.
29. Allshire RC, Ekwall K. 2015. Epigenetic regulation of chromatin states in *Schizosaccharomyces pombe*. *Cold Spring Harb Perspect Biol.*
30. Knott SRV, Viggiani CJ, Tavaré S, Aparicio OM. 2009. Genome-wide replication profiles indicate an expansive role for Rpd3L in regulating replication initiation timing or efficiency and reveal genomic loci of Rpd3 function in *Saccharomyces cerevisiae*. *Genes Dev.*
31. Connelly CF, Wakefield J, Akey JM. 2014. Evolution and Genetic Architecture of Chromatin Accessibility and Function in Yeast. *PLoS Genet* 10:e1004427.

32. Jamieson K, Rountree MR, Lewis ZA, Stajich JE, Selker EU. 2013. Regional control of histone H3 lysine 27 methylation in *Neurospora*. *Proc Natl Acad Sci U S A*.
33. Allshire RC, Javerzat JP, Redhead NJ, Cranston G. 1994. Position effect variegation at fission yeast centromeres. *Cell*.
34. Ivanova A V., Bonaduce MJ, Ivanov S V., Klar AJS. 1998. The chromo and SET domains of the Clr4 protein are essential for silencing in fission yeast. *Nat Genet*.
35. Shankaranarayana GD, Motamedi MR, Moazed D, Grewal SIS. 2003. Sir2 regulates histone H3 lysine 9 methylation and heterochromatin assembly in fission yeast. *Curr Biol*.
36. Futcher1 B, Carbon2 J. 1986. Toxic Effects of Excess Cloned Centromeres. *MOLECULAR AND CELLULAR BIOLOGY*.
37. Nakagawa H, Lee JK, Hurwitz J, Allshire RC, Nakayama JI, Grewal SIS, Tanaka K, Murakami Y. 2002. Fission yeast CENP-B homologs nucleate centromeric heterochromatin by promoting heterochromatin-specific histone tail modifications. *Genes Dev* 16:1766–1778.
38. Lewis ZA, Adhvaryu KK, Honda S, Shiver AL, Knip M, Sack R, Selker EU. 2010. DNA methylation and normal chromosome behavior in *neurospora* depend on five components of a histone methyltransferase complex, DCDC. *PLoS Genet*.
39. Honda S, Lewis ZA, Shimada K, Fischle W, Sack R, Selker EU. 2012. Heterochromatin protein 1 forms distinct complexes to direct histone deacetylation and DNA methylation. *Nat Struct Mol Biol*.
40. Honda S, Bicocca VT, Gessaman JD, Rountree MR, Yokoyama A, Yu EY, Selker JML, Selker EU. 2016. Dual chromatin recognition by the histone deacetylase complex HCHC is required for proper DNA methylation in *Neurospora crassa*. *Proc Natl Acad Sci U S A*.
41. Gessaman JD, Selker EU. 2017. Induction of H3K9me3 and DNA methylation by tethered heterochromatin factors in *Neurospora crassa*. *Proc Natl Acad Sci U S A*.
42. Schuettengruber B, Chourrout D, Vervoort M, Leblanc B, Cavalli G. 2007. Genome Regulation by Polycomb and Trithorax Proteins. *Cell*.
43. Margueron R, Reinberg D. 2011. The Polycomb complex PRC2 and its mark in life. *Nature*.
44. Kennison JA. 1995. The Polycomb and Trithorax Group Proteins of *Drosophila* : Trans-Regulators of Homeotic Gene Function . *Annu Rev Genet* 29:289–303.

45. Wang H, Wang L, Erdjument-Bromage H, Vidal M, Tempst P, Jones RS, Zhang Y. 2004. Role of histone H2A ubiquitination in Polycomb silencing. *Nature* 431:873–878.
46. Shao Z, Raible F, Mollaaghababa R, Guyon JR, Wu CT, Bender W, Kingston RE. 1999. Stabilization of chromatin structure by PRC1, a polycomb complex. *Cell* 98:37–46.
47. King IFG, Emmons RB, Francis NJ, Wild B, Müller J, Kingston RE, Wu C. 2005. Analysis of a Polycomb Group Protein Defines Regions That Link Repressive Activity on Nucleosomal Templates to In Vivo Function. *Mol Cell Biol* 25:6578–6591.
48. Turck F, Roudier F, Farrona S, Martin-Magniette M-L, Guillaume E, Buisine N, Gagnot S, Martienssen RA, Coupland G, Colot V. 2007. Arabidopsis TFL2/LHP1 Specifically Associates with Genes Marked by Trimethylation of Histone H3 Lysine 27. *PLoS Genet* 3:e86.
49. Zhang X, Germann S, Blus BJ, Khorasanizadeh S, Gaudin V, Jacobsen SE. 2007. The Arabidopsis LHP1 protein colocalizes with histone H3 Lys27 trimethylation. *Nat Struct Mol Biol* 14:869–871.
50. Lewis EB. 1978. A gene complex controlling segmentation in *Drosophila*. *Nature*. Nature Publishing Group.
51. Lee N, Maurange C, Ringrose L, Paro R. 2005. Suppression of Polycomb group proteins by JNK signaling induces transdetermination in *Drosophila* imaginal discs. *Nature* 438:234–237.
52. Katsuyama T, Paro R. 2011. Epigenetic reprogramming during tissue regeneration. *FEBS Lett*. FEBS Lett.
53. Boyer LA, Plath K, Zeitlinger J, Brambrink T, Medeiros LA, Lee TI, Levine SS, Wernig M, Tajonar A, Ray MK, Bell GW, Otte AP, Vidal M, Gifford DK, Young RA, Jaenisch R. 2006. Polycomb complexes repress developmental regulators in murine embryonic stem cells. *Nature* 441:349–353.
54. Posfai E, Kunzmann R, Brochard V, Salvaing J, Cabuy E, Roloff TC, Liu Z, Tardat M, van Lohuizen M, Vidal M, Beaujean N, Peters AHFM. 2012. Polycomb function during oogenesis is required for mouse embryonic development. *Genes Dev* 26:920–932.
55. Liu X, Kim YJ, Müller R, Yumul RE, Liu C, Pan Y, Cao X, Goodrich J, Chen X. 2011. AGAMOUS terminates floral stem cell maintenance in arabidopsis by

directly repressing WUSCHEL through recruitment of Polycomb Group proteins. *Plant Cell* 23:3654–3670.

56. He C, Chen X, Huang H, Xu L. 2012. Reprogramming of H3K27me3 Is Critical for Acquisition of Pluripotency from Cultured Arabidopsis Tissues. *PLoS Genet* 8.
57. Van Lohuizen M, Frasch M, Wientjens E, Berns A. 1991. Sequence similarity between the mammalian bmi-1 proto-oncogene and the Drosophila regulatory genes Psc and Su(z)2. *Nature* 353:353–355.
58. Jacobs JL, Kieboom K, Marino S, DePinho RA, Van Lohuizen M. 1999. The oncogene and Polycombgroup gene bmi-1 regulates cell proliferation and senescence through the ink4a locus. *Nature* 397:164–168.
59. Brockdorff N, Turner BM. 2015. Dosage compensation in mammals. *Cold Spring Harb Perspect Biol* 7.
60. Kinoshita T, Harada JJ, Goldberg RB, Fischer RL. 2001. Polycomb repression of flowering during early plant development. *Proc Natl Acad Sci U S A* 98:14156–14161.
61. Chanvivattana Y, Bishopp A, Schubert D, Stock C, Moon YH, Sung ZR, Goodrich J. 2004. Interaction of Polycomb-group proteins controlling flowering in Arabidopsis. *Development* 131:5263–5276.
62. Schubert D, Primavesi L, Bishopp A, Roberts G, Doonan J, Jenuwein T, Goodrich J. 2006. Silencing by plant Polycomb-group genes requires dispersed trimethylation of histone H3 at lysine 27. *EMBO J* 25:4638–4649.
63. Jiang D, Wang Y, Wang Y, He Y. 2008. Repression of FLOWERING LOCUS C and FLOWERING LOCUS T by the Arabidopsis Polycomb Repressive Complex 2 Components. *PLoS One* 3:e3404.
64. Mito Y, Henikoff JG, Henikoff S. 2007. Histone replacement marks the boundaries of cis-regulatory domains. *Science* (80- ) 315:1408–1411.
65. Deal RB, Henikoff JG, Henikoff S. 2010. Genome-wide kinetics of nucleosome turnover determined by metabolic labeling of histones. *Science* (80- ) 328:1161–1164.
66. Ku M, Koche RP, Rheinbay E, Mendenhall EM, Endoh M, Mikkelsen TS, Presser A, Nusbaum C, Xie X, Chi AS, Adli M, Kasif S, Ptaszek LM, Cowan CA, Lander ES, Koseki H, Bernstein BE. 2008. Genomewide analysis of PRC1 and PRC2 occupancy identifies two classes of bivalent domains. *PLoS Genet* 4.

67. Mendenhall EM, Koche RP, Truong T, Zhou VW, Issac B, Chi AS, Ku M, Bernstein BE. 2010. GC-Rich Sequence Elements Recruit PRC2 in Mammalian ES Cells. *PLoS Genet* 6:e1001244.
68. Sheldon CC, Hills MJ, Lister C, Dean C, Dennis ES, Peacock WJ. 2008. Resetting of FLOWERING LOCUS C expression after epigenetic repression by vernalization. *Proc Natl Acad Sci U S A* 105:2214–2219.
69. Wöhrmann HJP, Gagliardini V, Raissig MT, Wehrle W, Arand J, Schmidt A, Tierling S, Page DR, Schöb H, Walter J, Grossniklaus U. 2012. Identification of a DNA methylation-independent imprinting control region at the Arabidopsis MEDEA locus. *Genes Dev* 26:1837–1850.
70. Chujo T, Scott B. 2014. Histone H3K9 and H3K27 methylation regulates fungal alkaloid biosynthesis in a fungal endophyte-plant symbiosis. *Mol Microbiol*.
71. Connolly LR, Smith KM, Freitag M. 2013. The *Fusarium graminearum* Histone H3 K27 Methyltransferase KMT6 Regulates Development and Expression of Secondary Metabolite Gene Clusters. *PLoS Genet*.
72. Jamieson K, McNaught KJ, Ormsby T, Leggett NA, Honda S, Selker EU. 2018. Telomere repeats induce domains of H3K27 methylation in *Neurospora*. *Elife*.
73. Wiles ET, McNaught KJ, Kaur G, Selker JML, Ormsby T, Aravind L, Selker EU. 2020. Evolutionarily ancient BAH-PHD protein mediates Polycomb silencing. *Proc Natl Acad Sci U S A*.
74. Bicocca VT, Ormsby T, Adhvaryu KK, Honda S, Selker EU. 2018. ASH1-catalyzed H3K36 methylation drives gene repression and marks H3K27me<sub>2/3</sub>-competent chromatin. *Elife* 2018/11/24. 7.
75. Janevska S, Baumann L, Sieber CMK, Münsterkötter M, Ulrich J, Kämper J, Güldener U, Tudzynski B. 2018. Elucidation of the two H3K36me<sub>3</sub> histone methyltransferases set2 and ash1 in *fusarium fujikuroi* unravels their different chromosomal targets and a major impact of ash1 on genome stability. *Genetics*.
76. Lin CH, Li B, Swanson S, Zhang Y, Florens L, Washburn MP, Abmayr SM, Workman JL. 2008. Heterochromatin Protein 1a Stimulates Histone H3 Lysine 36 Demethylation by the *Drosophila* KDM4A Demethylase. *Mol Cell*.
77. Xu Q, Xiang Y, Wang Q, Wang L, Brind'Amour J, Bogutz AB, Zhang Y, Zhang B, Yu G, Xia W, Du Z, Huang C, Ma J, Zheng H, Li Y, Liu C, Walker CL, Jonasch E, Lefebvre L, Wu M, Lorincz MC, Li W, Li L, Xie W. 2019. SETD2 regulates the maternal epigenome, genomic imprinting and embryonic development. *Nat Genet*.

78. Bogutz AB, Brind'Amour J, Kobayashi H, Jensen KN, Nakabayashi K, Imai H, Lorincz MC, Lefebvre L. 2019. Evolution of imprinting via lineage-specific insertion of retroviral promoters. *Nat Commun*.
79. Lindroth AM, Yoon JP, McLean CM, Dokshin GA, Persson JM, Herman H, Pasini D, Miró X, Donohoe ME, Lee JT, Helin K, Soloway PD. 2008. Antagonism between DNA and H3K27 methylation at the imprinted *Rasgrf1* locus. *PLoS Genet*.
80. Wu H, Coskun V, Tao J, Xie W, Ge W, Yoshikawa K, Li E, Zhang Y, Sun YE. 2010. Dnmt3a-dependent nonpromoter DNA methylation facilitates transcription of neurogenic genes. *Science* (80- ).
81. Reddington JP, Perricone SM, Nestor CE, Reichmann J, Youngson NA, Suzuki M, Reinhardt D, Dunican DS, Prendergast JG, Mjoseng H, Ramsahoye BH, Whitelaw E, Greally JM, Adams IR, Bickmore WA, Meehan RR. 2013. Redistribution of H3K27me3 upon DNA hypomethylation results in de-repression of Polycomb target genes. *Genome Biol*.
82. Basenko EY, Sasaki T, Ji L, Prybol CJ, Burckhardt RM, Schmitz RJ, Lewis ZA. 2015. Genome-wide redistribution of H3K27me3 is linked to genotoxic stress and defective growth. *Proc Natl Acad Sci U S A*.
83. Jamieson K, Wiles ET, McNaught KJ, Sidoli S, Leggett N, Shao Y, Garcia BA, Selker EU. 2016. Loss of HP1 causes depletion of H3K27me3 from facultative heterochromatin and gain of H3K27me2 at constitutive heterochromatin. *Genome Res*.

## Figures

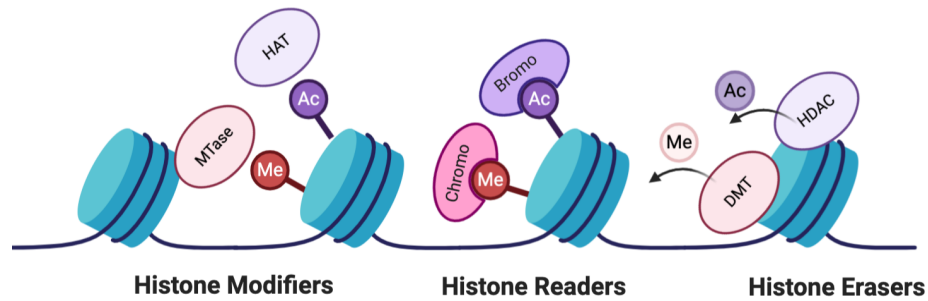


**Figure 1.1. Establishing the histone code.** Approximately 150 base pairs of DNA wrap around core histones to form a nucleosome. Histone tails which extend out of the nucleosome can be modified, interpreted, and erased to form a secondary “histone code” which can regulate cellular processes.

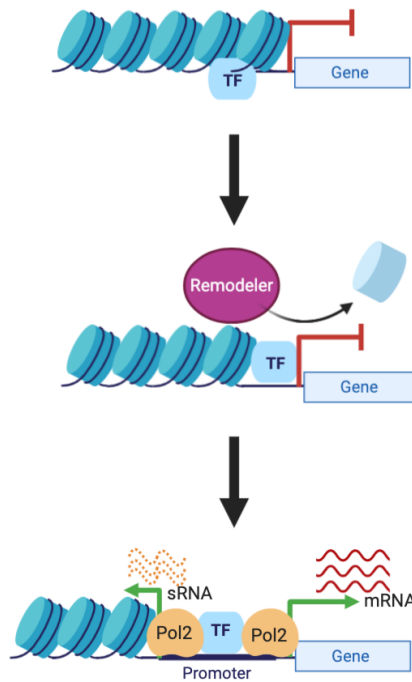


**Figure 1.2. Promoter dynamics and chromatin accessibility.** Inaccessible gene promoters are bound by activating transcription factors. Transcription factor binding can recruit chromatin remodeling enzymes which can move or evict nucleosomes. TF occupation in the now accessible promoter allows for binding by RNA polymerase II. Transcription at the promoter can be bidirectional, producing both mRNA products and short, non-coding RNAs.



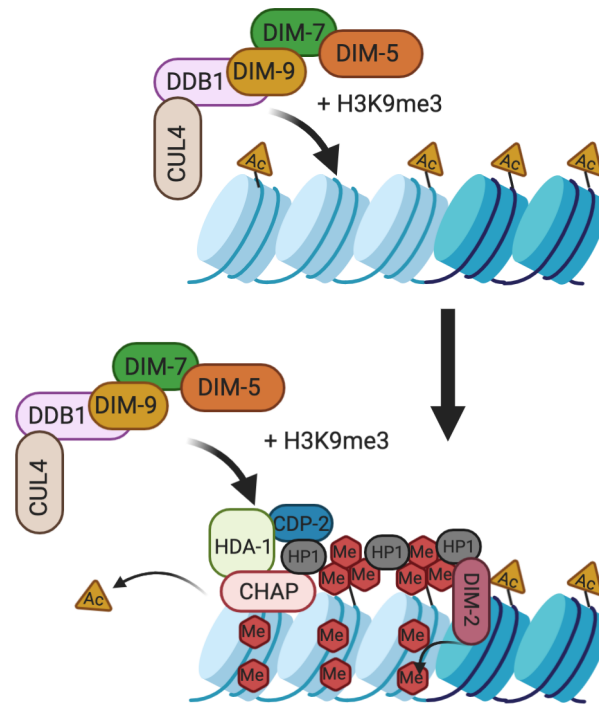


**Figure 1.3. Establishment of constitutive heterochromatin.** A: T-rich DNA (light blue) recruits the H3K9 methyltransferase complex DCDC. H3K9me3 is catalyzed by DIM-5. This H3K9me3 is bound by the H3K9me3 reader HP1, which recruits the histone deacetylase complex HCHC for histone deacetylation by HDA-1. HP1 further recruits the DNA methyltransferase DIM-2, and histone deacetylation by HCHC allows for further H3K9me3 by DCDC.

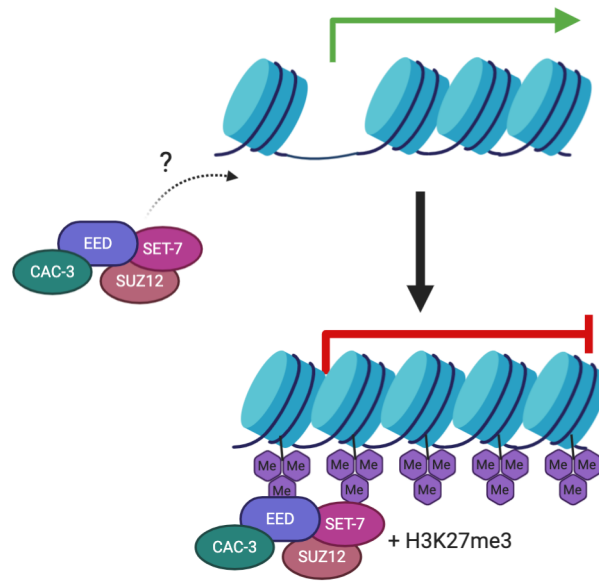


**Figure 1.4. Establishment of facultative heterochromatin.** Polycomb repressive complex 2 (PRC2) is recruited to chromatin by an unknown mechanism. PRC2 catalyzes H3K27me3 via the histone methyltransferase SET-7, resulting in gene repression.

CHAPTER 2

CHROMATIN ACCESSIBILITY PROFILING IN *NEUROSPORA CRASSA* REVEALS  
A ROLE FOR H3K36ME3 IN LIMITING CHROMATIN

---

Ferraro A.R., Courtney A.J., Lu Z., Kamei M., Schmitz R.J., and Lewis Z.A. To be  
submitted to *Genetics*

## Abstract

Regional differences in chromatin accessibility contribute to transcriptional regulation. Work in yeast and higher eukaryotes has described accessible regions, but little work has been done in filamentous fungi. Here we present a genome-scale characterization of accessible chromatin regions in *Neurospora crassa*, which revealed characteristic structural features of accessible and inaccessible chromatin. We report features of both accessible and inaccessible chromatin, including the presence of histone modifications, types of transcription, transcription factor binding, and nucleosome turnover dynamics. We also present a role for methylation of lysine 36 on histone H3 (H3K36me) in limiting chromatin accessibility in *N. crassa*. With recent work describing the role of ASH-1-mediated H3K36me<sub>2</sub> in gene repression and priming chromatin for deposition of H3K27me by Polycomb Repressive Complex, we wanted to know if H3K36me functions to repress chromatin accessibility in these regions. To determine whether ASH-1 or SET-2-mediated H3K36me was necessary for limiting chromatin accessibility, we created H3K36 point mutants mimicking acetylated H3K36 (H3K36Q) and unmodified H3K36 (H3K36R) and performed ATAC-seq in these strains as well as the H3K36 tri-methylase deletion mutant,  $\Delta$ set-2.

## Introduction

Functionally distinct chromatin environments are defined by characteristic molecular features including histone modifications, occupancy of DNA- and chromatin-binding proteins, and varying degrees of chromatin accessibility (for a review, see 1). Euchromatin is traditionally defined as transcriptionally active and marked by histone H3 acetylation (H3Kac), histone H3 lysine 4 methylation (H3K4me<sub>1/2/3</sub>) (10, 11), and

histone H3 lysine 36 trimethylation (H3K36me3) in bodies of transcribed genes, but not in promoters (12–14). Conversely, heterochromatin is transcriptionally repressed and marked by histone H3 lysine 9 methylation (H3K9me3) (2–4) or histone H3 lysine 27 methylation (H3K27me2me3) (5–8). In *N. crassa*, H3K36 methylation is also found in both promoters and gene bodies of silent genes (9). In addition to these contributing factors, chromatin environments can also be defined by the presence of histone variants such as histone H2A.Z, which is found surrounding transcriptional start sites and within vertebrate enhancers (10–14).

Euchromatic and heterochromatic environments display marked differences in the level of chromatin accessibility to DNA-binding proteins or other regulatory factors. The Assay for Transposase-Accessible Chromatin (ATAC-seq) method has proven to be useful tool for characterizing chromatin accessibility in eukaryotes at a higher resolution and with greater reproducibility than other methods such as DNaseI hypersensitivity (DNase-seq) or formaldehyde-assisted assays (FAIRE-seq) (15). This method has been used in yeasts, animals, and plants to identify promoter and enhancer environments (15–18); however, work in non-yeast fungi is limited. We have applied this technique to the model filamentous fungus *Neurospora crassa* in order to define chromatin features associated with accessible and inaccessible chromatin and to identify specific chromatin components that regulate chromatin accessibility patterns in the *N. crassa* genome. A recent study investigated histone modifications and small RNAs at *cis*-regulatory elements in cnidarians, fungi, and human cells, providing evidence that small RNAs or RNA polymerase activity are evolutionary conserved features of accessible chromatin (19); our work examines in more detail fundamental features of chromatin accessibility.

As an example, it has been well established that binding of pioneer transcription factors within promoter regions is important for creating an open chromatin environment and promoting transcriptional activity (20–23). Previous MNase experiments in *N. crassa* have shown that binding of the light-response master regulator white collar complex (WCC) subunit white collar 2 (*wc-2*) can change nucleosome organization at promoters of WCC-inducible genes (24). Additionally, application of ATAC-seq in the pathogenic basidiomycete *Cryptococcus neoformans* has demonstrated that transcription factor ZNF2 and the SWI/SNF complex create chromatin accessibility at filamentation genes during filamentation (18).

Recently, the Benner lab has developed a method of extracting and quantifying regulatory elements from bulk RNA in a panel of eukaryotes, including *N. crassa* (19). This method involves isolating capped small RNAs (csRNAs) that are the result of abortive transcription, resulting in putative regulatory RNAs that are ~40-60 bp in length. Through mapping and quantification of these small RNAs, Duttke et al. identified ~16,000 csRNAs, including unstable transcripts at gene-distal regions of highly expressed genes characteristic of regulatory RNAs of metazoan enhancers. Further, they identified an evolutionarily conserved role for active H3K27ac and H3K4me3 in the organisms studied. This study lacked chromatin accessibility data for *N. crassa*, and here we provide further evidence of large, highly accessible domains that are enriched with csRNAs, similar to enhancers.

Methylation of H3K36 is mediated by a single histone methyltransferase, SET2, in yeasts (25–28). This SET2-mediated H3K36me is associated with transcriptional elongation and recruits chromatin remodelers and histone deacetylases to repress spurious

intergenic transcription at cryptic promoters (for a review, see 28). *Neurospora* and the closely related *Fusarium fujikoro*i, however, encode two H3K36 methyltransferases (SET-2 and ASH-1) (29, 30). Like yeast SET2, *Neurospora* SET-2 trimethylates H3K36 along gene bodies and is presumably targeted by elongating RNA polymerase (29). *Neurospora* ASH-1, instead, deposits mono- and di-methylation on H3K36 residues across promoters and gene bodies of silent genes in a transcriptionally independent manner (9). These regions of ASH-1 catalyzed H3K36me<sub>2</sub> co-localize with H3K27me<sub>2/3</sub> and contribute to Polycomb Repressive Complex 2 (PRC2)-mediated repression. *Neurospora* genes marked by H3K36me<sub>2</sub> are transcriptionally repressed and prime chromatin for H3K27me<sub>2/3</sub> by PRC2.

We show here that promoters marked by H3K27me<sub>2/3</sub> and ASH1-dependent H3K36 methylation or ASH1-dependent H3K36 methylation alone are inaccessible. We used genetic manipulation of the essential H3K36 residue to test whether H3K36 methylation limits chromatin accessibility in *Neurospora*. We created single residue mutations of H3K36 by replacing H3K36 with a glutamine (H3K36Q) to mimic an acetylated H3K36 residue or replacing H3K36 with arginine, to mimic unmodified H3K36 (H3K36R) using the dominant selectable marker hygromycin to maintain these mutations within *N. crassa* cells. We then took advantage of the ability of *Neurospora* to maintain a mixed population of nuclei in heterokaryons and we manipulated the gene dosage of H3K36 mutant histones to examine the function of this residue. We have shown that disruption of H3K36me leads to hyperaccessibility in *Neurospora*. This indicates that H3K36 plays an important role in limiting chromatin accessibility in *Neurospora* promoters.

## Materials and Methods

### Culture growth conditions

All liquid cultures were grown in Vogel's minimal medium with 1.5% sucrose with shaking at 32° C for 18 hours. H3K36<sup>mut</sup> strains were grown and maintained in Vogel's minimal medium containing 100 ug/ml hygromycin (1x). Linear growth assays and ATAC-seq assays for H3K36<sup>mut</sup> strains contained 1x (100 ug/ml), 2x (200 ug/ml), or 5x (500 ug/ml) hygromycin in Vogel's minimal medium with 1.5% sucrose.

### Strain construction

Strains were constructed using *N. crassa* using standard protocols (31). H3K36 point mutants were made as described in (32). In brief, H3K36 mutations to glutamine or arginine were introduced by PCR using plasmid pK9L as the template. Mutant H3K36 plasmids were linearized with XbaI and introduced into *Neurospora* strain S302 by electroporation. Strain S302 has the *hH3* sequence from *Fusarium graminearum* in place of the native *Neurospora hH3* and deletion of *mus-51*. Heterokaryotic strains were isolated and maintained on hygromycin. Heterokaryotic strain genotypes were confirmed by PCR followed with Sanger sequencing.

All strains used in this study are listed in Table S1 and primers in Table S2.

### ATAC-seq

ATAC-seq was performed as described in (15, 16). In short, overnight mycelial cultures were lysed in lysis buffer (15 mM Tris pH 7.5; 2 mM EDTA; 0.5 mM spermine; 80 mM KCl; 20 mM NaCl; 15 mM (or 0.1% v/v)  $\beta$ -me; 0.3% TritonX-100) by placing mycelia in a petri dish and chopping mycelia with a razor blade. Nuclei were isolated through repeated filtering through miracloth followed by numerous rounds of gentle



centrifugation (1000 rpm for 5 minutes). Tn5 integration was performed using Tn5 transposase pre-loaded with Illumina sequencing adaptors ; samples were incubated for 30 minutes at 37° C and fragmented DNA was isolated using the Qiagen MinElute kit (Cat#. 28004). Sequencing libraries were constructed using Phusion (ThermoFisher Cat # F549N) and amplified with primers provided in (15). Libraries were cleaned using SeraPure beads (Fisher Cat. # 09-981-123) before submission for sequencing as described in (33). Libraries were sequenced on an Illumina NextSeq 500 instrument by Georgia Genomics Facility at University of Georgia.

### **Data Analysis**

ATAC-seq reads were trimmed and quality scored with TrimGalore! (<https://github.com/FelixKrueger/TrimGalore>). Trimmed reads were mapped to the NC12 genome (GCA\_000182925.2\_NC12) with BowTie2 using the `–very-sensitive` option and setting the maximum insert size set at 2000 bp (34).

Analysis of transcriptional start sites (TSSes) was performed on non-overlapping genes. In short, this list was generated by first generating a list of all TSSes in the *Neurospora* genome with the GenomicRanges package in R (35, 36). This list was compared to the genome annotation file using bedtools closest to identify the distances between TSSes (37). Only those genes with TSSes >1500 bp apart are included in the final non-overlapping genes list (n=5200).

Peaks were called using Genrich (<https://github.com/jsh58/Genrich>) using the ATAC setting (`-j`). Reads were separated by insert size using R (36), and peaks less than 115 bp were called using MACS2 with a q-value cutoff of 0.01 (38). FunCat2 (39) was used for genome ontology analysis. Heatmaps and metaplots were made using deepTools

(40). All peak comparisons were performed with bedtools (37). ATAC-seq peaks were annotated using ChIPseeker (41) (36).

Paired-end RNA-seq data was acquired from Joint Genomes Institute Community Sequencing Project 54089 and were mapped with HISAT2 (42) (38) using standard options. Counts were created with featureCounts (39) and analyzed in R (36). All heatmaps were made using deepTools, and reads were normalized in deepTools for counts per million (CPM) (40).

### **Chromatin Immunoprecipitation (ChIP-seq)**

ChIP-seq was performed as described in (32, 33) with the following antibodies: H3K27me2/3 (ActivMotif Cat# 39535, Lot# 1671401)2; H3K4me1; H3K4me2 (ActivMotif Cat# 29679, Lot# 31713007); H3K4me3 (Abcam Cat# ab1012); H3K36me3 (Abcam Cat# ab9050, Lot# GR300388-1); H3K9me3 (ActivMotif Cat# 39161, Lot# 14418003); H3K27ac; FLAG (Sigma Cat# F1804, Lot# SLBS3530V). Libraries were created and analyzed as described in (33). Libraries were sequenced as described above by Georgia Genomics Facility at University of Georgia. Motif analysis was performed with HOMER findMotif.pl using standard options (43). ChIP-seq peaks were called using MACS2, with a q-value cutoff of 0.01 (38).

MNase-seq for hH3-3xFLAG was performed in cells eight hours after copper induction. Cells were crosslinked in 1% formaldehyde and transferred to NPS buffer (10 mM Tris-HCl, pH 7.5; 50 mM NaCl; 25 mM MgCl; 1 mM CaCl) and sonicated to shear the chromatin. MNase was performed with 20 U/μl Takara MNase (Cat # 2910A) at 37°C for 60 minutes. MNase digestion was quenched with 10 mM EDTA and 100 mM NaCl. Anti-flag ChIP was performed as described above.

$\Delta$ set-2 H3K36me2 ChIP-seq was taken from (9) (SRS3667122). hH2Az-GFP was taken from SRX7873264. *wc-2-TAP* chip was taken from (44) (SRR1578072).

### **csRNA-seq analysis**

csRNA-seq was downloaded from SRA (SRR9916743, SRR9916744, SRR91745, SRR9916746, SRR916747, SRR916748, SRR916749, SRR916750) and mapped to the NC12 genome (GCA\_000182925.2\_NC12 ) and analyzed using csRNA tools developed in HOMER as described in (19).

### **Data availability**

Data will be available via Gene Expression Omnibus (GEO) upon submission.

### **Results**

#### **Characterization of accessible chromatin regions in *N. crassa***

To characterize accessible regions in *N. crassa*, we performed ATAC-seq on overnight wild type mycelial cultures. Because this assay is sensitive to contamination by mitochondria, we first performed ATAC-seq in nuclei that were sorted by flow cytometry and nuclei that were not sorted. We compared the number of total reads from each experiment that mapped to the genome. Sorted nuclei had a 98.4% mapping rate while unsorted nuclei had a 98.5% mapping rate (Table S3). We next looked at the number of reads that mapped to each chromosome of the *Neurospora* genome. Sorted nuclei had a somewhat reduced number of reads that mapped to mitochondria (~15%) when compared to unsorted nuclei (~27%) (Fig. S1A; Table S3).

We next examined the distribution of ATAC-seq reads in sorted versus unsorted nuclei. We first called ATAC-seq peaks using Genrich from wild type sorted and unsorted nuclei (using standard parameters: minimum area under the curve of 200 bp,

significance threshold  $> 1$ , and p-value  $< 0.01$ ). We identified 7132 ATAC-seq peaks in wild type unsorted cells and 5181 ATAC-seq peaks in wild type sorted cells. Of the peaks we identified in sorted cells, 92% overlapped with peaks called in unsorted cells by bedtools intersect ( $n = 4772$ ; Table S4).

We then plotted ATAC-seq enrichment in sorted and unsorted cells centered on the ATAC-seq peaks from unsorted nuclei. Comparison of these two experiments revealed that patterns of accessibility in *Neurospora* is unchanged in sorted and unsorted nuclei (Fig. S1B). This is confirmed in a browser shot of ATAC-seq reads of sorted and unsorted nuclei (Fig. S1C). Thus, sorting nuclei is not sufficient to remove all mitochondrial contamination, and it is more efficient and cost-effective to proceed with unsorted nuclei with downstream removal of mitochondrial reads via samtools. All remaining experiments were performed with unsorted nuclei.

We next wanted to determine what chromatin environments are enriched with ATAC-seq signal. To do this, we first visually inspected ATAC-seq enrichment across the *N. crassa* genome using the Integrated Genomics Viewer (IGV). We found that chromatin accessibility is enriched in promoters and intergenic regions, yet limited or absent in gene bodies (Fig. 1A). Additionally, facultative and constitutive heterochromatin marked by H3K27me2/3 or H3K9me3, respectively, have low levels of chromatin accessibility (Figure 1A).

To quantify the level of accessibility in heterochromatin and euchromatin, we used bedtools intersect to determine the number of ATAC-accessible regions that overlap with H3K27me2/3 or H3K9me3 and have ATAC-seq enrichment (Table S5). H3K27me2/3 is enriched in 309 domains covering 6% of the genome (45). We identified

68 ATAC-seq peaks that overlap with called H3K27me2/3. The average density of ATAC-seq peaks in these domains is 0.27 peaks per 10kb. We also wanted to quantify the number and density of peaks in constitutive heterochromatin marked by H3K9me3. 454 domains are enriched for H3K9me3 covering approximately 18% of the genome. 198 ATAC-seq peaks overlapped with H3K9me3 with an average peak density of 0.32 peaks per 10 kb. The remaining 6620 ATAC-seq peaks are found in regions that lack H3K9me3 or H3K27me2/3, with an average density in euchromatin of 2.1 ATAC-seq peaks per 10 kb.

In general, accessible regions appeared to be restricted to promoter regions of *N. crassa* genes (Fig. 2.1A). To determine if accessibility was a global feature of promoters, we averaged ATAC data across all promoters and plotted the distribution (Fig. 2.1B). This confirmed that ATAC-accessible regions are present in 5' regions of genes. We next wanted to ask if *N. crassa* promoters exhibit distinct patterns of accessibility. We did this by plotting a heatmap of ATAC-seq enrichment across 3000 bp (+/- 1500 bp) of DNA centered on the transcription start site (TSS) of each *Neurospora* gene (Fig. 2.1C). It was difficult to discern organization of accessible regions at the single-gene level because the *N. crassa* genome is compact and many intergenic regions contain a second promoter within the 3000 base pair window plotted for each gene (e.g. nearby or divergently transcribed genes share the same intergenic space; Fig. 2.1C, Left). To remove this confounding variable and better ascertain the diversity of accessible chromatin structures in *N. crassa* promoters, we examined the distribution of ATAC-seq reads only for genes without another annotated transcriptional start site within 1500 base pairs, which is the average intergenic space in *N. crassa* (Table S2.6; see Materials and Methods) (46). We

interrogated the TSSes of these genes and performed naïve k-means clustering to determine patterns of accessibility within promoter regions. Here we show six k-means clusters to illustrate groups of genes with distinct patterns of chromatin accessibility at gene promoters (Fig. 2.1C, Right). This analysis reveals that the size and pattern of ATAC-accessible chromatin varies throughout the *Neurospora* genome. For example, Cluster 1 and 2 show broad, highly accessible domains, with Cluster 1 showing some extension into the gene body compared to Cluster 2. Cluster 3 shows a narrow region of high accessibility at the TSS, whereas Cluster 4 ATAC-seq enrichment has a similar enrichment pattern with a moderately lower level of enrichment. Cluster 5 enrichment is lower and broader than Clusters 1-4, and Cluster 6 shows general depletion of ATAC-seq signal. While the differences between some of these clusters may be subtle, we feel the separation as shown illustrates the nuanced variety of chromatin accessibility patterns in *N. crassa* promoters.

Given the differences in ATAC-seq enrichment levels and patterns in *N. crassa* promoters, we wanted to know if there was a correlation between promoter structure and transcript level. Violin plots of transcripts per million (TPM) of genes within each k-means cluster reveals little difference in transcriptional activity between clusters (Fig. 2.1D). This suggests that chromatin accessibility in *N. crassa* does not necessarily result in mRNA transcription. Instead, it is likely that accessible chromatin regions correspond to binding sites of both transcriptional activators and repressors.

We next asked if distinct promoter structures were enriched for any functional categories of genes. To do this, we used peaks called from unsorted nuclei, as described above (n = 7132). We then ranked peaks by size and focused on accessible regions

greater than 2 kb ( $n = 84$ ). We wanted to know what genes could be associated with these accessible regions, and possibly regulated by complex promoters with large accessible regions, so we annotated peaks to their closest genes (Table S2.4; Fig. 2.1E). Gene Ontology (GO) analysis of the genes annotated to these regions revealed that genes with large, hyperaccessible promoter regions are significantly enriched for sequence-specific DNA binding, transcription factor activity, and regulation of transcription (Fig. 2.1F; Table S2.7). Closer inspection of these genes also reveals that they are involved in cellular processes including light response, conidial separation, and other master regulatory functions, including the carbon catabolite repressor *cre-1*, and a member of the light-response pioneer factor complex WCC, *white collar 1* (*wc-1*).

Because gene annotation software determines annotated genes based on distance from the feature of interest, and these regions could annotate to more than one gene, we were concerned that the annotation software was giving us inaccurate results. We therefore completed the same analysis using Cluster 1 and Cluster 2 from Fig. 1C (Table S2.6). Our analyses revealed that Cluster 2 is enriched for genes which are annotated to have transcriptional roles (i.e. RNA Pol2 activity, TF binding, and sequence-specific DNA binding), while Cluster 1 is more enriched for signal transduction activity (Fig. S2.2; Table S2.7). This supports our finding that hyperaccessible regions are enriched for transcription-associated genes from our annotated peak analysis.

### **ATAC-seq is a powerful tool to characterize pioneer transcriptional factors**

We hypothesized that DNA-binding proteins compete with nucleosomes to create accessible regions. To determine if this is indeed the case, we examined rates of nucleosome exchange across the *N. crassa* genome using an inducible hH3-3xFLAG

protein. We first introduced an H3-3xFLAG fusion protein (*hH3:3xflag*) under the control of a copper-inducible promoter, and we confirmed that the H3-3xFLAG protein is induced under copper limiting conditions and incorporated into chromatin (Fig. 2.2A). We then performed ChIP-seq following MNase digestion (MNase-ChIP) to identify regions with high H3-3xFLAG enrichment, reasoning that incorporation of newly synthesized H3-3xFLAG would preferentially occur in regions with high rates of nucleosome turnover (i.e. due to competition between TFs and nucleosomes). Similar approaches have been validated in other systems (44). We plotted H3-3xFLAG enrichment after 8 hours of induction and found high levels of H3 turnover correspond to ATAC-seq peaks (Fig. 2.2B). We then examined nucleosome turnover (i.e. H3-3xFLAG enrichment) across all ATAC-seq peaks. These data reveal ATAC regions exhibit high nucleosome turnover (Fig. 2C).

We next wanted to investigate the co-occurrence and relative contributions of various chromatin features that function to maintain chromatin structure in *N. crassa*. As a proof of concept, we first asked if disruption of the White Collar Complex (WCC) would lead to altered patterns of accessible chromatin measured by ATAC-seq. Transcription factors have been demonstrated to provide a mechanism for creating chromatin accessibility at gene promoters, and Sancar and colleagues previously implicated WCC in maintenance of accessible chromatin using MNase assays in wild type and strains lacking a functional WCC. Thus, WCC is proposed to function as a pioneer transcription factor to open chromatin (24). We asked if ATAC data might provide comparable or even more robust results than MNase assays by performing ATAC-seq assays in wild type and the *wc-2* mutant. We plotted ATAC-seq reads across



all WCC binding sites (44) for wild type and the *wc-2* mutant. We observed a striking reduction of ATAC accessibility in the  $\Delta wc-2$  mutant. These data confirm that transcription factors are key drivers of open chromatin (Fig. 2.2D,E). To rule out the possibility that our observation of reduced chromatin accessibility at WC-2 binding sites in  $\Delta wc-2$  is not an experimental artefact, we compared heatmaps of wild type ATAC-seq and  $\Delta wc-2$  ATAC-seq and found no overall loss in ATAC-seq enrichment genome-wide (Fig. S2.4).

### **ATAC-seq regions are associated with non-coding transcriptional activity**

We next wanted to identify other chromatin features that correlate with accessible chromatin. Recent work identified small abortive transcripts (capped small RNAs; csRNAs) in *Neurospora* (19), raising the possibility that small RNAs or active transcription is a feature of accessible chromatin in filamentous fungi. These small RNAs are short (< 60 bp); can be stable or unstable, as determined by read depth when compared to total RNA; and can be uni-directional, originating from the plus or minus strand, or bi-directional. Additionally, these RNAs are associated with accessible regions in other eukaryotes, as demonstrated by Duttke et al. (19).

To determine if these abortive transcripts are features of accessible regions in *N. crassa*, we compared the previously published csRNA transcript data to our ATAC-seq data. We first asked if regions that generate csRNA transcripts are accessible. We created a heatmap centered on the TSS of csRNAs sorted by stability and directionality as defined above. When we compare these transcripts to chromatin accessibility data, we find that the TSSes of csRNAs are accessible (Fig 2.3A). Similarly, a plot of csRNA transcripts across all ATAC-seq peaks reveals that csRNA transcription is occurring

adjacent to many accessible chromatin regions, however not all accessible chromatin regions contain high levels of csRNAs (Fig. 2.3B).

To quantify the extent of overlap between chromatin accessibility and csRNA transcripts. We used bedtools intersect to determine accessible chromatin regions that contain csRNA transcripts (Table S2.9) and found that 73% of accessible chromatin regions (n = 5213) overlap with at least one annotated csRNA transcript. Conversely, only 60% of csRNA transcripts (n = 9709) are found within accessible chromatin regions. Many of these csRNA transcripts appeared to flank accessible chromatin regions. This is a feature that is common among higher eukaryotic promoters and enhancers,. We therefore examined enrichment of csRNAs within 100 bp of accessible chromatin in *Neurospora* using bedtools closest. We found that 83% of ATAC-seq peaks either contained or occurred within 100bp of an annotated csRNA transcript (n = 5939). Conversely, approximately 9% of csRNAs were identified within these 100-bp regions (n = 1570). In total, 69% of csRNA transcripts either overlapped or were within 100 bp of an ATAC-seq peak (n = 11,393). Together, these data indicate that transcriptional activity is a widespread feature of accessible regions in *N. crassa*.

### **H3K36me is refractory to chromatin accessibility**

To identify additional chromatin features that are associated with accessible regions, we plotted enrichment of ChIP-seq data for various chromatin marks surrounding accessible regions (Fig. 2.4A). We performed naïve k-means clustering to construct heatmaps using all chromatin features to define patterns of chromatin features at both accessible and inaccessible regions. A heatmap centered on ATAC-seq peaks and reveals that all regions of accessibility are marked with the active chromatin marks

H3K27ac. The density of full length mRNA-seq reads was also plotted across these ATAC-seq peaks, indicating the direction of productive transcription. The heatmap in Fig. 2.4A further supports the conclusion that transcription of mRNAs is not associated with all accessible chromatin regions, as shown by the low level of mRNA enrichment in Clusters 3 and 4. H3K4me was correlated with productive transcripts but was not associated with accessible chromatin regions.

H2A.Z is associated with accessible regions in other organisms (10, 11, 14, 47–49). Moreover, H2A.Z is reportedly required for normal chromatin accessibility in in Embryonic Stem Cells (50). We compared previously published H2A.Z ChIP-seq (45) data to our ATAC-seq data and found that H2A.Z was enriched flanking most, but not all ATAC peaks (e.g. see Cluster 3). We then carried out ATAC-seq experiments in wild type and  $\Delta hH2Az$ , which revealed that loss of H2A.Z did not have alter global patterns of chromatin accessibility in *Neurospora* (Fig. 2.4C).

Recent work has identified a novel role of ASH-1-mediated H3K36me2 in gene repression in *Neurospora* (9). Namely, Bicocca et al. identified regions of the *Neurospora* genome that were both transcriptionally repressed and marked by H3K27me2/3 and H3K36me2 (9). We compared these data with our chromatin accessibility data and found a small number of ATAC-seq peaks that are marked by these repressive chromatin marks (Cluster 4 of Fig. 2.4A). Small regions of accessibility have been identified in facultative heterochromatin in other organisms; ATAC-seq experiments in *Drosophila* show that chromatin accessibility within Polycomb-target regions is limited to sites of Polycomb recruitment in a developmental-dependent manner (51). We therefore hypothesized that these may be PREs and ran a motif analysis of the sequences underlying these peaks

using HOMER (43). We did not identify any statistically significant DNA sequence motifs in these regions (Figure S2.4). Next, we compared the pattern of ATAC-seq, H3K27me2/3 and ASH1-catalyzed H3K36 methylation across unique promoters. A heatmap centered on the TSS of distinct promoters shows that promoters marked by H3K27me2/3 and H3K36me2 or H3K36me2 alone are highly inaccessible (Fig. 2.4).

### **Genetic analysis of H3K36 reveals a role in limiting chromatin accessibility in *Neurospora***

We wanted to determine if H3K27 or H3K36 methylation is important for limiting chromatin accessibility. We first performed ATAC-seq in a *Δset-7* mutant and plotted the data across promoters as in Figure 2.4C. We observed no increase in accessibility globally or with H3K27me2/3 regions (Fig S2.5A). We next focused on H3K36 methylation. ASH-1 is essential in *N. crassa*, making it difficult to examine the role of H3K36me2 in *Neurospora*. We instead made single point mutations in histone H3: H3K36Q (lysine to glutamine; acetyl mimic) and H3K36R (lysine to arginine: unmodified lysine mimic) marked with a hygromycin resistance gene (*H3K36<sup>mut</sup>:hyg*) using a *Neurospora* strain in which the native histone H3 had been replaced by the closely related *Fusarium graminearum* histone H3 (*hH3::FgH3:bar*) (32). Primary transformants backcrossed to a wild-type *Neurospora* strain yielded no progeny with the *H3K36<sup>mut</sup>* genotype, supporting the finding by Adhvaryu and Selker that H3K36 is a critical residue for *Neurospora* (29). We took advantage of the fact that primary transformants of *N. crassa* contain a mixture of untransformed (wild type) and transformed *H3K36<sup>mut</sup>* nuclei, which enabled us to modulate the ratio of wild type to *H3K36<sup>mut</sup>* nuclei within *Neurospora* cells by using varying concentrations of hygromycin

(Fig. 2.5A). Sanger sequencing of the hH3 locus at increasing concentrations of hygromycin revealed that at 5x hygromycin concentration resulted in a 50% allele ratio of the *H3K36<sup>mut</sup>* genotype within the cell population (Fig. 2.5B). Linear growth experiments of these strains also revealed a dose-dependent growth phenotype in H3K36R and H3K36Q (Fig. S2.5B).

We performed ATAC-seq in the *H3K36<sup>mut</sup>* strains with 5x hygromycin concentrations. We also performed ATAC-seq in the H3K36me3 methyltransferase deletion *Δset-2* to determine if changes in chromatin accessibility were due to H3K36me2 or H3K36me3. To understand the role of H3K36me2 in accessibility, we called ATAC-seq peaks in all strains and combined them into a master peak file to isolate all potential accessible chromatin regions and merged overlapping peaks using bedtools merge (Table S10). We plotted ATAC-seq enrichment over all peaks in order of enrichment (Fig. 2.5C). While *Δset-2* exhibits mild increase in accessibility compared to wild type, *H3K36<sup>mut</sup>* strains exhibit hyperaccessibility compared to wild type and *Δset-2*.

We used bedtools intersect to determine peaks that overlap between wild type and *H3K36<sup>mut</sup>* strains using bedtools intersect (Table S2.10). Our peak calling in H3K36Q and H3K36R grown in 5x hygromycin identified 5776 and 3108 peaks, respectively. We found that 96% of peaks in H3K36Q overlapped with wild type peaks (n = 5587), and 99% of peaks in H3K36R overlapped with wild type peaks (n = 3087). Because almost all peaks identified in *H3K36<sup>mut</sup>* strains overlapped with wild type strains, we next plotted ATAC-seq enrichment across all genes in the same order as Figure 2.4C, but with the regions scaled to include the gene body and 500 bp up and downstream of the gene (Fig.

2.5D). We observed subtle gains in silent H3K36me3 or H3K27me3 regions (Clusters 1 and 2), and a more striking increase in accessibility within typically accessible regions.

## Discussion

We have presented the first analysis of promoter structure and chromatin accessibility in a filamentous fungus using ATAC-seq. While these studies were first developed in yeast and later applied to higher eukaryotes, filamentous fungi are important in ecological, clinical, and evolutionary contexts and *Neurospora crassa* is an important model for chromatin and epigenetic studies due to shared pathways with higher eukaryotes. Our analyses have revealed properties of accessible promoter regions in filamentous fungi. It is also the first experimentally demonstrated report that facultative and constitutive heterochromatin regions are inaccessible in *N. crassa*. Notably, we show that accessible promoters are not necessarily correlated with transcription. Conversely, there is a strong correlation between accessible chromatin and H3 turnover. We present a model in which accessible chromatin results from a competition between promoters and DNA-binding transcription factors. Indeed, we confirm using ATAC-seq that WCC is required to open chromatin in WCC target promoters. Our data suggest that ATAC-seq provides a more robust method to analyze pioneer transcription factor activity than previously used methods such as MNase.

Our findings in combination with findings from Duttke et al. demonstrate that abortive transcription is a key feature of accessible chromatin, raising the possibility that enhancer-like elements are present in fungi. These have traditionally been considered to be absent from simpler eukaryotes but work in *Neurospora* and the cnidarian *Nematostella* (19, 52) suggest that these may in fact be evolutionarily conserved

mechanisms of eukaryotic gene regulation. In higher eukaryotes, short unstable RNAs typically flank enhancers and promoters. Our integration of csRNA-seq and ATAC-seq suggests that these RNAs also exist in *Neurospora*. These RNAs may serve a number of different functions: (1) They could simply be results of promiscuous Pol II activity and play no real function at all; (2) These could be regulatory RNAs; or (3) The act of transcription may be important in maintaining open chromatin in filamentous fungi. Recently, a new model of promoter/enhancer characterization has been proposed in which genomic regulatory elements have enhancer and promoter potential (53). This model defines promoters and enhancers as regulatory elements at any accessible chromatin region bound by transcription factors, with the ability to recruit Pol II and initiate transcription at either edge, which can positively influence transcription initiation at other regulatory elements. Therefore, it is likely that these RNAs themselves may not be regulatory, but Pol II recruitment to regulatory elements leads to some level of transcription, and the occupancy of Pol II at these sites helps to maintain their accessibility.

We did find a subset of annotated csRNA loci that were not associated with ATAC-seq peaks; however, these may reflect differences in growth conditions used for our ATAC-seq experiments and the csRNA experiments carried out by Duttke et al. Experimental variations including growth conditions, single versus mixed tissue type, and light exposure can produce quite varied results in *Neurospora* expression profiles. It will be important, therefore, to perform more in-depth at these putative *cis*-regulatory regions to determine the role and abundance of these types of RNAs. Importantly, the growth conditions of the csRNA-seq experiments performed by Duttke et al. vary from our

ATAC-seq protocol: csRNA-seq cultures were grown for two days at constant light, while ATAC-seq cultures were grown overnight at constant light. Therefore, matched experiments will allow for more fine-tuned associations between csRNA production and chromatin accessibility.

The presence of H3K27me<sub>2/3</sub> in a small number of accessible chromatin regions also presents an interesting finding, suggesting that polycomb response elements may exist in filamentous fungi. While recent work has identified telomere repeat sequences and the presence of H3K36me<sub>2</sub> as prerequisites for H3K27me via PRC2 (54, 55), the mechanism of H3K27me establishment in fungi remains elusive. More work will need to be done to determine if these accessible polycomb-target regions are indeed playing a role in recruitment of PRC2 and establishment of H3K27me. Our results support the findings reported in Bicocca et al., and suggest that H3K36me plays a role in gene repression. We extend these findings by showing that H3K27me<sub>2/3</sub> and ASH1-dependent H3K36 methylation are correlated with inaccessible chromatin in *Neurospora*.

Anti-sense transcription at the *Neurospora frq* locus has been demonstrated to regulate circadian clock function via H3K36me<sub>3</sub> (56, 57). The anti-sense transcript of *frq* (*qrf*) results in Pol II stalling at the *frq* locus, premature termination of transcription, and establishment of H3K36me<sub>3</sub>, which precludes binding by White Collar Complex (WCC) and therefore prevents initiation of sense transcription of *frq* and disrupts circadian clock function (56). Additional work in *Aspergillus nidulans* has demonstrated that loss of the lysine demethylase KdmB led to a transcription-independent increase of H3K36me<sub>3</sub> at secondary metabolism biosynthesis clusters and global increased gene expression,



suggesting that this transcription-independent H3K36me3 acts as a transcriptional repressor in *A. nidulans* (58).

Importantly, we identified a potential role for H3K36me in limiting chromatin accessibility in *Neurospora*. Our genetic manipulation of H3K36 resulted in an increased accessibility phenotype within normally accessible chromatin regions. We hypothesize that insertion of H3K36<sup>MUT</sup> histones into the genome is stochastic; however, our experimental system does not provide a means of identifying the locations of H3K36<sup>MUT</sup> histones. A tagged histone mutant will need to be constructed to test this. Additionally, future ChIP-seq experiments in these *H3K36<sup>mut</sup>* strains will provide insight into any changes in histone modifications upon disruption of H3K36.

Additionally, it is possible that disruption of any lysine residue on a given histone could disrupt chromatin accessibility. Recent modeling using known affinity data of DNA with histones in different charge states does predict that change in H3K36 charge can lead to significant loosening of chromatin at the entry/exit position of nucleosomes (~20 bp preceding the section of the nucleosome that interacts with the globular domains of core histones) (59). This could provide insight into our hyperaccessibility phenotype, and possibly the essentiality of the H3K36 residue in *Neurospora*. It is possible that maintenance of charge state on this residue is critical for maintaining histone-DNA interactions. The same effect was predicted for H3K27ac, which provides support for this residue as a key factor in establishing chromatin accessibility. Importantly, this work did not find widespread changes in accessibility with all charge-altering post-translation modifications on all residues. This supports a hypothesis that our increased accessibility

phenotype is unique to H3K36. Further experimental work like ours exploring other lysine residues can provide more insight into this.

The recent work investigating H3K36me in *Neurospora* could provide a model for gene repression in these fungi and has been proposed as a gene repression mechanism in fungi lacking H3K27me3 (4, 58). For example, ASH1-mediated H3K36me2 has also been studied in *Fusarium fujikoro*. *F. fujikoro* strains lacking ASH-1 mediated H3K36me2 exhibited increased expression of secondary metabolism biosynthetic clusters (30). H3K36me3 also performs a repressive role in *S. cerevisiae* and *S. pombe*, where it is responsible for repressing cryptic transcription and heterochromatic silencing via recruitment of nucleosome remodelers and histone deacetylases (60–62). In *Aspergillus*, H3K36me3 was shown to contribute to silencing of the sterigmatocystin biosynthesis cluster (63). It is possible, therefore, that H3K36me plays a conserved role in gene repression in fungi, namely by contributing to a repressive local chromatin architecture, as suggested by the work here.

## References

1. Klemm SL, Shipony Z, Greenleaf WJ. 2019. Chromatin accessibility and the regulatory epigenome. *Nat Rev Genet* 2019/01/25. 20:207–220.
2. Allshire RC, Javerzat JP, Redhead NJ, Cranston G. 1994. Position effect variegation at fission yeast centromeres. *Cell*.
3. Schotta G, Ebert A, Reuter G. 2003. SU(VAR)3-9 is a conserved key function in heterochromatic gene silencing. *Genetica*.
4. Reyes-Dominguez Y, Bok JW, Berger H, Shwab EK, Basheer A, Gallmetzer A, Scazzocchio C, Keller N, Strauss J. 2010. Heterochromatic marks are associated with the repression of secondary metabolism clusters in *Aspergillus nidulans*. *Mol Microbiol*.

5. Czermin B, Melfi R, McCabe D, Seitz V, Imhof A, Pirrotta V. 2002. Drosophila enhancer of Zeste/ESC complexes have a histone H3 methyltransferase activity that marks chromosomal Polycomb sites. *Cell*.
6. Margueron R, Reinberg D. 2011. The Polycomb complex PRC2 and its mark in life. *Nature*.
7. Jamieson K, Rountree MR, Lewis ZA, Stajich JE, Selker EU. 2013. Regional control of histone H3 lysine 27 methylation in Neurospora. *Proc Natl Acad Sci U S A*.
8. Connolly LR, Smith KM, Freitag M. 2013. The Fusarium graminearum Histone H3 K27 Methyltransferase KMT6 Regulates Development and Expression of Secondary Metabolite Gene Clusters. *PLoS Genet*.
9. Bicocca VT, Ormsby T, Adhvaryu KK, Honda S, Selker EU. 2018. ASH1-catalyzed H3K36 methylation drives gene repression and marks H3K27me2/3-competent chromatin. *Elife*2018/11/24. 7.
10. Guillemette B, Bataille AR, Gévry N, Adam M, Blanchette M, Robert F, Gaudreau L. 2005. Variant histone H2A.z is globally localized to the promoters of inactive yeast genes and regulates nucleosome positioning. *PLoS Biol*.
11. Barski A, Cuddapah S, Cui K, Roh TY, Schones DE, Wang Z, Wei G, Chepelev I, Zhao K. 2007. High-Resolution Profiling of Histone Methylations in the Human Genome. *Cell*.
12. Bargaje R, Alam MP, Patowary A, Sarkar M, Ali T, Gupta S, Garg M, Singh M, Purkanti R, Scaria V, Sivasubbu S, Brahmachari V, Beena Pillai. 2012. Proximity of H2A.Z containing nucleosome to the transcription start site influences gene expression levels in the mammalian liver and brain. *Nucleic Acids Res*.
13. Weber CM, Ramachandran S, Henikoff S. 2014. Nucleosomes are context-specific, H2A.Z-Modulated barriers to RNA polymerase. *Mol Cell*.
14. Dai X, Bai Y, Zhao L, Dou X, Liu Y, Wang L, Li Y, Li W, Hui Y, Huang X, Wang Z, Qin Y. 2018. Erratum: H2A.Z Represses Gene Expression by Modulating Promoter Nucleosome Structure and Enhancer Histone Modifications in Arabidopsis (*Molecular Plant* (2017) 10(10) (1274–1292) (S1674205217302708) (10.1016/j.molp.2017.09.007)). *Mol Plant*.
15. Buenrostro JD, Giresi PG, Zaba LC, Chang HY, Greenleaf WJ. 2013. Transposition of native chromatin for fast and sensitive epigenomic profiling of open chromatin, DNA-binding proteins and nucleosome position. *Nat Methods* 10:1213–1218.

16. Lu Z, Hofmeister BT, Vollmers C, DuBois RM, Schmitz RJ. 2017. Combining ATAC-seq with nuclei sorting for discovery of cis-regulatory regions in plant genomes. *Nucleic Acids Res* 2016/12/03. 45:e41.
17. Satpathy AT, Saligrama N, Buenrostro JD, Wei Y, Wu B, Rubin AJ, Granja JM, Lareau CA, Li R, Qi Y, Parker KR, Mumbach MR, Serratelli WS, Gennert DG, Schep AN, Corces MR, Khodadoust MS, Kim YH, Khavari PA, Greenleaf WJ, Davis MM, Chang HY. 2018. Transcript-indexed ATAC-seq for precision immune profiling. *Nat Med* 2018/04/25. 24:580–590.
18. Lin J, Zhao Y, Ferraro AR, Yang E, Lewis ZA, Lin X. 2019. Transcription factor Znf2 coordinates with the chromatin remodeling SWI/SNF complex to regulate cryptococcal cellular differentiation. *Commun Biol* 2.
19. Duttke SH, Chang MW, Heinz S, Benner C. 2019. Identification and dynamic quantification of regulatory elements using total RNA. *Genome Res* 29:1836–1846.
20. Zaret KS, Carroll JS. 2011. Pioneer transcription factors: Establishing competence for gene expression. *Genes Dev*.
21. Magnani L, Eeckhoutte J, Lupien M. 2011. Pioneer factors: Directing transcriptional regulators within the chromatin environment. *Trends Genet*.
22. Soufi A, Garcia MF, Jaroszewicz A, Osman N, Pellegrini M, Zaret KS. 2015. Pioneer transcription factors target partial DNA motifs on nucleosomes to initiate reprogramming. *Cell*.
23. Meers MP, Janssens DH, Henikoff S. 2019. Pioneer Factor-Nucleosome Binding Events during Differentiation Are Motif Encoded. *Mol Cell*.
24. Sancar C, Ha N, Yilmaz R, Tesorero R, Fisher T, Brunner M, Sancar G. 2015. Combinatorial Control of Light Induced Chromatin Remodeling and Gene Activation in *Neurospora*. *PLoS Genet*.
25. Strahl BD, Grant PA, Briggs SD, Sun Z-W, Bone JR, Caldwell JA, Mollah S, Cook RG, Shabanowitz J, Hunt DF, Allis CD. 2002. Set2 Is a Nucleosomal Histone H3-Selective Methyltransferase That Mediates Transcriptional Repression. *Mol Cell Biol*.
26. Lickwar CR, Rao B, Shabalin AA, Nobel AB, Strahl BD, Lieb JD. 2009. The set2/Rpd3S pathway suppresses cryptic transcription without regard to gene length or transcription frequency. *PLoS One* 4.

27. Venkatesh S, Smolle M, Li H, Gogol MM, Saint M, Kumar S, Natarajan K, Workman JL. 2012. Set2 methylation of histone H3 lysine 36 suppresses histone exchange on transcribed genes. *Nature*.
28. McDaniel SL, Strahl BD. 2013. Stress-Free with Rpd3: a Unique Chromatin Complex Mediates the Response to Oxidative Stress. *Mol Cell Biol* 33:3726–3727.
29. Adhvaryu KK, Morris SA, Strahl BD, Selker EU. 2005. Methylation of histone H3 lysine 36 is required for normal development in *Neurospora crassa*. *Eukaryot Cell*.
30. Janevska S, Baumann L, Sieber CMK, Münsterkötter M, Ulrich J, Kämper J, Guldener U, Tudzynski B. 2018. Elucidation of the two H3K36me3 histone methyltransferases set2 and ash1 in *fusarium fujikuroi* unravels their different chromosomal targets and a major impact of ash1 on genome stability. *Genetics*.
31. Colot H V., Park G, Turner GE, Ringelberg C, Crew CM, Litvinkova L, Weiss RL, Borkovich KA, Dunlap JC. 2006. A high-throughput gene knockout procedure for *Neurospora* reveals functions for multiple transcription factors. *Proc Natl Acad Sci U S A*.
32. Sasaki T, Lynch KL, Mueller C V., Friedman S, Freitag M. 2014. Heterochromatin controls  $\gamma$ H2A localization in *Neurospora crassa*. *Eukaryot Cell*.
33. Ferraro AR, Lewis ZA. 2018. ChIP-seq analysis in *Neurospora crassa* *Methods in Molecular Biology*.
34. Langmead B, Salzberg SL. 2012. Fast gapped-read alignment with Bowtie 2. *Nat Methods* 2012/03/06. 9:357–359.
35. Lawrence M, Huber W, Pagès H, Aboyoun P, Carlson M, Gentleman R, Morgan MT, Carey VJ. 2013. Software for Computing and Annotating Genomic Ranges. *PLoS Comput Biol*.
36. R Core Team. 2014. R Core Team (2014). R: A language and environment for statistical computing. R Found Stat Comput Vienna, Austria URL <http://wwwR-project.org/>.
37. Quinlan AR, Hall IM. 2010. BEDTools: A flexible suite of utilities for comparing genomic features. *Bioinformatics*.
38. Zhang Y, Liu T, Meyer CA, Eeckhoutte J, Johnson DS, Bernstein BE, Nusbaum C, Myers RM, Brown M, Li W, Liu XS. 2008. Model-based analysis of ChIP-Seq (MACS). *Genome Biol* 2008/09/19. 9:R137.
39. Ruepp A, Zollner A, Maier D, Albermann K, Hani J, Mokrejs M, Tetko I, Guldener U, Mannhaupt G, Munsterkotter M, Mewes HW. 2004. The FunCat, a

- functional annotation scheme for systematic classification of proteins from whole genomes. *Nucleic Acids Res* 2004/10/16. 32:5539–5545.
40. Ramirez F, Ryan DP, Gruning B, Bhardwaj V, Kilpert F, Richter AS, Heyne S, Dundar F, Manke T. 2016. deepTools2: a next generation web server for deep-sequencing data analysis. *Nucleic Acids Res* 2016/04/16. 44:W160-5.
  41. Yu G, Wang LG, He QY. 2015. ChIP seeker: An R/Bioconductor package for ChIP peak annotation, comparison and visualization. *Bioinformatics*.
  42. Kim D, Langmead B, Salzberg SL. 2015. Hisat2. *Nat Methods*.
  43. Benner C, Heinz S, Glass CK. 2017. HOMER - Software for motif discovery and next generation sequencing analysis. [Http://HomerUcsdEdu/](http://HomerUcsdEdu/).
  44. Smith KM, Sancar G, Dekhang R, Sullivan CM, Li S, Tag AG, Sancar C, Bredeweg EL, Priest HD, McCormick RF, Thomas TL, Carrington JC, Stajich JE, Bell-Pedersen D, Brunner M, Freitag M. 2010. Transcription factors in light and circadian clock signaling networks revealed by genomewide mapping of direct targets for neurospora white collar complex. *Eukaryot Cell*.
  45. Courtney AJ, Kamei M, Ferraro AR, Gai K, Hu Q, Honda S, Lewis ZA. 2020. The histone variant H2A.Z is required to establish normal patterns of H3K27 methylation in *Neurospora crassa*. *bioRxiv*.
  46. Borkovich KA, Alex LA, Yarden O, Freitag M, Turner GE, Read ND, Seiler S, Bell-Pedersen D, Paietta J, Plesofsky N, Plamann M, Goodrich-Tanrikulu M, Schulte U, Mannhaupt G, Nargang FE, Radford A, Selitrennikoff C, Galagan JE, Dunlap JC, Loros JJ, Catcheside D, Inoue H, Aramayo R, Polymenis M, Selker EU, Sachs MS, Marzluf GA, Paulsen I, Davis R, Ebbole DJ, Zelter A, Kalkman ER, O'Rourke R, Bowring F, Yeadon J, Ishii C, Suzuki K, Sakai W, Pratt R. 2004. Lessons from the genome sequence of *Neurospora crassa*: tracing the path from genomic blueprint to multicellular organism. *Microbiol Mol Biol Rev* 2004/03/10. 68:1–108.
  47. Guillemette B, Gaudreau L. 2006. H2A.Z: A histone variant that decorates gene promoters. *Medecine/Sciences*.
  48. Creighton MP, Markoulaki S, Levine SS, Hanna J, Lodato MA, Sha K, Young RA, Jaenisch R, Boyer LA. 2008. H2AZ Is Enriched at Polycomb Complex Target Genes in ES Cells and Is Necessary for Lineage Commitment. *Cell*.
  49. Latorre I, Chesney MA, Garrigues JM, Stempor P, Appert A, Francesconi M, Strome S, Ahringer J. 2015. The DREAM complex promotes gene body H2A.Z for target repression. *Genes Dev*.

50. Hu G, Cui K, Northrup D, Liu C, Wang C, Tang Q, Ge K, Levens D, Crane-Robinson C, Zhao K. 2013. H2A.Z facilitates access of active and repressive complexes to chromatin in embryonic stem cell self-renewal and differentiation. *Cell Stem Cell*.
51. Abed JA, Ghotbi E, Ye P, Frolov A, Benes J, Jones RS. 2018. De novo recruitment of polycomb-group proteins in drosophila embryos. *Dev*.
52. Schwaiger M, Schönauer A, Rendeiro AF, Pribitzer C, Schauer A, Gilles AF, Schinko JB, Renfer E, Fredman D, Technau U. 2014. Evolutionary conservation of the eumetazoan gene regulatory landscape. *Genome Res*.
53. Andersson R, Sandelin A. 2020. Determinants of enhancer and promoter activities of regulatory elements. *Nat Rev Genet*.
54. Jamieson K, McNaught KJ, Ormsby T, Leggett NA, Honda S, Selker EU. 2018. Telomere repeats induce domains of H3K27 methylation in *Neurospora*. *Elife*.
55. Wiles ET, McNaught KJ, Kaur G, Selker JML, Ormsby T, Aravind L, Selker EU. 2020. Evolutionarily ancient BAH-PHD protein mediates Polycomb silencing. *Proc Natl Acad Sci U S A*.
56. Xue Z, Ye Q, Anson SR, Yang J, Xiao G, Kowbel D, Glass NL, Crosthwaite SK, Liu Y. 2014. Transcriptional interference by antisense RNA is required for circadian clock function. *Nature*.
57. Sun G, Zhou Z, Liu X, Gai K, Liu Q, Cha J, Kaleri FN, Wang Y, He Q. 2016. Suppression of WHITE COLLAR-independent frequency transcription by histone H3 lysine 36 methyltransferase SET-2 is necessary for clock function in *Neurospora*. *J Biol Chem*.
58. Gacek-Matthews A, Berger H, Sasaki T, Wittstein K, Gruber C, Lewis ZA, Strauss J. 2016. KdmB, a Jumonji Histone H3 Demethylase, Regulates Genome-Wide H3K4 Trimethylation and Is Required for Normal Induction of Secondary Metabolism in *Aspergillus nidulans*. *PLoS Genet*.
59. Fenley AT, Anandakrishnan R, Kidane YH, Onufriev A V. 2018. Modulation of nucleosomal DNA accessibility via charge-altering post-translational modifications in histone core. *Epigenetics and Chromatin*.
60. Smolle M, Venkatesh S, Gogol MM, Li H, Zhang Y, Florens L, Washburn MP, Workman JL. 2012. Chromatin remodelers Isw1 and Chd1 maintain chromatin structure during transcription by preventing histone exchange. *Nat Struct Mol Biol*.

61. DeGennaro CM, Alver BH, Marguerat S, Stepanova E, Davis CP, Bahler J, Park PJ, Winston F. 2013. Spt6 Regulates Intragenic and Antisense Transcription, Nucleosome Positioning, and Histone Modifications Genome-Wide in Fission Yeast. *Mol Cell Biol*.
62. Suzuki S, Kato H, Suzuki Y, Chikashige Y, Hiraoka Y, Kimura H, Nagao K, Obuse C, Takahata S, Murakami Y. 2016. Histone H3K36 trimethylation is essential for multiple silencing mechanisms in fission yeast. *Nucleic Acids Res*.
63. Gacek-Matthews A, Noble LM, Gruber C, Berger H, Sulyok M, Marcos AT, Strauss J, Andrianopoulos A. 2015. KdmA, a histone H3 demethylase with bipartite function, differentially regulates primary and secondary metabolism in *Aspergillus nidulans*. *Mol Microbiol*.

## Tables

**Table S1. Strains used in this study**

Strain ID	Genotype
FGSC4200	Wild type
S630	<i>hH2A.z::hyg</i>
FGSC11124	<i>wc-2::hyg</i>
S564	<i>csr-1::pTCU-1:hH3:3x-FLAG:hyg</i>
Aft35-1,-2,-3	<i>FgH3::NcH3K36Q::hyg</i>
Aft34-1,-2,-3	<i>FgH3::NcH3K36R::hyg</i>

**Table S2. Primers used in this study**

Primer name	Sequence
MF hH3 StuSplit	CCCGGTCCGCACATACATAA
H3K36 genotype internal	GGCGAGCTGGATGTCCTTG
H3 geno R	GGCGAGCTGGATGTCCTTG
K36R_F	GCG GTG TCC GCA AGC CCC ACC



	GTT ACA AGC CCG GTA CCG TCG CTC TC
K36R_R	CGG TGG GGC TTG CGG ACA CCG CCG GTG GAG GGG GCG GAC TTG
K36Q_F	GCG GTG TCC AGA AGC CCC ACC GTT ACA AGC CCG GTA CCG TCG CTC TC
K36Q_R	CGG TGG GGC TTC TGG ACA CCG CCG GTG GAG GGG GCG GAC TTG

**Table S3. Mapping statistics of sorted and unsorted nuclei**

Sample	Total Reads	Mapped Reads	% Mapped Reads	Chromoso mal reads	Mitochond rial Reads	% Mitochond rial Reads
Sorted	41,725,868	41,0725,868	98.4392	35,587,105	6,138,763	14.7121
Unsorted	34,429,284	33,905,374	98.4783	25,119,456	9,609,828	27.0

**Table S4. WT ATAC-seq peaks**

ATAC-seq peaks called in WT sorted and unsorted strains. Overlapping peaks between unsorted and sorted strains. Annotated WT sorted peaks.

**Table S5. ATAC-seq peaks in heterochromatin regions**

Peaks that overlap with H3K27me3 regions and H3K9me3 regions.

**Table S6. Nonoverlapping genes**

Non-overlapping genes used for heatmaps. Clustered list of these regions.

**Table S7. GO analyses**

GO analysis results for ATAC regions > 2kb, as well as Clusters 1 and 2.

**Table S8. WC-2 peaks**

WC-2 ChIP peaks.

**Table S9. csRNA-seq data**

csRNA-seq TSS clusters and all overlaps.

**Table S10. H3K36mut Peaks**

Peaks called in H3K36mut strains and all overlaps.

## Figures

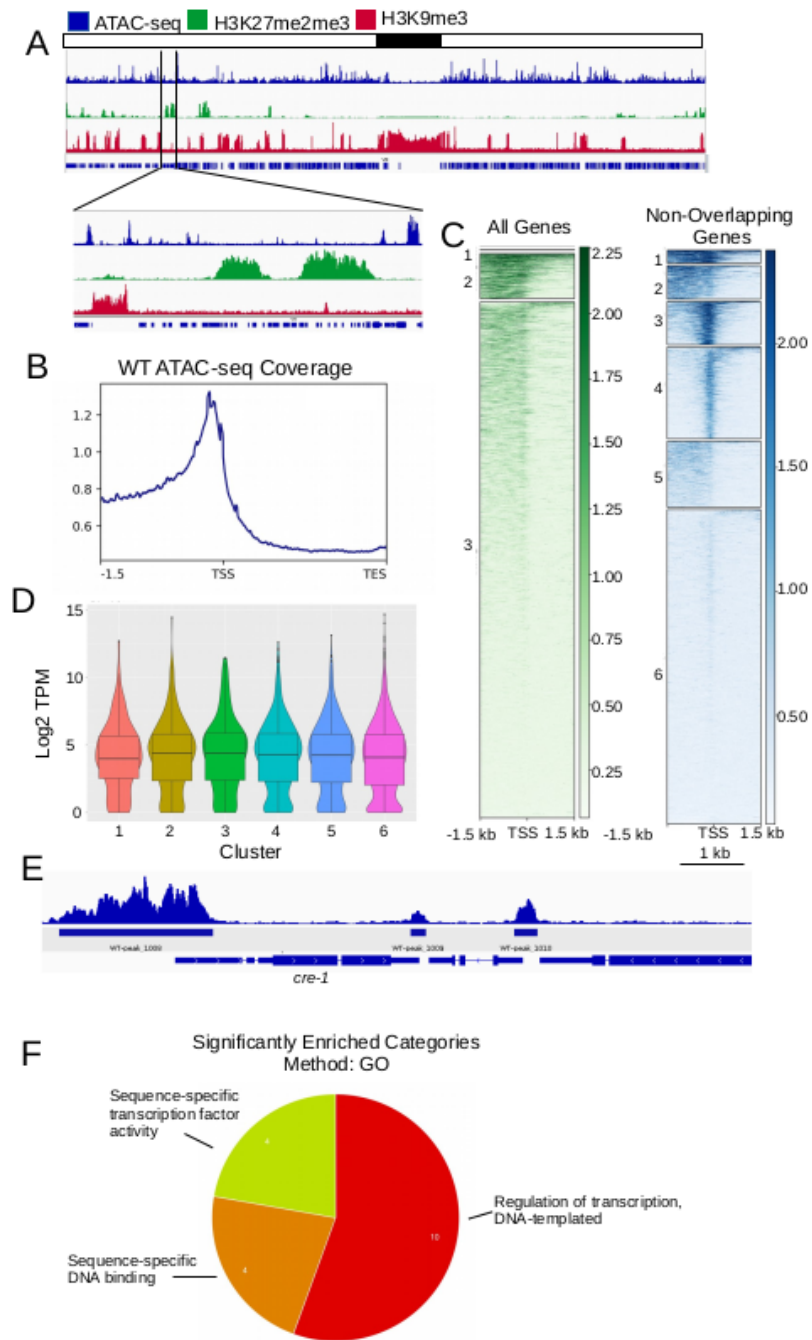


Figure 2.1. Open chromatin is present in gene promoters and absent from heterochromatin. (A) IGV browser shots showing wild type ATAC-seq (blue), H3K27me3 (green) and H3K9me3 (red) localization on Linkage Group VII. (B) Metaplot

showing the average enrichment of ATAC-seq experiments across all *N. crassa* genes. (C) A k-means clustered heatmap centered on the TSS of all genes (left;  $k = 3$ ) versus unique genes (right;  $k = 6$ ) illustrates distinct patterns of chromatin accessibility in promoters. (D) Violin plots of transcript per million (TPM) values of genes visualized in C. TPM values are plotted in the same order as clusters in C. (E) Representative browser shot of *cre-1* (carbon catabolite repression) shows a large domain of chromatin accessibility (2520 bp). (F) GO analysis shows enrichment for DNA binding and transcription factor activity of genes with large intergenic hyperaccessible domains.

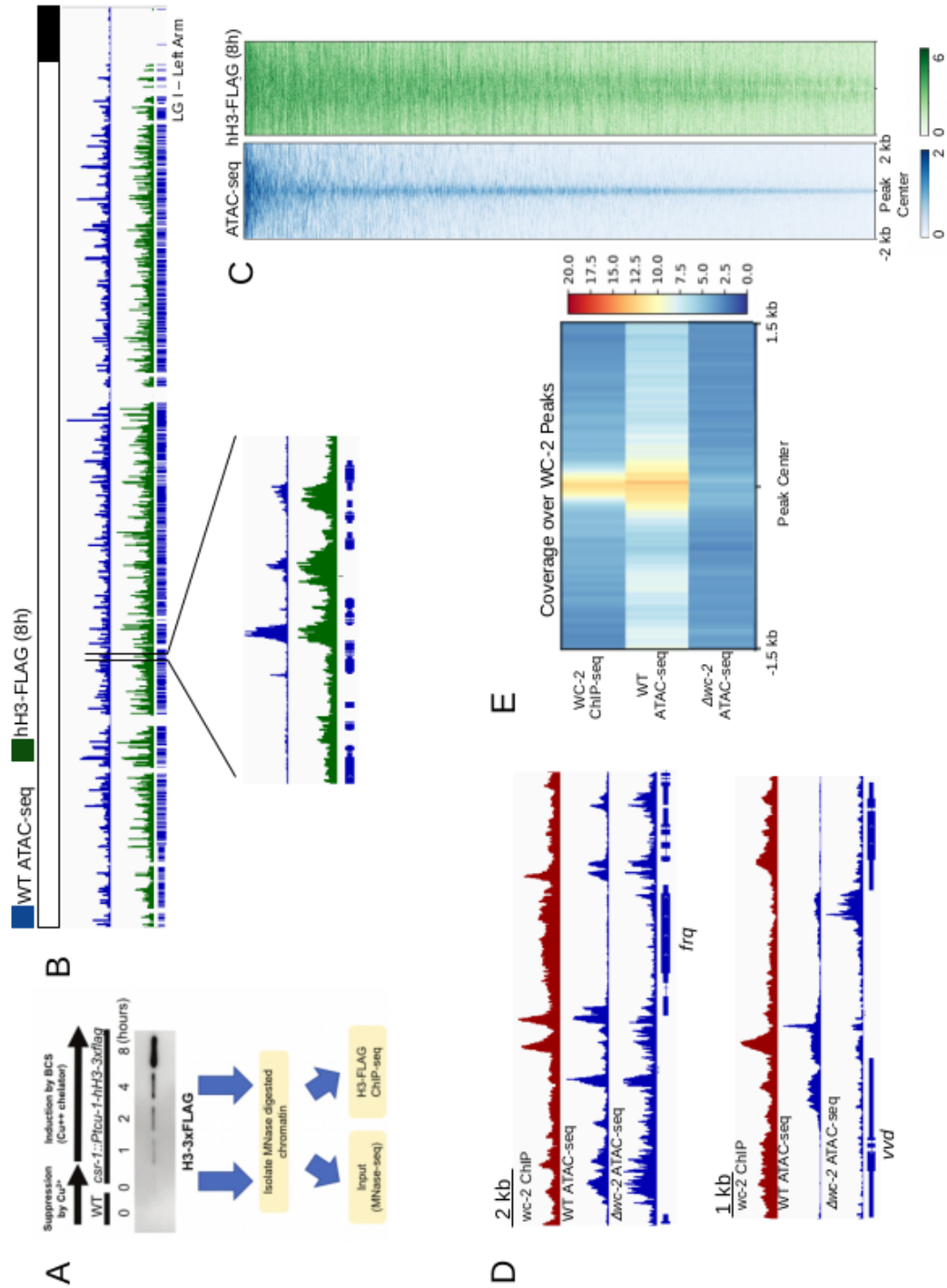


Figure 2.2. Chromatin accessibility is associated with nucleosome turnover and transcription factor binding. (A) Diagram of scheme using ectopic histone H3 under the control of a copper-regulated promoter to measure integration of new H3 (i.e. hH3

turnover). Western blot shows protein levels at 0, 1, 2, 3, 4, and 8 h after induction of H3-3XFLAG. (B) A browser shot of the left arm of Linkage Group 1 (LGI-Left Arm) showing the overlap of histone turnover and chromatin accessibility. (C) The heatmap shows global overlap of chromatin accessibility and histone turnover. The heatmaps are centered on ATAC-seq peaks and ordered by peak size. (D) Representative browser shot of the *frq* locus and *vvd* locus showing enrichment of chromatin accessibility in WT and a  $\Delta wc-2$  mutant. (E) A heatmap showing global enrichment of ChIP-seq and ATAC-seq experiments. Heatmap is centered on WC-2 peaks.

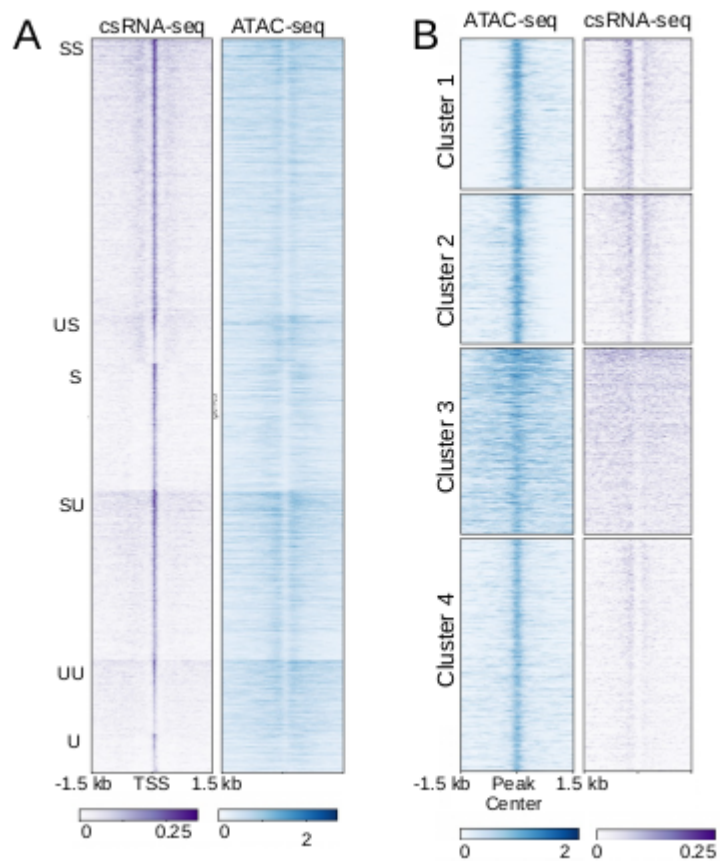


Figure 2.3. Chromatin accessibility is associated with non-coding transcriptional activity.

(A) A heatmap of csRNA-seq reads centered on the TSS of csRNA transcripts ranked by enrichment of each subclass of csRNAs (SS: bi-directional stable; US: unstable pos-strand, stable neg-strand; S: stable unidirectional; SU: stable pos-strand, unstable neg-strand; UU: bidirectionally unstable; U: unidirectional unstable). (B) Heatmap centered on ATAC-seq peaks shows enrichment of csRNAs in relation to accessible chromatin regions.

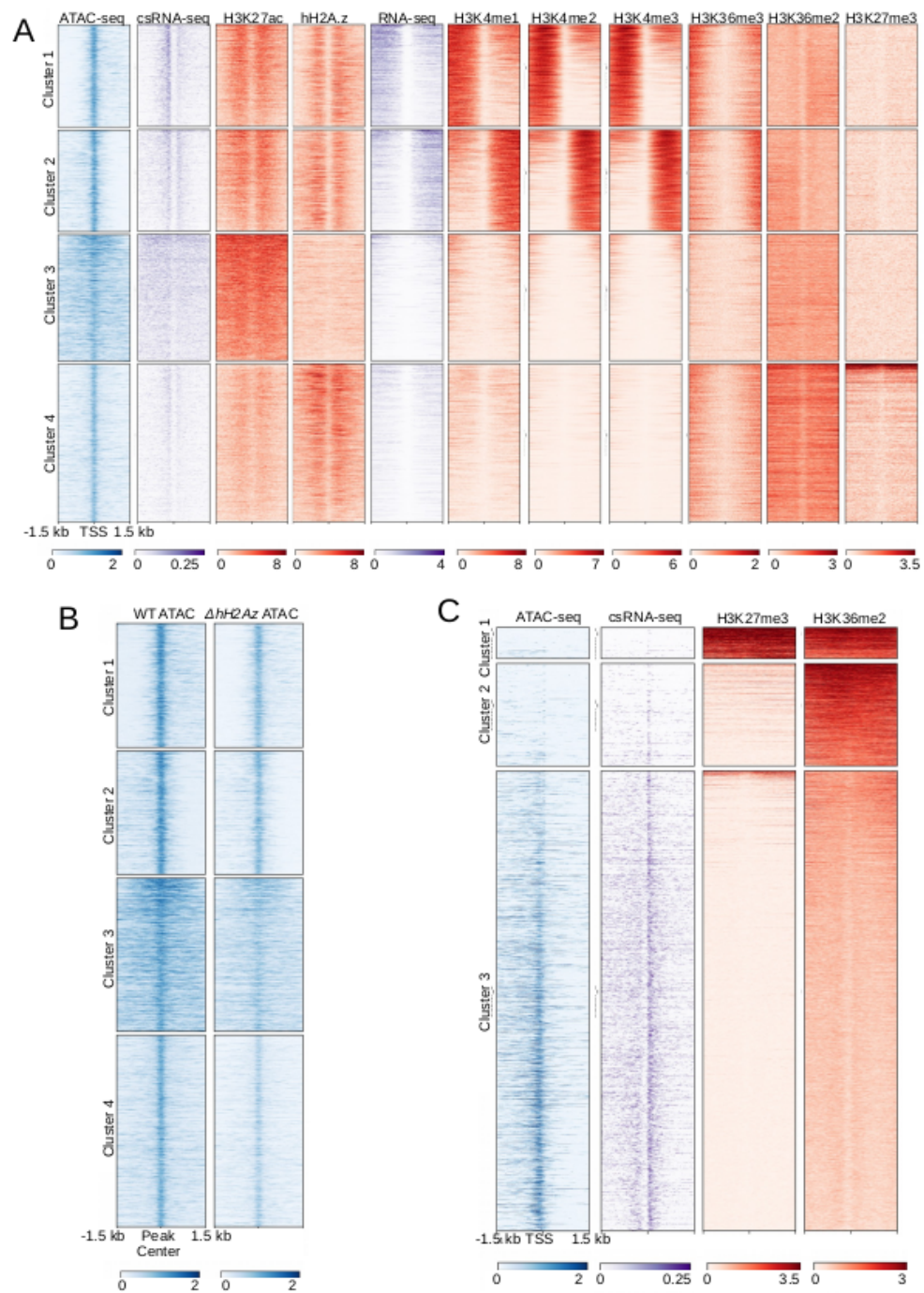
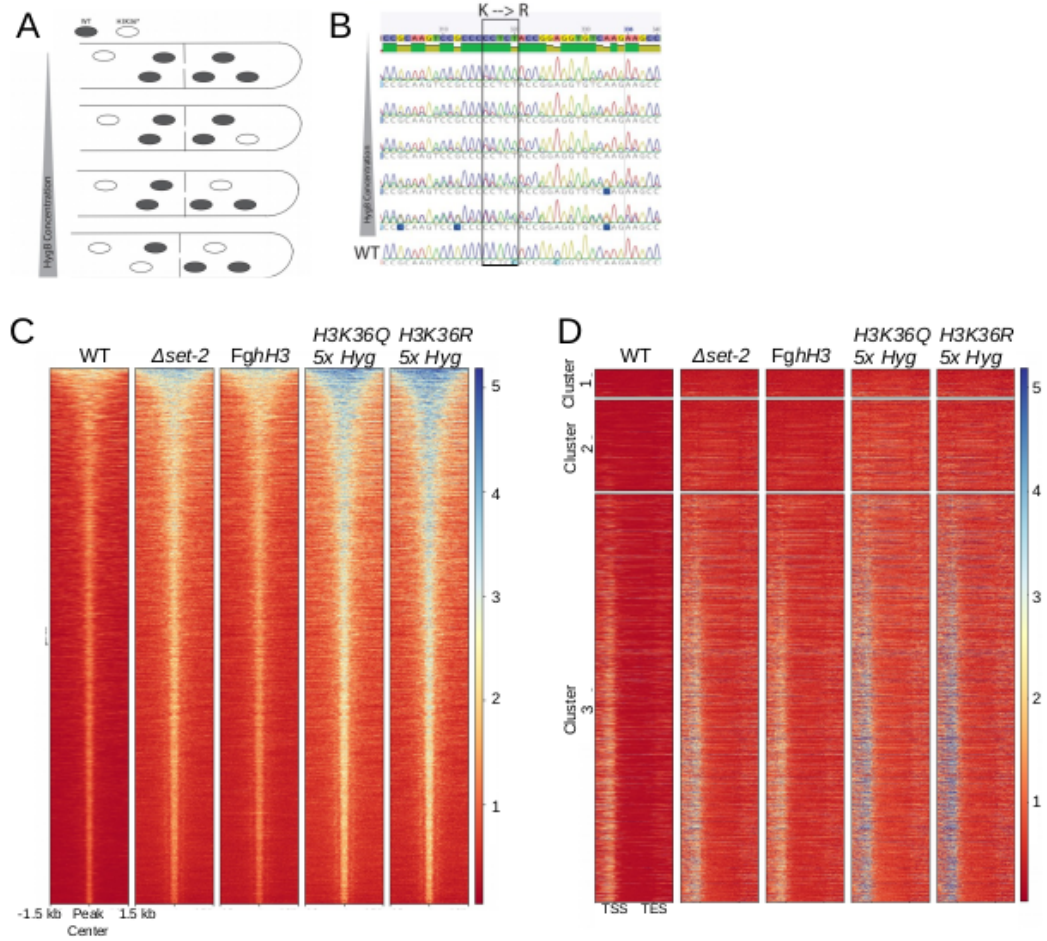


Figure 2.4. Examination of chromatin features associated with ATAC-seq accessible regions (A) Heatmaps display enrichment for the indicated chromatin feature centered on all ATAC-seq peaks. (B) Heatmap of wild type and  $\Delta H2Az$  ATAC-seq. Heatmaps are



centered on wild type ATAC-seq peaks. (C) Heatmap centered on TSSes of distinct promoters showing enrichment of chromatin accessibility, H3K27me2/3, and H3K36me2. TSSes are k-means clustered by patterns of enrichment in all samples.




















**Figure 2.5. Genetic analysis of H3K36 shows a role in maintaining chromatin accessibility in *Neurospora*.** (A) Scheme for modulating concentration of nuclei of mixed genotypes using increasing levels of hygromycin. (B) Sanger sequencing traces of histone H3 showing allele ratio via nucleotide frequencies of *H3K36<sup>mut</sup>* at 0x-5x hygromycin concentration. (C) Heatmap showing ATAC-seq enrichment centered on all possible ATAC-seq peaks in wild type, *FghH3*,  $\Delta$ *set-2*, H3K36Q and H3K36R grown in 5x hygromycin. (D) Heatmap showing ATAC-seq enrichment centered on gene bodies with +/- 500 bp flanks. Heatmaps are sorted as in Figure 4C.



Heatmap of ATAC-seq enrichment surrounding ATAC-seq peaks called from unsorted nuclei. Patterns of enrichment do not change in sorted versus unsorted nuclei. (C)













Representative browser shot of the left arm for LG I am showing overlap of sorted and unsorted nuclei ATAC-seq experiments.

## HOMER Known Motif Results

Rank/Motif	Name	P-value	log P-value	log P-value (Shannon)	# Target Sequences with Motif	% of Target Sequences with Motif	# Background Sequences with Motif	% of Background Sequences with Motif
1 	MYB10(MYB)colanp-MYB10-DAP-Seq(GSE8143)/Homer	1e-4	-5.282e+003.0836		30.0	25.41%	3235.8	3.36%
2 	TRIP3(MYB)colanp-Trip3-DAP-Seq(GSE8143)/Homer	1e-3	-4.480e+003.1844		34.0	28.33%	3036.1	3.34%
3 	FUS3(ARID1P)colanp-FUS3-DAP-Seq(GSE8143)/Homer	1e-3	-7.735e+003.1487		36.0	23.33%	4087.5	4.38%
4 	NPY3(CAAT)Promoter/Homer	1e-3	-7.253e+003.1487		37.0	25.80%	4286.3	3.49%
5 	BCS1(MYB)colanp-BCS1-DAP-Seq(GSE8143)/Homer	1e-3	-6.814e+003.1999		32.0	32.32%	7239.0	3.61%
6 	MYB3(MYB)Arabidopsis-MYB3-ChIP-Seq(GSE8064)/Homer	1e-2	-6.706e+003.1999		33.0	48.33%	3328.9	3.29%
7 	ATG17274(MYB)colanp-ATG17274-DAP-Seq(GSE8143)/Homer	1e-2	-6.575e+003.1999		35.0	22.86%	4186.4	3.39%
8 	Hind13(Homer)colanp-Hind13-Flag-ChIP-Seq(GSE8064)/Homer	1e-2	-6.526e+003.1999		37.0	25.80%	5027.2	3.19%
9 	Atg4300C2021colanp-Atg4300-DAP-Seq(GSE8143)/Homer	1e-2	-6.122e+003.2453		48.0	76.33%	2312.9	32.86%
10 	MYB121(MYB)colanp-MYB121-DAP-Seq(GSE8143)/Homer	1e-2	-6.108e+003.2453		36.0	23.33%	4729.4	3.89%
11 	HY5(ARID1P)colanp-HY5-DAP-Seq(GSE8143)/Homer	1e-2	-5.986e+003.2453		36.0	23.33%	4815.6	3.81%
12 	MYB2(MYB)colanp-MYB2-DAP-Seq(GSE8143)/Homer	1e-2	-5.955e+003.2453		27.0	39.71%	3041.8	23.81%
13 	MYB2(MYB)colanp-MYB2-DAP-Seq(GSE8143)/Homer	1e-2	-5.384e+003.3551		33.0	33.32%	3736.1	3.64%
14 	HRF103(Homer)HRF103-CLIP-Seq(GSE7820)/Homer	1e-2	-5.180e+003.4844		25.0	36.76%	3885.3	22.58%
15 	ATG17274(MYB)colanp-ATG17274-DAP-Seq(GSE8143)/Homer	1e-2	-5.146e+003.4844		36.0	23.33%	5241.6	3.19%
16 	ATG17274(MYB)colanp-ATG17274-DAP-Seq(GSE8143)/Homer	1e-2	-4.996e+003.4254		34.0	35.29%	3455.9	21.63%
17 	E-box(Arabidopsis)Promoter/Homer	1e-2	-4.541e+003.4254		7.0	18.29%	3444.0	3.38%

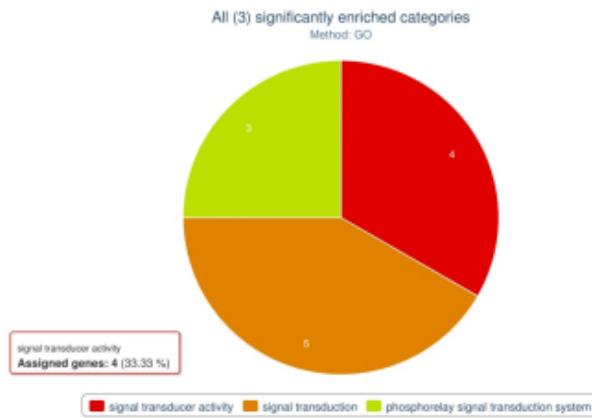
## HOMER de novo Motif Results

\* - possible false positive

Rank/Motif	P-value	log P-value	% of Targets	% of Background	STD(Bg STD)	Best Match/Details
1* 	1e-10	-2.323e+01	11.76%	0.33%	58.2bp (72.2bp)	bys/dmmpmm(SeSICMC)/fly(0.668) <a href="#">More Information</a>   <a href="#">Similar Motifs Found</a>
2* 	1e-9	-2.291e+01	25.00%	3.44%	49.9bp (76.3bp)	BARHL1/MA0677.2/Jaspar(0.718) <a href="#">More Information</a>   <a href="#">Similar Motifs Found</a>
3* 	1e-9	-2.110e+01	11.76%	0.43%	61.6bp (68.8bp)	Dux/MA0611.1/Jaspar(0.899) <a href="#">More Information</a>   <a href="#">Similar Motifs Found</a>
4* 	1e-8	-2.065e+01	23.53%	3.45%	64.3bp (77.7bp)	PH0158.1_Rhox11_2/Jaspar(0.681) <a href="#">More Information</a>   <a href="#">Similar Motifs Found</a>
5* 	1e-8	-2.001e+01	16.18%	1.35%	61.4bp (71.3bp)	SNRNP70(RRM)/Homo_sapiens-RNCMPT00070-PBM/HughesRNA(0.675) <a href="#">More Information</a>   <a href="#">Similar Motifs Found</a>
6* 	1e-8	-1.889e+01	11.76%	0.57%	57.9bp (73.8bp)	KLF10(Zf)HEK293-KLF10.GFP-ChIP-Seq(GSE58341)/Homer(0.850) <a href="#">More Information</a>   <a href="#">Similar Motifs Found</a>
7* 	1e-7	-1.637e+01	35.29%	10.79%	50.7bp (88.1bp)	SD0001.1_at_AC_acceptor/Jaspar(0.679) <a href="#">More Information</a>   <a href="#">Similar Motifs Found</a>
8* 	1e-5	-1.351e+01	14.71%	2.06%	48.0bp (68.3bp)	brk/dmmpmm(Papatsenko)/fly(0.778) <a href="#">More Information</a>   <a href="#">Similar Motifs Found</a>
9* 	1e-4	-1.044e+01	4.41%	0.09%	47.1bp (57.6bp)	ERF5/MA1225.1/Jaspar(0.738) <a href="#">More Information</a>   <a href="#">Similar Motifs Found</a>
10* 	1e-2	-6.467e+00	1.47%	0.00%	0.0bp (22.7bp)	RAP26/MA1221.1/Jaspar(0.777) <a href="#">More Information</a>   <a href="#">Similar Motifs Found</a>
11* 	1e-2	-5.774e+00	1.47%	0.01%	6.8bp (10.2bp)	PH0146.1_Pou3f1/Jaspar(0.662) <a href="#">More Information</a>   <a href="#">Similar Motifs Found</a>
12* 	1e0	-1.500e+00	1.47%	0.37%	2.6bp (50.0bp)	SeqBias: polyA-repeat(0.913) <a href="#">More Information</a>   <a href="#">Similar Motifs Found</a>

**Figure S2.2. Motif analysis results.** Both known and *de novo* motif analyses of ATAC-seq peaks within H3K27me2/3 regions as determined by HOMER.

## Cluster 1 GO Results



## Cluster 2 GO Results

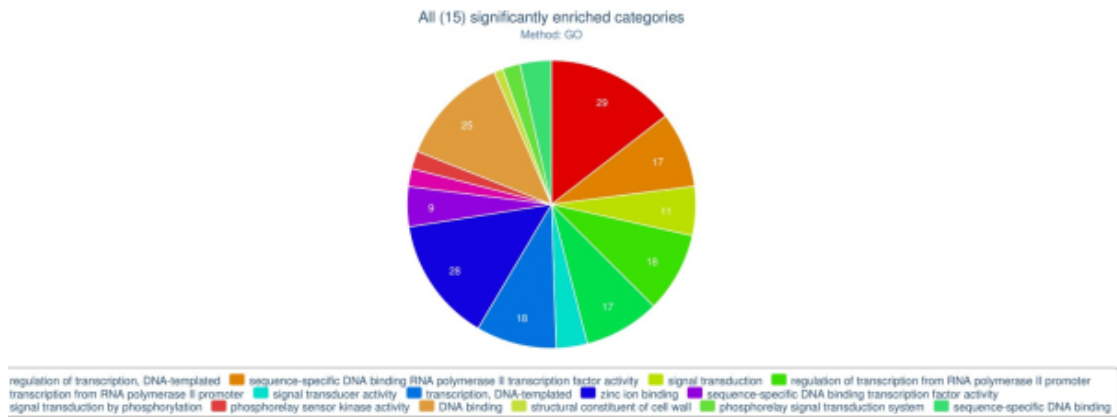


**Figure S2.3. GO analysis of genes from Cluster 1 and Cluster 2 in Fig. 1C.**

Gene Ontology (GO) analysis results for genes whose TSSes fall in either Cluster 1 or Cluster 2 in Fig. 1C.

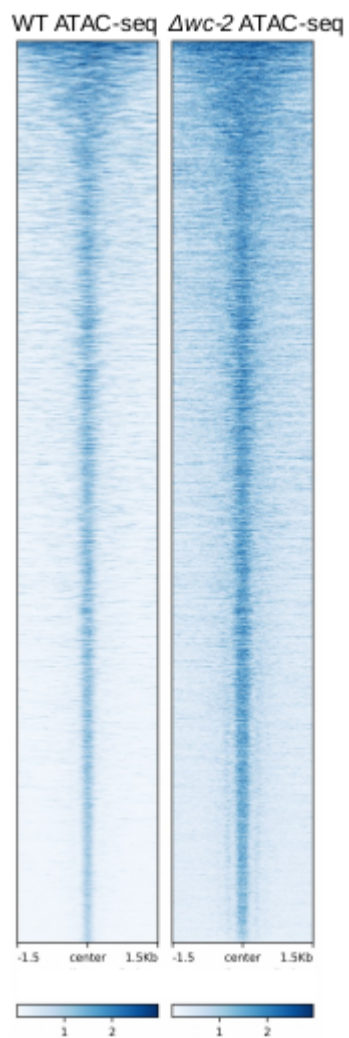


**Figure S2.4. Comparison of ATAC-seq experiments in wild type and  $\Delta wc-2$ .**

Heatmap showing ATAC-seq enrichment of all ATAC-seq peaks in wild type and  $\Delta wc-2$ .

Heatmap is centered on wild type ATAC-seq peaks.

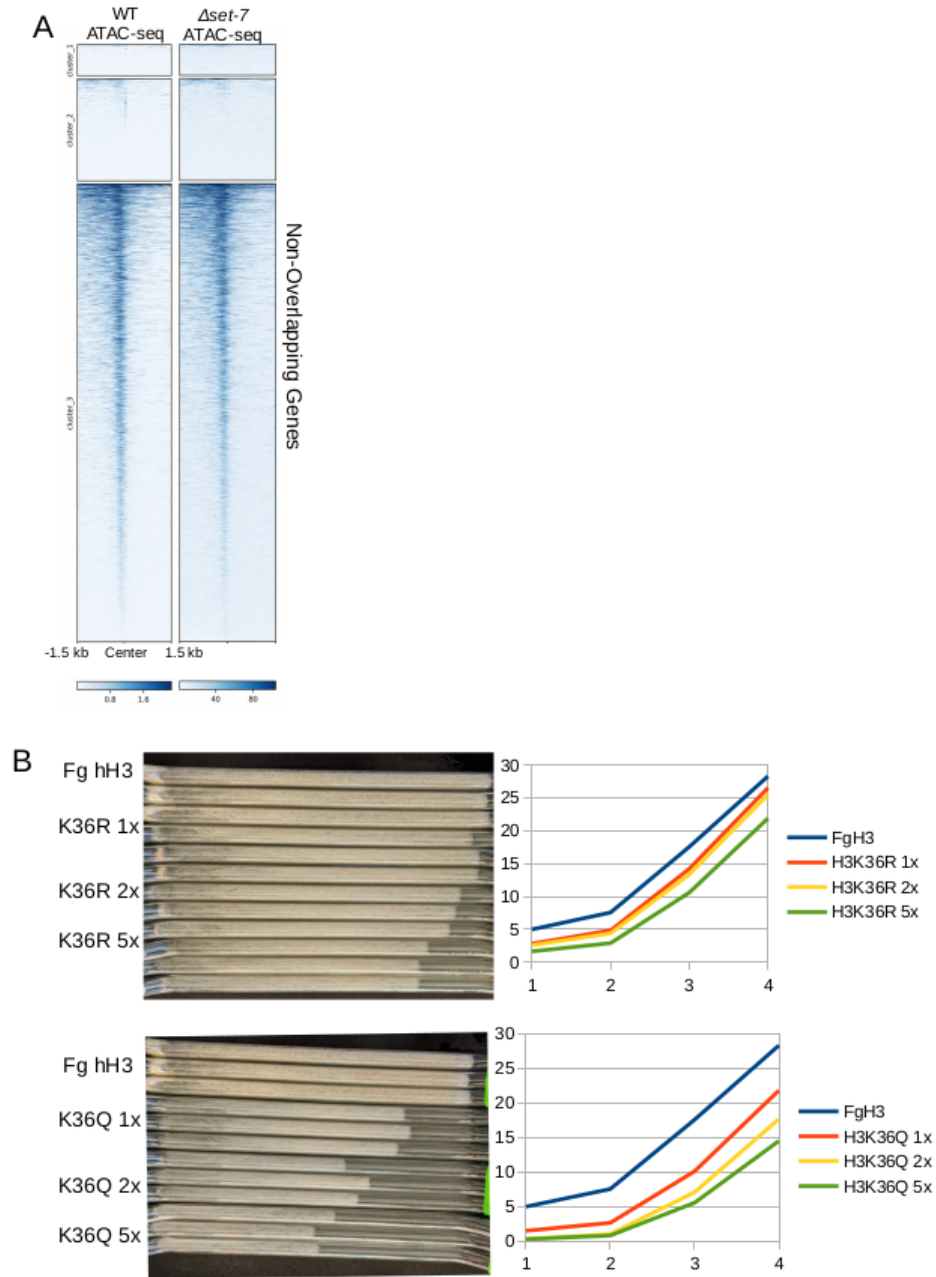


**Figure S2.5. Linear growth assay of  $H3K36^{mut}$  strains** (A) Heatmaps of ATAC-seq reads in wild type and  $\Delta set-7$  centered on TSSes and ordered as in Figure 4C. (B)  $H3K36^{MUT}$  rates of linear growth in the presence of hygromycin and wild type growth rate without hygromycin. Line graphs show linear growth rate. Photos are race tubes at completion of the experiment.



## CHAPTER 3

HDA-1 IS NEEDED FOR NORMAL PATTERNS OF H3K27ME3 IN *NEUROSPORA*

*CRASSA*

---

Ferraro A.R. and Lewis Z.A. To be submitted to *Genetics*

## Abstract

Reversible post-translational modifications to histone tails are important for establishing chromatin domains. Acetylation of some lysine residues on histones, which are established by histone acetyltransferases, create a relaxed chromatin environment by disrupting interactions between DNA and histone tails or by recruiting chromatin reader proteins. This modification is reversible by histone deacetylases (HDACs), and this deacetylation is critical for creating repressive heterochromatin domains. Limited studies in *Neurospora* implicated the sirtuins NST-1, -3, and -5 involved in formation and silencing of PRC2-mediated H3K27me3 domains, and HDA-1 of the heterochromatin-specific deacetylase complex HCHC is important for maintaining but not establishing heterochromatin domains. We performed a targeted transcriptional screen of all viable HDAC deletion mutants in *Neurospora* to identify putative HDACs involved in PRC2-mediated repression. We discovered that  $\Delta hda-1$  was the only single HDAC mutant to show upregulation of PRC2-target genes. ChIP-seq investigation showed that H3K27me3 re-localizes to heterochromatin domains in  $\Delta hda-1$ . We also found that  $\Delta hda-1$  exhibited isolated loss of H3K9me3. Lastly, we identified an ectopic H3K27me2/3 phenotype in a *nst-3* null mutant.

## Introduction

Histone deacetylases (HDACs) are a class chromatin modifying enzymes that play an important role in establishing chromatin environments by modulating lysine residue charge on histone tails. These changes in charge can affect chromatin-DNA interaction or act as a signaling molecule for recruitment of downstream chromatin-associated machinery. HDACs have been shown to play a critical role in disease development in mammals, including cancer development, by disrupting normal patterns of histone modifications and downstream regulation of gene transcription. HDACs also play a role in production of small, non-coding RNAs by releasing

paused RNA polymerase II (Pol2) at cis-regulatory regions, including enhancer regions (1).

Extensive work in yeast has demonstrated that HDACs are critical for heterochromatin formation, silencing of cryptic intergenic transcription, and stress response (2–5) , among other roles including cell cycle regulation and DNA repair mechanisms (2, 3).

There are three classes of HDACs:  $\text{Zn}^+$ -dependent HDACs (Classes I and II) and sirtuins (Class III). Class I and II HDACs are homologous to *Saccharomyces cerevisiae* Hos3 and *Schizosaccharomyces pombe* Clr3 and require  $\text{Zn}^+$  to catalyze lysine deacetylation. Sirtuins are homologous to *S. cerevisiae* Sir2 and are dependent on  $\text{NAD}^+$  to deacetylate lysine residues; the byproducts of these reactions are important components of other pathways within the cell (6, 7).

Studying HDACs in higher eukaryotes has proven to be difficult due to the presence of many copies of homologous HDAC genes. Functional redundancy within this gene family, combined with promiscuity of these enzymes, makes it difficult to pinpoint the role of a single HDAC in biological processes. Additionally, HDACs can act on both histone and non-histone substrates, further clouding analysis of these enzymes. *Neurospora* possesses a relatively small family of HDACs, with the presence of four  $\text{Zn}^+$ -dependent histone deacetylases (*hda-1/-2/-3/-4*) and seven sirtuins (*nst-1/-2/-3/-4/-5/-6/-7*).

We wanted to understand the role of HDACs in regulation of repressive heterochromatin domains in *Neurospora*. Two types of heterochromatin are present in *Neurospora*: constitutive heterochromatin and facultative heterochromatin. Constitutive heterochromatin is found at centromeres and repeat-rich regions of the genome and is characterized by cytosine methylation, trimethylation of lysine 9 on histone H3 (H3K9me3), and histone hypoacetylation. Conversely, facultative heterochromatin is established at conditionally repressed genes by polycomb

repressive complex 2 (PRC2) and is characterized by trimethylation of lysine 27 on histone H3 (H3K27me3).

Some work has been done in *Neurospora* to characterize the role of HDACs in these processes, however these studies were limited and lacked whole-genome characterization of the effect of HDACs in global chromatin domains (8–11). For example, a ChIP-qPCR examination of a reporter strain using dominant selectable markers found that the sirtuins NST-1,-3, and -5 were important for silencing at telomere regions in *Neurospora* (11).

Investigation of the *Neurospora* HDAC HDA-1 has defined its role in a larger deacetylation complex HCHC (HP-1, CDP-2, HDA-1, CHAP) and is a key factor in establishing heterochromatin domains and DNA methylation in *Neurospora* by interaction with the heterochromatin-associated protein heterochromatin protein 1 (HP1) (8). HDA-1 deacetylates H2B and to a lesser extent H3 (10). A tethering scheme involving a LexAO locus within euchromatin also determined that HDA-1 is necessary for maintenance of heterochromatin, but not de novo establishment, providing some insight into the greater role of HDA-1 in heterochromatin formation in *Neurospora*. The *Schizosaccharomyces pombe* homolog of HDA-1 (Clr3) is important for heterochromatin formation and transcriptionally-linked histone deacetylation. These processes recruit chromatin remodelers leading to a condensed chromatin state and subsequent repression (12).

Prior studies have shown the importance of HDACs in *Neurospora* but have yet to look at global patterns of histone modifications or the role of HDACs in transcriptional regulation in *Neurospora*. Here, we have interrogated all non-essential histone deacetylases to determine their possible role in PRC2-mediated repression in *Neurospora* by RNA-seq and ChIP-seq. Our RNA-seq experiments identified  $\Delta hda-1$  as the only HDAC to have a significant increase in

transcription of PRC2-target genes. Our ChIP-seq studies established that *hda-1* exhibits selective loss of H3K9me3 and re-localization of H3K27me3 to heterochromatin domains. We have also demonstrated that  $\Delta$ *nst-3* exhibits spreading of H3K27me3 into heterochromatin domains with limited loss of H3K27me3 in native facultative heterochromatin domains.

## **Methods**

### **Strains and growth conditions**

Strains are listed in Table 1. All strains except *nst-3*<sup>RIP</sup> were acquired from the *Neurospora* whole-genome knockout collection (16). Strains were grown in Vogel's minimal medium with 1.5% sucrose. Strain genotypes were verified by visualization of gene loci in Integrated Genomics Viewer (IGV) from sequencing data (Fig. S3.1).

### **Chromatin Immunoprecipitation (ChIP)**

ChIP was performed as described in (17) for H3K27me2/3 (Active Motif Mouse Monoclonal, Catalog # 39535, Lot# 16714012) and H3K9me3 (Active Motif Rabbit Catalog # 39162). Sequencing libraries were created and analyzed as described in (17). Libraries were sequenced as described above by Georgia Genomics Facility at University of Georgia.

### **Data analysis**

#### ChIP-seq

ChIP-seq reads were cleaned and trimmed using TrimGalore! Trimmed reads were mapped with BWA using the mem option with flagged secondary hits (bwa mem -M). Peaks were called using MACS2 using the broad option without input and with a q-value of 0.01. Peak files were merged to combine proximal peaks within 10kb domains using bedtools merge. Peak files were compared with bedtools intersect or subtract. Bigwig files for visualization were made using deepTools bamCoverage with the following options: -bs1 --normalizeUsing CPM, --

ignoreDuplicates. Heatmaps were created using deepTools computeMatrix plotHeatmap.

Karyoplots were created using karyoploteR using bigwig files from deepTools output. Browser tracks were created with IGV.

### RNA-seq

RNA-seq reads were acquired from JGI Community Sequencing Grant 54039. Paired RNA-seq reads were first de-interleaved using bbmap's reformat.sh. Paired read files were then trimmed using trimGalore!. Trimmed reads were mapped to the NC12 genome using HISAT2 with standard options. Read counts were created using featureCounts with the following options: -t exon -g gene\_name -s2 -p -primary. A gtf of the assembled chromosome only was used. Counts to transcripts per million (TPM) normalization was performed in R.

TPM read counts were used to make heatmaps with heatmap.2. Hierarchical clustering of standardized read counts was performed in heatmap.2 with the standard options (clustering\_method = ward.D, clustering\_distance\_cols = Euclidian) and rows were scaled to give a z-score. Volcano plots were created in R with EnhancedVolcano.

## **Results**

### ***Ahda-1* shows increased expression of PRC2-target genes**

HDACs have been implicated in control of PRC2-mediated repression in *Neurospora* (10, 11). However, these studies lacked genome-wide analysis of the effect HDACs on gene expression. We performed RNA-seq in single deletion mutants in the 10 non-essential *Neurospora* HDACs in an attempt to understand how HDACs contribute to PRC2-mediated repression in *Neurospora*. A boxplot of log2-transformed transcripts per million (TPM) of read counts of PRC2-target genes shows that *Ahda-1* has the largest increase in the mean expression of these genes (Fig. 3.1A). Principal component analysis of PRC2-target gene expression values

shows that  $\Delta hda-1$  is unique in its expression profile, supporting our finding that it is the only single HDAC deletion mutant to have increased mean expression of these genes (Fig. S3.2).

Hierarchical clustering analysis of normalized expression values of all strains studied shows that  $\Delta hda-1$  upregulates a small number of genes globally compared to other HDACs (Fig. 3.1B). Focusing in on PRC2-target genes shows a higher expression level of a subset of genes that is not shared between other HDACs (Fig. 3.1B).

Differential expression analysis of  $\Delta hda-1$  reveals 749 genes were differentially expressed in  $\Delta hda-1$  genome-wide ( $n = 10,560$ ; Fig. 3.1C). Of these differentially expressed genes,  $\Delta hda-1$  has 624 genes that were significantly different from wild type, with a log2 fold change  $> 2$  and 125 genes with a log2 fold change  $< 2$ , and an adjusted p-value  $< 0.05$ .

Differential expression analysis of PRC2-target genes reveals that 90 genes were differentially expressed in  $\Delta hda-1$  versus wild type with a log2 fold change  $> 2$  and adjusted p-value  $< 0.05$  ( $n = 642$ ; Fig. 3.1C). Gene ontology analysis of upregulated PRC2-target genes reveals no significant functional categories. This is expected due to a majority of PcG-target genes being uncharacterized in *N. crassa* (13).

### **$\Delta hda-1$ shows re-localization of H3K27me2/3 and isolated depletion of H3K9me3**

There are two possible means by which HDA-1 is affecting PRC2-mediated silencing. The first is that HDA-1 is directly regulating PRC2-mediated silencing and/or H3K27me3 deposition. The second is that HDA-1 is preventing H3K27me3 redistribution to constitutive heterochromatin like other members of the constitutive heterochromatin pathway. To test these two hypotheses, we performed ChIP-seq for H3K9me3 and H3K27me2/3 in an *hda-1* deletion mutant.

We first examined H3K27me2/3 enrichment at PRC2-target genes that are upregulated in *Δhda-1* and found reduced H3K27me2/3 (Fig. 3.2A). We next plotted a heatmap of H3K27me2/3 enrichment at genes showing at least 1.5 fold change increase in expression and genes with < 1.5-fold increase in expression (Fig. 3.2B). We found that genes marked by H3K27me2/3 that had at least a 1.5-fold increase in expression exhibited depleted H3K27me2/3 while those with < 1.5-fold increase did not. Peak analysis in wild type *Δhda-1* identified 148 H3K27me2/3 peaks that are maintained between wild type and *Δhda-1*, as depicted in the Venn diagram in Fig. 3.2D.

Because loss of H3K9me3 in the histone methyltransferase deletion mutant *Δdim-5* leads to redistribution of H3K27me2/3 and HDA-1 has a role in constitutive heterochromatin maintenance, we hypothesized that *Δhda-1* may also be exhibiting losses of H3K9me3 and resulting in re-localization of H3K27me2/3. This would explain the increased number of H3K27me2/3 regions in *Δhda-1*. To test whether *Δhda-1* exhibited changes in H3K9me3 distribution, we performed ChIP-seq for H3K9me3 in a *Δhda-1* strain and found that *Δhda-1* exhibits isolated losses of H3K9me3 (Fig. 3.3A). To determine the extent of H3K9me3 loss in *Δhda-1*, we mapped enrichment of H3K9me3 in WT and *Δhda-1* as a heatmap centered on the 5' or 3' ends of heterochromatin domains ranked by H3K9me3 enrichment in WT (Fig. 3.3B). Peak analysis of H3K9me3 reveals that 247 of the 299 wild type H3K9me3 regions are maintained in *Δhda-1*.

We next wanted to examine the relationship between H3K27me2/3 re-localization and H3K9me3 loss in *Δhda-1*. We plotted H3K9me3 and H3K27me2/3 enrichment across constitutive heterochromatin regions as described above (Fig. 3.3C). We ranked regions by loss of H3K9me3 in *Δhda-1*. Gain of H3K27me2/3 in *Δhda-1* is not limited to regions of H3K9me3



loss, as not all regions lacking H3K9me3 gain H3K27me2/3, and H3K27me2/3 is gained in some regions which maintain H3K9me3 in  $\Delta hda-1$ . Globally, 241 H3K27me2/3 peaks are found within H3K9me3 regions in  $\Delta hda-1$ , and only 59 H3K9me3 peaks are unique to wild type. This indicates that H3K27me2/3 is enriched in constitutive heterochromatin in  $\Delta hda-1$ , but H3K27me2/3 is not lost in all facultative heterochromatin domains as seen in other heterochromatin mutants, as demonstrated in the Venn diagram in Fig. 3.2D.

Together, these results indicate that HDA-1 controls H3K9me3 in distinct regions of the *Neurospora* genome, but it is not necessary for genome-wide patterns of H3K9me3. HDA-1 is also important for limiting H3K27me2/3 and preventing invasion of PRC2 into heterochromatin.

#### ***Δnst-3* exhibits ectopic H3K27me2/3 enrichment**

As part of our screen, we also performed H3K27me2/3 ChIP-seq in all available single HDAC mutants. Examination of these ChIP-seq experiments showed that *nst-3<sup>RIP</sup>* showed a distinct ectopic enrichment of H3K27me2/3 (Fig.3. 4). NST-3, along with NST-1 and NST-5, has been reported to contribute to subtelomeric gene repression and reduced H3K27me3 in a reporter strain (11). This study lacked genome-wide transcriptional data or global characterization of H3K27me3 in a *nst-3* mutant, however. Our RNA-seq analysis revealed only 31 PRC2-target genes that were upregulated in *Δnst-3* (Fig. 3B).

To compare patterns of H3K27me2/3 in *nst-3<sup>RIP</sup>* we first plotted a karyoplot of wild type H3K9me3 and H3K27me2/3 enrichment and H3K27me2/3 in *nst-3<sup>RIP</sup>* and  $\Delta hda-1$  (Fig. 3.5A). We found that *nst-3<sup>RIP</sup>* does exhibit changes in the distribution of H3K27me2/3 genome-wide with increased enrichment in heterochromatin similar to  $\Delta hda-1$ . Unlike  $\Delta hda-1$ , however, we found that H3K27me2/3 is gained in heterochromatin domains and mostly intact in native H3K27me2/3. A heatmap of native H3K27me2/3 domains centered on the 5' and 3' boundaries

in wild type and *nst-3<sup>RIP</sup>* shows that H3K27me2/3 enrichment is extended beyond the normal boundaries of these domains (Fig. 3.5B). Likewise, a heatmap of constitutive heterochromatin domains centered on the 5' or 3' boundaries show gains in some, but not all, domains.

Additionally, this H3K27me2/3 enrichment extends beyond the normal boundaries of these domains (Fig. 3.5C). Peak analysis revealed a total of 387 H3K27me2/3 peaks in *nst-3<sup>RIP</sup>*. Of these, there are 233 regions of H3K27me2/3 that overlap with wild type H3K9me3 in *nst-3<sup>RIP</sup>*.

Taken together, these results indicate that NST-3 plays a role in limiting the spread of H3K27me2/3, but not is not important in native H3K27me2/3 enrichment.

## Discussion

Here we have provided genome-wide examination into the role of HDACs in regulating PRC2-mediated H3K27me. While sirtuins NST-1,-3,-5 have been implicated in telomeric silencing in *Neurospora*, we have not identified significant loss of H3K27me2/3 in single NST mutants. It is possible that there is functional redundancy between these sirtuins, and investigation of combinatorial deletions will reveal changes in H3K27me2/3 patterns.

We have provided evidence that histone deacetylase activity is important for regulating H3K27me3 localization in *Neurospora*. Namely, we have identified HDA-1 as an important component in preventing invasion of PRC2 into heterochromatin domains. Additionally, we have shown that HDA-1 is important for maintaining H3K9me3 at some, but not all, heterochromatin domains in the *N. crassa* genome. Tethering of heterochromatin machinery to an artificial heterochromatin domain in *Neurospora* have shown that HDA-1 is necessary for maintenance, but not establishment, of H3K9me3 (12). Additionally, HDA-1 is important for proper DNA methylation in *Neurospora* (8, 9) and binding of the H3K9me3 reader and structural protein HP1 (8). It is unclear, however, whether sites of preserved H3K9me3 in *Δhda-1* are sites of new

H3K9me3 establishment or if maintenance of H3K9me3 is redundantly regulated, and this phenotype merely incomplete maintenance.

We also identified a fraction of heterochromatin domains that gain H3K27me2/3 in *Δhda-1*. Interestingly, H3K9me3 is maintained at some of these domains. Additionally, we do not observe a complete loss of H3K27me2/3 in native facultative heterochromatin domains, unlike other heterochromatin deficient mutants such as *Δdim-5* or *Δhpo* (14, 15). One hypothesis for this relocalization is that PRC2 is recruited to sites of histone acetylation. There is some evidence of this in *Neurospora*, as an H3K9ac mimic (H3K9Q) also exhibits translocation of H3K27me2/3 to heterochromatin in *N. crassa* (14) This can be tested in *Neurospora* easily by examining patterns of H3K27me2/3 in various histone acetylation mimic mutants.

The combination of H3K27me2/3 re-localization in *Δhda-1* and ectopic H3K27me2/3 in *nst-3<sup>RIP</sup>* suggests that both HDACs contribute to H3K27me2/3 localization; HDA-1 contributes to excluding H3K27me2/3 from heterochromatin domains while NST-3 appears to limit spreading of H3K27me2/3 outside of facultative heterochromatin domains. It is unclear whether NST-3 and HDA-1 share substrates, however HDACs are promiscuous and depend greatly on their associated HDAC complex for targeting. Therefore, it is possible that roaming activity of NST-3 could contribute to this shared phenotype. Investigation of *Δhda-1;Δnst-3* would provide insight into whether these two HDACs are indeed functionally redundant or acting in a shared pathway.

## References

1. Release of promoter-proximal paused Pol II in response to histone deacetylase inhibition.
2. Knott SRV, Viggiani CJ, Tavaré S, Aparicio OM. 2009. Genome-wide replication profiles indicate an expansive role for Rpd3L in regulating replication initiation timing or efficiency and reveal genomic loci of Rpd3 function in *Saccharomyces cerevisiae*. *Genes Dev.*

3. Aparicio JG, Viggiani CJ, Gibson DG, Aparicio OM. 2004. The Rpd3-Sin3 Histone Deacetylase Regulates Replication Timing and Enables Intra-S Origin Control in *Saccharomyces cerevisiae*. *Mol Cell Biol*.
4. Rundlett SE, Carmen AA, Kobayashi R, Bavykin S, Turner BM, Grunstein M. 1996. HDA1 and RPD3 are members of distinct yeast histone deacetylase complexes that regulate silencing and transcription. *Proc Natl Acad Sci U S A*.
5. Seto E, Yoshida M. 2014. Erasers of histone acetylation: The histone deacetylase enzymes. *Cold Spring Harb Perspect Biol*.
6. North BJ, Verdin E. 2004. Sirtuins: Sir2-related NAD-dependent protein deacetylases. *Genome Biol*.
7. De Ruijter AJM, Van Gennip AH, Caron HN, Kemp S, Van Kuilenburg ABP. 2003. Histone deacetylases (HDACs): Characterization of the classical HDAC family. *Biochem J*.
8. Honda S, Lewis ZA, Shimada K, Fischle W, Sack R, Selker EU. 2012. Heterochromatin protein 1 forms distinct complexes to direct histone deacetylation and DNA methylation. *Nat Struct Mol Biol*.
9. Honda S, Bicocca VT, Gessaman JD, Rountree MR, Yokoyama A, Yu EY, Selker JML, Selker EU. 2016. Dual chromatin recognition by the histone deacetylase complex HCHC is required for proper DNA methylation in *Neurospora crassa*. *Proc Natl Acad Sci U S A*.
10. Smith KM, Dobosy JR, Reifsnyder JE, Rountree MR, Anderson DC, Green GR, Selker EU. 2010. H2B- and H3-specific histone deacetylases are required for DNA methylation in *Neurospora crassa*. *Genetics*.
11. Smith KM, Kothe GO, Matsen CB, Khlafallah TK, Adhvaryu KK, Hemphill M, Freitag M, Motamedi MR, Selker EU. 2008. The fungus *Neurospora crassa* displays telomeric silencing mediated by multiple sirtuins and by methylation of histone H3 lysine 9. *Epigenetics Chromatin*.
12. Gessaman JD, Selker EU. 2017. Induction of H3K9me3 and DNA methylation by tethered heterochromatin factors in *Neurospora crassa*. *Proc Natl Acad Sci U S A*.
13. Jamieson K, Rountree MR, Lewis ZA, Stajich JE, Selker EU. 2013. Regional control of histone H3 lysine 27 methylation in *Neurospora*. *Proc Natl Acad Sci U S A*.
14. Basenko EY, Sasaki T, Ji L, Prybol CJ, Burckhardt RM, Schmitz RJ, Lewis ZA. 2015. Genome-wide redistribution of H3K27me3 is linked to genotoxic stress and defective growth. *Proc Natl Acad Sci U S A*.

15. Jamieson K, Wiles ET, McNaught KJ, Sidoli S, Leggett N, Shao Y, Garcia BA, Selker EU. 2016. Loss of HP1 causes depletion of H3K27me3 from facultative heterochromatin and gain of H3K27me2 at constitutive heterochromatin. *Genome Res.*
16. Colot H V., Park G, Turner GE, Ringelberg C, Crew CM, Litvinkova L, Weiss RL, Borkovich KA, Dunlap JC. 2006. A high-throughput gene knockout procedure for *Neurospora* reveals functions for multiple transcription factors. *Proc Natl Acad Sci U S A.*
17. Ferraro AR, Lewis ZA. 2018. ChIP-seq analysis in *Neurospora crassa* *Methods in Molecular Biology.*

## Tables

**Table 3.1. Strains used in this study**

Strain	Genotype	Source
S2 (FGSC4200)	wild type	This study
FGSC12003	<i>hda-1::hph</i>	This study
FGSC11158	<i>hda-2::hph</i>	This study
FGSC11175	<i>hda-4::hph</i>	This study
FGSC12403	<i>nst-1::hph</i>	This study
FGSC12078	<i>nst-2::hph</i>	This study
NCU03059	<i>nst-3::hph</i>	This study
FGSC11165	<i>nst-4::hph</i>	This study
FGSC14806	<i>nst-5::hph</i>	This study
NCU05972	<i>nst-6::hph</i>	This study
FGSC16002	<i>nst-7::hph</i>	This study

S208	<i>nst-3</i> <sup>RIP</sup>	Smith et al. (11)
------	-----------------------------	-------------------

**Table 3.2. *Δhda-1* DGE values**

**Table 3.3 *Δhda-1* H3K27me2/3 peaks**

**Table 3.4 *Δhda-1* H3K9me3 peaks**

**Table 3.5 *Δhda-1* and WT H3K27me2/3 overlapping peaks**

**Table 3.6 *Δhda-1* H3K27me2/3 and WT H3K9me3 overlapping peaks**

**Table 3.7 *Δhda-1* H3K9me3 and WT H3K9me3 overlapping peaks**

**Table 3.6 *Δnst-3* DGE values**

**Table 3.7 *nst-3*RIP H3K27me2/3 peaks**

**Table 3.8 *nst-3* RIP H3K27me2/3 and WT H3K27me2/3 overlapping peaks**

**Table 3.9 *nst-3*RIP H3K27me2/3 and WT H3K9me3 overlapping peaks**

## Figures

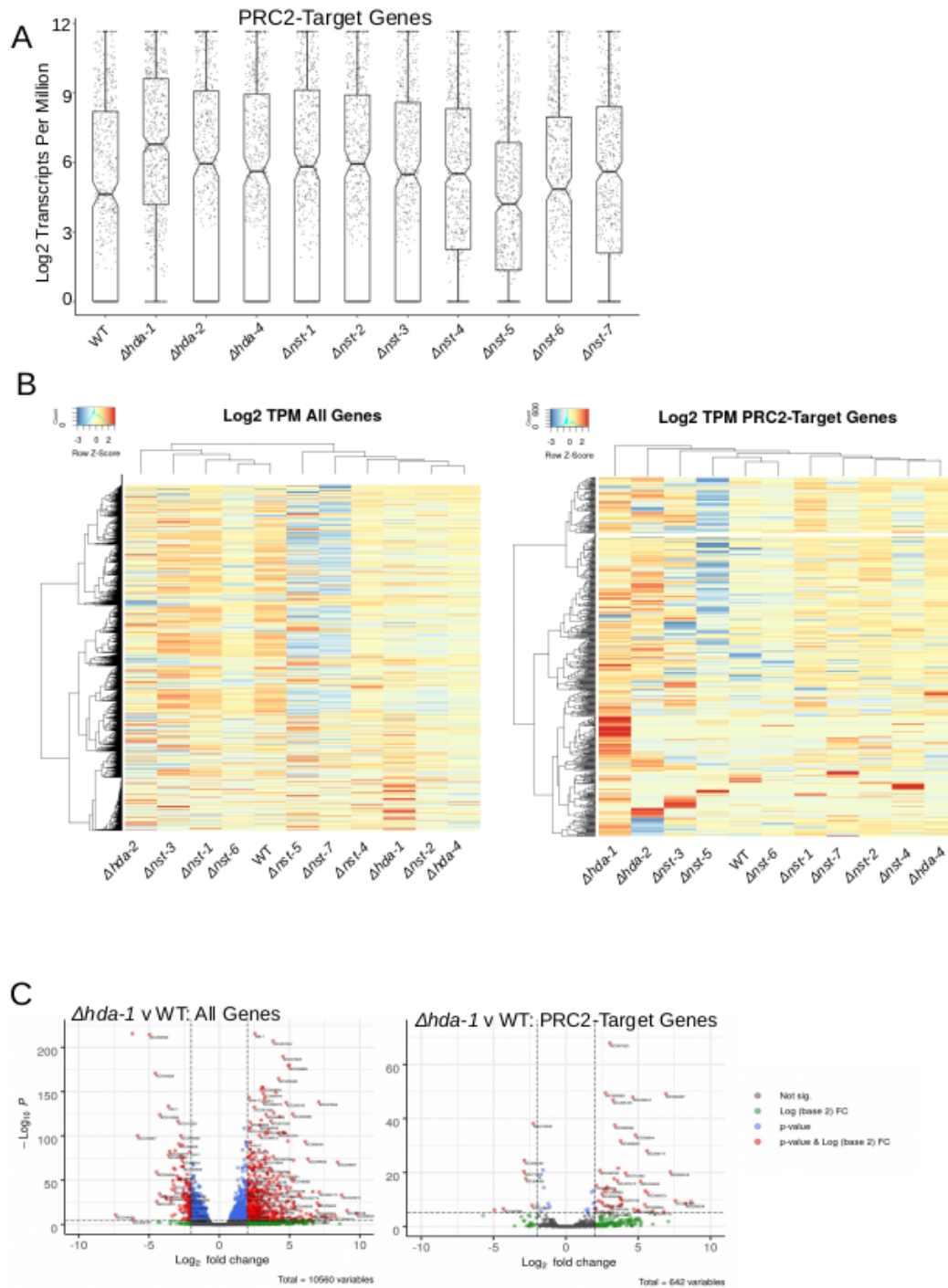


**Figure 3.1. *Δhda-1* shows increased expression of PRC2-target genes.** (A) Box plot of transcripts per million (TPM) of PcG-target genes (n = 679) in wild type and all non-essential HDAC deletion mutants. (B) Hierarchical-clustered heatmap of TPM-normalized read counts of

all genes and PRC2-target genes. (C ) Volcano plots showing differentially expressed genes in *Δhda-1* and wild type in all genes or PcG-target genes. Cut-offs:  $\log_2$  fold-change  $> 2$  and  $\text{padj} < 0.05$ .



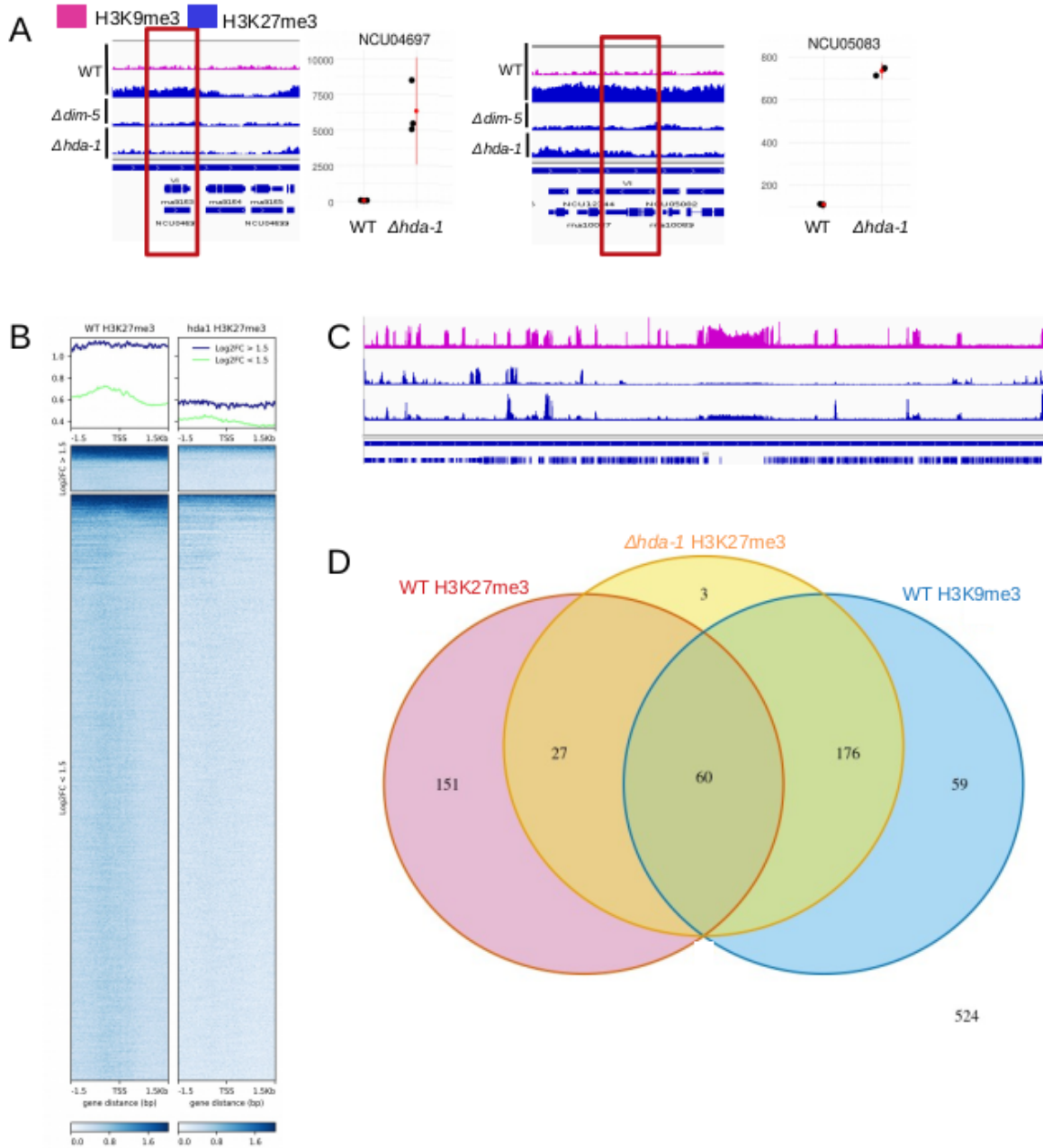


**Figure 3.2.  $\Delta hda-1$  shows loss of H3K27me2/3.** (A) Browser shots of two genes that are significantly up-regulated in  $\Delta hda-1$ : browser shot showing reduced H3K27me2/3 and dot plot showing up-regulation in  $\Delta hda-1$ . Red dot: mean expression value. Red line: standard error. (B) Heatmap of H3K27me2/3 across the transcription start site (TSS) of all genes. Top: Genes with  $> 1.5$ -fold increase in expression. Bottom: all other genes. (C) IGV browser shot of Linkage

Group VII showing H3K27me2/3 changes in *Δhda-1*. Wild type H3K9me3 shown as a control.

(D) Venn diagram showing overlap of H3K27me2/3 in wild type and *Δhda-1* and overlap with wild type H3K9me3.

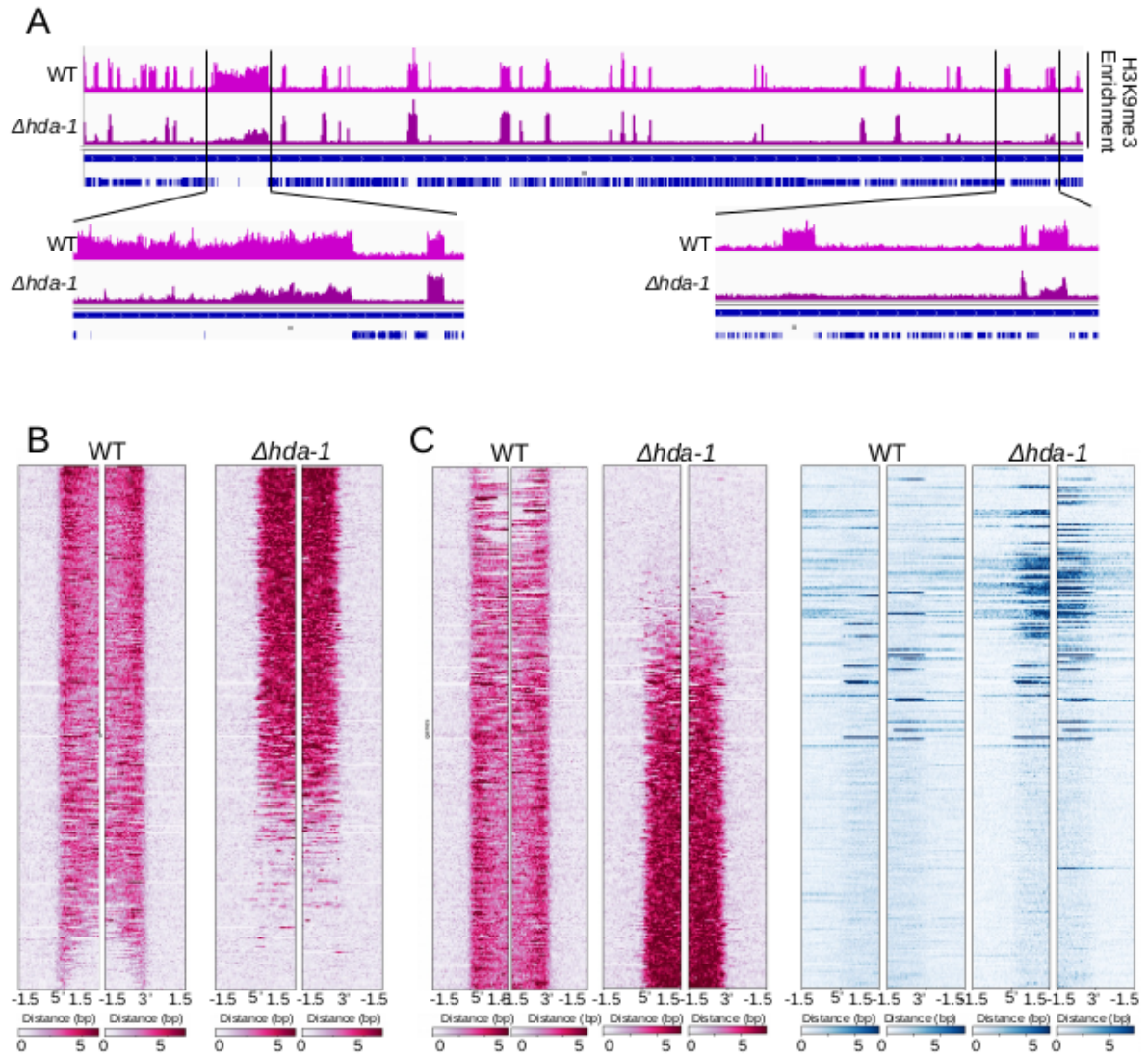


**Figure 3.3.  $\Delta hda-1$  shows isolated loss of H3K9me3.** (A) IGV browser shot of Linkage Group III showing changes in H3K9me3 in wild type versus  $\Delta hda-1$ . (B) Heatmap of H3K9me3 regions sorted by wild type enrichment in wild type and  $\Delta hda-1$ . Heatmaps are centered on 5' and 3' boundaries of H3K9me3. (C) Heatmap of H3K9me3 and H3K27me2/3 in wild type and  $\Delta hda-1$  sorted by H3K9me3 enrichment in  $\Delta hda-1$ . Heatmaps are centered on 5' and 3' boundaries of H3K9me3.

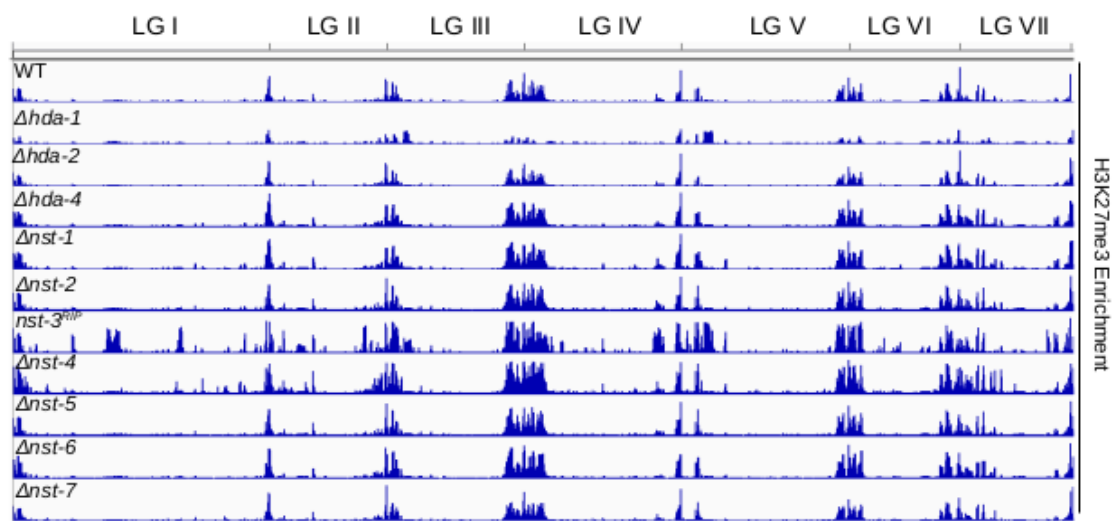


**Figure 3.4. H3K27me2/3 enrichment across all non-essential HDACs.** IGV browser shot of H3K27me2/3 across all linkage groups.



boundaries of H3K27me2/3 enrichment.. (C ) Heatmap showing enrichment of H3K27me2/3 in heterochromatin regions in *nst-3<sup>RIP</sup>* centered on 5' or 3' boundaries of H3K9me3. (D) Venn diagram showing overlap of H3K27me2/3 in wild type,  $\Delta hda-1$ , and *nst-3<sup>RIP</sup>* and wild type H3K9me3.

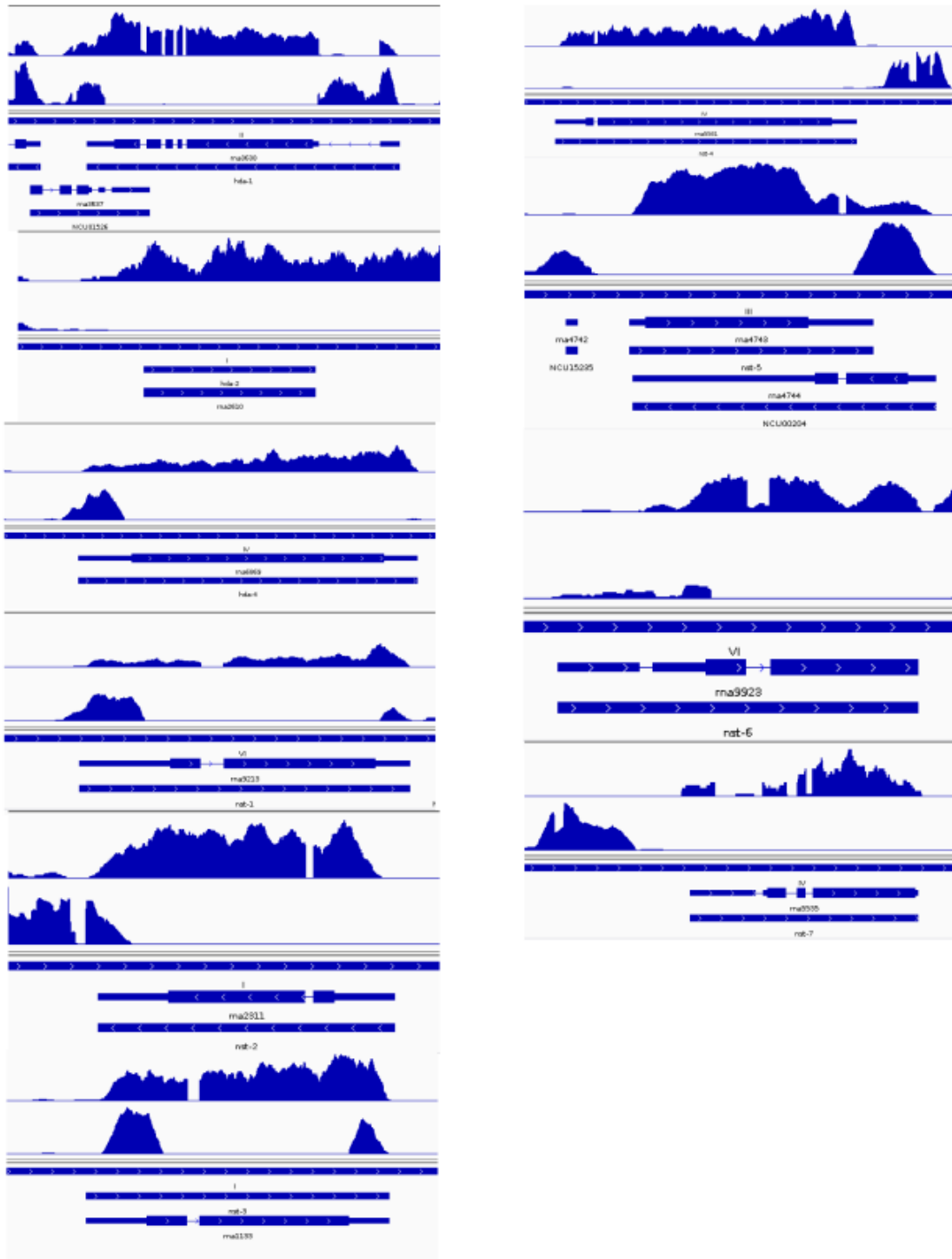
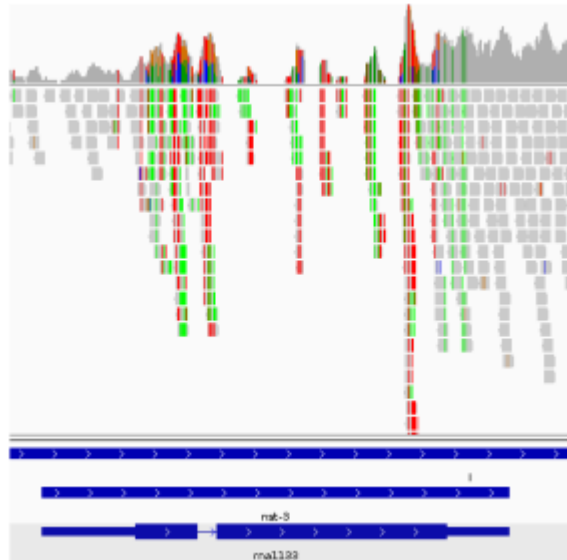
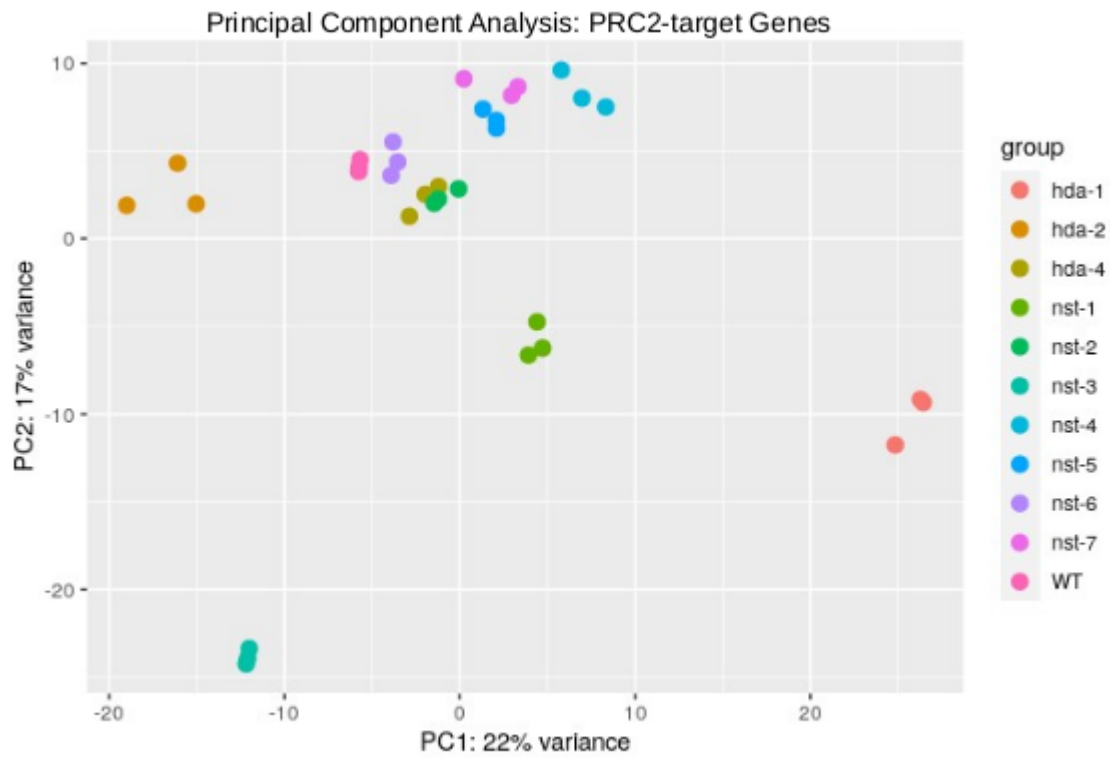


Figure S3.1. Browser verification of HDAC deletions from RNA-seq data.



**Figure S3.2. Browser verification of *nst-3RIP* allele from ChIP-seq data.**





**Figure S3.4. Principal Components Analysis of PRC2-target gene expression counts data.**

## CHAPTER 4

### H3K36ME3 EPIGENETICALLY COMPENSATES FOR THE LOSS OF

#### **Introduction**

Constitutive heterochromatin domains are important for maintaining stability of the genome, with these domains establishing and maintaining centromeres or preventing transcription of toxic genetic elements such as transposable elements or repeat sequences. Disruption of these domains leads to invasion by facultative heterochromatin machinery, with Polycomb Repressive Complex 2 (PRC2) invading constitutive heterochromatin domains and establishing H3K27me3 in *Neurospora* while also exhibiting loss of H3K27me3 at native PcG domains (1, 2).

It is unclear how PRC2 is recruited to heterochromatin domains, however it is believed that HP1 acts as to exclude PcG machinery, thereby preventing establishment of H3K27me3 in normal cells. Given that loss of H3K9me3 results in loss of HP1 binding, it is plausible that PRC2 is thusly able to invade constitutive heterochromatin domains in the case of disrupted establishment and maintenance machinery. It is important to note that removal of the H3K27me3 methyltransferase SET-7 in DIM-5-deficient or HP1-deficient backgrounds results in a rescued growth and DNA damage sensitivity phenotypes. Furthermore, 3D organization studies in *Neurospora* show that loss of H3K9me3 and H3K27me3 do not lead to changes in organization of chromatin within the nucleus (3). This raises the possibility that there are underlying or compensatory chromatin marks contributing to maintenance of some heterochromatin functions in *Neurospora*.

Recent work in *Neurospora* has identified ASH-1-mediated H3K36 methylation as a factor that contributes to normal patterns of H3K27me3 by PRC2 (4). We have also identified H3K36 as an important residue for maintaining inaccessibility of chromatin within the *Neurospora* genome. We therefore posited that H3K36me could be contributing to maintaining heterochromatin function in *Neurospora* cells lacking other repressive heterochromatin marks.

Here, we show that H3K36me3 is enriched in heterochromatin domains in mutants lacking dim-5 or HP1. We also show that double mutants for dim-5 and set-7 also exhibit enrichment of H3K36me3 in constitutive heterochromatin domains. Importantly, normal patterns of H3K36me3 are not disrupted, and deletion of the DNA methyltransferase DIM-2 does not result in enrichment of H3K36me3, indicating that this phenotype is independent of H3K9me3 and DNA methylation, but may be HP1- dependent. ATAC-seq experiments in histone methyltransferase mutants indicate that chromatin structure is relatively stable in histone methyltransferase mutants. However, ATAC-seq studies in single residue point mutations H3K36Q and H3K36R also show that heterochromatin domains in these mutants exhibit increased chromatin accessibility, providing further evidence for H3K36me in maintaining an inaccessible chromatin state in *Neurospora*.

## **Methods**

### **Strains and growth conditions**

Strains are listed in Table 4.1. All strains were grown in Vogel's minimal medium with 1.5% sucrose overnight with shaking. H3K36MUT strains were grown in the presence of 1x or 5x hygromycin (100 ug/ml or 500 ug/ml).

## **ATAC-seq**

ATAC-seq was performed as described in (5, 6). In short, overnight mycelial cultures were lysed in lysis buffer (15 mM Tris pH 7.5; 2 mM EDTA; 0.5 mM spermine; 80 mM KCl; 20 mM NaCl; 15 mM (or 0.1% v/v)  $\beta$ -me; 0.3% TritonX-100), and nuclei were isolated through repeated filtering through miracloth followed by numerous rounds of gentle centrifugation (1000 rpm for 5 minutes). Tn5 integration was performed using Tn5 transposase pre-loaded with Illumina sequencing adaptors ; samples were incubated for 30 minutes at 37° C and fragmented DNA was isolated using the Qiagen MinElute kit (Cat#. 28004). Sequencing libraries were constructed using Phusion (ThermoFisher Cat # F549N) and amplified with primers provided in (5). Libraries were cleaned using SeraPure beads (Fisher Cat. # 09-981-123) before submission for sequencing as described in (7) . Libraries were sequenced on an Illumina NextSeq 500 instrument by Georgia Genomics Facility at University of Georgia.

### *Mapping and data analysis*

ATAC-seq reads were trimmed and quality scored with TrimGalore! (<https://github.com/FelixKrueger/TrimGalore>). Trimmed reads were mapped to the NC12 genome (GCA\_000182924.2\_NC12) with BowTie2 using the `–very-sensitive` option and setting the maximum insert size set at 2000 bp (8). ATAC-seq reads were counted using featureCounts (9) and downstream analysis was performed in R (10).

## **Chromatin Immunoprecipitation (ChIP-seq)**

ChIP-seq was performed as described in (7, 11) for H3K27me2/3 (Active Motif Mouse Monoclonal, Catalog # 39535, Lot# 16714012), H3K36me3 (Abcam Rabbit Catalog # ab9050, Lot # GR300388-1), and H3K9me3 (Active Motif Rabbit Catalog # 39162). Sequencing libraries

were created and analyzed as described in (7). Libraries were sequenced as described above by Georgia Genomics Facility at University of Georgia.

### *Mapping and data analysis*

ChIP-seq reads were cleaned and trimmed using TrimGalore! (<https://github.com/FelixKrueger/TrimGalore>) Trimmed reads were mapped to the NC12 genome (GCA\_000182924.2\_NC12) with BWA (12) using the mem option with flagged secondary hits (bwa mem -M). Peaks were called using MACS2 (13) using the broad option without input and with a q-value of 0.01. Peak files were merged to combine proximal peaks within 10kb domains using bedtools merge. Peak files were compared with bedtools (14) intersect or subtract. Bigwig files for visualization were made using deepTools bamCoverage with the following options: -bs1 --normalizeUsing CPM, --ignoreDuplicates. Heatmaps were created using deepTools computeMatrix and plotHeatmap. Browser tracks were created with Integrated Genomics Viewer (IGV) (15) .

## **Results**

H3K27me<sub>2/3</sub> invades heterochromatin in *Neurospora* mutants deficient in heterochromatin machinery (1, 2). Given recent findings that H3K36me and H3K27me co-localize in *Neurospora* and that ASH-1-mediated H3K36me<sub>2</sub> was needed for normal localization of H3K27me<sub>2/3</sub>, we wanted to know if H3K36me was also re-localizing to heterochromatin in heterochromatin-deficient *Neurospora* strains. We tested this by performing ChIP-seq for H3K36me<sub>3</sub> in mutants lacking individual constitutive heterochromatin pathway components, diagrammed in Fig. 4.1A. We focused on the H3K9 methyltransferase DIM-5, the H3K9me<sub>3</sub> reader HP1, the histone deacetylase (HDAC) HDA-1, and the DNA methyltransferase DIM-2.

Deletion of these genes focuses on different parts of the heterochromatin pathway (nucleation, spreading, and maintenance), allowing investigation into all aspects of the pathway.

Visualization of our ChIP-seq experiments in the genome browser revealed that H3K36me3 is enriched in heterochromatin domains to varying extents in  $\Delta dim-5$ ,  $\Delta hpo$ , and  $\Delta hda-1$ , but not in the DNA methyltransferase mutant  $\Delta dim-2$  (Fig. 4.1B). Enrichment of H3K36me3 in heterochromatin mimics that of H3K27me3 in the H3K9me3 methyltransferase deletion mutant  $\Delta dim-5$  in  $\Delta dim-5$  and  $\Delta hpo$ , with enrichment at heterochromatin domains throughout the genome (Fig. 51B). Meanwhile,  $\Delta hda-1$  exhibits regional gains of H3K36me3 at some but not all heterochromatin regions. To determine global changes in H3K36me3 enrichment in these mutants, we plotted a heatmap of H3K9me3 and H3K36me3 at all heterochromatin domains, with heatmaps centered on the 5' or 3' boundary of these domains (Fig. 4.1C). H3K36me3 enrichment is increased in all heterochromatin domains similar to H3K27me2/3 in  $\Delta dim-5$  and  $\Delta hpo$ , with mild increase in  $\Delta hda-1$  and no change in  $\Delta dim-2$ .

We next wanted to know if enrichment of H3K36me3 in heterochromatin was dependent on H3K27me2/3, so we performed ChIP-seq for H3K36me3 in strains lacking the single deletion mutant for the H3K27 methyltransferase ( $\Delta set-7$ ) and a strain lacking both DIM-5 and SET-7 ( $\Delta dim-5; \Delta set-7$ ). Investigation of ChIP-seq results in the genome browser showed no clear enrichment for H3K36me3 in heterochromatin domains in  $\Delta set-7$  (Fig. 4.3A). Additionally,  $\Delta dim-5; \Delta set-7$  shows a mild increase of H3K36me3 in heterochromatin domains. Heatmaps of H3K36me3 enrichment in heterochromatin domains of these mutants shows a mild increase of H3K36me3 in heterochromatin in  $\Delta dim-5; \Delta set-7$  that is not present in the  $\Delta set-7$  single mutant (Fig. 4.2C). Taken together, these results suggest that disruption of heterochromatin, and not the

presence of H3K27me<sub>2/3</sub>, is responsible for H3K36me<sub>3</sub> enrichment in constitutive heterochromatin in *Neurospora*.

We next wanted to investigate changes in H3K36me<sub>3</sub> in  $\Delta hda-1$  more closely. Because we previously identified a selective re-localization phenotype of H3K27me<sub>2/3</sub> in  $\Delta hda-1$ , we wanted to know if H3K36me<sub>3</sub> and H3K27me<sub>2/3</sub> occupied the same regions in this strain. Investigation of Linkage Group III on the genome browser shows that H3K36me<sub>3</sub> and H3K27me<sub>2/3</sub> share similar patterns of enrichment in  $\Delta hda-1$  (Fig. 4.3A). We next looked globally at H3K36me<sub>3</sub> and H3K27me<sub>2/3</sub> by plotting a heatmap enrichment centered on the edges of facultative heterochromatin and sorted by H3K36me<sub>3</sub> enrichment in  $\Delta hda-1$ . These suggest that H3K36me<sub>3</sub> and H3K27me<sub>2/3</sub> are linked in this strain.

Heterochromatin mutants exhibit mislocalized H3K27me<sub>2/3</sub>, with loss of H3K27me<sub>2/3</sub> at native regions and enrichment at heterochromatin, so we wanted to know if normal patterns of H3K36me<sub>3</sub> are also disturbed. To measure this, we first plotted a heatmap of H3K36me<sub>3</sub> centered on gene bodies with flanks of 1500 bp upstream and 500 bp of the gene. These show that normal patterns of H3K36me<sub>3</sub> are not disturbed in heterochromatin mutants (Fig. 4.4A). We next confirmed this by plotting average H3K36me<sub>3</sub> across these same regions, which shows unchanged patterns of H3K36me<sub>3</sub> in any strain studied (Fig. 4.4B).

Heterochromatin-deficient *Neurospora* mutants that also lack H3K27me<sub>2/3</sub> are viable (1). To determine if H3K36me<sub>3</sub> is functionally important in *Neurospora* heterochromatin mutants, we crossed strains lacking the H3K36 methyltransferase SET-2 and the H3K9 methyltransferase DIM-4. We were unable to isolate any  $\Delta set-2;\Delta dim-5$  progeny from this cross, indicating that *set-2* and *dim-5* are synthetically lethal and H3K36me<sub>3</sub> is functionally important in some capacity in *Neurospora* (Table 4.2).

Recent 3D chromatin interaction studies in *Neurospora* found that disruption of H3K27me3 or H3K9me3 did not affect overall chromatin organization within the nucleus (3). Given our findings that H3K36me3 appears is gained at heterochromatin domains in the absence of key heterochromatin components, we reasoned that H3K36me3 might functionally compensate for the lack of normal heterochromatin in these mutants. To test this, we asked if the H3K36 residue was important for restricting chromatin accessibility in heterochromatin domains.

We performed ATAC-seq in mutants with single point mutations of the H3K36 residue described in Sasaki et al. (11) (H3K36Q to mimic acetylated lysine or H3K36R to mimic unmodified lysine) and well-characterized histone methyltransferase mutants: *Δset-7* (H3K27me2me3), *Δdim-5* (H3K9me3), *Δset-2* (H3K36me3), and *Δdim-5; Δset-7*. We also included *Δeaf-3*, which is the homolog of *Saccharomyces cerevisiae* Eaf3p and is involved in silencing of cryptic promoters within gene bodies in yeast (16), and the histone variant *ΔhH2A.z*, which has been linked to depleted H3K27me2/3 (17). To determine any changes in chromatin accessibility, we counted ATAC-seq reads in heterochromatin domains in these strains. We then divided size-normalized counts (counts per million; CPM) in mutants by their wild type controls and plotted their distribution as violin plots. We found that H3K36Q and H3K36R showed increased chromatin accessibility in heterochromatin domains compared to histone methyltransferase mutants and *ΔhH2A.z* (Fig. 4.5A). We next performed the same analysis in all intergenic regions to determine whether this phenotype was specific to heterochromatin domains and not all intergenic regions. We did not see the same changes in chromatin accessibility in all intergenic regions, suggesting that this phenotype is specific to heterochromatin (Fig. 4.5B).



## Discussion

Maintenance of repressive heterochromatin is important for cell survival. While loss of H3K9me3 or its reader protein HP1 can disrupt heterochromatin domains, it does not affect overall 3D organization of the genome within the nucleus. An obvious explanation for this would be that H3K27me3 replaces H3K9me3 in heterochromatin domains and provides a mechanism for maintenance of heterochromatin structure. However, loss of both H3K9me3 and H3K27me3 still does not lead to wide changes in 3D genome structure within the cell. Our discovery of H3K36me3 as a compensatory mechanism for the loss of H3K9me3 or HP1, regardless of the presence of H3K27me3, while maintaining normal patterns of H3K36me3 provides an explanation for this. It is possible that H3K36me3 acts as a “last ditch effort” in the cell to maintain repressive heterochromatin domains in *Neurospora*.

There is evidence of H3K36me3 within pericentromeric heterochromatin in mouse, and association with HP1a has also been demonstrated (18, 19). Therefore, it is possible that the presence of H3K36me3 in heterochromatin domains of strains lacking H3K9me3 could provide binding sites for HP1 and maintained 3D chromatin architecture. However, HP1 has not yet been shown to interact with H3K36me3 in *Neurospora*, and HP1 occupancy in strains lacking H3K9me3 is absent within heterochromatin. Additionally, 3D chromatin organization studies have not been performed in strains lacking H3K36me3 or HP1.

Our genetic manipulation of H3K36 supports this hypothesis. By disrupting H3K36 and performing chromatin accessibility assays, we have shown that regions which are normally inaccessible exhibit small gains in accessibility in H3K36<sup>mut</sup>. Namely, there is an increase in chromatin accessibility in constitutive heterochromatin domains that is not exhibited in histone methyltransferase deletion mutants. More work will need to be done to determine any interplay

between H3K36 and heterochromatin domains. Namely, these experiments need to be repeated in a heterochromatin mutant background. Additionally, we assume that integration of H3K36<sup>mut</sup> molecules is stochastic. There may be protective measures such as repressive heterochromatin structures that prevent integration of these histones into chromatin. Recent work assaying turnover of histone H3 via ChIP-seq for FLAG-tagged hH3 after induction showed that *Δhpo* and *Δhda-1* showed increased turnover within heterochromatin domains. Therefore, the heterokaryotic nature of our H3K36<sup>mut</sup> strains may prevent integration of mutant histones into protected regions of the genome. Future studies combining histone turnover and H3K36 point mutants in these genetic backgrounds will be critical to gaining a more complete understanding the role of H3K36me3 in this epigenetic compensation.

## References

1. Basenko EY, Sasaki T, Ji L, Prybol CJ, Burckhardt RM, Schmitz RJ, Lewis ZA. 2015. Genome-wide redistribution of H3K27me3 is linked to genotoxic stress and defective growth. *Proc Natl Acad Sci U S A*.
2. Jamieson K, Wiles ET, McNaught KJ, Sidoli S, Leggett N, Shao Y, Garcia BA, Selker EU. 2016. Loss of HP1 causes depletion of H3K27me3 from facultative heterochromatin and gain of H3K27me2 at constitutive heterochromatin. *Genome Res*.
3. Klocko AD, Ormsby T, Galazka JM, Leggett NA, Uesaka M, Honda S, Freitag M, Selker EU. 2016. Normal chromosome conformation depends on subtelomeric facultative heterochromatin in *Neurospora crassa*. *Proc Natl Acad Sci U S A*.
4. Bicocca VT, Ormsby T, Adhvaryu KK, Honda S, Selker EU. 2018. ASH1-catalyzed H3K36 methylation drives gene repression and marks H3K27me2/3-competent chromatin. *Elife*2018/11/24. 7.
5. Buenrostro JD, Giresi PG, Zaba LC, Chang HY, Greenleaf WJ. 2013. Transposition of native chromatin for fast and sensitive epigenomic profiling of open chromatin, DNA-binding proteins and nucleosome position. *Nat Methods* 10:1213–1218.
6. Lu Z, Hofmeister BT, Vollmers C, DuBois RM, Schmitz RJ. 2017. Combining ATAC-seq with nuclei sorting for discovery of cis-regulatory regions in plant genomes. *Nucleic Acids Res*2016/12/03. 45:e41.

7. Ferraro AR, Lewis ZA. 2018. ChIP-seq analysis in *Neurospora crassa* *Methods in Molecular Biology*.
8. Langmead B, Salzberg SL. 2012. Fast gapped-read alignment with Bowtie 2. *Nat Methods* 2012/03/06. 9:357–359.
9. Liao Y, Smyth GK, Shi W. 2013. The Subread aligner: Fast, accurate and scalable read mapping by seed-and-vote. *Nucleic Acids Res*.
10. R Core Team. 2014. R Core Team (2014). R: A language and environment for statistical computing. R Found Stat Comput Vienna, Austria URL <http://www.R-project.org/>.
11. Sasaki T, Lynch KL, Mueller C V., Friedman S, Freitag M. 2014. Heterochromatin controls  $\gamma$ H2A localization in *Neurospora crassa*. *Eukaryot Cell*.
12. Li H, Durbin R. 2009. Fast and accurate short read alignment with Burrows-Wheeler transform. *Bioinformatics*.
13. Zhang Y, Liu T, Meyer CA, Eeckhoute J, Johnson DS, Bernstein BE, Nusbaum C, Myers RM, Brown M, Li W, Liu XS. 2008. Model-based analysis of ChIP-Seq (MACS). *Genome Biol* 2008/09/19. 9:R137.
14. Quinlan AR, Hall IM. 2010. BEDTools: A flexible suite of utilities for comparing genomic features. *Bioinformatics*.
15. Robinson PN, Zemojtel T. 2017. Integrative genomics viewer (IGV): Visualizing alignments and variants *Computational Exome and Genome Analysis*.
16. Rundlett SE, Carmen AA, Kobayashi R, Bavykin S, Turner BM, Grunstein M. 1996. HDA1 and RPD3 are members of distinct yeast histone deacetylase complexes that regulate silencing and transcription. *Proc Natl Acad Sci U S A*.
17. Courtney AJ, Kamei M, Ferraro AR, Gai K, Hu Q, Honda S, Lewis ZA. 2020. The histone variant H2A.Z is required to establish normal patterns of H3K27 methylation in *Neurospora crassa*. *bioRxiv*.
18. Lin CH, Li B, Swanson S, Zhang Y, Florens L, Washburn MP, Abmayr SM, Workman JL. 2008. Heterochromatin Protein 1a Stimulates Histone H3 Lysine 36 Demethylation by the *Drosophila* KDM4A Demethylase. *Mol Cell*.
19. Lin CH, Paulson A, Abmayr SM, Workman JL. 2012. HP1a targets the *Drosophila* KDM4A demethylase to a subset of heterochromatic genes to regulate H3K36me3 levels. *PLoS One*.

## Tables

**Table 4.1 Strains used in the study**

Strain ID	Genotype
S2	Wild type
S132	<i>dim-5::hph</i>
S189	<i>hpo::hph</i>
S238	<i>set-7::hph</i>
S355	<i>dim-5::hph; set-7::hph</i>
S124	<i>dim-2::hph</i>
S518	<i>set-2::hph</i>
FGSC14841	<i>eaf-3::hph</i>
ACx11-8	<i>hh2az::hph</i>
FGSC12003	<i>hda-1::hph</i>
Aft34-1,-2,-3	<i>FgH3:bar;H3K36R:hph</i>
Aft35-1,-2,-3	<i>FgH3:bar;H3K36Q:hph</i>

**Table 4.2. Cross analysis of  $\Delta set-2$  x  $\Delta dim-5$**

Strain	Genotype	Expected (%)	Actual (%)
Wild Type	H3K36me3+;H3K9me3+	25	49
$\Delta set-2$	H3K36me3-	25	11
$\Delta dim-5$	H3K9me3-	25	40
$\Delta set-2;\Delta dim-5$	H3K36me3-;H3K9me3-	25	

*n*=163

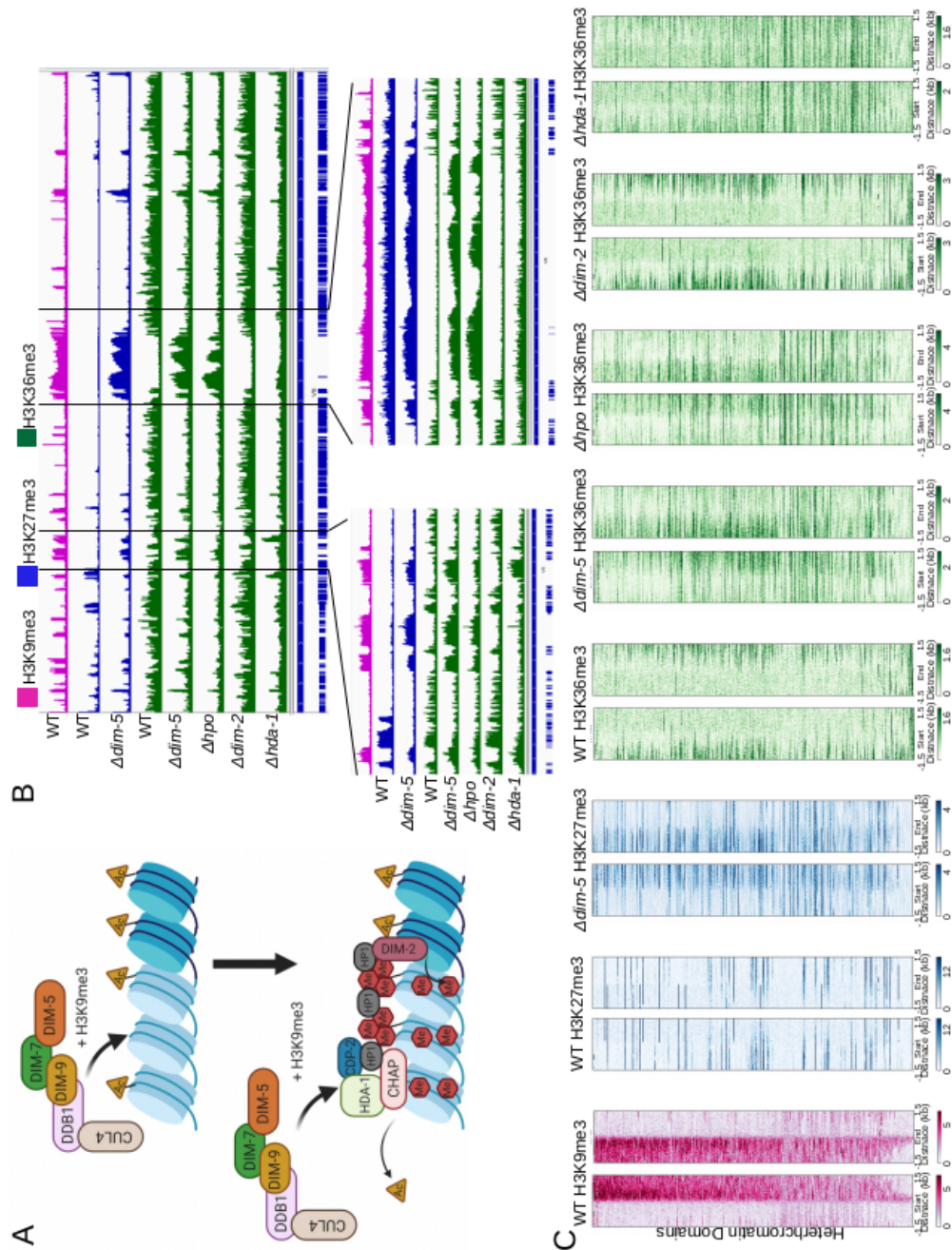


**Figure 4.1. H3K36me3 is enriched in heterochromatin in heterochromatin mutants. (A)**

Model of the *Neurospora* heterochromatin pathway. (B) Representative browser shot of

H3K36me3 enrichment in various mutants. (C) Heatmap of the indicated histone mark centered 5' and 3' ends of heterochromatin domains.

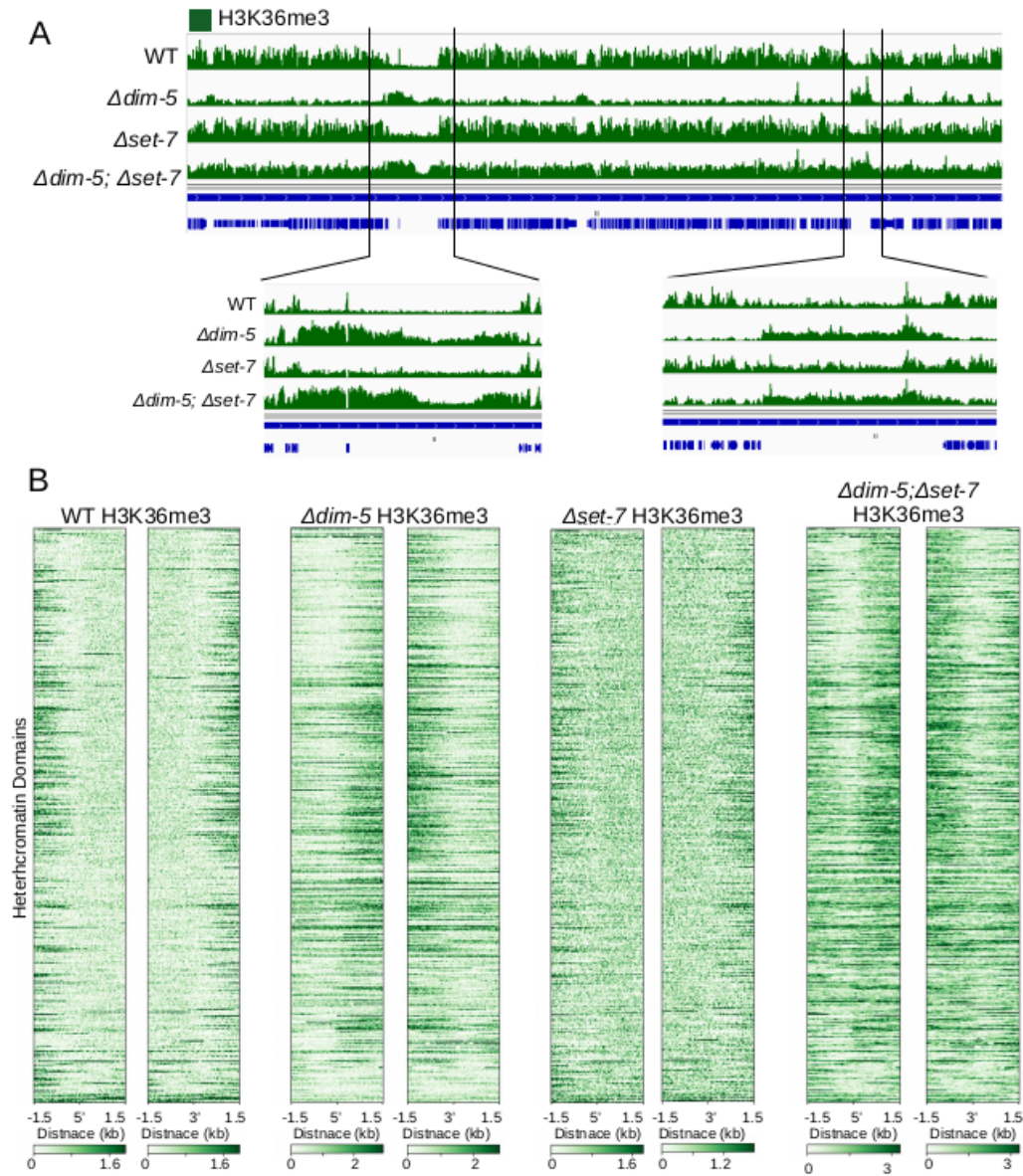


**Figure 4.2. H3K36me3 enrichment in heterochromatin is not dependent on H3K27me3. (A)**

Representative browser shot of Linkage Group II showing H3K36me3 enrichment in wild type,  $\Delta dim-5$ ,  $\Delta set-7$ , and  $\Delta dim-5; \Delta set-7$  shows enrichment of H3K36me3 in  $\Delta dim-5$  and  $\Delta dim-5; \Delta set-7$ , but not  $\Delta set-7$ . (B) Heatmaps showing global enrichment of H3K36me3 in wild type,  $\Delta dim-5$ ,  $\Delta set-7$ , and  $\Delta dim-5; \Delta set-7$ . Wild type and  $\Delta dim-5$  data are re-plotted from figure 4.1.



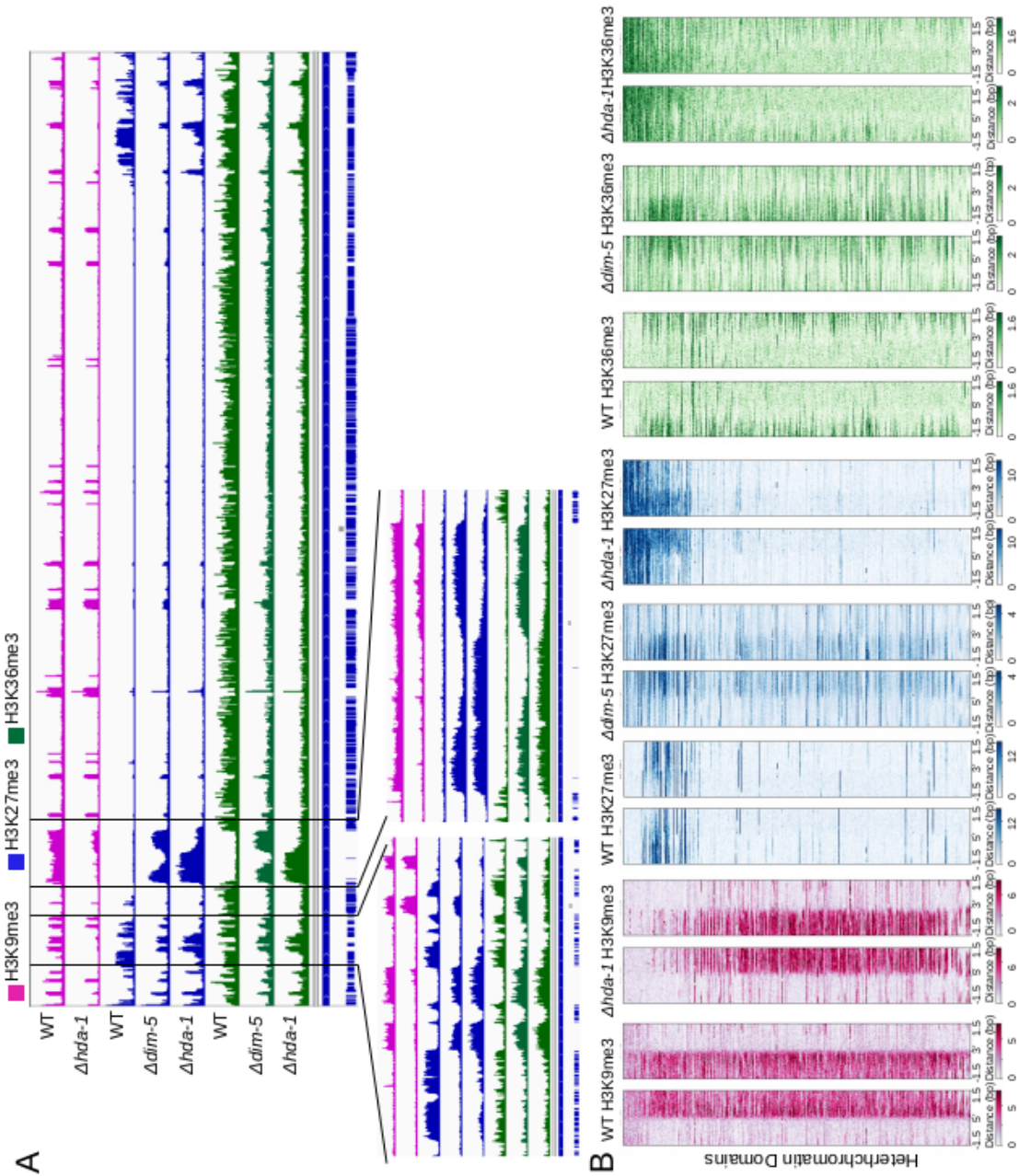


**Figure 4.3.  $\Delta hda-1$  shows limited increase in H3K36me3 in heterochromatin domains. (A)** Representative browser shot of Linkage Group III showing H3K27me2/3 and H3K36me3 in wild type,  $\Delta dim-5$ , and  $\Delta hda-1$ . **(B)** Heatmaps showing global enrichment of H3K27me2/3 and H3K36me3 in wild type,  $\Delta dim-5$ , and  $\Delta hda-1$ . Heatmaps are sorted by H3K36me3 enrichment in  $\Delta hda-1$ .

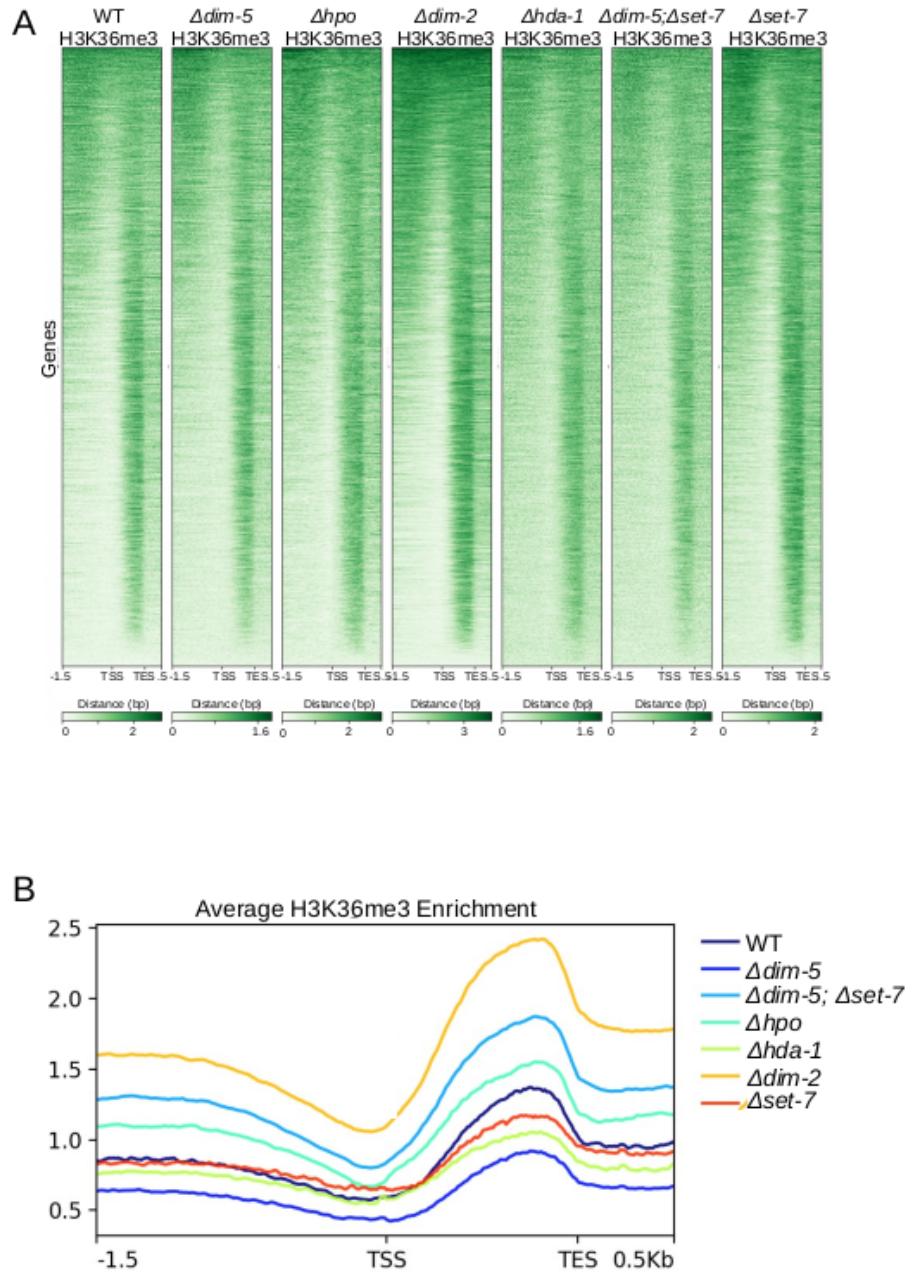


**Figure 4.4. H3K36me3 enrichment unchanged in genic regions in heterochromatin**

**mutants.** (A) Heatmaps of H3K36me3 centered on gene bodies with 1500 bp flanks upstream and 500 bp flanks downstream of genes. (B) Metaplot of average H3K36me3 enrichment across the *Neurospora* genome, centered as in A.



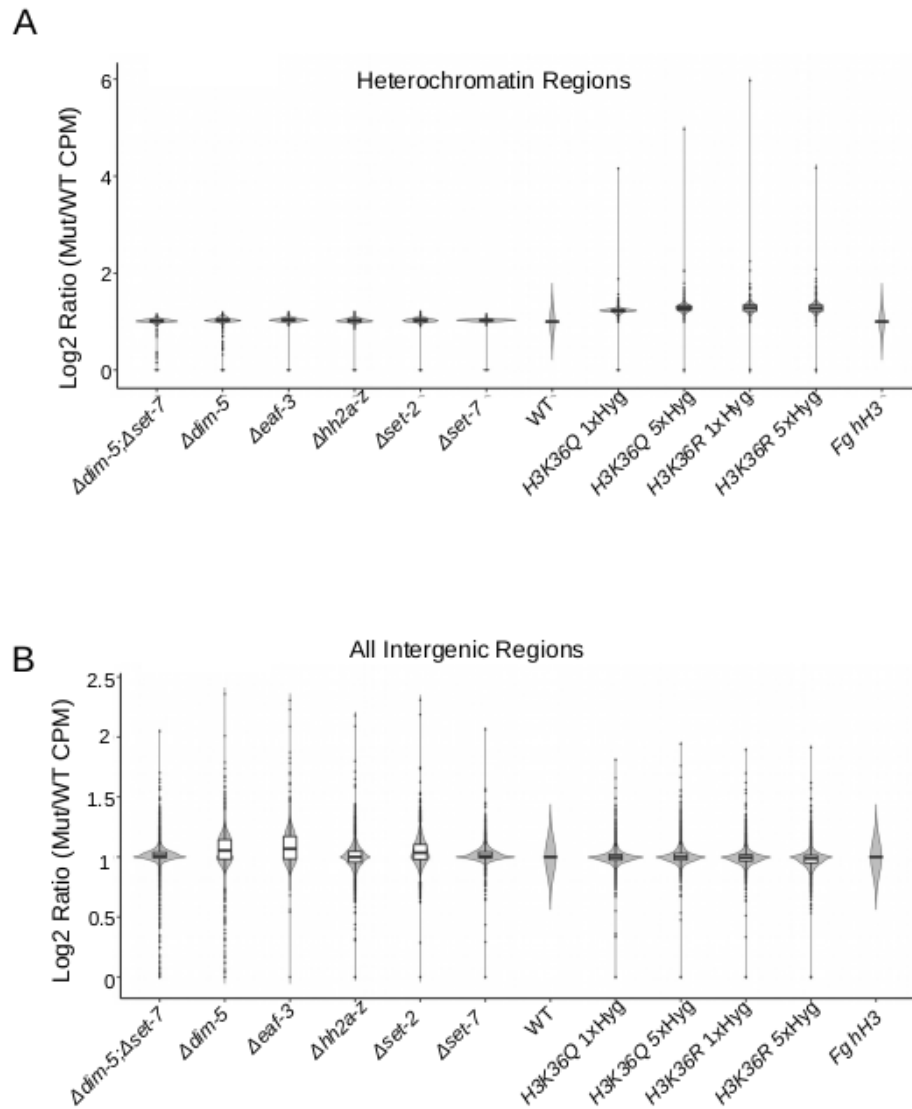


**Figure 4.5. H3K36 is important for maintaining inaccessibility in heterochromatin domains.** (A) Read counts from ATAC-seq experiments were performed in heterochromatin regions and raw counts were converted to counts per million (CPM). CPM values for mutant strains were divided by their wild type control (wild type for deletion mutants and *F. graminearum* H3 for H3K36MUT strains) and the log2 ratio of Mut/WT CPMs were plotted as a violin plot. (B) The same analysis from A was performed on all intergenic regions as a control.

## CHAPTER 5

### DISCUSSION

The work presented here provides important contributions to our understanding of fundamental mechanisms that contribute to control and function of local chromatin environment in eukaryotes. First, it provides the first holistic integration of chromatin accessibility data with histone modifications in a filamentous fungus. It also provides a new mechanism for creating a repressive chromatin environment at gene promoters, where H3K36me is associated with both gene repression and inaccessible chromatin. Next, it provides evidence of histone deacetylases in maintaining distinct heterochromatin domains: conditionally repressed facultative heterochromatin and constitutive heterochromatin, where disruption of either HDA-1 or NST-3 results in mislocalization of facultative heterochromatin within constitutive heterochromatin domains, and in the case of HDA-1, proper distribution of H3K9me3. Lastly, this work shows a new role for H3K36me3: epigenetic compensation in the loss of normal heterochromatin. Disruption of heterochromatin in *Neurospora* has been shown to result in re-distribution of H3K27me3 into heterochromatin domains. The underlying mechanism for this has not been demonstrated. The discovery of H3K36me3 in heterochromatin domains of heterochromatin-deficient mutants and its independence from H3K27me3 provides a possible mechanism that warrants further investigation.

#### ***Neurospora* provides evidence of fundamental mechanisms of regulation of accessible chromatin**

Integration of chromatin accessibility data with histone modification data provide important new information about the competitive relationship between histones, histone

modifications, and DNA-binding by transcription factors. This is the first integration of multiple genomics datasets to define chromatin environment in a filamentous fungus, and it draws key parallels between *Neurospora* and higher eukaryotes. For example, chromatin within gene promoters is accessible and marked by active histone modifications, while chromatin within gene bodies or repressive domains is inaccessible.

Chromatin accessibility and pioneer transcription factor binding dynamics have been identified in *Neurospora* using the well-characterized white collar complex (WCC) subunit white-collar 2 (WC-2). Previous work using MNase-based assays of nucleosome organization at WCC-target sites has shown that WCC can act as a pioneer factor and mediate nucleosomal rearrangement at these sites (1). This work expands on these findings by showing that WCC binding and subsequent nucleosomal rearrangement directly mediates chromatin accessibility at WCC-binding sites. This provides not only a means of examining transcription factor binding dynamics in a high throughput way, i.e. by performing ATAC-seq on a panel of transcription factor deletion mutants but supports a fundamental mechanism for transcription factor-mediated chromatin reorganization in eukaryotes.

This study also revealed large regions of hyperaccessible chromatin near master regulatory genes in *Neurospora* which share properties with enhancer elements in higher eukaryotes, namely H3K27ac and transcription of small RNAs. This is a feature that has previously been considered to be absent from fungi and other lower eukaryotes, yet the work here shows that these domains are indeed present and perhaps functionally important. Identification and characterization of these regions in *Neurospora* supports a new model of promoter and enhancer dynamics, where both contain transcriptional potential and act as recruitment sites for transcriptional machinery. Enhancers, therefore, would merely be promoters

that have the potential to positively regulate transcription of other genes (2). This new model, and the first identification of potential enhancer-like elements in a filamentous fungus, widens the scope of transcriptional regulation in eukaryotes and provides a possible evolutionary foundation for cis-regulatory elements in eukaryotes. More work needs to be done to fully understand the role of these hyperaccessible regions in *Neurospora*, and this can be easily addressed by genetic manipulation of these regions and so-called “promoter-bashing” experiments designed to assay the role of promoter and enhancer regions on transcription of a reporter gene (3, 4). Additionally, investigation of fungi with larger genomes and higher transposon loads could very well possess distal enhancer elements similar to those found in plants and animals as a result of transposable element insertion that separates regulatory elements from target genes on a linear chromosome. This would provide much stronger evidence for an evolutionary conservation for these cis-regulatory elements throughout eukaryotes.

This work also characterizes small, non-coding transcripts identified by Duttke et al. (5) flanking accessible chromatin regions in *Neurospora*. It is unclear if these small RNAs are playing a regulatory role in any system. However, growing evidence from fungal model systems suggests that some RNAs play a larger role in regulation of cellular processes through phase separation (6, 7). This model demonstrates transcription of RNAs whose tertiary structures are key for mediating the formation of regulatory micro-environments that are necessary for cellular processes such as cell cycle progression or whose misregulation are key factors in development of neurodegenerative diseases (8, 9). Importantly, these transcripts are independent from mRNA transcripts. This raises an interesting role for the small RNAs identified and could support phase separation as a fundamental mechanism for regulation of cellular processes in eukaryotes.

## **HDA-1 provides a unifying mechanism for maintenance of heterochromatin domains**

In animals and fungi, disruption of constitutive heterochromatin marks leads to re-localization of H3K27me3 from normal sites to constitutive heterochromatin regions, which typically lack H3K27me3. In animals, hypomethylation of DNA within heterochromatin regions leads to translocation of H3K27me3 and expression of genes normally silenced by H3K27me3 (10–13). Likewise, similar disruption of DNA methylation, and not H3K9me3, in *Arabidopsis* results similar relocalization of H3K27me3. In *Neurospora*, H3K9me3 and HP1 but not DNA methylation seems to be the critical factor in limiting H3K27me3 within constitutive heterochromatin domains (14, 15).

The observed movement of H3K27me3 in  $\Delta hda-1$  may provide a unifying mechanistic explanation for this phenomenon that is observed in animals and fungi. Histone deacetylation is a shared feature of heterochromatin formation from yeast to humans (for a review, see 16), and HDA-1 was shown to be important for maintenance but not establishment of heterochromatin in *Neurospora* (17).

These studies also reveal possible redundancies between two classes of HDACs in *Neurospora*. The Class II HDAC HDA-1 and Class III sirtuin NST-3 both exhibit changes in H3K27me3, which includes localization in constitutive heterochromatin domains. While H3K27me3 is maintained in normal regions in *nst-3<sup>RIP</sup>*, it does also exhibit enrichment of H3K27me3 in heterochromatin domains. There are two explanations for this: (1) there is functional redundancy between HDA-1 and NST-3 or (2) NST-3 acts on a non-histone substrate to mediate heterochromatin formation. Redundancy within HDAC proteins is a well-defined feature of these enzymes. HDACs are also rather promiscuous and depend heavily on their associated HDAC complex for targeting (18–20). This is in stark contrast to histone

methyltransferase, which have been shown to be rather specific in substrate activity (21, 22). The human sirtuin SIRT1 directly modulates activity of the H3K9 methyltransferase SUV39H1 (23), and SIRT1 deletion cells exhibit significantly decreased H3K9me3 enrichment. Therefore, it is possible that NST-3 is acting in a similar manner to regulate activity of heterochromatin machinery. Investigation into post-translational modifications of histone methyltransferase is lacking in *Neurospora*, and characterization of this type of regulation of chromatin-associated proteins can provide important mechanistic insights into regulation and control of these proteins at a fundamental level.

### **A new role for H3K36me3**

This work identifies an important phenotype for H3K36me3 dynamics in *Neurospora*. Namely, it identifies a new role for H3K36me3 in compensating for the loss of heterochromatin. H3K36me3 has been implicated in gene repression in *S. cerevisiae* and *S. pombe*, but links to heterochromatin function in higher eukaryotes have been limited. In animals, H3K36me has been linked DNA methylation and gene repression during development via imprinting during oocyte development. Transcription of long terminal repeats results in SETD2-mediated, transcriptionally-linked H3K36me3, which recruits the DNA methyltransferase DNMT3A and results in de novo establishment of DNA methylation in nearby gene bodies and gene repression throughout development (24). Additionally, mouse embryos lacking maternal SETD2 exhibit a loss of genomic imprinting, ectopic H3K27me2/3, and aberrant DNA methylation (25). This phenotype is strikingly similar to human cancers which exhibit changes in H3K36me3 and ectopic H3K27me2/3. Namely, the onco-histone H3K36M is involved in the development of chondroblastomas and sarcomas, and these cells exhibit disrupted heterochromatin and ectopic H3K27me3 at intergenic regions normally occupied by H3K36me (26).

The enrichment of H3K36me3 observed in heterochromatin domains of *Neurospora* heterochromatin mutants suggests a fundamental mechanism for this histone modification in creating a local chromatin environment that maintains the function of repressive heterochromatin. There is much work to be done to understand the mechanism and function of this enrichment of H3K36me3 in heterochromatin. First, the preliminary findings of increased chromatin accessibility within heterochromatin domains of H3K36 point mutants needs to be replicated. Next, if H3K36 is indeed important for maintaining a repressive chromatin environment in heterochromatin mutants, the H3K36 mutant histones must be studied in a heterochromatin mutant background (i.e.  $\Delta hpo$ ), where there could be a significant increase of accessibility within heterochromatin domains. Findings from these experiments, however, could contribute greatly to our understanding of H3K36 and its role as an onco-histone or in complicated silencing mechanisms like genomic imprinting.

## References

1. Sancar C, Ha N, Yilmaz R, Tesorero R, Fisher T, Brunner M, Sancar G. 2015. Combinatorial Control of Light Induced Chromatin Remodeling and Gene Activation in *Neurospora*. PLoS Genet.
2. Andersson R, Sandelin A. 2020. Determinants of enhancer and promoter activities of regulatory elements. Nat Rev Genet.
3. Engstrom EM, Izhaki A, Bowman JL. 2004. Promoter bashing, microRNAs, and Knox genes. New insights, regulators, and targets-of-regulation in the establishment of lateral organ polarity in *Arabidopsis*. Plant Physiol.
4. Dunn A, Marinotti O, Xie X, James A. 2011. Towards a conserved cis-regulatory module with cross-strain/species application for driving anti-pathogen effector transgenes: Comparative transcriptomics to discover early bloodmeal-responsive, cis-regulatory sequences from mosquito midgut RNA-SEQ. Am J Trop Med Hyg.
5. Duttke SH, Chang MW, Heinz S, Benner C. 2019. Identification and dynamic quantification of regulatory elements using total RNA. Genome Res 29:1836–1846.

6. Zhang H, Elbaum-Garfinkle S, Langdon EM, Taylor N, Occhipinti P, Bridges AA, Brangwynne CP, Gladfelter AS. 2015. RNA Controls PolyQ Protein Phase Transitions. *Mol Cell*.
7. Langdon EM, Qiu Y, Niaki AG, McLaughlin GA, Weidmann CA, Gerbich TM, Smith JA, Crutchley JM, Termini CM, Weeks KM, Myong S, Gladfelter AS. 2018. mRNA structure determines specificity of a polyQ-driven phase separation. *Science* (80- ).
8. Maharana S, Wang J, Papadopoulos DK, Richter D, Pozniakovsky A, Poser I, Bickle M, Rizk S, Guillén-Boixet J, Franzmann TM, Jahnel M, Marrone L, Chang YT, Sterneckert J, Tomancak P, Hyman AA, Alberti S. 2018. RNA buffers the phase separation behavior of prion-like RNA binding proteins. *Science* (80- ).
9. Wang J, Choi JM, Holehouse AS, Lee HO, Zhang X, Jahnel M, Maharana S, Lemaitre R, Pozniakovsky A, Drechsel D, Poser I, Pappu R V., Alberti S, Hyman AA. 2018. A Molecular Grammar Governing the Driving Forces for Phase Separation of Prion-like RNA Binding Proteins. *Cell*.
10. Peters AHFM, Kubicek S, Mechtler K, O'Sullivan RJ, Derijck AAHA, Perez-Burgos L, Kohlmaier A, Opravil S, Tachibana M, Shinkai Y, Martens JHA, Jenuwein T. 2003. Partitioning and Plasticity of Repressive Histone Methylation States in Mammalian Chromatin. *Mol Cell*.
11. Lindroth AM, Yoon JP, McLean CM, Dokshin GA, Persson JM, Herman H, Pasini D, Miró X, Donohoe ME, Lee JT, Helin K, Soloway PD. 2008. Antagonism between DNA and H3K27 methylation at the imprinted *Rasgrf1* locus. *PLoS Genet*.
12. Wu H, Coskun V, Tao J, Xie W, Ge W, Yoshikawa K, Li E, Zhang Y, Sun YE. 2010. Dnmt3a-dependent nonpromoter DNA methylation facilitates transcription of neurogenic genes. *Science* (80- ).
13. Reddington JP, Perricone SM, Nestor CE, Reichmann J, Youngson NA, Suzuki M, Reinhardt D, Dunican DS, Prendergast JG, Mjoseng H, Ramsahoye BH, Whitelaw E, Greally JM, Adams IR, Bickmore WA, Meehan RR. 2013. Redistribution of H3K27me3 upon DNA hypomethylation results in de-repression of Polycomb target genes. *Genome Biol*.
14. Basenko EY, Sasaki T, Ji L, Prybol CJ, Burckhardt RM, Schmitz RJ, Lewis ZA. 2015. Genome-wide redistribution of H3K27me3 is linked to genotoxic stress and defective growth. *Proc Natl Acad Sci U S A*.
15. Jamieson K, Wiles ET, McNaught KJ, Sidoli S, Leggett N, Shao Y, Garcia BA, Selker EU. 2016. Loss of HP1 causes depletion of H3K27me3 from facultative heterochromatin and gain of H3K27me2 at constitutive heterochromatin. *Genome Res*.



16. Grewal SIS, Jia S. 2007. Heterochromatin revisited. *Nat Rev Genet*.
17. Gessaman JD, Selker EU. 2017. Induction of H3K9me3 and DNA methylation by tethered heterochromatin factors in *Neurospora crassa*. *Proc Natl Acad Sci U S A*.
18. Seto E, Yoshida M. 2014. Erasers of histone acetylation: The histone deacetylase enzymes. *Cold Spring Harb Perspect Biol*.
19. Lemon DD, Harrison BC, Horn TR, Stratton MS, Ferguson BS, Wempe MF, McKinsey TA. 2015. Promiscuous actions of small molecule inhibitors of the protein kinase D-class IIa HDAC axis in striated muscle. *FEBS Lett*.
20. Kelly RDW, Chandru A, Watson PJ, Song Y, Blades M, Robertson NS, Jamieson AG, Schwabe JWR, Cowley SM. 2018. Histone deacetylase (HDAC) 1 and 2 complexes regulate both histone acetylation and crotonylation in vivo. *Sci Rep*.
21. Zhang X, Yang Z, Khan SI, Horton JR, Tamaru H, Selker EU, Cheng X. 2003. Structural basis for the product specificity of histone lysine methyltransferases. *Mol Cell*.
22. del Rizzo PA, Trievel RC. 2011. Substrate and product specificities of SET domain methyltransferases. *Epigenetics*.
23. Vaquero A, Scher M, Erdjument-Bromage H, Tempst P, Serrano L, Reinberg D. 2007. SIRT1 regulates the histone methyl-transferase SUV39H1 during heterochromatin formation. *Nature*.
24. Bogutz AB, Brind'Amour J, Kobayashi H, Jensen KN, Nakabayashi K, Imai H, Lorincz MC, Lefebvre L. 2019. Evolution of imprinting via lineage-specific insertion of retroviral promoters. *Nat Commun*.
25. Xu Q, Xiang Y, Wang Q, Wang L, Brind'Amour J, Bogutz AB, Zhang Y, Zhang B, Yu G, Xia W, Du Z, Huang C, Ma J, Zheng H, Li Y, Liu C, Walker CL, Jonasch E, Lefebvre L, Wu M, Lorincz MC, Li W, Li L, Xie W. 2019. SETD2 regulates the maternal epigenome, genomic imprinting and embryonic development. *Nat Genet*.
26. Lu C, Jain SU, Hoelper D, Bechet D, Molden RC, Ran L, Murphy D, Venneti S, Hameed M, Pawel BR, Wunder JS, Dickson BC, Lundgren SM, Jani KS, De Jay N, Papillon-Cavanagh S, Andrulis IL, Sawyer SL, Grynspan D, Turcotte RE, Nadaf J, Fahiminiyah S, Muir TW, Majewski J, Thompson CB, Chi P, Garcia BA, Allis CD, Jabado N, Lewis PW. 2016. Cancer: Histone H3K36 mutations promote sarcomagenesis through altered histone methylation landscape. *Science* (80- ).

APPENDIX A

CHIP-SEQ ANALYSIS IN *NEUROSPORA CRASSA*

---

Ferraro A.R. and Lewis Z.A. 2018. *Methods in Molecular Biology: Fungal Genomics*. 1775:241-250. Reprinted here with the permission of the publisher.

## Summary/Abstract

Chromatin immunoprecipitation paired with next generation sequencing (ChIP-seq) can be used to determine genome-wide distribution of transcriptions factors, transcriptional machinery, or histone modifications. DNA-protein interactions are covalently crosslinked with the addition of formaldehyde. Chromatin is prepared and sheared, then immunoprecipitated with the appropriate antibody. After reversal of crosslinking and treating with protease, the resulting DNA fragments are sequenced and mapped to the reference genome to determine overall enrichment. Here we describe a method of ChIP-seq for investigating protein-DNA interactions in the filamentous fungus *Neurospora crassa*.

Key Words (5-10): chromatin immunoprecipitation, protein-DNA interactions, histone modifications, transcription factor binding

## 1. Introduction

Protein-DNA interactions regulate diverse nuclear processes such as gene expression, DNA repair and maintenance, chromosome segregation, and establishing and maintaining epigenetic modifications. The advent of chromatin immunoprecipitation (ChIP) has proven to be critical in the study of protein-DNA interactions and associated processes. ChIP followed by high throughput sequencing (ChIP-seq) has become a standard method in genome biology, allowing researchers to look at diverse DNA-protein interactions, including histone occupation, transcription factor binding, histone modifications, histone turnover, and other features of the genome-wide chromatin landscape including base modifications.

ChIP was first described by Gilmour and Lis [1] as a method to investigate localization of regulatory factors such as RNA polymerase II (Pol II) and histone occupation in *Drosophila* [2]. These original studies were performed with UV crosslinking followed by restriction digest and Southern blotting. Reversible formaldehyde crosslinking was introduced by Solomon *et al.* [3] to determine the association of Pol II with heat shock protein (*hsp*) genes in *Drosophila*. Chromatin was fragmented via sonication or restriction digest followed by immunoprecipitation of covalently crosslinked protein-DNA complexes with the appropriate antibodies. After immunoprecipitation, crosslinking of immunoprecipitated protein-DNA complexes was reversed with heat, and remaining DNA fragments were analyzed by Southern blot. Reversible crosslinking has allowed for the advancement of ChIP applications, including ChIP followed by microarray (ChIP-chip), ChIP followed by quantitative polymerase chain reaction (ChIP-qPCR), and ChIP followed by next generation sequencing (ChIP-seq).

Early application of ChIP in fungi was described in *Saccharomyces cerevisiae* [4] and *Schizosaccharomyces pombe* [5]. Here we describe a ChIP-seq method for use in the filamentous fungus *Neurospora crassa*, which is a derivation of the protocol originally developed by Tamaru and colleagues [6]. Chromatin fractions are prepared by covalent formaldehyde crosslinking and fragmentation by sonication. Fragmented chromatin is then immunoprecipitated with the appropriate antibody bound to agarose beads. Covalent crosslinking of protein-DNA complexes is then reversed by heat, and the chromatin fractions are treated with RNase and proteinase. Remaining DNA fragments are purified, and Illumina sequencing libraries are then prepared and sequenced (Figure 1). Additionally, we provide a brief summary of available methods for downstream analysis of sequencing results and a sample pipeline for data analysis (Figure 2).

## 2. Materials

### 2.1 Chromatin Immunoprecipitation:

1. ChIP Lysis buffer without protease inhibitors: 50 mM HEPES (pH7.5), 140 mM NaCl, 1 mM EDTA, 1% Triton X-100, 0.1% deoxycholate. Combine 160.6 ml sterile distilled water, 10 ml 1 M HEPES-KOH or HEPES-NaOH (pH 7.5), 7 ml 4 M NaCl, 400  $\mu$ l 0.5 M EDTA, 20 ml 10% Triton X-100, 2 ml 10% DOC. Store at 4° C.
2. ChIP Lysis buffer + 0.5M NaCl: 50 mM HEPES (pH 7.5), 500 mM NaCl, 1 mM EDTA, 1% Triton X-100, 0.1% deoxycholate. Combine 142.6 ml sterile distilled water, 10 ml 1 M HEPES-KOH or HEPES-NaOH (pH 7.5), 25 ml 4M NaCl, 400  $\mu$ l 0.5 M EDTA, 20 ml 10% Triton X-100, 2 ml 10% DOC. Store at 4° C.
3. ChIP LiCl Wash Buffer: 1 mM Tris-HCl, 250 mM LiCl, 0.5% NP-40, 0.5% deocycholate, 1mM EDTA. Combine 167.6 ml sterile distilled water, 2 ml 1M Tris-HCl (pH 8.0), 10 ml 5 M LiCl, 10 ml 10% NP40, 10 ml 10% DOC, 400  $\mu$ l 0.5 M EDTA, Store at 4° C.
4. TE buffer: 10 mM Tris-HCl (pH 7.4), 1 mM EDTA
5. ChIP TES Buffer: 50 mM Tris-HCl, 10 mM EDTA, 1% SDS. Combine 41.5 ml sterile distilled water, 2.5 ml 1M Tris-HCl (pH 8.0), 1 ml 0.5 M EDTA, 5 ml 10% SDS. Store at room temperature.
6. Roche Complete Protease inhibitor cocktail tablets
7. PMSF: 100 mM in isopropanol. Store at room temperature.
8. 37% formaldehyde
9. 2.5 M glycine
10. Santa Cruz Biotechnology A/G agarose beads

11. 10 mg/ml RNase A
12. 20 mg/ml Proteinase K
13. Ambion 5  $\mu$ M Glycogen
14. 3 M sodium acetate (pH 5.2)
15. Phenol:chloroform:isoamyl alcohol (25:24:1)
16. Chloroform
17. Phosphate Buffered Saline

## 2.2 Library preparation

1. Ampure XP PCR purification beads
2. 10 mM Tris-HCl (pH7.5)
3. Double strand adaptor for Illumina sequencing: (NEB or comparable supplier)
4. Dual index primers for library amplification (NEB or comparable supplier)
5. NEB Ultra II End Repair Module
6. NEBNext Ultra II Q5 Hot Start HiFi PCR Master Mix
7. T4 DNA ligase

## 3. Methods

### 3.1 Chromatin Immunoprecipitation

#### Day 1

1. Grow 5 ml overnight culture in liquid medium.

#### Day 2: Cross-linking, shearing, immunoprecipitation

1. Collect mycelia by vacuum filtration using a Buchner funnel and wash mycelium with 100 mL of PBS.
2. Cross-linking:

- a. Transfer mycelia to 10 ml PBS in a 125-ml Erlenmeyer flask.
  - b. Add 270  $\mu$ l of 37% formaldehyde for a final concentration of 1%.
  - c. Incubate on rotating platform for 30 minutes at room temperature.
  - d. Add 500  $\mu$ l 2.5 M glycine to each sample to quench the formaldehyde. Let samples sit at room temperature for 5 minutes.
  - e. Collect mycelia by filtration. Wash with PBS.
  - f. Transfer mycelia to a 1.5-ml microcentrifuge tube.
3. Lysing cells:
  - a. Add 100  $\mu$ l PMSF and 1 Roche protease inhibitor tablet to 9.9 ml ChIP lysis buffer.
  - b. Re-suspend mycelia in 500  $\mu$ l ice cold ChIP lysis buffer with PMSF and protease inhibitors.
  - c. Lyse mycelia by sonicating (see Note 1).
4. Shearing chromatin:
  - a. Shear chromatin by sonicating (see Note 1).
  - b. Centrifuge samples at 14k RPM for 5 min at 4° C.
  - c. Transfer supernatant containing sheared chromatin to a new tube.
  - d. Save 20  $\mu$ l of sheared chromatin extract in new tube and store at -20° C. This will be your input. Use the remaining extract for immunoprecipitation.
5. Equilibration of protein A/G coupled Agarose Beads and overnight binding:
  - a. Aliquot 20  $\mu$ l agarose beads per reaction + 10% total volume into a 1.5-ml microcentrifuge tube.
  - b. Spin at 5000 RPM for 1 minute. Discard supernatant.

- c. Resuspend beads in 1 ml ChIP lysis buffer without protease inhibitors.
- d. Repeat steps (b-c).
- e. Resuspend beads in original volume (20  $\mu$ l/sample + 10%) ChIP lysis buffer without protease inhibitors.
- f. Add 20  $\mu$ l equilibrated protein A/G beads to each sample. Add 1-3  $\mu$ l desired antibody.
- g. Incubate overnight at 4° C on rotator to allow antibody binding.

#### Day 3: Cold washes

1. Spin samples at 5000 RPM for 1 minute to pellet beads. Discard the supernatant by pipetting. Be sure not to disrupt the pellet.
2. Add 1 ml ice-cold ChIP lysis buffer without protease inhibitors to each sample. Incubate for 10 minutes at 4° C on a rotating platform.
3. Spin samples for 1 minute at 5000 RPM at 4° C. Discard the supernatant.
4. Repeat (Steps 2-3).
5. Wash (as in Steps 2-3) with ice-cold ChIP lysis buffer + 0.5M NaCl.
6. Wash (as in Steps 2-3) with ice-cold LiCl wash buffer.
7. Wash (as in Steps 2-3) with ice-cold TE buffer.
8. Collect immunoprecipitated chromatin by adding 62.5  $\mu$ l TES buffer to each sample. Incubate at 65° C for 10 minutes. Mix by inversion several times during incubation.
9. Spin at 5000 RPM for 1 minute. Transfer supernatant to a new 1.5-ml microcentrifuge tube and save.
10. Repeat (Steps 8-9), saving the supernatant in the same microcentrifuge tube as Step 9.
11. Remove input sample (from Day 2) from -20° C. Add 105  $\mu$ l TES to each input sample.



12. De-crosslink samples by incubating overnight at 65° C.

Day 4: Final chromatin precipitation

1. Add 125 µl sterile distilled water and 2.5 µl 10 mg/ml RNaseA to samples. Incubate for 2 h at 50° C. Mix samples by vortexing multiple times during incubation.
2. Add 6.25 µl 20 mg/ml Proteinase K. Incubate for 2 h at 50° C. Mix samples by vortexing multiple times during incubation.
3. Add 250 µl phenol:chloroform:isoamyl alcohol to each sample. Mix well by vortexing.
4. Spin at 14k RPM for 5 minutes. Transfer the aqueous layer to a new 1.5-ml microcentrifuge tube.
5. Add 250 µl chloroform. Mix well by vortexing.
6. Spin at 14k RPM for 5 minutes. Transfer the aqueous layer to a new 1.5-ml microcentrifuge tube.
7. Add 1 µl glycogen, 25 µl 3M Na-Acetate (pH 5.2), and 865 µl 100% ethanol to each sample. Precipitate overnight at -20° C.

Day 5: Cleanup and elution

1. Retrieve samples from -20° C.
2. Spin at 14k RPM for 10 minutes. Discard the supernatant.
3. Add 300 µl 70% ethanol to each sample.
4. Spin at 14k RPM for 5 minutes. Discard the supernatant.
5. Air dry samples or dry in Speed Vac.
6. Resuspend samples in 25 µl TE.
7. Store at -20° C.

### 3.2 Library preparation

#### End Repair

1. Thaw End Repair buffer on ice. Vortex thoroughly to make sure all buffer components are in solution.
2. In a low-bind PCR tube, mix 25.5  $\mu$ l ChIP DNA, 3  $\mu$ l 10X End Repair Reaction buffer, 1.5  $\mu$ l End Prep Enzyme Mix
3. Incubate 30 min @ 20°C, 30 min @ 65°C, Hold @ 4°C

#### Perform Adaptor Ligation

1. Thaw 10x Adaptor Ligation buffer on ice. Vortex thoroughly to make sure all buffer components are in solution.
2. Dilute double stranded Illumina adaptor to 1.5  $\mu$ M in 10 mM Tris.
3. Add the following directly to end repair mix: 4  $\mu$ l of 10x Ligase Buffer with dATP, 2  $\mu$ l of T4 DNA Ligase, 2  $\mu$ l of double stranded adaptor, 2  $\mu$ l of water.
4. Incubate overnight @ 16°C

#### Bead Cleanup 1

1. Add 40  $\mu$ l of AmpPure beads and mix by pipetting up and down 10 times.
2. Incubate 5 minutes at room temperature.
3. Place on magnet stand for 5 minutes to clear supernatant.
4. Carefully remove supernatant. Be sure to avoid removing beads.
5. Leaving the tubes on the magnet stand, add 200  $\mu$ l freshly prepared 80% ethanol.
6. Incubate 30 seconds and remove ethanol wash. Be sure to avoid removing beads.
7. Repeat steps 5 and 6.

8. Air dry beads for 5 minutes on magnet stand with lid open. Be sure not to overdry, as this will make elution difficult.
9. Remove tubes from magnet and elute DNA in 22  $\mu$ l of 10mM Tris-HCl (pH 7.5-8.0). Mix solution up and down, incubating beads for 5 minutes at room temperature to elute DNA.
10. Place tubes on magnet stand and transfer 20  $\mu$ l of supernatant to a new PCR tube.

#### Amplify by PCR

1. In a low-bind PCR tube, combine 20  $\mu$ l Adaptor ligated DNA fragments, 5ul dual index primer mix containing 10  $\mu$ M of each primer (use unique dual index combination for each sample you plan to multi-plex), 25ul 2x Q5 Hot start polymerase master mix.
2. Amplify libraries
  - a. Denature @ 98°C for 30 sec
  - b. For 2 – 12 cycles (Note 3):
    - i. 98°C for 10 seconds
    - ii. 55°C for 30 seconds
    - iii. 72°C for 60 seconds
  - c. 72°C 3 minutes (final extension)
  - d. Hold at 10°C

#### Final Bead Cleanup

1. Add 50  $\mu$ l of SeraPure beads (1:1 ratio) and mix by pipetting up and down 10 times
2. Incubate 5 minutes at room temp
3. Place on magnet for 5 minutes to clear supernatant
4. Remove supernatant
5. Leaving the tubes on the magnet stand, add 200  $\mu$ l freshly prepared 80% ethanol.

6. Incubate 30 seconds and remove ethanol.
7. Repeat steps 5 and 6.
8. Air dry beads for 5 minutes on magnet with lid open. Be sure not to overdry.
9. Remove tubes from magnet and elute DNA in 15  $\mu$ l of 10mM Tris-HCl (pH 7.5-8.0). Mix solution up and down, incubating beads for 5 minutes at room temperature to elute DNA.
10. Transfer 13  $\mu$ l of supernatant to a new tube. Be sure not to carry over beads, as they will inhibit downstream applications. If carry over occurs, add solution to magnet a second time.
11. Quantify using a bioanalyzer or Qbit fluorometer. If sufficient material is obtained, run 10 – 20 ng of library DNA on a 1.5% agarose gel to confirm correct size distribution and lack of primer dimers.
12. Dilute samples to a concentration of 10 nM. For the 40 Mb *Neurospora* genome, 50 – 80 individual ChIP-seq samples can be pooled and sequenced on a single flow cell of an Illumina Next-Seq or Hi-Seq instrument. Most ChIP-seq experiments in fungi will require a minimum of 1 – 4 million sequence reads generated using an Illumina sequencing instrument.

### 3.3 Data analysis

Several analysis options exist for ChIP-seq data. While the specifics of these options may differ based on specific experimental details, the overall approach will require several key steps. Here we will present a general workflow, as well as a small sample of available analysis software.

1. Pre-process sequence reads: Duplicate reads should be removed and Illumina adaptor sequences should be trimmed from any reads that contain them. This is done using FastQC [7] or similar software.

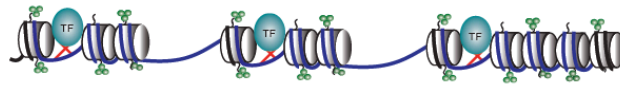
2. Align reads to reference genome using a short read aligner such as bowtie2 [8] or the Burrows-Wheeler Aligner [9].
3. Visualize sequence alignments in a genome browser such as the Broad Integrative Genome Viewer [10] or Gbrowser [11].
4. Perform project specific analyses such as peak calling, analysis of differential enrichment, Motif analysis, etc. HOMER [12], MACS [13], or SICER [14] are commonly used software packages for ChIP-seq analyses.

#### 4. Notes

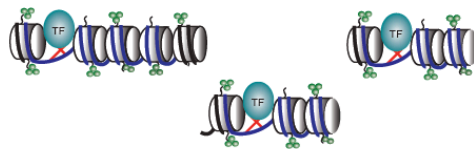
1. Sonication conditions will need to be optimized to ensure proper tissue homogenization and chromatin shearing. Check efficiency by running sheared chromatin on a 1.5% agarose gel to ensure a fragment size of 500 bp.
2. *N. crassa* genomes contain A:T-rich domains, which can be under-represented due to PCR bias [15]. Bias can be reduced by limiting the number of PCR cycles used to amplify libraries. Be sure to optimize the amplification step to determine the appropriate number of PCR cycles for your samples.

## Figures

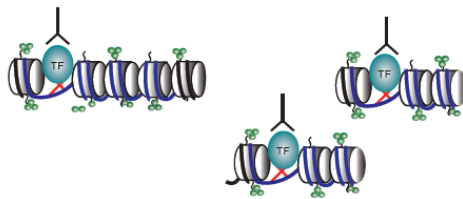
1. Crosslink and extract chromatin.



2. Shear chromatin by sonication.



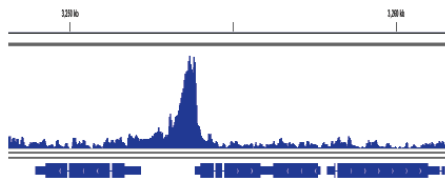
3. Immunoprecipitate.



4. Reverse crosslinking and purify DNA.



5. Sequence and analyze.



```

ATCATTTGTCGG
GGTACTTGACTG
GACACTGTCAC
CATTGGACGT
  
```

**Figure 1. Schematic diagram of a ChIP-seq experiment.** DNA-binding proteins are covalently cross-linked to chromatin in vivo. The chromatin fiber is sheared by sonication into small fragments, which are subjected to immunoprecipitation using an antibody that binds a specific DNA-binding protein. Shown here as a transcription factor (TF). Following immunoprecipitation, the crosslinks are reversed and DNA is purified, sequenced, and analyzed.

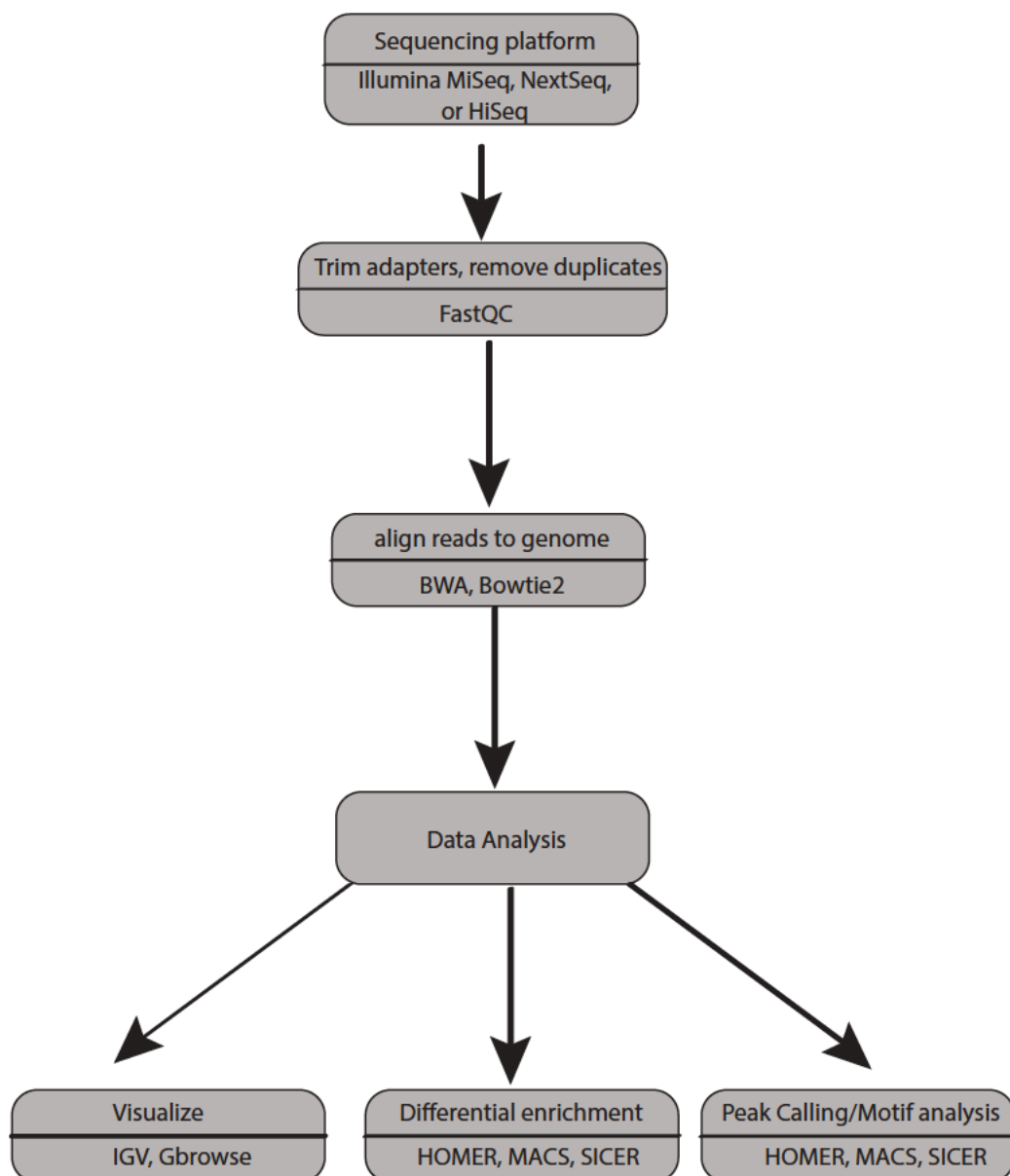


**Figure 2. General bioinformatics workflow for ChIP-seq analysis.** Individual ChIP-seq analysis pipelines will vary based on the specific ChIP-seq application, but analyses workflows include several basic steps. Most ChIP-seq experiments in fungi will require a minimum of 1 – 4 million sequence reads generated using an Illumina sequencing instrument. Raw sequence reads should be pre-processed using a program such as FastQC [7], to remove Illumina adaptor sequences, and remove PCR and optical duplicates. Pre-processed reads are then aligned to a

reference genome using a short read aligner such as bowtie2 [8] or the Burrows-Wheeler Aligner [9]. Aligned reads can be visualized using genome browser software, such as the Broad Integrative Genomics Viewer [10] or Gbrowse [11]. Aligned reads can then analyzed using a variety of software packages, depending on the specific goals of the ChIP-seq. For example, software such as HOMER [12], MACS [13], or SICER [14] can be used to call peaks, identify DNA sequence motifs, or perform differential enrichment analyses.

## References

1. Gilmour DS, Lis JT (1985) In vivo interactions of RNA polymerase II with genes of *Drosophila melanogaster*. *Molecular and cellular biology* 5 (8):2009-2018
2. Champlin DT, Frasch M, Saumweber H, Lis JT (1991) Characterization of a *Drosophila* protein associated with boundaries of transcriptionally active chromatin. *Genes & development* 5 (9):1611-1621
3. Solomon MJ, Larsen PL, Varshavsky A (1988) Mapping protein-DNA interactions in vivo with formaldehyde: evidence that histone H4 is retained on a highly transcribed gene. *Cell* 53 (6):937-947
4. Tanaka T, Knapp D, Nasmyth K (1997) Loading of an Mcm protein onto DNA replication origins is regulated by Cdc6p and CDKs. *Cell*
5. K Ekwall JP (1999) Fission yeast chromosome analysis: Fluorescence in-situ hybridization (FISH) and chromatin immunoprecipitation (CHIP). In: *Chromosome Structural Analysis: A Practical Approach*. Oxford University Press, Oxford, UK,
6. Tamaru H, Zhang X, McMillen D, Singh PB, Nakayama J-i, Grewal SI, Allis DC, Cheng X, Selker EU (2003) Trimethylated lysine 9 of histone H3 is a mark for DNA methylation in *Neurospora crassa*. *Nature Genetics* 34 (1):75-79. doi:10.1038/ng1143
7. Andrews S (2010) FastQC: a quality control tool for high throughput sequence data. Available online at <http://www.bioinformatics.babraham.ac.uk/projects/fastqc>
8. Langmead B, Salzberg SL (2012) Fast gapped-read alignment with Bowtie 2. *Nature methods*. doi:10.1038/nmeth.1923
9. Li H, Durbin R (2009) Fast and accurate short read alignment with Burrows–Wheeler transform. *Bioinformatics*. doi:10.1093/bioinformatics/btp324
10. Robinson JT, Thorvaldsdóttir H, Winckler W (2011) Integrative genomics viewer. *Nature* .... doi:10.1038/nbt.1754



11. Stein LD (2002) The Generic Genome Browser: A Building Block for a Model Organism System Database. *Genome Research* 12 (10):1599-1610. doi:10.1101/gr.403602
12. Heinz S, Benner C, Spann N, Bertolino E, Lin YC, Laslo P, Cheng JX, Murre C, Singh H, Glass CK (2010) Simple combinations of lineage-determining transcription factors prime cis-regulatory elements required for macrophage and B cell identities. *Molecular cell* 38 (4):576-589
13. Feng J, Liu T, Zhang Y (2011) Using MACS to identify peaks from ChIP Seq data. *Current Protocols in Bioinformatics*. doi:10.1002/0471250953.bi0214s34
14. Xu S, Grullon S, Ge K, Peng W (2014) Spatial clustering for identification of ChIP-enriched regions (SICER) to map regions of histone methylation patterns in embryonic stem cells. *Stem Cell Transcriptional Networks: ...*
15. Ji L, Sasaki T, Sun X, Ma P, Lewis ZA, Schmitz RJ (2014) Methylated DNA is over-represented in whole-genome bisulfite sequencing data. *Frontiers in genetics* 5:341. doi:10.3389/fgene.2014.00341

## APPENDIX B

### DECTIN-1 TARGETED ANTIFUNGAL LIPOSOMES EXHIBIT ENHANCED EFFICACY

---

Ambati S., Ferraro A.R., Kang, S.E., Lin J., Lin X., Momany M., Lewis Z.A., Meagher R.B.  
2018. *mSphere*. doi: 10.1128/mSphere.00025-19. Reprinted here with the permission of  
the publisher.

## Abstract

*Aspergillus species* cause pulmonary invasive aspergillosis resulting in nearly a hundred thousand deaths each year. Patients at the greatest risk of developing life-threatening aspergillosis have weakened immune systems and/or various lung disorders. Patients are treated with antifungals such as amphotericin B (AmB), caspofungin acetate, or triazoles (itraconazole, voriconazole etc.), but these antifungal agents have serious limitations due to lack of sufficient fungicidal effect and human toxicity. Liposomes with AmB intercalated into the lipid membrane (AmBisome®, AmB-LLs), have several-fold reduced toxicity compared to detergent solubilized drug. However, even with the current antifungal therapies, one-year survival among patients is only 25 to 60%. Hence, there is a critical need for improved antifungal therapeutics.

Dectin-1 is a mammalian innate immune receptor in the membrane of some leukocytes that binds as a dimer to beta-glucans found in fungal cell walls, signaling fungal infection. Using a novel protocol, we coated AmB-LLs with Dectin-1's beta-glucan binding domain to make DEC-AmB-LLs. DEC-AmB-LLs bound rapidly, efficiently, and with great strength *Aspergillus fumigatus* and to *Candida albicans* and *Cryptococcus neoformans*, highly divergent fungal pathogens of global importance. By contrast, un-targeted AmB-LLs and BSA-coated BSA-AmB-LLs showed 200-fold lower affinity for fungal cells. DEC-AmB-LLs reduced the growth and viability of *A. fumigatus* an order of magnitude more efficiently than untargeted control liposomes delivering the same concentrations of AmB, in essence decreasing the effective dose of AmB. Future efforts will focus on examining pan-antifungal targeted liposomal drugs in animal models of disease.

## Importance

The fungus *Aspergillus fumigatus* causes pulmonary invasive aspergillosis resulting in nearly a hundred thousand deaths each year. Patients are often treated with antifungal drugs such as amphotericin B (AmB) loaded into liposomes, AmB-LLs, but all antifungal drugs including AmB-LLs have serious limitations due to human toxicity and insufficient fungal cell killing. Even with the best current therapies, one-year survival among patients with invasive aspergillosis is only 25 to 60%. Hence, there is a critical need for improved antifungal therapeutics.

Dectin-1 is a mammalian protein that binds to beta-glucan polysaccharides found in nearly all fungal cell walls. We coated AmB-LLs with Dectin-1 to make DEC-AmB-LLs. DEC-AmB-LLs bound strongly to fungal cells, while AmB-LLs had little affinity. DEC-AmB-LLs killed or inhibited *A. fumigatus* ten times more efficiently than untargeted liposomes, decreasing the effective dose of AmB. Dectin-1-coated drug-loaded liposomes targeting fungal pathogens have the potential to greatly enhance antifungal therapeutics.

## Introduction

Hundreds of fungal species indigenous to our environment cause a wide variety of diseases including aspergillosis, blastomycosis, candidiasis, cryptococcosis, coccidioidomycosis (valley fever), and *Pneumocystis pneumonia* (PCP). Collectively, pathogenic fungi infect many different organs, but lungs are the most common site for deep mycoses. Globally, aspergillosis, candidiasis, and cryptococcosis kill about one million or more people each year (1, 2).

*Aspergillus fumigatus* and related *Aspergillus species* cause aspergillosis (2). Patients at the greatest risk of developing life-threatening aspergillosis have weakened immune systems, for example from stem cell or organ transplants, or have various lung diseases, including tuberculosis, chronic obstructive pulmonary disease, cystic fibrosis, or asthma. Among immunocompromised patients, aspergillosis is the second most common fungal infection, after candidiasis (3, 4). Additional costs associated with treating invasive aspergillosis are estimated at \$40,000 per child and \$10,000 per adult. Patients with aspergillosis are treated with antifungals such as AmB, caspofungin, or triazoles. Even with antifungal therapy, however, one-year survival among immunocompromised patients with aspergillosis is only 25 to 60%. Furthermore, all known antifungal agents that treat aspergillosis are quite toxic to human cells (5, 6).

AmB is the most commonly used agent for many kinds of fungal infections, including aspergillosis. Because AmB binds the fungal plasma membrane sterol ergosterol more efficiently than the mammalian sterol cholesterol, AmB is more toxic to fungal cells. The side effects of AmB include neurotoxicity and/or nephrotoxicity and/or hepatotoxicity (5, 6) and can result in death of the patient (1).

AmB loaded liposomes, AmB-LLs, penetrate more efficiently into various organs (7, 8), penetrate the cell wall (9), and show reduced toxicity at higher, more effective doses of AmB

than the second most commonly used AmB product, deoxycholate detergent-solubilized AmB (5, 6, 10, 11). AmB is an amphipathic molecule. Its long lipophilic polyene end intercalates into the lipid bilayer of liposomes, while its hydrophilic end is positioned on the liposomal surface as modeled in **Fig. 1**. Commercial untargeted spherical AmB-LLs are called AmBisome® (12, 13). However, AmB-LLs still produce AmB human toxicity, such as renal toxicity in 50% of patients (5, 6, 11). When infected mice are treated with AmB-LLs, viable numbers of *A. fumigatus* cells in homogenized lung tissue were only reduced by 70% (14, 15), leaving large fungal cell populations behind. This large residual fungal population may result in recurrence and subsequent mortality after treatment. We explored the targeting of AmB-LLs to *Aspergillus fumigatus* cells to meet the pressing need to improve the quality of antifungal drug formulations (1).

Liposomes biochemically resemble endogenous exosomes (16-18). They efficiently penetrate the endothelial barrier and reach target cells deep in most major organs for the “passive delivery” of variously loaded therapeutic drugs (19-23). Targeted liposomes have binding specificity for a plasma membrane antigen to enable the “active delivery” of a packaged therapeutic to diseased cells. Targeting is most commonly achieved with a monoclonal antibody such that immunoliposomes bind a specific cell type or types. Over 100 publications, most focused on particular types of cancer cells, show that targeted immunoliposomes improve the cell-type specificity of drug delivery and reduce toxicity. Therapeutic drug loaded immunoliposomes include those targeting cells expressing the VEGF-Receptors-2 and -3 (24), the oxytocin receptor (25), the epidermal growth factor receptor, EGFR (26), CD4 (27), and HER2 (28, 29). The active delivery of immunoliposomes generally improves cell-type specificity and drug effectiveness by 3- to 10-fold (25, 30, 31) over passive delivery. A wide variety of

drugs have been delivered via targeted liposomes including toxins such as doxorubicin, paclitaxel, and rapamycin (32, 33), growth hormones such as Transforming Growth Factor-beta (34), and analgesics such as the indomethacin (25). We are unaware of any reports of immunoliposomes specifically targeting antifungals to invasive fungal cells; however, the immuno-targeting of AmB loaded liposomes to the vessel wall of pulmonary capillary cells in *A. fumigatus* infected mouse lungs results in increased mouse survival rates (15).

Dectin-1 is a transmembrane receptor expressed in natural killer lymphocytes encoded by the *CLEC7A* (*C-Type Lectin Domain Containing 7A, beta-Glucan Receptor*) gene in mice and humans. Dectin-1 binds various beta-glucans in fungal cell walls and is the primary receptor for transmembrane signaling of the presence of cell wall components from the surface of fungal cells, stimulating an innate immune response (35-38). Human and mouse Dectin-1 are 244 and 247 amino acid-long plasma membrane proteins, respectively, although there are mRNA splice variants producing shorter human isoforms. Dectin-1 floats in the membrane as a monomer, but binds to beta-glucans as a dimer as modeled in our design of Dectin-1 targeted liposomes shown in **Fig. 1** (39). The 176 amino acid long (20 kDa) extracellular C-terminal beta-glucan binding domain is often manipulated alone as sDectin-1. The beta 1 $\rightarrow$ 3 glucans are a structurally diverse class of polysaccharides, and as such, sDectin-1 binds various model beta-glucans differentially with IC<sub>50</sub>s ranging from 2.6 mM to 2.2 pM (38). sDectin-1 is reported to recognize *A. fumigatus* cell wall components much more efficiently on germinating conidia and germ tubes than on dormant conidia or mature hyphae (40, 41). Having pan-fungal binding activity, Dectin-1 may provide broader antifungal targeting abilities for liposomes than a monoclonal antibody (42).

The goal of our research has been to develop a targeted liposomal strategy that improves antifungal drug delivery and enhances therapeutic efficacy. To begin to address this goal, we

tested the hypothesis that AmB-LLs targeted directly to beta-glucans in the cell wall of *A. fumigatus* by sDectin-1 will have enhanced antifungal activity over current untargeted AmB-LLs.

## Results

***Preparation of AmB loaded sDectin-1-coated liposomes.*** Pegylated liposomes were remotely loaded with 11 moles percent AmB relative to moles of liposomal lipids to make control AmB-LLs, which are similar in structure and AmB concentration to commercial unpegylated AmBisome® preparations (**Materials and Methods, Supplemental Table S1**). sDectin-1 (DEC, **Supplemental Fig. S1, Fig. S2**) and bovine serum albumin (BSA) were coupled to a pegylated lipid carrier, DSPE-PEG. One mole percent DSPE-PEG-DEC was incorporated into AmB-LLs to make sDectin-1-coated DEC-AmB-LLs (**Fig. 1**) and 0.33 mole percent DSPE-PEG-BSA was incorporated into AmB-LLs to make BSA-AmB-LLs. This mole ratio of 22 kDa sDectin-1 and 65 kDa BSA results in equivalent microgram amounts of protein coating each set of liposomes. Because these protein coated liposomes were made from the same AmB-LLs, all three liposomal preparations contain 11 moles percent AmB relative to moles of lipid. Two moles percent of DHPE-Rhodamine were loaded into all three classes of liposome (**Fig. 1**).

***sDectin-1-coated liposomes DEC-AmB-LLs bind strongly to fungal cells.*** In assays performed on *A. fumigatus* germlings, rhodamine red fluorescent DEC-AmB-LLs bound strongly to germinating conidia and to germ tubes as shown in **Fig. 2**. The sDectin-1-targeted liposomes often bound in large numbers that formed aggregates at particular regions. While 100 nm liposomes are too small to be resolved by light microscopy, individual liposomes were visible as somewhat uniformly sized small red fluorescent dots (orange arrows, **Fig. 2A**), which are easily



detected due to their each containing an estimated 3,000 rhodamine molecules (**Fig. 1**). From examinations of larger fields of germlings it appears that essentially all germlings bind DEC-AmB-LLs (**Fig. 2C and 2D**). AmBisome-like AmB-LLs (**Fig. 2B**) and BSA coated liposomes, BSA-AmB-LLs (**Fig. 2E & 2F**), did not bind detectably to germinating conidia or germtubes when tested at the same concentration. Maximum labeling by DEC-AmB-LLs was achieved within 15 to 30 min and the strong red fluorescent signals of DEC-AmB-LLs bound to cells were maintained for weeks, when fixed cells were stored in the dark in phosphate buffered saline (PBS) at 4°C.

DEC-AmB-LLs also bound to germinating conidia and most hyphae from more mature cultures as shown in **Fig. 3**. Again, the sDectin-1-targeted liposomes often bound in aggregates, but some fairly uniformly sized individual small red dots are visible (orange arrows, **Fig. 3A**), which appear to be individual fluorescent liposomes. AmB-LLs did not bind significantly to older conidia or mature hyphae (**Fig. 3E & 3F**), nor did BSA-AmB-LLs.

On plates covered with dense layers of mature hyphae, the number of bound liposomes and liposome aggregates were counted in multiple fluorescent images. DEC-AmB-LLs bound to both formalin fixed (**Fig. 4A-C**) and live (**Fig. 4D-F**) *A. fumigatus* cells 100- to 200-fold more efficiently than AmB-LLs or BSA-AmB-LLs. Labeling by DEC-AmB-LLs was inhibited 50-fold by the inclusion of soluble beta-glucan and laminarin, but not sucrose, confirming that binding was beta-glucan specific (**Fig. 4G-4I**). Finally, DEC-AmB-LLs labeled *Cryptococcus neoformans* cells and *Candida albicans* pseudohyphae (**Supplemental Fig. S3**), while control liposomes did not. However, the frequency of DEC-AmB-LL binding to *C. albicans* pseudohyphae was very low. In short, Dectin-coated AmB loaded liposomes bound efficiently to a variety of fungal cells, while control liposomes did not.

***Killing and growth inhibition of fungi by DEC-AmB-LLs.*** We performed various fungal cell growth and viability assays after treating *A. fumigatus* with liposomes delivering AmB concentrations near its estimated ED50 of 2 to 3 uM AmB (43) or below its estimated MIC of 0.5 uM for various strains of *A. fumigatus* (44). In most of these experiments, 4,500 conidia were germinated and incubated for 12 to 72 hr in 96 well microtiter plates along with drug loaded liposomes. Longer incubation times were often needed to resolve differences among the liposome preparation delivering higher concentrations of AmB. **Fig. 5** shows that targeted DEC-AmB-LLs killed or inhibited the growth of *A. fumigatus* cells far more efficiently than BSA-AmB-LLs or uncoated AmB-LLs delivering the same concentrations of AmB. Assays with CellTiter-Blue reagent, which assesses cytoplasmic reductase activity as a proxy for cell integrity and viability, showed that treating cells with DEC-AmB-LLs delivering 3 uM AmB killed *A. fumigatus* more than an order of magnitude more effectively than AmBisome-like AmB-LLs or BSA coated liposomes, BSA-AmB-LLs (**Fig. 5A**). As a second method to score liposomal AmB activity, we measured hyphal length. Hyphal length assays gave a similar result, showing that DEC-AmB-LLs delivering 3 uM AmB were far more effective at inhibiting hyphal growth than AmB-LLs or BSA-AmB-LLs (**Fig 5B**). To confirm that DEC-AmB-LLs were still functional in an alternate sDectin-1 renaturation buffer, we executed a complete biological replicate experiment, wherein sDectin-1 and liposomes were prepared in RN#8 buffer instead of RN#5 (see Materials and Methods). We obtained a similar although less dramatic result with these liposomes delivering 3 uM AmB (**Fig. 5C and 5D**).

A third assay of liposomal AmB activity was employed, which measured the percent of conidia that germinated in the presence of the various liposomal preparations (**Fig. 5E and 5F**). DEC-AmB-LLs delivering as little as 0.09 uM and 0.187 uM AmB inhibited the germination of

*A. fumigatus* conidia significantly better than AmB-LLs or BSA-AmB-LL. The dose response to DEC-AmB-LL was based on a germination assay performed after a fixed period of growth using AmB concentrations from 0.09 to 3  $\mu$ M is shown in **Fig. 5G**. DEC-AmB-LLs outperform AmB-LLs and BSA-AmB-LLs over a wide range of concentrations.

***Reduced animal cell toxicity of DEC-AmB-LLs.*** AmB-LLs and AmB deoxycholate micelles were slightly more toxic to HEK293 human embryonic kidney cells than DEC-AmB-LLs or BSA-AmB-LLs based on CellTiter-Blue assays of cell viability (**Supplemental Fig. S4**).

## Discussion

We demonstrated that sDectin-1-targeted, AmB-loaded DEC-AmB-LLs are significantly more effective at binding to and inhibiting the growth of fungal cells and are slightly less toxic to human cells than uncoated AmB-LLs. The biochemical manipulation of mouse or human sDectin-1 has been complicated because the proteins easily aggregate and become insoluble and inactive in aqueous buffers. The problem of protein aggregation and insolubility may partly be due their composition, due to the presence of 11 to 13% hydrophobic amino acids and three disulfide crosslinks in their carbohydrate recognition domains. A wide variety of protein chemical manipulations have been applied to improve sDectin-1 solubility with mixed success. For example, the solubility and utility of sDectin-1 was increased by tethering it to the 56 amino acid long B1 domain of Streptococcal Protein G (45) or more commonly to the 232 amino acid long Fc constant region of IgG1 antibody (41). Bacterially produced, non-glycosylated sDectin-1 renatured from inclusion bodies and de-glycosylated and native mammalian cell produced sDectin-1 all retain indistinguishable beta-glucan binding activity (39, 46, 47). Therefore, we proceeded with sDectin-1 production in *E. coli*, with the potential for highest yield and lowest

cost. We overcame sDectin-1's solubility problems by combining a variety of old and new approaches including, (1) the use of a very short charged peptide tag LysHisLys, (2) the inclusion of 6 M guanidine hydrochloride (GuHCl) during protein extraction, purification, and chemical modification, (3) the inclusion of the protein solubilizing agent, arginine, during renaturation, liposomal loading, and storage, and (4) the inclusion of a sulfhydryl reducing agent 2-mercaptoethanol in all steps.

sDectin-1 is reported to bind efficiently to *A. fumigatus* germinating conidia and germ tubes, but inefficiently if at all to mature hyphae and not at all to un-germinated conidia (40, 41, 48). Our data with sDectin-1-coated AmB loaded liposomes are partially consistent with previous observations, except that we observed reasonably efficient staining of mature hyphae (**Fig. 3 & 4**). Poor cell or hyphal binding may be explained by polymorphic expression of beta-glucans in different stages of fungal cell growth (48, 49). During infection, however, interaction with host immune cells reportedly expose otherwise masked  $\beta$ -glucans (50), enhancing the potency of the targeted DEC-AmB-LLs. Herein, sDectin-1-coated fluorescent DEC-AmB-LLs bound efficiently to germinating conidia, germ tubes, and hyphae, suggesting our modified sDectin-1 presented on the surface of liposomes retained its ability to form complexes with affinity for fungal beta-glucans expressed at various stages of growth. Our data showed for the first time that in vitro chemically modified sDectin-1 (DSPE-PEG-DEC) retained its fungal cell binding specificity. Furthermore, DEC-AmB-LLs binding was rapid and remained stably bound to cells for weeks. Perhaps the greater avidity of liposome coated with ~1,500 sDectin-1 molecules insured the rapid efficient binding and very slow release of bound liposomes, parallel to the avidity of pentameric IgM antibody. The presence of thousands rhodamine molecules on each liposome (**Fig. 1**) should have greatly increased the chance of detecting unambiguous

fluorescent signals relative to detecting the binding of sDectin-1 dimers as reported in previous studies. DEC-AmB-LLs bound very efficiently to both live and formalin fixed hyphae. Side-by-side comparisons are needed to determine if formalin fixation improved binding or blocked access to beta-glucans.

In a large number of experiments using different binding buffers including BSA and various incubation periods we never detected any significant affinity of uncoated AmB-LLs or BSA-AmB-LLs for fungal cells, with one exception. In preliminary experiments in which BSA was omitted during the incubation, we observed BSA-AmB-LLs bound modestly well to *A. fumigatus* germinated conidia, while we still did not observe AmB-LLs binding. By contrast, Chavan et al. (51) detected efficient binding of fluorescent pegylated liposomes to primary tips and septa on *A. fumigatus* hyphae even in the presence of serum (51). We cannot account for this disparity between their data and ours, except that their liposomes had a different lipid composition and lacked both sDectin-1 and AmB (**Supplemental Table S1**).

*Aspergillus*, *Candida*, and *Cryptococcus species* belong to three evolutionarily disparate groups of fungi: the Hemiascomycetes, Euascomycetes, and Hymenomycetes, respectively, and are separated from common ancestry by hundreds of millions of years (52). DEC-AmB-LLs bound specifically to all three. This suggests the beta-glucans found in the outer cell wall of many pathogenic fungi will be conserved enough in structure to bind sDectin-1 targeted liposomes if they are accessible. However, beta-glucan expression and masking from host detection may vary widely among fungal species (48, 49, 53). Our assays also showed very inefficient binding of DEC-AmB-LLs to *C. albicans*, consistent with the masking of beta-glucans reported for this species (54-56). We did not test for binding to zygomycete pathogens, but a targeted liposome approach may also increase drug efficacy for at least some members of

the Mucorales. For example, beta-glucans in the *Rhizopus oryza* cell wall induce a Dectin-1-dependent response (57).

In various biological and experimental replicate experiments using different assay methods, we showed that DEC-AmB-LLs killed or inhibited *A. fumigatus* cells far more efficiently than AmBisome-like AmB-LLs delivering the same level of AmB. In all of our experiments, DEC-AmB-LLs were from several fold to more than an order of magnitude more fungicidal than control liposomes over a wide variety of AmB concentrations tested that were near or below the estimated ED50 of 3  $\mu$ M. We detected significantly stronger activity of DEC-AmB-LLs over AmB-LLs even at AmB concentrations as low as 0.094  $\mu$ M AmB, well below AmB's MIC. DEC-AmB-LLs significantly decreased the amount of AmB required for an ED50 or a MIC for *A. fumigatus*. The time of incubation with drug loaded liposomes strongly influences the ability to resolve differences among the three liposome preparations. For example, when all three liposome preparations delivered high AmB concentrations (e.g., 0.75, 1.5 and 3  $\mu$ M) they caused a lag in the germination of conidia. Hence, longer incubation periods were needed to allow sufficient fungal growth to resolve the improved performance of DEC-AmB-LLs. Short incubation periods were needed to resolve differences at low AmB concentrations (e.g., 0.37, 0.18, 0.94  $\mu$ M). Thus, we were unable to obtain a dose response curve that reflected the optimal performance of DEC-AmB-LLs over a wide range of AmB concentrations. Finally, AmB containing liposomes were added to plates at the same time as conidia during the growth inhibition assays. Thus, the CellTiter-Blue and hyphal length assays combined inhibition of germination, germling growth, and hyphal extension, but may be skewed toward inhibition of early stages of growth. Future inhibition studies are needed that focus just on hyphal stages to

make this work even more relevant to a clinical setting, but our observation that older hyphae are bound by DEC-AmB-LLs suggest that improved killing of mycelia are likely.

Looking forward, there are a number of important variables we have not yet explored. For example, we coated liposomes with a single concentration of sDectin-1, approximately 1,500 molecules per liposome and do not know if this is the optimal concentration for cell binding and drug delivery. Also, although DEC-AmB-LL were superior in all aspects to AmB-LLs we do not know the ratio of growth inhibition to killing at different AmB concentrations. Efficient killing can be followed by rapid outgrowth of the remaining cells obscuring the results. This is particularly relevant to the treatment of aspergillosis, because current drug formulations only partially reduce the fungal cell load in mice and humans. An important next step in our research needs be an examination of the performance sDectin-1-coated antifungal drug loaded liposomes in animal models of fungal diseases. Only one human mutation in Dectin-1 Y238Term, very close to its natural termination codon 245, has been reported at the Human Gene Mutation Database (58). Hence the human sDectin-1 sequence itself may not present problems of immunogenicity in a clinical setting. However, we do not know if the design of liposomal sDectin-1 that included a LysHisLys peptide tag for lysine coupling to a lipid carrier will be immunogenic.

In summary, sDectin-1 polypeptides conjugated to a pegylated lipid carrier and inserted as monomers into liposomes must float together to form functional dimers or multimers as they bind beta-glucans or we would not have observed the strong efficient binding of DEC-AmB-LLs to fungal cells. Our DEC-AmB-LLs efficiently bind beta-glucans in the cell walls of diverse fungal species. Multiple growth and viability assays on DEC-AmB-LLs delivering AmB concentrations from 0.094 to 3  $\mu$ M suggest that sDectin-1-coated liposomes greatly improved the

performance of liposomal AmB. Taking these results altogether, it is reasonable to propose that sDectin-1-coated liposomes have significant potential as pan-fungal carriers for targeting antifungal therapeutics.

## **Materials and Methods**

**Fungal growth.** *Aspergillus fumigatus* strain A1163 was transformed with plasmid pBV126 described in Kang et al. (59) carrying green fluorescent protein EGFP under the control of *Magnaporthe oryzae* ribosomal protein 27 promoter to make strain AEK012. AEK012 was used to monitor fungal cells in some experiments. *A. fumigatus* spores were inoculated on Petri plates containing Vogel's Minimal Media (VMM, 1% glucose, 1.5% Agar) and grown for 7 days, at which time conidia were collected in PBS + 0.1% Tween. For fluorescent liposome localization and for growth inhibition and killing assays 20,000 and 4,500 AEK012 conidia were plated on 24 well and 96 well plates, respectively, in VMM, 1% glucose, 0.5% BSA at 37°C for various time periods ranging from 8 hr to 56 hr (60, 61). *Candida albicans* Sc5314 and *Cryptococcus neoformans* H99 were pre-grown in YPD liquid media overnight. The cells were then washed 3 times with sterile water and resuspended in VMM media and grown on poly-L-lysine coated plates at 35°C for 10 hours. All fungal cell growth was carried out in a BSL2 laboratory. Prior to liposomal staining most fungal preparations were washed 3 times with PBS, fixed in 4% formaldehyde in PBS for 15 to 60 mins, washed twice and stored at 4°C in PBS.

**Production of soluble Dectin-1.** The sequence of the codon-optimized *E. coli* expression construct with MmsDectin-1lyshis (NCBI BankIT #2173810) cloned into pET-45B (GenScript) is shown in **Supplemental Fig. S1**. The sequence encodes a slightly modified 198 a.a. long sDectin-1 protein containing a vector specified N-terminal (His)<sub>6</sub> affinity tag, a flexible GlySer spacer, two lysine residues, another flexible spacer followed by the C-terminal 176 a.a. long



murine sDectin-1 domain. *E. coli* strain BL21 containing the MmsDectin-1-pET45B plasmid were grown overnight in 1 L of Luria broth without IPTG induction (**Supplemental Fig. S2**). Modified sDectin-1 was extracted from cell pellets in pH = 8.0, 6 M GuHCl (Fisher BioReagents BP178), 0.1 M Na<sub>2</sub>HPO<sub>4</sub>/NaH<sub>2</sub>PO<sub>4</sub>, 10 mM Triethanolamine, 100 mM NaCl, 5 mM 2-mercaptoethanol, 0.1% Triton-X100, which was modified from a GuHCl buffer used in an earlier study (62). sDectin-1 was bound to a nickel affinity resin (QiaGen, #30210) in this same buffer, washed in same adjusted to pH 6.3, and eluted in this buffer adjusted to pH 4.5. The pH of the eluted protein was immediately neutralized to pH 7.2 with 1 M pH 10.0 M triethanolamine for long term storage. Forty milligrams of greater than 95% pure protein was recovered per liter of Luria broth (**Supplemental Fig. S2**). Samples of sDectin-1 at 6  $\mu$ g/ $\mu$ L in this same GuHCl buffer with freshly added 5 mM 2-mercaptoethanol were adjusted to pH 8.3 with 1 M pH 10 triethanolamine and reacted with a 4-molar excess of DSPE-PEG-3400-NHS (Nanosoft polymers, 1544-3400) for 1 hr at 23°C to make DSPE-PEG-DEC. Gel exclusion chromatography on Bio-Gel P-6 acrylamide resin (Bio-Rad #150-0740) in renaturation and storage buffer RN#5 (0.1 M NaH<sub>2</sub>PO<sub>4</sub>, 10 mM Triethanolamine, pH 8.0, 1 M L-Arginine, 100 mM NaCl, 5 mM EDTA, 5 mM 2-mercaptoethanol) removed un-incorporated DSPE-PEG and GuHCl (45, 63). DSPE-PEG-BSA was prepared from BSA (Sigma, A-8022) by the same protocol, minus the GuHCl from DSPE-PEG labeling buffers and L-Arginine from RN#5 buffer.

***Remote loading of AmB, sDectin-1, BSA, and Rhodamine into liposomes.*** Sterile pegylated liposomes were obtained from FormuMax Sci. Inc. (DSPC:CHOL:mPEG2000-DSPE, 53:47:5 mole ratio, 100 nm diameter, 60  $\mu$ mole/mL lipid in a liposomal suspension, FormuMax #F10203A). Small batches of liposomes were remotely loaded with 11 moles percent AmB (AmB, Sigma A4888) relative to 100% liposomal lipid to make AmBisome-like AmB-LLs used

throughout this study. For example, AmB (2.8 mg, 3  $\mu$ moles or 20 moles %) AmB was dissolved in 13  $\mu$ L DMSO by heating 10 to 20 min and with occasional mixing at 60°C to make an oil-like clear brown AmB solution. Two hundred and fifty  $\mu$ L of sterile liposomal suspension (15  $\mu$ moles of liposomal lipid in 50% liposome suspension) was added to the AmB-oil and mixed on a rotating platform for 3 days at 37°C, followed by centrifugation for 10min at 100xg to pellet the AmB oil. Dissolving this oil phase in 0.5 mL DMSO and spectrophotometry at A407 relative to AmB standards in DMSO showed that 1.3  $\mu$ moles AmB remained undissolved and 1.7  $\mu$ moles of AmB (11 moles percent) were retained in liposomes. Subsequent gel exclusion chromatography of loaded liposomes over a 10 mL BioGel A-0.5 M agarose resin (BioRad 151-0140) revealed no detectable AmB in the salt volume and essentially all of the AmB was retained by liposomes. Longer incubations resulted in higher percentages of AmB in liposomes. Commercial AmBisome® (Gilead) liposomes are not pegylated and contain 10.6 moles percent AmB relative to lipid (**Supplemental Table S1**).

The DSPE-PEG-sDectin-1 and DSPE-PEG-BSA conjugates in RN#5 buffer and PBS, respectively, were integrated via their DSPE moiety into the phospholipid bilayer membrane of AmB-LLs at 1.0 and 0.33 moles percent of protein relative to moles of liposomal lipid by 30 to 60 min incubation at 60°C to make DEC-AmB-LLs and BSA-AmB-LLs. We had previously determined that both arginine and guanidine prevented sDectin-1 aggregation and were aids to functional renaturation as shown for other proteins (64-66). However, the arginine in RN#5 is a reported inhibitor of *Aspergillus* growth (67). Therefore, we examined a second method of preparing liposomes in which the newly coupled DSPE-PEG-sDectin-1 was exchanged into renaturation buffer RN#8 (50 mM carbonate pH 8.5, 0.5 M guanidine hydrochloride, 250 mM NaCl, 2 mM 2-mercaptoethanol, 0.1 % triton, 20% glycerol) and loaded into liposomes in RN#8.

We concluded that DSPE-PEG-sDectin-1 and liposomes prepared using in RN#5 were slightly superior at labeling fungal cells than those prepared in RN#8. During this same 60°C incubation, the red fluorescent tag, Lissamine rhodamine B-DHPE (Invitrogen, #L1392) was also incorporated at two moles percent relative to liposomal lipid into sDectin-1 and BSA coated liposomes and AmB-LLs (68-70). Gel exclusion chromatography on BioGel A-0.5 M resin confirmed that Rhodamine and protein insertion into liposomes were essentially quantitative. DEC-AmB-LLs stored at 4°C in RN#5 retained fungal cell binding specificity for 2 months.

***Microscopy of liposome binding.*** Formalin fixed or live fungal cells were incubated with liposomes in liposome dilution buffer LDB1 (PBS pH 7.2, 5% BSA, 1 mM 2-mercaptoethanol, 5 mM EDTA) at 23°C. Unbound liposomes washed out after 15 min to 1 hr incubation with 4 changes of LDB1. Images of rhodamine red fluorescent liposomes, green EGFP *A. fumigatus* and differential interference contrast (DIC) illuminated cells were taken on microscope slides under oil immersion at 63x on a Leica DM6000B automated microscope. Five to six Z-stack images were recorded at one micron intervals and merged in Adobe Photoshop CC2018 using the Linear Dodge method. Bright field and red and green fluorescent images were taken directly of cells on microtiter plates at 20X and 40X on an Olympus IX70 Inverted microscope and an Olympus PEN E-PL7 digital camera and the bright field and/or colored layers merged in Photoshop.

***Cell growth and viability assays.*** Liposomal stocks were stored at 900  $\mu$ M AmB and diluted first 5 to 10-fold into liposome dilution LDB2 (PBS pH 7.2, 0.5% BSA, 1 mM 2-mercaptoethanol) and then into growth media to achieve the indicated final AmB concentrations. Control cells received an equivalent amount of LDB2. CellTiter-Blue cell viability assays were conducted as per the manufacturer's instructions (Promega, document #G8080) using 20  $\mu$ L of resazurin reagent to treat 100  $\mu$ L of fungal or animal cells in growth media and incubating for 2

to 4 hours at 37°C. Red fluorescence of electrochemically reduced resorufin product (Ex485/Em590) was measured in a Biotek Synergy HT microtiter plate reader. Data from six wells was averaged for each data point and standard errors calculated. Data for germination and hyphal length assays were collected manually from multiple photographic images taken at 10X and/or 20X.

### **Acknowledgements**

We would like to thank Dr. Zachary Wood for his instructive discussions concerning the renaturation and stabilization of sDectin-1 and Dr. Bradley Phillips for discussion on the clinical use of and problems with AmB. Funding was provided as follows: SA and RBM (University of Georgia Research Foundation, Inc. UGARF, NIAID R21 AI144498, NIH National Center for Advancing Translational Sciences #UL1TR002378), ARF (National Science Foundation Graduate Research Fellowship Program Grant No. 1443117), ZAL (RSG-14-184-01-DMC from the American Cancer Society), XL (NIAID 1R01AI140719), MM and SEK (UGA President's Interdisciplinary Seed Grant Program). None of the authors have any financial conflict of interest.

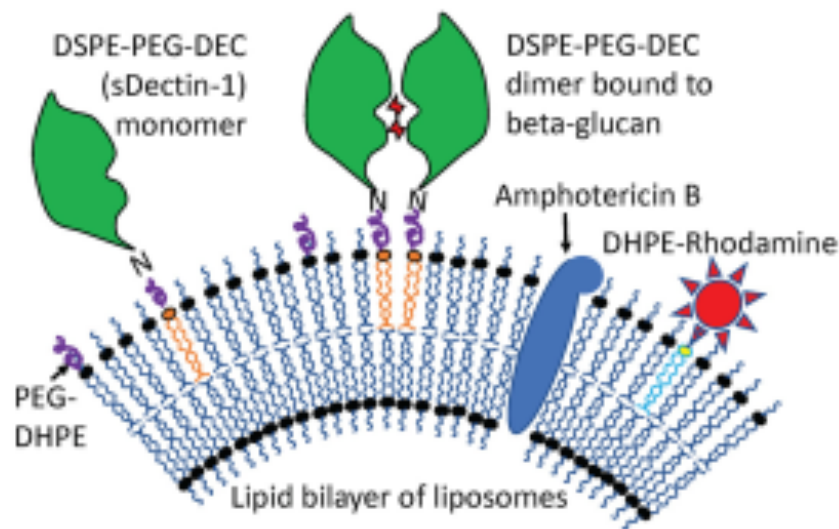


**Fig. 1. Model of DEC-AmB-LLs, liposomes loaded with sDectin-1, AmB, and rhodamine.**

AmB (AmB, blue oval structure) was intercalated into the lipid bilayer of 100 nm diameter liposomes. sDectin-1 (DEC, green globular structure) was coupled to the lipid carrier DSPE-PEG. Both DSPE-PEG-DEC and red fluorescent DHPE-Rhodamine (red star) were also inserted into the liposomal membrane. sDectin-1, Rhodamine, AmB and liposomal lipids were in a 1:2:11:100 mole ratio, respectively (Supplemental Table S1). Two sDectin-1 monomers (two DSEP-PEG-DEC molecules) must float together in the membrane to bind strongly to cell wall beta-glucans (red sugar moieties). The two liposomal controls examined were BSA-AmB-LLs that contain an equal microgram amount of 65 kDa BSA in place of 22 kDa sDectin-1 (i.e., 0.33:2:11:100 mole ratio) and AmB-LLs lacking any protein coating (0:2:11:100 mole ratio). From these mole ratios, the surface area of an 100 nm diameter liposome, and the published estimate of  $5 \times 10^6$  lipid molecules per  $10^6 \text{ nm}^2$  of lipid bilayer(71), we estimated that there were approximately 3,000 Rhodamine molecules in each liposome preparation and 1,500 sDectin-1 monomers in each DEC-AmB-LL. Note that for simplicity the proper ratios of these molecules are not shown in the figure.



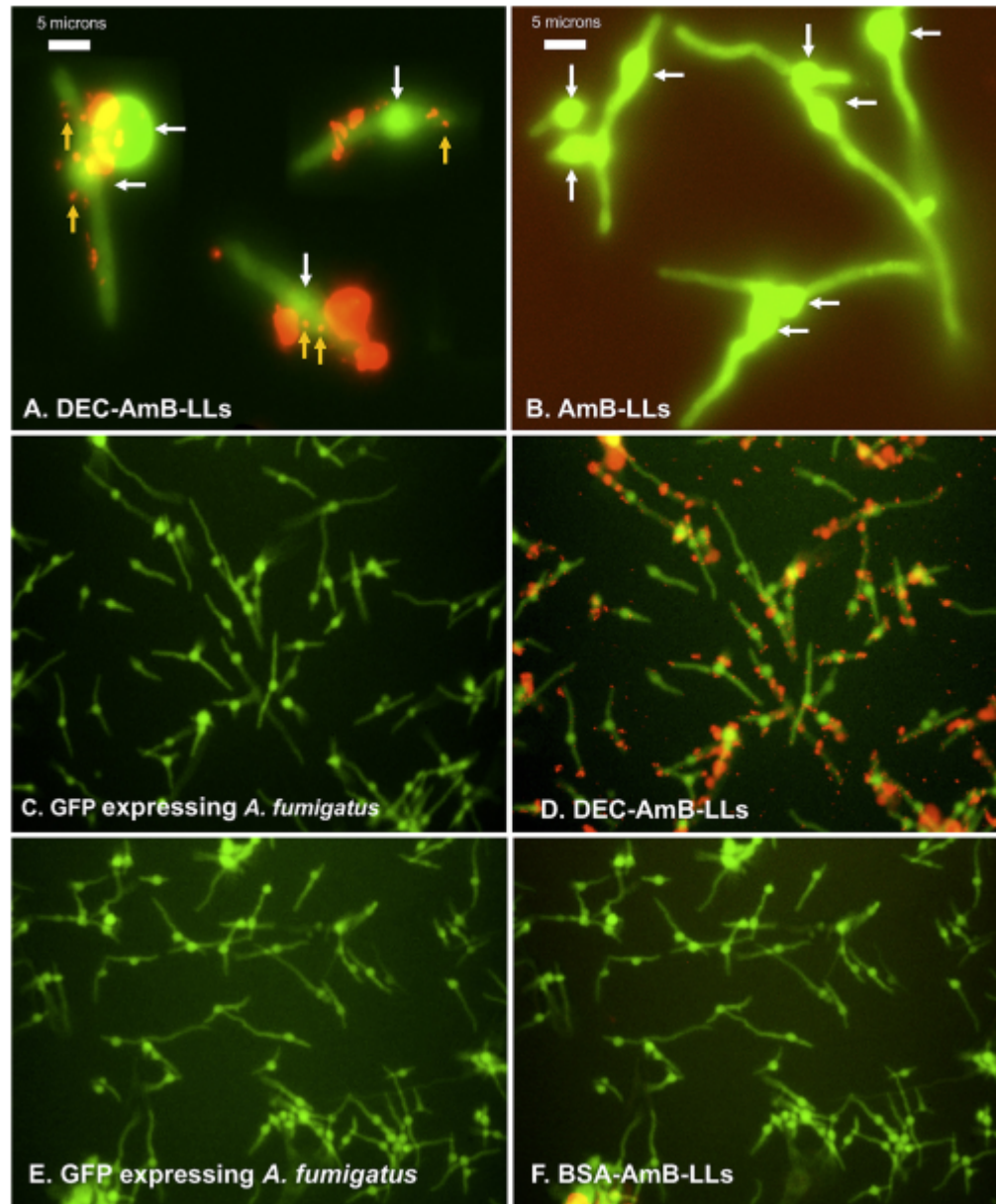


**Fig. 2. sDectin-1-coated DEC-AmB-LLs bound strongly to germinating conidia and germ tubes of *A. fumigatus*, while AmB-LLs and BSA-AmB-LLs did not.** *A. fumigatus* conidia were germinated and grown for 8 to 10 hr in VMM + 1% glucose at 37°C in 24 well microtiter plates before being fixed and stained with fluorescent liposomes. A. Rhodamine red fluorescent DEC-AmB-LLs bound swollen conidia (white arrows) and germ tubes of *A. fumigatus*. B. Rhodamine red fluorescent AmB-LLs did not bind at detectable frequencies. No AmB-LLs were detected even when the red channel was enhanced as

in this image. The smallest red dots in plate A represent individual 100 nm diameter liposomes viewed based on their fluorescence (orange arrows). Large clusters of liposomes form the more brightly red stained areas. C & D were stained with DEC-AmB-LLs. E & F stained with BSA-AmB-LLs. C & E were photographed in the green fluorescent channel, while in D and F green and red fluorescent channels were combined. A through F. Cells were grown for 8 to 10 hr in VMM + 1% glucose at 37°C. Labeling was performed in LDB1 for 60 min. All three liposomes preparations were diluted 1:100 such that liposomal sDectin-1 and BSA proteins were at final concentrations of 1 µg/100 µL. Germlings were viewed in the green channel alone for cytoplasmic fluorescent EGFP expression and red channel for rhodamine fluorescent liposomes. A & B were photographed at 63X under oil immersion in a compound fluorescence microscope and red fluorescence was further enhanced in B to detect potentially individual liposomes. C through F were photographed at 20x on an inverted fluorescence microscope.



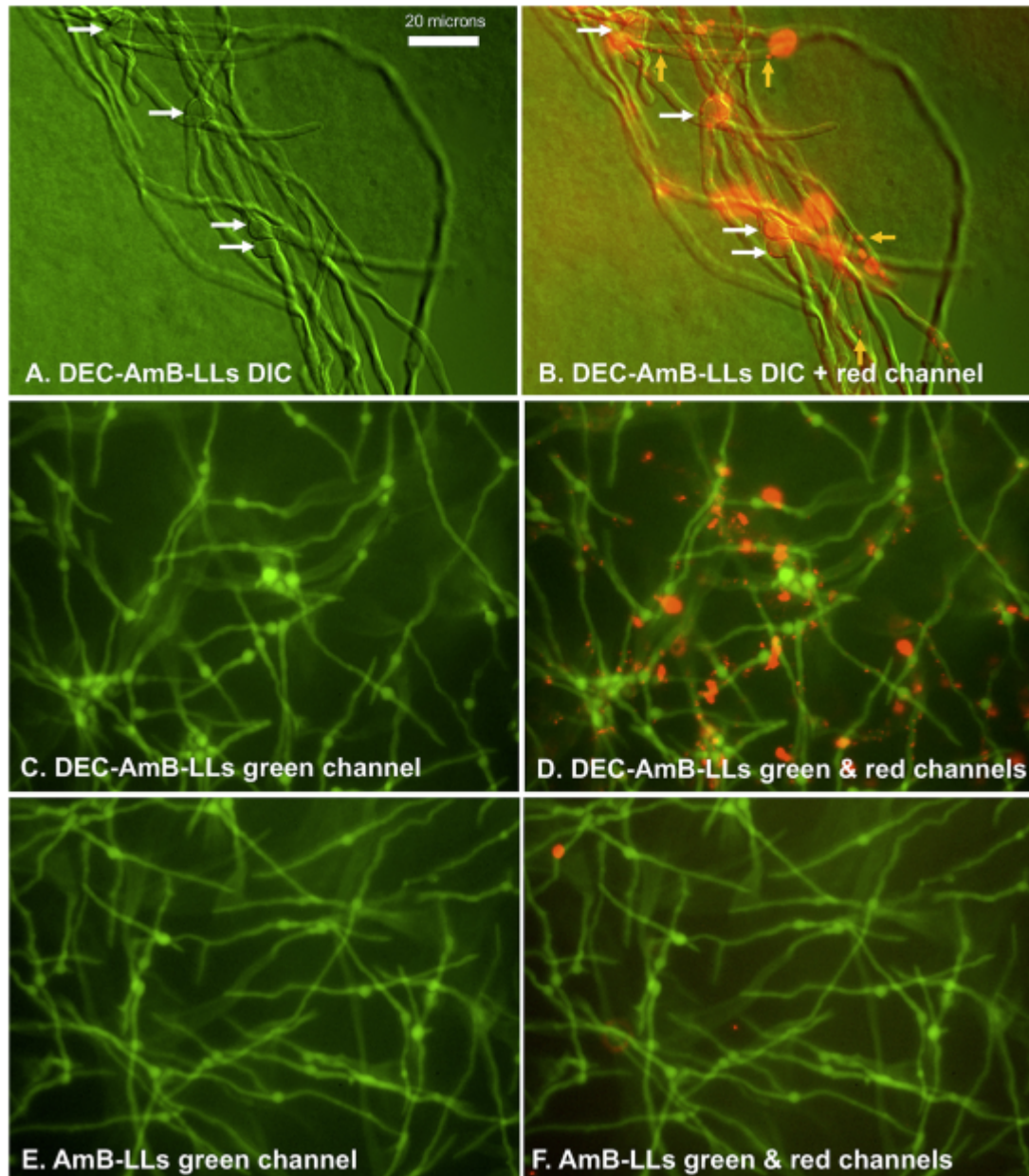


**Fig. 3. sDectin-1-coated DEC-AmB-LLs bound germinating conidia and hyphae of mature *A. fumigatus* cells, while untargeted AmB-LLs and BSA-AmB-LLs did not.** *A. fumigatus* conidia were germinated and grown for 16 hr in VMM + 1% glucose at 37°C in 24 well microtiter plates before being fixed and stained with fluorescent liposomes. A. through D. Cells were stained with rhodamine red fluorescent DEC-AmB-LL diluted 1:100 such that sDectin-1 was at 1  $\mu$ g/100  $\mu$ L, and E. and F. with the equivalent amount of red fluorescent AmB-LLs for 60 min. A. DIC image alone. B. Combined DIC and red

fluorescence image. A and B. show that Rhodamine fluorescent DEC-AmB-LLs bound to germinating conidia (white arrows) and hyphae. In B the smallest red dots represent individual 100 nm liposomes (orange arrows). C through F examined cytoplasmic green fluorescent EGFP and the red fluorescence of liposomes. C & D show that nearly all conidia and most hyphae stained with DEC-AmB-LLs. E & F show that AmB-LLs did not bind. A & B were photographed at 63X under oil immersion and C through F were photographed at 20X on an inverted fluorescent microscope.

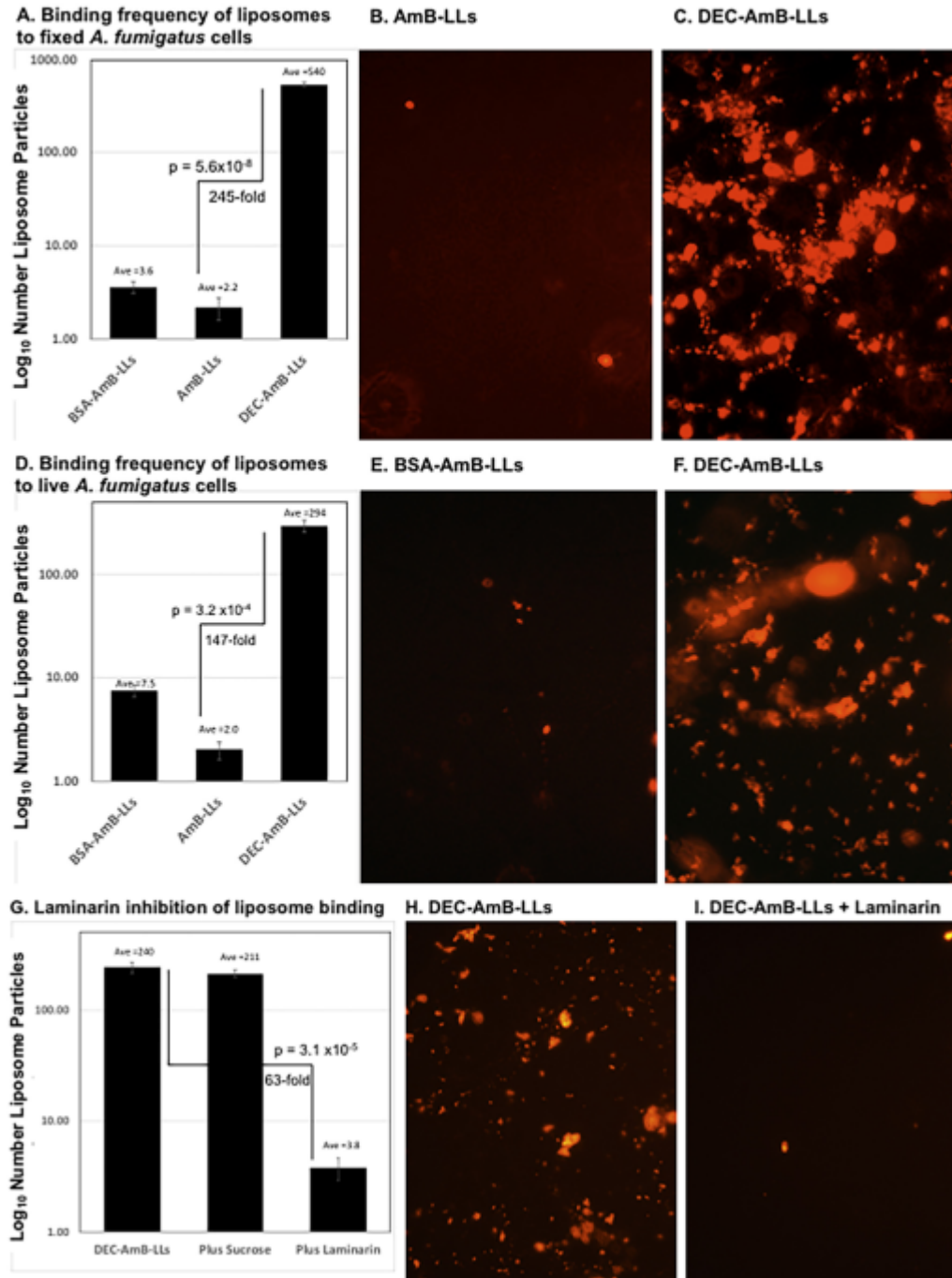


**Fig. 4. sDectin-1-coated DEC-AmB-LLs bound two orders of magnitude more frequently to *A. fumigatus* than control AmB-LLs and binding was inhibited by a soluble beta-glucan.**

Samples of 4,500 *A. fumigatus* conidia were germinated & grown at 37°C for 36 hours in VMM+1% glucose, fixed in formalin or examined live, and incubated for 1 hr with 1:50 dilutions of liposomes in liposome dilution buffer LDB1. Unbound liposomes were washed out.

Multiple fields of red fluorescent images were photographed at 20X and red fluorescence enhanced equivalently for all images. Each photographic field contained approximately 25 swollen conidia and an extensive network of hyphae (not shown). A, B, & C. Labeling formalin fixed cells. D, E, & F. Labeling live cells. G, H, & I. Inhibition of DEC-AmB-LL labeling of fixed cells by 1 mg/mL laminarin, a soluble beta-glucan vs 1 mg/mL sucrose as a control. A, D, & G. The number of red fluorescent liposomes and clusters of liposomes were counted, averaged per field and plotted on a  $\log_{10}$  scale. The numerical average is indicated above each bar and on the vertical axis. Standard errors are shown. Fold differences and p-values are indicated for the performance of DEC-AmB-LLs relative to AmB-LLs. Examples of photographic fields of liposomes used to construct the adjacent bar graphs are shown in B, C, E, F, H, & I.

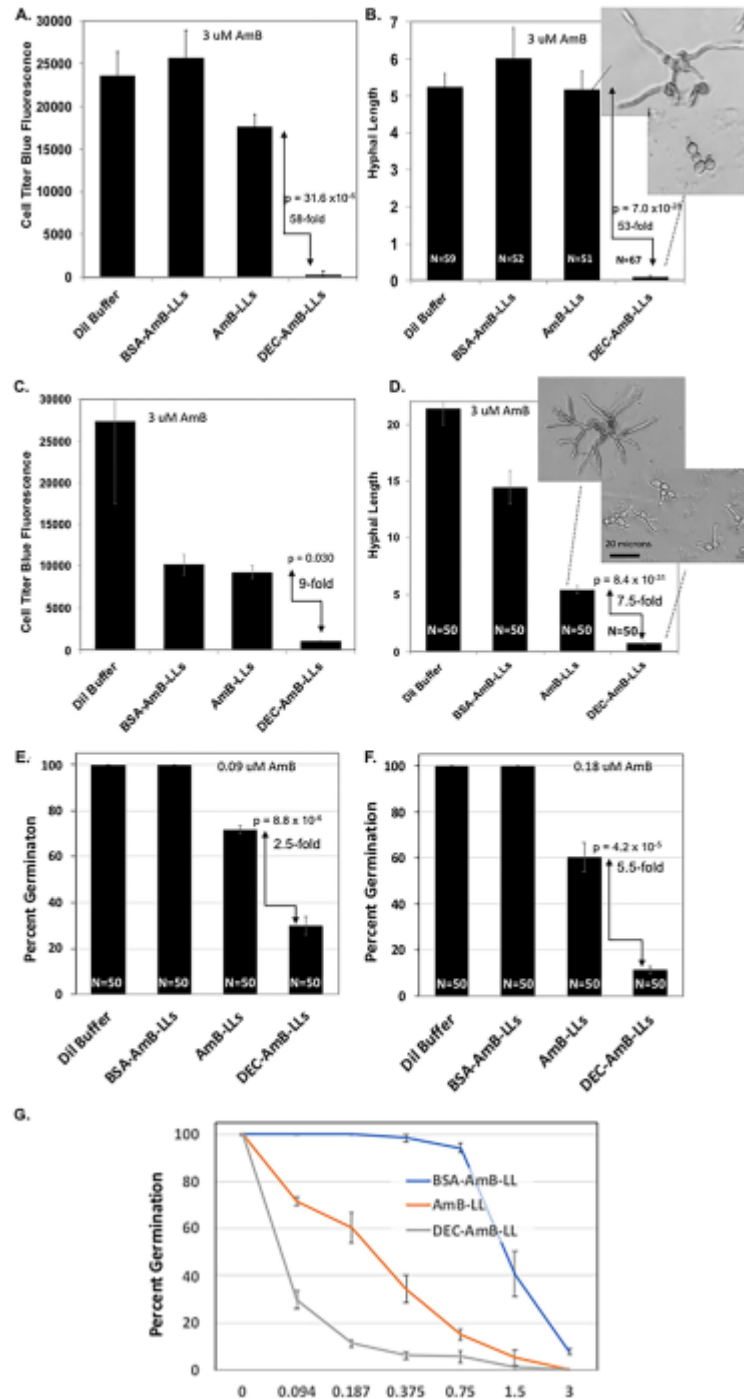


**Fig. 5.** DEC-AmB-LLs inhibited the growth *A. fumigatus* far more efficiently than AmB-LLs. Samples of 4,500 *A. fumigatus* conidia were germinated & grown in 96 well microtiter plates in VMM+1% glucose for 8 to 56 hr at 37°C and treated at the same time with liposome

preparations delivering the indicated concentrations of AmB to the growth media (A through D, 3  $\mu$ M AmB, a 1:300 fold dilution of all three liposome preparations), E. 0.09  $\mu$ M, F. 0.18  $\mu$ M, G. 0.9 to 3  $\mu$ M) or an equivalent amount of liposome dilution buffer LDB2. Viability and growth were estimated using CellTiter-Blue reagent (A & C) or by measuring hyphal length (B & D) or by scoring percent germination (E, F, & G). Background fluorescence from wells with CellTiter-Blue reagent in the media, but lacking cells and liposomes was subtracted. Standard Errors are indicated. Fold differences and p-values are indicated for comparisons of the performance of DEC-AmB-LLs to AmB-LLs. Inset photos in B & D show examples of the length of hyphae assayed for AmB-LLs and DEC-AmB-LL treated sample. One unit of hyphal length in B & D equals 5 microns. Cells were grown for 8 to 56 hrs. A & B and C & D compare the results from two biological replicate experiments with independently conjugated sDectin-1 and assembled liposomes.

## Supplemental Tables and Figures

**Supplemental Table S1. Liposome compositions.** Comparison of the chemical composition of liposomes discussed in the manuscript.

**Supplemental Fig. S1. The modified mouse sDectin-1 DNA *MmsDectin1lyshis* and protein *MmsDectin-1*.** **A.** The codon optimized DNA sequence of *MmsDECTIN1lyshis* was cloned into pET-45B. NCBI BankIT submission #2173810. Length: 577 bp, Vector pET-45b sequence highlighted in red with start codon underlined, Cloning sites in green, Codons for Gly Ser (G,S) flexible linker residues in yellow, reactive lys (K) residues in purple, Mouse sDecetin-1 in light blue, terminal Ala codon in yellow to put stop codons in frame, stop codons in bold. **B.** The modified mouse sDectin-1 protein being synthesized. N terminus and His tag from pET-45B vector in red, Gly Ser (GS) flexible linker residues in yellow, reactive lys (K) residues in purple, Mouse sDecetin-1 in light blue. Final Ala residue/codon to put stop codons and PacI site in frame. 199 amino acids, MW 22,389.66 g/mole. Theoretical pI 7.74.

**Supplemental Fig. S2. SDS PAGE analysis of sDectin-1 in cell extracts and after affinity purification.** sDectin-1 protein was produced in the BL21 strain of *E. coli* grown in Luria Broth over night from the pET-45B plasmid without IPTG induction. The protein was solubilized in GuHCl buffers, purified by Ni-NTA resin and examined by SDS PAGE after GuHCl was removed by dialysis. Extraction of protein into buffers that also contained reducing agent 2-mercaptoethanol and Triton-X100 detergent greatly increased recovery from insoluble inclusion bodies (center lanes) relative to buffers without them (right lanes). Protein was examined on a 12% acrylamide gel stained with Coomassie Blue. The approximate molecular weight of modified sDectin-1 22 kDa is indicated. Extraction of these cells with urea buffers even at 60°C yielded very little protein (not shown).

**Supplemental Fig. S3. sDectin-coated liposomes, DEC-AmB-LLs, bound strongly to *Candida albicans* and *Cryptococcus neoformans* cells.** A., C. & E. are bright field images of *C. albicans* strain Sc5314 and *C. neoformans* strain H99 labeled with DEC-AmB-LLs diluted 1:100 in LDB1. B., D. & F. are the combined bright field and red fluorescence images showing that rhodamine red fluorescent DEC-AmB-LLs bound strongly to these cells. Plain uncoated AmB-LLs and BSA-AmB-LLs did not bind detectably to these cells (not shown). A & B were photographed at 63X under oil immersion, C through F at 20X on an inverted fluorescent microscope.

**Supplemental Fig. S4. sDectin-1-coated DEC-AmB-LLs and BSA coated BSA-AmB-LLs were less toxic to HEK293 cells than uncoated AmB-LLs.** Human Embryonic Kidney HEK293 cells grown to 30 to 40 percent cell density in RPMI lacking red indicator dye in 96 well microtiter plates. Cells were treated for 2 hours with the AmB loaded liposomes indicated or a deoxycholate micelle suspension of AmB (DOC), washed twice and then incubated for additional 16 hrs. All treatments delivered a final concentration of 30 or 15  $\mu$ M of AmB into the media. The 0  $\mu$ M control wells received an amount of liposome dilution buffer LDB2 equivalent to the 30  $\mu$ M treatment. CellTiter-Blue assays estimated cell viability and survival. Background fluorescence from wells with CellTiter-Blue reagent in the media, but lacking cells and liposomes was subtracted. Standard errors are indicated. Percent difference and p-values are indicated for comparisons of the performance of DEC-AmB-LLs to AmB-LLs.



## References

1. **Brown GD, Denning DW, Gow NA, Levitz SM, Netea MG, White TC.** 2012. Hidden killers: human fungal infections. *Sci Transl Med* **4**:165rv113.
2. **CDC.** 2018. Fungal Diseases.  
<https://www.cdc.gov/fungal/diseases/aspergillosis/definition.html>.
3. **Low CY, Rotstein C.** 2011. Emerging fungal infections in immunocompromised patients. *F1000 Med Rep* **3**:14.
4. **Zaoutis TE, Heydon K, Chu JH, Walsh TJ, Steinbach WJ.** 2006. Epidemiology, outcomes, and costs of invasive aspergillosis in immunocompromised children in the United States, 2000. *Pediatrics* **117**:e711-716.
5. **Dupont B.** 2002. Overview of the lipid formulations of amphotericin B. *J Antimicrob Chemother* **49 Suppl 1**:31-36.
6. **Allen U.** 2010. Antifungal agents for the treatment of systemic fungal infections in children. *Paediatrics & Child Health* **15**:603-608.
7. **Lopez-Berestein G, Rosenblum MG, Mehta R.** 1984. Altered tissue distribution of amphotericin B by liposomal encapsulation: comparison of normal mice to mice infected with *Candida albicans*. *Cancer Drug Deliv* **1**:199-205.
8. **Mehta R, Lopez-Berestein G, Hopfer R, Mills K, Juliano RL.** 1984. Liposomal amphotericin B is toxic to fungal cells but not to mammalian cells. *Biochim Biophys Acta* **770**:230-234.

9. **Walker L, Sood P, Lenardon MD, Milne G, Olson J, Jensen G, Wolf J, Casadevall A, Adler-Moore J, Gow NAR.** 2018. The Viscoelastic Properties of the Fungal Cell Wall Allow Traffic of AmBisome as Intact Liposome Vesicles. *MBio* **9**.
10. **Wong-Beringer A, Jacobs RA, Guglielmo BJ.** 1998. Lipid formulations of amphotericin B: clinical efficacy and toxicities. *Clin Infect Dis* **27**:603-618.
11. **Tonin FS, Steimbach LM, Borba HH, Sanches AC, Wiens A, Pontarolo R, Fernandez-Llimos F.** 2017. Efficacy and safety of amphotericin B formulations: a network meta-analysis and a multicriteria decision analysis. *J Pharm Pharmacol* **69**:1672-1683.
12. **Stone NR, Bicanic T, Salim R, Hope W.** 2016. Liposomal Amphotericin B (AmBisome((R))): A Review of the Pharmacokinetics, Pharmacodynamics, Clinical Experience and Future Directions. *Drugs* **76**:485-500.
13. **Adler-Moore JP, Proffitt RT.** 2008. Amphotericin B lipid preparations: what are the differences? *Clin Microbiol Infect* **14 Suppl 4**:25-36.
14. **Graybill JR, Bocanegra R, Gonzalez GM, Najvar LK.** 2003. Combination antifungal therapy of murine aspergillosis: liposomal amphotericin B and micafungin. *J Antimicrob Chemother* **52**:656-662.
15. **Otsubo T, Maruyama K, Maesaki S, Miyazaki Y, Tanaka E, Takizawa T, Moribe K, Tomono K, Tashiro T, Kohno S.** 1998. Long-circulating immunoliposomal amphotericin B against invasive pulmonary aspergillosis in mice. *Antimicrob Agents Chemother* **42**:40-44.

16. **Kooijmans SA, Vader P, van Dommelen SM, van Solinge WW, Schiffelers RM.** 2012. Exosome mimetics: a novel class of drug delivery systems. *Int J Nanomedicine* **7**:1525-1541.
17. **Ha D, Yang N, Nadithe V.** 2016. Exosomes as therapeutic drug carriers and delivery vehicles across biological membranes: current perspectives and future challenges. *Acta Pharm Sin B* **6**:287-296.
18. **Ragusa M, Barbagallo D, Purrello M.** 2015. Exosomes: nanoshuttles to the future of BioMedicine. *Cell Cycle* **14**:289-290.
19. **Song YK, Liu F, Chu S, Liu D.** 1997. Characterization of cationic liposome-mediated gene transfer in vivo by intravenous administration. *Hum Gene Ther* **8**:1585-1594.
20. **Song YK, Liu F, Chu S, Liu D.** 2008. Characterization of cationic liposome-mediated gene transfer in vivo by intravenous administration. *Hum Gene Ther* **8**:1585-1594.
21. **Kamimura K, Liu D.** 2008. Physical approaches for nucleic acid delivery to liver. *AAPS J* **10**:589-595.
22. **Barua S, Mitrugotri S.** 2014. Challenges associated with Penetration of Nanoparticles across Cell and Tissue Barriers: A Review of Current Status and Future Prospects. *Nano Today* **9**:223-243.
23. **Yuan F, Leunig M, Huang SK, Berk DA, Papahadjopoulos D, Jain RK.** 1994. Microvascular permeability and interstitial penetration of sterically stabilized (stealth) liposomes in a human tumor xenograft. *Cancer Res* **54**:3352-3356.

24. **Orleth A, Mamot C, Rochlitz C, Ritschard R, Alitalo K, Christofori G, Wicki A.** 2016. Simultaneous targeting of VEGF-receptors 2 and 3 with immunoliposomes enhances therapeutic efficacy. *J Drug Target* **24**:80-89.
25. **Paul JW, Hua S, Ilicic M, Tolosa JM, Butler T, Smith R.** 2017. Drug Delivery to the Human and Mouse Uterus using Immunoliposomes Targeted to the Oxytocin Receptor. *Am J Obstet Gynecol* doi:10.1016/j.ajog.2016.08.027.
26. **Limasale YD, Tezcaner A, Ozen C, Keskin D, Banerjee S.** 2015. Epidermal growth factor receptor-targeted immunoliposomes for delivery of celecoxib to cancer cells. *Int J Pharm* **479**:364-373.
27. **Ramana LN, Sharma S, Sethuraman S, Ranga U, Krishnan UM.** 2015. Stealth anti-CD4 conjugated immunoliposomes with dual antiretroviral drugs--modern Trojan horses to combat HIV. *Eur J Pharm Biopharm* **89**:300-311.
28. **Shigehiro T, Kasai T, Murakami M, Sekhar SC, Tominaga Y, Okada M, Kudoh T, Mizutani A, Murakami H, Salomon DS, Mikuni K, Mandai T, Hamada H, Seno M.** 2014. Efficient drug delivery of Paclitaxel glycoside: a novel solubility gradient encapsulation into liposomes coupled with immunoliposomes preparation. *PLoS One* **9**:e107976.
29. **Cirstoiu-Hapca A, Buchegger F, Lange N, Bossy L, Gurny R, Delie F.** 2010. Benefit of anti-HER2-coated paclitaxel-loaded immuno-nanoparticles in the treatment of disseminated ovarian cancer: Therapeutic efficacy and biodistribution in mice. *Journal of Controlled Release* **144**:324-331.

30. **Mamot C, Drummond DC, Noble CO, Kallab V, Guo Z, Hong K, Kirpotin DB, Park JW.** 2005. Epidermal growth factor receptor-targeted immunoliposomes significantly enhance the efficacy of multiple anticancer drugs in vivo. *Cancer Res* **65**:11631-11638.
31. **Koren E, Apte A, Jani A, Torchilin VP.** 2012. Multifunctional PEGylated 2C5-immunoliposomes containing pH-sensitive bonds and TAT peptide for enhanced tumor cell internalization and cytotoxicity. *J Control Release* **160**:264-273.
32. **Schneider M.** 2017. Anti-EGFR-immunoliposomes Loaded With Doxorubicin in Patients With Advanced Triple Negative EGFR Positive Breast Cancer. *ClinicalTrials.gov*.
33. **Eloy JO, Petrilli R, Chesca DL, Saggioro FP, Lee RJ, Marchetti JM.** 2017. Anti-HER2 immunoliposomes for co-delivery of paclitaxel and rapamycin for breast cancer therapy. *Eur J Pharm Biopharm* **115**:159-167.
34. **Zheng Y, Tang L, Mabardi L, Kumari S, Irvine DJ.** 2017. Enhancing Adoptive Cell Therapy of Cancer through Targeted Delivery of Small-Molecule Immunomodulators to Internalizing or Noninternalizing Receptors. *ACS Nano* **11**:3089-3100.
35. **Drummond RA, Brown GD.** 2011. The role of Dectin-1 in the host defence against fungal infections. *Curr Opin Microbiol* **14**:392-399.
36. **Goodridge HS, Underhill DM, Touret N.** 2012. Mechanisms of Fc receptor and dectin-1 activation for phagocytosis. *Traffic* **13**:1062-1071.

37. **Hollmig ST, Ariizumi K, Cruz PD, Jr.** 2009. Recognition of non-self-polysaccharides by C-type lectin receptors dectin-1 and dectin-2. *Glycobiology* **19**:568-575.
38. **Adams EL, Rice PJ, Graves B, Ensley HE, Yu H, Brown GD, Gordon S, Monteiro MA, Papp-Szabo E, Lowman DW, Power TD, Wempe MF, Williams DL.** 2008. Differential high-affinity interaction of dectin-1 with natural or synthetic glucans is dependent upon primary structure and is influenced by polymer chain length and side-chain branching. *J Pharmacol Exp Ther* **325**:115-123.
39. **Brown J, O'Callaghan CA, Marshall AS, Gilbert RJ, Siebold C, Gordon S, Brown GD, Jones EY.** 2007. Structure of the fungal beta-glucan-binding immune receptor dectin-1: implications for function. *Protein Sci* **16**:1042-1052.
40. **Gersuk GM, Underhill DM, Zhu L, Marr KA.** 2006. Dectin-1 and TLRs permit macrophages to distinguish between different *Aspergillus fumigatus* cellular states. *J Immunol* **176**:3717-3724.
41. **Steele C, Rapaka RR, Metz A, Pop SM, Williams DL, Gordon S, Kolls JK, Brown GD.** 2005. The beta-glucan receptor dectin-1 recognizes specific morphologies of *Aspergillus fumigatus*. *PLoS Pathog* **1**:e42.
42. **Momany M, Lindsey R, Hill TW, Richardson EA, Momany C, Pedreira M, Guest GM, Fisher JF, Hessler RB, Roberts KA.** 2004. The *Aspergillus fumigatus* cell wall is organized in domains that are remodelled during polarity establishment. *Microbiology* **150**:3261-3268.

43. **Monteiro MC, de la Cruz M, Cantizani J, Moreno C, Tormo JR, Mellado E, De Lucas JR, Asensio F, Valiante V, Brakhage AA, Latge JP, Genilloud O, Vicente F.** 2012. A new approach to drug discovery: high-throughput screening of microbial natural extracts against *Aspergillus fumigatus* using resazurin. *J Biomol Screen* **17**:542-549.
44. **Davis SA, Vincent BM, Endo MM, Whitesell L, Marchillo K, Andes DR, Lindquist S, Burke MD.** 2015. Nontoxic antimicrobials that evade drug resistance. *Nat Chem Biol* **11**:481-487.
45. **Dulal HP, Nagae M, Ikeda A, Morita-Matsumoto K, Adachi Y, Ohno N, Yamaguchi Y.** 2016. Enhancement of solubility and yield of a beta-glucan receptor Dectin-1 C-type lectin-like domain in *Escherichia coli* with a solubility-enhancement tag. *Protein Expr Purif* **123**:97-104.
46. **Gantner BN, Simmons RM, Underhill DM.** 2005. Dectin-1 mediates macrophage recognition of *Candida albicans* yeast but not filaments. *EMBO J* **24**:1277-1286.
47. **Ariizumi K, Shen GL, Shikano S, Xu S, Ritter R, 3rd, Kumamoto T, Edelbaum D, Morita A, Bergstresser PR, Takashima A.** 2000. Identification of a novel, dendritic cell-associated molecule, dectin-1, by subtractive cDNA cloning. *J Biol Chem* **275**:20157-20167.
48. **Hohl TM, Van Epps HL, Rivera A, Morgan LA, Chen PL, Feldmesser M, Pamer EG.** 2005. *Aspergillus fumigatus* triggers inflammatory responses by stage-specific beta-glucan display. *PLoS Pathog* **1**:e30.

49. **Heinsbroek SE, Brown GD, Gordon S.** 2005. Dectin-1 escape by fungal dimorphism. *Trends Immunol* **26**:352-354.
50. **Hopke A, Nicke N, Hidu EE, Degani G, Popolo L, Wheeler RT.** 2016. Neutrophil Attack Triggers Extracellular Trap-Dependent Candida Cell Wall Remodeling and Altered Immune Recognition. *PLoS Pathog* **12**:e1005644.
51. **Chavan NL, Young JK, Drezek RA, Lewis R, Bikram M.** 2012. Interactions of liposome carriers with infectious fungal hyphae reveals the role of beta-glucans. *Mol Pharm* **9**:2489-2496.
52. **Kuramae EE, Robert V, Snel B, Weiss M, Boekhout T.** 2006. Phylogenomics reveal a robust fungal tree of life. *FEMS Yeast Res* **6**:1213-1220.
53. **Kontoyiannis DP.** 2016. A Potential Explanation of a Positive Serum beta-Glucan Assay in Mucormycosis. *Open Forum Infect Dis* **3**:ofw209.
54. **Davis SE, Hopke A, Minkin SC, Jr., Montedonico AE, Wheeler RT, Reynolds TB.** 2014. Masking of beta(1-3)-glucan in the cell wall of *Candida albicans* from detection by innate immune cells depends on phosphatidylserine. *Infect Immun* **82**:4405-4413.
55. **Pradhan A, Avelar GM, Bain JM, Childers DS, Larcombe DE, Netea MG, Shekhova E, Munro CA, Brown GD, Erwig LP, Gow NAR, Brown AJP.** 2018. Hypoxia Promotes Immune Evasion by Triggering beta-Glucan Masking on the *Candida albicans* Cell Surface via Mitochondrial and cAMP-Protein Kinase A Signaling. *MBio* **9**.



56. **Lamaris GA, Lewis RE, Chamilos G, May GS, Safdar A, Walsh TJ, Raad, II, Kontoyiannis DP.** 2008. Caspofungin-mediated beta-glucan unmasking and enhancement of human polymorphonuclear neutrophil activity against *Aspergillus* and non-*Aspergillus* hyphae. *J Infect Dis* **198**:186-192.
57. **Chamilos G, Ganguly D, Lande R, Gregorio J, Meller S, Goldman WE, Gilliet M, Kontoyiannis DP.** 2010. Generation of IL-23 producing dendritic cells (DCs) by airborne fungi regulates fungal pathogenicity via the induction of T(H)-17 responses. *PLoS One* **5**:e12955.
58. **HGMD.** 2019. Human Gene Mutation Database.  
<http://www.hgmd.cf.ac.uk/ac/index.php>. Accessed
59. **Khang CH, Park SY, Lee YH, Kang S.** 2005. A dual selection based, targeted gene replacement tool for *Magnaporthe grisea* and *Fusarium oxysporum*. *Fungal Genet Biol* **42**:483-492.
60. **Momany M.** 2001. Chapter 7. Using Microscopy to explore the duplication cycle, p 119-125. *In* Talbot NJ (ed), *Molecular and cellular biology of filamentous fungi: a practical approach* Oxford University Press, University of Exeter, Exeter, UK.
61. **Sasaki T, Lynch KL, Mueller CV, Friedman S, Freitag M, Lewis ZA.** 2014. Heterochromatin controls gammaH2A localization in *Neurospora crassa*. *Eukaryot Cell* **13**:990-1000.

62. **Brown J, Esnouf RM, Jones MA, Linnell J, Harlos K, Hassan AB, Jones EY.** 2002. Structure of a functional IGF2R fragment determined from the anomalous scattering of sulfur. *EMBO J* **21**:1054-1062.
  
63. **Ejima D, Kohei Tsumoto K, Arakawa T.** 2005. Biotech Applications of Arginine: Novel Uses in Protein Production, Processing, Analysis, and Formulation. *BioProcess Technical* **Dec.:**20-28.
  
64. **Chen J, Liu Y, Wang Y, Ding H, Su Z.** 2008. Different effects of L-arginine on protein refolding: suppressing aggregates of hydrophobic interaction, not covalent binding. *Biotechnol Prog* **24**:1365-1372.
  
65. **Shah D, Shaikh AR.** 2016. Interaction of arginine, lysine, and guanidine with surface residues of lysozyme: implication to protein stability. *J Biomol Struct Dyn* **34**:104-114.
  
66. **Tsumoto K, Umetsu M, Kumagai I, Ejima D, Arakawa T.** 2003. Solubilization of active green fluorescent protein from insoluble particles by guanidine and arginine. *Biochem Biophys Res Commun* **312**:1383-1386.
  
67. **Clement DJ, Attwell NA, Stanley MS, Clipson NJ, Hooley P, Fincham DA.** 1995. Salt sensitivity and arginine toxicity in *Aspergillus nidulans*. *Biochem Soc Trans* **23**:24S.
  
68. **Yao L, Daniels J, Wijesinghe D, Andreev OA, Reshetnyak YK.** 2013. pHLP(R)-mediated delivery of PEGylated liposomes to cancer cells. *J Control Release* **167**:228-237.

69. **He J, Evers DL, O'Leary TJ, Mason JT.** 2012. Immunoliposome-PCR: a generic ultrasensitive quantitative antigen detection system. *J Nanobiotechnology* **10**:26.
70. **Garrett FE, Goel S, Yasul J, Koch RA.** 1999. Liposomes fuse with sperm cells and induce activation by delivery of impermeant agents. *Biochim Biophys Acta* **1417**:77-88.
71. **Alberts B, Johnson A, Lewis J, Raff M, Roberts K, Walter P.** 2008. Molecular Biology of the Cell (5th Edition), p 1539-1600. *In* Edition t (ed), Molecular Biology of the Cell. Garland Science, Taylor and Francis Group, USA.

## APPENDIX C

### TRANSCRIPTION FACTOR ZNF2 COORDINATES WITH THE CHROMATIN REMODELING SWI/SNF COMPLEX TO REGULATE DIFFERENTIATION IN *CRYPTOCOCCUS NEOFORMANS*

---

Lin J., Zhao Y., Ferraro A.R., Yang E., Lewis Z.A., Lin X. 2019. *Nat. Com. Biol.*  
doi: 10.1038/s42003-019-0665-2. Reprinted here with the permission of the publisher.

## Abstract

Cellular differentiation is instructed by development regulators in coordination with chromatin remodeling complexes. Much information about their coordination comes from studies in the model ascomycetous yeasts. It is not clear, however, of the kind of information that can be extrapolated to species of other phyla in Kingdom Fungi. In the basidiomycete *Cryptococcus neoformans*, the transcription factor Znf2 controls yeast-to-hypha differentiation. Through a forward genetic screen, we identified the basidiomycete-specific factor Brf1 and discovered that it works together with Snf5 in the SWI/SNF chromatin remodeling complex in concert with existent Znf2 to execute cellular differentiation. We demonstrated that SWI/SNF assists Znf2 opening up the promoter regions of hyphal specific genes, including the *ZNF2* gene itself. In addition, this complex supports Znf2 to fully associate with its target regions. Importantly, our findings revealed key differences in composition and biological function of the SWI/SNF complex in the two major phyla of Kingdom Fungi.

## Introduction

Cellular differentiation allows genetically identical cells to exhibit distinct phenotypes and carry out distinct cellular functions. Human cells, for example, can differentiate into more than 120 cell types. Although functional and morphological differences are most pronounced in higher eukaryotes, cellular differentiation is a universal phenomenon, often directed by differential gene expression. In eukaryotes, nucleosomes serve as a general barrier preventing gene transcription because eukaryotic genomic DNA is packed into chromatin. Hence, chromatin regulation is a necessity for transcription in eukaryotes, brought about by specific regulatory mechanisms that make certain genomic DNA regions accessible to transcription factors and RNA polymerase II. The ATP-dependent switch/sucrose non-fermentable (SWI/SNF) chromatin

## Abstract

Cellular differentiation is instructed by development regulators in coordination with chromatin remodeling complexes. Much information about their coordination comes from studies in the model ascomycetous yeasts. It is not clear, however, of the kind of information that can be extrapolated to species of other phyla in Kingdom Fungi. In the basidiomycete *Cryptococcus neoformans*, the transcription factor Znf2 controls yeast-to-hypha differentiation. Through a forward genetic screen, we identified the basidiomycete-specific factor Brf1 and discovered that it works together with Snf5 in the SWI/SNF chromatin remodeling complex in concert with existent Znf2 to execute cellular differentiation. We demonstrated that SWI/SNF assists Znf2 opening up the promoter regions of hyphal specific genes, including the *ZNF2* gene itself. In addition, this complex supports Znf2 to fully associate with its target regions. Importantly, our findings revealed key differences in composition and biological function of the SWI/SNF complex in the two major phyla of Kingdom Fungi.

## Introduction

Cellular differentiation allows genetically identical cells to exhibit distinct phenotypes and carry out distinct cellular functions. Human cells, for example, can differentiate into more than 120 cell types. Although functional and morphological differences are most pronounced in higher eukaryotes, cellular differentiation is a universal phenomenon, often directed by differential gene expression. In eukaryotes, nucleosomes serve as a general barrier preventing gene transcription because eukaryotic genomic DNA is packed into chromatin. Hence, chromatin regulation is a necessity for transcription in eukaryotes, brought about by specific regulatory mechanisms that make certain genomic DNA regions accessible to transcription factors and RNA polymerase II. The ATP-dependent switch/sucrose non-fermentable (SWI/SNF) chromatin

remodeling family mainly facilitates *in cis* sliding and/or *in trans* ejecting of nucleosomes on DNA <sup>1</sup>, allowing activation or repression of gene transcription. Through modulating gene expression, the SWI/SNF family of complexes are critical to a variety of cellular processes including stemness, differentiation, and development. Remarkably, about 20% of cancer types bear mutations in SWI/SNF subunits in humans <sup>2</sup>.

The SWI/SNF complex is the first ATP-dependent chromatin remodeling complex of the SWI/SNF family identified. To avoid confusion, we use the term “family” when we discuss the SWI/SNF family of complexes. The SWI/SNF complex is composed of 12 subunits in *Saccharomyces cerevisiae* and 11-15 subunits in humans <sup>3,4</sup>. However, most human SWI/SNF subunits have several isoforms, permitting dozens of combinatorial assemblies and a spectrum of related complexes <sup>5</sup>. It is therefore challenging to attribute observed phenotypes based on a mutation of a particular subunit to the function of a specific complex. In *S. cerevisiae* and *Schizosaccharomyces pombe*, there are only two complexes in the SWI/SNF family: the SWI/SNF complex and the RSC (remodeling structure of chromatin) complex. These two complexes have their distinct catalytic and accessory subunits while sharing a small set of common subunits <sup>6,7</sup>. The relative simplicity in these model ascomycete yeasts has facilitated the investigation of the molecular functions of SWI/SNF complexes and individual subunits. It is unclear, however, what functions and features of the SWI/SNF complexes established in these two model yeast species can be extrapolated to other eukaryotic species, including other distantly related fungal species.

In contrast to these model yeasts, the human fungal pathogen *Cryptococcus neoformans* belongs to a different phylum in Kingdom Fungi: Basidiomycota. Basidiomycetes diverged from ascomycetes about 1 billion years ago and share key features with higher eukaryotes that are

absent from the model yeasts. For instance, >90% of the protein-coding genes in *C. neoformans* contain multiple introns and epigenetic regulation like RNAi and DNA methylation plays important roles in its biology<sup>8-12</sup>. In addition, *C. neoformans* can exist in multiple morphotypes, including basidiospore, blastospore, chlamydospore, yeast, titan cell, pseudohypha, hypha, clamp, and basidium. Cellular differentiation in *C. neoformans* is an area of great interest as morphological changes are associated with its pathogenicity<sup>13</sup>. For instance, yeasts and spores are infectious and virulent<sup>14,15</sup>; titan cells are proposed to be dormant and stress-resistant in hosts<sup>16,17</sup>; pseudohyphae and hyphae are attenuated in virulence in mammalian hosts<sup>18,19</sup>. In the environment, however, hyphae are an integral part of its life cycle and the filamentous forms (pseudohyphae and hyphae) confer cryptococcal resistance to its natural predators (e.g. soil amoeba)<sup>20</sup>.

The yeast-to-hypha transition is the best-understood cellular differentiation pathway in *C. neoformans*. During bisexual reproduction, compatible **a** and  $\alpha$  yeast partners conjugate after activating their pheromone sensing cascade, and the resulting **a**- $\alpha$  dikaryotic zygote differentiates to hyphae. Some aerial hyphae eventually develop into fruiting bodies and generate infectious meiotic basidiospores. We previously discovered that *C. neoformans*, in the absence of a compatible mating partner, can undergo similar cellular differentiation events (self-fruiting or unisexual reproduction)<sup>21</sup>, with the exception that the non-self-recognition system (the pheromone sensing cascade) is dispensable<sup>22,23</sup>. A zinc-finger transcription factor, Znf2, is an absolutely required master regulator for hyphal growth in this organism<sup>19,22-24</sup>. Deletion of *ZNF2* confines *C. neoformans* cells to the yeast form and overexpression of *ZNF2* drives filamentation regardless of growth conditions<sup>19,24</sup>. Whether chromatin remodeling factors coordinate with Znf2 to control the yeast-hypha differentiation in this basidiomycete is unknown.



The *SWI* (switch) and *SNF* (sucrose nonfermenting) genes were initially discovered in *S. cerevisiae* through genetic screens aimed towards identifying factors that control the induction of the endonuclease HO required for mating type switching or the induction of the invertase Suc2 required for sucrose metabolism<sup>25,26</sup>. It later became apparent that these genes encode subunits of two large protein complexes (SWI/SNF and RSC), which are global regulators of transcription through ATP-dependent chromatin remodeling.

Here, through a forward genetic screen in a *ZNF2* overexpression strain in *C. neoformans*, we identified two genes, *SNF5* and *BRF1*, that are essential for hyphal differentiation even when Znf2 protein is produced. Snf5 is a conserved core subunit in the SWI/SNF complex, while *BRF1* encodes a novel basidiomycete-specific protein with an AT-rich interacting domain (ARID). Excitingly, we discovered that Brf1 works together with Snf5 in the SWI/SNF complex in regulating hyphal differentiation. We demonstrated that Brf1 is essential for transcriptional induction of *ZNF2* and is required for Znf2's full association to the promoter regions of its downstream target genes, including the *ZNF2* gene itself. Furthermore, the promoter region of *ZNF2* and its downstream targets important for filamentation become transcriptionally inaccessible in the absence of *BRF1* or *SNF5*. This is the first identification and functional characterization of a phylum-specific subunit in the SWI/SNF complex in basidiomycetes. Our findings also revealed major and intriguing differences in composition and biological functions of the SWI/SNF complex and the RSC complex between the two major phyla in the Kingdom Fungi.

## **Results**

### **Nuclear Znf2 fails to induce hyphae in insertional mutants**

We previously demonstrated the key function of *ZNF2* in regulating yeast-to-hypha transition. However, the Znf2 partner(s) in regulating this cell differentiation remain elusive<sup>24</sup>. Here, we recruited a reporter strain to identify Znf2-related factors through a forward genetic screen. In this reporter strain, the native *ZNF2* gene is deleted and an ectopic copy of mCherry-fused *ZNF2* is expressed under the control of an inducible promoter of a copper transporter *CTR4* (XL280α, *znf2::NAT/ P<sub>CTR4-2</sub>-mCherryZNF2-NEO*). This reporter strain switched from yeasts to hyphae when *ZNF2* was induced in response to copper limitation in the presence of the copper chelator bathocuproinedisulfonic acid (BCS) (Fig. 1a), as we expected based on our previous studies<sup>24,27</sup>. The production of Znf2 can be monitored through the nuclear localized mCherry fluorescence signal (Fig. 1a). Here we used insertional mutagenesis through *Agrobacterium*-mediated transformation (AMT) and generated 88,000 T-DNA insertional mutants in this reporter strain background. We screened these mutants visually for smooth yeast colonies on filamentation-inducing V8 agar medium containing BCS (Fig. 1b). 84 filamentation-defective mutants were isolated (strains AMT001-AMT084, Supplementary Table 1).

We next examined the 84 isolated mutants for their cellular morphology, and the expression and localization of mCherry-tagged Znf2 protein upon induction. Fifty-eight of these mutants showed nuclear mCherry-Znf2 localization while 26 had altered subcellular distribution of the fluorescence signal. The mutants with mis-localized Znf2 signal will help understand how Znf2 protein is regulated through trafficking, post-translational modification, and/or stability. In this study, however, we set to identify factors that are required for nuclear localized Znf2 protein to exert its function. Thus, we decided to follow up the 58 mutants with Znf2 expressed and properly localized to the nucleus. Among these mutants, only 25 candidate mutants showed only yeast cellular morphology in the population and nuclear mCherry-Znf2 signal when cultured in

YPD+BCS inducing condition (Supplementary Table 1). These 25 mutants were chosen for further analyses.

Multiple T-DNA insertions and cryptic mutations could occur during *Agrobacterium*-mediated transformation<sup>28,29</sup>. To determine if the T-DNA insertion is genetically linked to the non-filamentous phenotype in these 25 mutants, we backcrossed these 25 mutants (in the  $\alpha$  mating type) to the wild-type congenic mating partner XL280a, micro-dissected the meiotic basidiospores, and analyzed the phenotypes of the progeny. If the genome of the insertional mutant harbors only one copy of the T-DNA, which carries the hygromycin selection marker *HYG*, we would expect a 1:1 ratio of hygromycin sensitive ( $HYG^S$ ) and hygromycin resistant ( $HYG^R$ ) progeny. If that single T-DNA insertion caused the non-filamentous phenotype, then all  $HYG^R$  progeny would be non-filamentous while all  $HYG^S$  progeny would be filamentous under a *Znf2*-inducing condition. In comparison, when multiple T-DNAs inserted in the genome, the ratio between  $HYG^S$  and  $HYG^R$  meiotic progeny would be 1:3 (two unlinked insertions) or lower ( $>2$  unlinked T-DNA insertions). Based on our genetic linkage analyses of the meiotic progeny dissected from the 25 crosses, 8 out of the 25 mutants likely harbor a sole T-DNA insertion that is genetically linked to their non-filamentous phenotype on media containing BCS (Fig. 1c).

### **Two candidates were identified as filamentation activators**

To identify the genes affected by the T-DNA insertions in the selected 8 mutants, we used genome sequencing approach developed by Dr. Alspaugh's group<sup>29</sup>. The 8 mutants carry not only the T-DNA insertion ( $HYG^R$  marker), but also the *znf2* $\Delta$  construct ( $NAT^R$  marker) and the *P<sub>CTR4-2</sub>-mCherryZNF2* construct ( $NEO^R$  marker). Because all three drug selection markers share the same promoter and terminator sequences, we decided to sequence their meiotic

progeny derived from the backcrosses that have only the T-DNA insertion (HYG<sup>R</sup>). From the genome sequences of the 8 “clean” insertional mutants, we identified 8 insertion sites (Supplementary Table 2), including two singleton and six paired insertions. Singleton insertions could be the result of big chromosomal fragment deletion or chromosomal rearrangement <sup>29</sup>, and so we did not pursue them further. The remaining six paired insertions revealed four possible disrupted genetic loci (Fig. 1d), with two loci being inserted twice independently in different isolates. *CND05760* encodes the Ste11 $\alpha$  MAP kinase and previously had been shown to be involved in the pheromone sensing cascade, but is not essential for filamentation <sup>23</sup>. To verify the role of the other three identified genes *CNK02410*, *CNA02310*, and *CNA07190* in filamentation, we carried out independent targeted gene deletion in the wild-type XL280 $\alpha$  background. *CNK02410* encodes Ssn6, a general transcriptional co-repressor <sup>30</sup>. Deletion of *SSN6* reduced filamentation in the wild type background (Fig. 1e). *CNA02310* and *CNA07190* were recovered twice from independent insertions (Fig. 1d), and independent targeted deletion of these two genes in the wild type background nearly abolished filamentation, similar to the corresponding insertional mutants (Fig. 1c and 1e). Thus, *CNA02310* and *CNA07190* are essential for yeast-hypha transition in *C. neoformans*.

*CNA07190* encodes Snf5 (1784 aa, 195 kDa), a core subunit of the conserved SWI/SNF chromatin remodeling complex. Snf5 is critical for cellular differentiation in all organisms tested, including ascomycetous and basidiomycetous fungi <sup>31-36</sup>. For instance, deletion of *SNF5* in the basidiomycete *Coprinopsis cinerea*, commonly known as the gray shag mushroom, results in severe defects in dikaryon development and fruiting <sup>34,35</sup>. In *C. neoformans*, *SNF5* was shown to be critical for bisexual reproduction in the serotype A H99 strain background, as a bilateral *snf5* $\Delta$  x *snf5* $\Delta$  cross yielded no mating hyphae or fruiting body <sup>28</sup>. Consistently, we found that

a bilateral cross between *snf5* $\Delta\alpha$  and *snf5* $\Delta\mathbf{a}$  mutants in XL280 background yielded no mating hyphae (Fig. 2a). This result indicates that the function of Snf5 is conserved in both serotypes of *C. neoformans*. Besides Snf5, no other subunits in the SWI/SNF complex have been identified or characterized in *C. neoformans*.

*CNA02310* encodes an uncharacterized novel protein (1033 aa, 112 kDa). The predicted protein has an AT-rich interacting domain (ARID) but no other recognizable domains. Because it is basidiomycete specific (Supplementary Fig. 1), we named this gene *BRF1* (basidiomycete-specific regulator of filamentation 1).

### **Brf1 functions in the same biological process as Snf5**

Brf1 and Snf5 share a similar function in filamentation. As mentioned earlier, independent deletion of *SNF5* or *BRF1*, or their disruption by T-DNA insertion abolished or nearly abolished self-filamentation (Fig. 1e). Unilateral crosses between the *snf5* $\Delta$  or the *brf1* $\Delta$  mutant in the  $\alpha$  mating type with a non-self-filamentous reference  $\mathbf{a}$  strain (*snf5* $\Delta\alpha$  x  $\mathbf{a}$  or *brf1* $\Delta\alpha$  x  $\mathbf{a}$ ) on V8 medium produced fewer mating hyphae (Supplementary Fig. 2a), likely due to their reduced cell fusion efficiency (Supplementary Fig. 2b). Bilateral crosses between the mutant partners (*snf5* $\Delta\alpha$  x *snf5* $\Delta\mathbf{a}$  or *brf1* $\Delta\alpha$  x *brf1* $\Delta\mathbf{a}$ ) did not produce any aerial mating hyphae or sexual spores (Fig. 2a). As bisexual mating or self-filamentation on V8 medium is mostly driven by the pheromone signaling cascade, we decided to examine the impact of these mutations on filamentation independent of the pheromone cascade on V8 medium supplemented with a high concentration of copper (500 $\mu$ M CuSO<sub>4</sub>). We previously showed that self-filamentation under this condition is independent of the nonself-recognition system<sup>22</sup>. Neither the *brf1* $\Delta$  mutant nor the *snf5* $\Delta$  mutant filamented under this condition (Fig. 2a), confirming the similarly critical role of Brf1 and Snf5 in filamentation.

Brf1 and Snf5 also share similar function in other assays. Here we examined the *brf1*Δ mutant and the *snf5*Δ mutant for their susceptibility to heat stress (37°C), osmotic stress (1M NaCl or KCl), or cell wall stress (0.5% Congo Red). Both the *brf1*Δ and the *snf5*Δ mutants showed slightly increased sensitivity to osmotic stress and both mutants grew similarly in other conditions tested (Fig. 2b). The increased sensitivity to the osmosis stresses in the *brf1*Δ mutant might due to the decreased transcript level of genes involved in anion and ion transportation (Supplementary Table 4), which was not observed in the *znf2*Δ mutant. *SNF5* is known to be required for normal growth on media with disaccharide sucrose or trisaccharide raffinose as the sole carbon source<sup>28</sup>. Here we found that the *brf1*Δ mutant showed a similar defect in growth on the raffinose medium as the *snf5*Δ mutant (Fig. 2c-2d). Neither the *brf1*Δ mutant nor the *snf5*Δ mutant showed any significant defect in growth when glucose was used as the sole carbon source (Fig. 2c-2d). It is notable the growth defect on raffinose medium is shared between the *brf1*Δ and the *snf5*Δ mutant, but not with the *znf2*Δ mutant. The data suggest that Brf1 has a role in certain stress responses that is independent of Znf2.

Given the striking resemblance of the *brf1*Δ mutant and the *snf5*Δ mutant, we postulate that Brf1 functions in the same biological pathway as Snf5. To test this hypothesis, we constructed the *brf1*Δ*snf5*Δ double mutant. If *BRF1* and *SNF5* work in the same pathway, we expect that the double deletion mutant would show similar phenotypes as the single gene deletion mutants. Indeed, the *brf1*Δ*snf5*Δ double mutant behaved similarly as the *brf1*Δ or the *snf5*Δ single mutant in all assays (stress tolerance, filamentation, and growth on the raffinose medium) (Fig. 2b-2d). When we tagged Brf1 with tdTomato controlled by a constitutively active promoter (*P<sub>TEF1</sub>-BRF1*-tdTomato), it restored the filamentation defect of the *brf1*Δ mutant (Supplementary Fig. 4a), indicating functionality of the tagged Brf1. The tagged Brf1 localized

to the nucleus (Supplementary Fig. 4a), as is Snf5<sup>37</sup>. Taken together, we propose that Brf1 functions together with Snf5.

As Snf5 is a conserved and core subunit of the SWI/SNF complex, we postulate that this novel protein Brf1 may also function in this chromatin remodeling complex. Every known SWI/SNF complex incorporates a subunit with an ARID domain<sup>38-40</sup>, which can bind to DNA<sup>39</sup>. In the ascomycete fungal pathogen *Candida albicans*, Swi1, the ARID-containing subunit in the SWI/SNF complex, is critical for filamentation and virulence<sup>31-33</sup>. The *C. neoformans* genome carries three genes encoding ARID-containing proteins: *RUM1α* (CND05870), *AVC1* (CNK00710), and *BRF1*. None of these three cryptococcal genes showed high sequence homology to either *SWI1* or *SOL1*, the ARID containing subunit in the SWI/SNF complex in *S. cerevisiae* or *S. pombe*. Even for the small ARID domain region, the amino acid sequence homology is only 24% identical between Swi1 and Brf1. However, in terms of domain architecture, Brf1 is more similar to ScSwi1 or SpSol1 than Avc1 or Rum1α (Fig. 3a). Consistent with our idea that Brf1, but not Avc1 or Rum1α, works in the same complex as Snf5, deletion of *BRF1*, but not *AVC1* or *RUM1α*, caused defects in filamentation (Fig. 3b) and slowed growth on raffinose medium (Supplementary Fig. 3). We therefore hypothesize that Brf1 is the ARID subunit of the SWI/SNF complex in the basidiomycete *Cryptococcus neoformans*.

### **Brf1 is a basidiomycete-specific subunit of SWI/SNF**

If Brf1 and Snf5 work together in the SWI/SNF complex, we expect that Brf1 and Snf5 interact with each other, either directly or indirectly through other subunits of the SWI/SNF complex. To test the hypothesis, we performed co-immunoprecipitation assays coupled with mass spectrometry using the FLAG-tagged Brf1 as the bait. As *BRF1* is a lowly expressed gene based on our and others' transcriptome data<sup>41</sup>, we used the constitutively active *TEF1* promoter

to drive the expression of FLAG-tagged Brf1 protein and it restored the *brf1*Δ's mating deficiency (Supplementary Fig. 4b). We then carried out Co-IP/MS in two independent isolates and the wild-type H99 strain without any tag was used as the negative control. We applied the following criteria to exclude nonspecific proteins: (i) proteins shared among the samples and the negative control, (ii) proteins not shared between samples of the two  $P_{TEF1}$ -*BRF1*-CBP-2xFLAG strains, and (iii) non-nuclear localized proteins as Brf1 localizes to the nucleus. In addition to the bait protein Brf1, we identified many putative SWI/SNF components that are homologous to the SWI/SNF complex subunits in *S. cerevisiae* and/or *S. pombe*, including Snf5, Snf2, Arp4, Arp9, Rsc6, and Rsc8 (Table 1).

The SWI/SNF complex and the RSC complex of the SWI/SNF family are assembled modularly, with some subunits/modules shared by both complexes<sup>5,42,43</sup>. In *S. cerevisiae* and *S. pombe*, homologues of Arp4, Arp9, Rsc6, and Rsc8 participate in both the SWI/SNF complex and the RSC complex. Since Brf1 pulled down subunits unique to the SWI/SNF complex and the ones shared by both complexes, we speculate that Brf1 is SWI/SNF-specific in *C. neoformans*. In most fungal species examined, the SWI/SNF complex and the RSC complex each harbors a Snf5 domain-containing subunit, with Snf5 in the SWI/SNF complex and Sfh1 in the RSC complex (Fig. 3c). When we used the mNeonGreen-tagged RSC-specific protein Sfh1 (CNC06140) to perform co-immunoprecipitation in *C. neoformans*, the Sfh1 pulled down RSC-specific subunits including Rsc1, Rsc7, and Rsc9. In addition, tagged Sfh1 pulled down the shared subunits including Snf2, Arp4, Arp9, Rsc6, and Rsc8 (Supplementary Table 3). However, Sfh1 did not pull down Brf1 or the SWI /SNF-specific subunit Snf5. Taken together, these lines of evidence support that Brf1 is a subunit specific to the SWI/SNF complex in *C. neoformans*.



Based on the Co-IP data and the homology of the SWI/SNF and RSC subunits among *S. cerevisiae*, *S. pombe* and *C. neoformans*, we inferred that Brf1 and Snf5 are subunits specific to the SWI/SNF complex (blue) while Sfh1, Rsc1, Rsc4, Rsc7, and Rsc9 are subunits specific to the RSC complex (yellow in Table 2). Snf2, Arp4, Arp9, Rsc6 and Rsc8 are the shared subunits between the SWI/SNF and the RSC complexes in *C. neoformans* (green in Table 2, Supplementary Fig. 5a). Consistent with the idea that these two complexes have overlapping and distinct subunits, the transcript levels of the shared components are generally higher (green) than the complex-specific subunits (yellow or blue) based on a cell-cycle-regulated transcriptome data<sup>41</sup> (Fig. 3d). In *S. cerevisiae*, the RSC complex is approximately 10 times more abundant at the protein level than the SWI/SNF complex<sup>44</sup>. Consistently, the genes encoding for the RSC subunits are expressed at higher levels than those encoding the SWI/SNF subunits in *S. cerevisiae* (Fig. 3d). In both *S. cerevisiae* and *S. pombe*, many subunits in the RSC complex are essential for growth, including Sfh1 and Rsc9 (Table 2)<sup>6,44,45</sup>. By contrast, the RSC-specific *SFH1* and *RSC9* genes are not essential for growth in *C. neoformans* as the gene deletion mutants are viable, albeit with slower growth on either nutrient rich media or minimum media (Fig. 3f-g). Surprisingly, deletion of the SNF/SWI complex specific *BRF1* or *SNF5* did not cause any growth defects in growth under the same conditions (Fig. 3f-g). Remarkably, the *snf5Δsfh1Δ* double mutant, where both the SWI/SNF-specific subunit Snf5 and the RSC-specific subunit Sfh1 were knocked out, was still viable despite a much more pronounced growth defect (Fig. 3g). Thus, the SWI/SNF complex functionally differ from the RSC complex in *C. neoformans*. Neither the RSC complex nor both RSC and SWI/SNF complexes together are essential in this basidiomycetous fungus, in contrast to what is known in ascomycetes.

Given that the two SWI/SNF complex specific subunits Brf1 and Snf5, and none of the RSC complex specific subunits were identified from our genetic screen, we predicate that the SWI/SNF complex, but not the RSC complex, specifically regulates the yeast-hypha differentiation in *C. neoformans*. To test this hypothesis, we examined the impact of the disruption of the SWI/SNF complex (*brf1*Δ and *snf5*Δ) or the RSC complex (*sfh1*Δ and *rsc9*Δ) on filamentation. Indeed, the RSC complex mutants, *sfh1*Δ and *rsc9*Δ, were still filamentous on V8 medium, in contrast to the yeast growth of the SWI/SNF complex mutants *brf1*Δ and *snf5*Δ (Fig. 3e). The findings support the view that the SWI/SNF complex, but not the RSC complex, is critical for yeast-to-hyphal differentiation in *C. neoformans*.

### ***BRF1* is required for the induction of the *ZNF2* transcripts**

The evidence presented so far supports the idea that Brf1 and Snf5 work together in the SWI/SNF complex. Here we used Brf1 to dissect the relationship between the SWI/SNF complex and Znf2 in controlling morphogenesis in *C. neoformans*. To study the genetic relationship between Brf1 and Znf2, we set up a cross between a *brf1*Δ/*BRF1*<sup>oe</sup> α strain and a *znf2*Δ/*ZNF2*<sup>oe</sup> a strain. We micro-dissected meiotic progeny from the cross and confirmed the genotypes of the progeny by diagnostic PCRs (Fig. 4a). As expected, progeny of the wild-type genotype were self-filamentous, while progeny of the *znf2*Δ or the *brf1*Δ genotype were non-filamentous. *ZNF2*<sup>oe</sup>*znf2*Δ strains were filamentous, but not *ZNF2*<sup>oe</sup>*brf1*Δ (Fig. 4b). This result is consistent with our earlier observation that overexpression of *ZNF2* did not restore filamentation in the *brf1*<sup>Tn</sup> insertional mutant (Fig. 1c). Likewise, *BRF1*<sup>oe</sup>*brf1*Δ strains were filamentous, but not *BRF1*<sup>oe</sup>*znf2*Δ (Fig. 4b). These results indicate that overexpression of *BRF1* restored filamentation in the *brf1*Δ mutant, but it could not bypass the requirement of Znf2. Taken

together, overexpression of either *BRF1* or *ZNF2* cannot override the absence of the other, and both are essential for yeast-hypha differentiation in *C. neoformans*.

We next analyzed the transcriptomes of wild type, *brf1* $\Delta$ , *brf1* $\Delta$ /*BRF1*<sup>oe</sup>, and *ZNF2*<sup>oe</sup> strains cultured under filamentation-repressing YPD medium and filamentation-inducing V8 medium (Supplementary Table 4). More than 60% of the differentially expressed genes (up-regulated or down-regulated) in the *brf1* $\Delta$  were shared with the *znf2* $\Delta$  mutants under filamentation-inducing condition (Fig. 4c). Remarkably, more than 95% (95/99) of the overlapping genes were down-regulated upon deletion of *BRF1* or *ZNF2*, suggesting that Brf1 and Znf2 activate these genes during hyphal differentiation. As *ZNF2*/filamentation is primarily induced by the pheromone pathway when cells are cultured on V8 medium <sup>22</sup>, it is not surprising that deletion of either *BRF1* or *ZNF2* dampened the induction of the pheromone sensing pathway genes, including *MF $\alpha$*  (pheromone gene, 181 fold reduction), *STE3 $\alpha$*  (pheromone receptor gene, 14 fold reduction), *STE6* (pheromone exporter gene, 7 fold reduction), *CPK1* (pheromone MAPK gene, 5.1 fold reduction), and *MAT2* (pheromone transcription factor gene, 9 fold reduction) (Fig. 4c, right panel). The reduced activation of the pheromone sensing pathway in the *brf1* $\Delta$  mutant likely caused reduced cell fusion which we observed earlier (Supplementary Fig. 2b). On the other hand, much fewer genes were differentially expressed in the *brf1* $\Delta$  and the *znf2* $\Delta$  mutants under YPD filamentation-suppression condition (Supplementary Fig. 6, Supplementary Table 4).

The transcript level of *ZNF2* in the wild type increased 32-fold under filamentation-inducing condition compare to filamentation suppressing condition. In the absence of *BRF1*, however, the *ZNF2* transcript level remained extremely low, similar to the basal level when cells were cultured under filamentation-suppressing condition (Fig. 4d). Ectopic expression of *BRF1*

under the control of *TEF1* constitutive promoter in the *brf1* $\Delta$  strain restored the dramatic induction of the *ZNF2* transcript level under filamentation-inducing condition (Fig. 4d). By contrast, constitutive expression of *ZNF2* (54.75 fold increase) had minimal impact on the transcript level of *BRF1* (1.27 fold increase). The transcript of *BRF1* remained at a low and steady level when cells were cultured either in YPD or on V8 medium. The steady level of *BRF1* transcripts was also observed at different stages of the cell cycle (Fig. 3d) <sup>41</sup>. The results indicate that *BRF1* itself is expressed at a low but constant level and is not influenced by Znf2. The induction of *ZNF2*, however, requires Brf1.

### **Brf1 and Znf2 work in concert in cellular differentiation**

The SWI/SNF chromatin-remodeling complex is known to evict or slide nucleosomes to change chromatin structure. As Brf1 is required for *ZNF2* induction, we postulate that deletion of *BRF1* impairs chromatin remodeling at the *ZNF2* promoter region, which consequently diminishes transcription induction of *ZNF2*. Moreover, we showed earlier that when the Znf2 protein was produced due to ectopic expression controlled by a non-native promoter, it still failed to drive filamentation in the absence of Brf1 (Fig. 1c and 4b). Therefore, beyond transcription activation of *ZNF2*, Brf1 is critical for existent Znf2 protein to execute its function. We thus hypothesize that Brf1 is required for chromatin remodeling not only at the promoter region of *ZNF2*, but also those of Znf2's targets.

To determine if the ability of Znf2 to bind to its downstream targets is affected by the SWI/SNF complex, we conducted chromatin-immunoprecipitation (ChIP) experiments using 3xFLAG-tagged Znf2 as the bait. The FLAG tagged Znf2 was expressed under the control of the inducible *CTR4* promoter in the wild type or in the *brf1* $\Delta$  mutant background. We compared the relative abundance of precipitated genetic loci pulled down by the tagged Znf2 using qPCR.

Here we chose the locus of the filamentation marker gene *CFL1* as a proxy for Znf2 downstream targets<sup>23,27,46,47</sup>. We included six regions upstream of the transcription start site (TSS) of *CFL1*, one region spanning the TSS, one region shortly downstream of the TSS, and one region within the ORF (Supplementary Fig. 7a). We found that Znf2 strongly binds to the *CFL1* promoter. Interestingly, when we tested the *ZNF2* locus by ChIP-qPCR, we also found higher abundance of the promoter region than its ORF region (Supplementary Fig. 7b). The data suggest that Znf2 associates with its own promoter and it likely autoregulates itself. Autoregulation is not uncommon for transcription factors. Interestingly, the association of Znf2 to the promoter regions of *CFL1* and *ZNF2* decreased 2-3 folds in the absence of Brf1 (Fig. 5a, Supplementary Fig. 7). The result supports the idea that the SWI/SNF complex helps Znf2 associate with its downstream targets, including *ZNF2* itself. We further investigated the requirement of Brf1 for Znf2's binding to its targets by analyzing the sequencing results of the same ChIP samples. A total of 361 potential Znf2-binding regions were identified (Fig. 5b, Supplementary Table 5). Consistent with our ChIP-qPCR results (Fig. 5a), the Znf2's binding to most of its downstream sites was dampened upon the disruption of Brf1, including *ZNF2* and *CFL1* promoter regions (Fig. 5b). The finding is consistent with our earlier transcriptome data showing that *BRF1* is required for *ZNF2* transcription induction and that *brf1*Δ cells share more than 60% of the differentially expressed genes with *znf2*Δ cells when cultured under filamentation-inducing condition (Fig. 4d). Thus, Brf1, a subunit of the chromatin-remodeling SWI/SNF complex, is required for full association of the transcription factor Znf2 with its downstream targets.

To test if Brf1 is affecting the cell differentiation through chromatin remodeling of *ZNF2* and Znf2 target regions, we employed the assay for transposase-accessible chromatin followed by next generation sequencing (ATAC-seq)<sup>48,49</sup> and compared genetic regions with open

chromatin structures in wild type, grown on V8 or YPD, as well as in the *znf2Δ*, *snf5Δ*, and *brf1Δ* strains cultured on V8. We included the *brf1Δ/BRF1<sup>oc</sup>* strain in our analyses as an additional control. As expected, accessible chromatin fell in the gene promoter regions, with expressed genes having a higher level of accessibility based on the relative enrichment of ATAC-seq reads (Fig. 5c). Globally, chromatin accessibility was similar in all strains tested (Fig. 5d). When we examined the chromatin accessibility levels of the 361 regions that Znf2 potentially binds to based on the Znf2 ChIP data (Fig. 5b), we noticed a significant reduction in chromatin accessibility in the *brf1Δ* and the *snf5Δ* mutant strains across most of the regions (Fig. 5e). In fact, upon deletion of *BRF1* or *SNF5*, the chromatin accessibility of the 361 regions in the cells cultured under the filamentation-inducing condition looked alike the wild-type cells grown under the filamentation-suppression condition (Fig. 5e). Ten of the Brf1-dependent ATAC-seq peaks overlapped with genes that are up-regulated when cells are cultured in hyphal-promoting growth conditions based on the transcriptome data. RNA-seq, ChIP-seq, and ATAC-seq reads for three of these genes, along with a control gene CNA07690 that does not require Brf1 for its open chromatin are shown in Fig. 5f. Most noticeably, the promoter region of the filamentation marker gene *CFL1* is the most significantly differentially accessible region ( $\log_{10}[\text{likelihood}] = 29.678$ ) (Fig. 5x). *CFL1* is one of the highest induced genes controlled by Znf2<sup>24</sup>. Disruption of either Brf1, Snf5, or Znf2 abolished the chromatin accessibility of the *CFL1* promoter (ATAC), where Znf2 binds to (ChIP) (Fig. 5b, 5f). Accordingly, the transcript level of *CFL1* was almost undetectably low when *BRF1* or *ZNF2* was deleted. The overexpression of *BRF1* in the *brf1Δ* mutant restored chromatin accessibility of the *CFL1* promoter and its transcript level (Fig. 5f). Similarly, we found that the *ZNF2* promoter region became inaccessible in the *brf1Δ* and the *znf2Δ* mutant. Collectively, these data support the interdependence between the transcription

factor Znf2 and the SWI/SNF complex in opening up chromatin to facilitate transcription of filamentation genes.

## Discussion

Chromatin remodeling plays critical roles in cellular differentiation in eukaryotes. The model ascomycetous yeast species *S. cerevisiae* and *S. pombe* have offered a relatively simple system for mechanistic studies in this research area. Basidiomycetous fungi resemble more of the higher eukaryotes in terms of genome structures, epigenetic regulation, and transcriptome complexity, but research on chromatin remodeling in this major phylum of the fungal kingdom is spotty.

In this study, we identified and characterized, for the first time, a basidiomycete specific factor Brf1 that serves as a critical subunit in the SWI/SNF complex. We demonstrated that Brf1, together with the conserved and previously known subunit Snf5 of the SWI/SNF complex, are essential for hyphal growth and sexual development in the basidiomycete *C. neoformans*. This complex remodels the chromatin structure of the promoter regions of filamentation genes to make them accessible for transcription (Fig. 5g). Brf1 is vital not only for transcriptional induction of *ZNF2*, but also full association of Znf2 protein to the promoters of its downstream targets like *CFL1* and also the *ZNF2* gene itself. Our findings are consistent with published literature in other organisms, in which the SWI/SNF complex contributes to the DNA binding of the transcription factor <sup>50,51</sup>. The SWI/SNF complex has been shown being targeted to specific genetic loci by sequence-specific transcription factors and acetylation of histone tails <sup>50,52,53</sup>. In the ascomycetous fungus *C. albicans*, the transcription factor Efg1 recruits the histone acetyltransferase complex NuA4 to the promoters of hypha-associated genes, allowing in turn the recruitment of the SWI/SNF complex to activate their transcription to drive morphological

transition<sup>54</sup>. We reason that Znf2 may recruit the SWI/SNF complex to its target sites given that deletion of *ZNF2* caused the loss of open chromatin at the *CFL1* promoter region (Fig. 5b-5f). That said, we could not establish direct physical interaction between Znf2 and the SWI/SNF complex via Co-IP experiment after multiple attempts. Although we cannot rule out the possibility of direct physical interaction between Znf2 and the SWI/SNF complex, as we have not test the interaction of Znf2 with all the individual subunits in this complex, it is possible the interaction is too weak or transient to be captured by our assay, or histone modifications or the modification enzymes are involved. Several subunits in the SWI/SNF complex possess domains that recognize histone modifications, such as bromodomains for histone acetylation<sup>55</sup>. How exactly the SWI/SNF complex works with Znf2 in *C. neoformans* to control differentiation warrants further investigation.

Our findings also revealed striking differences in the two complexes (SWI/SNF and RSC) within the SWI/SNF family in Ascomycota and Basidiomycota. In *Saccharomyces* and *Schizosaccharomyces* species, most subunits in the RSC complex are essential for growth, including the catalytic ATPase subunit Snf2 (or SpSnf22), Sfh1, and Rsc9<sup>44,45,56</sup> (Table 2). By contrast, deletion of the shared ATPase catalytic subunit Snf2 is not lethal in *C. neoformans*. Consistently, deletion of both *SNF5* (SWI/SNF-specific) and *SFH1* (RSC-specific) together slowed growth but did not cause lethality (Fig. 3g). Thus, either the SWI/SNF complex, the RSC complexes, or both combined, are likely not essential for growth in this basidiomycete. Hence, despite conserved compositions among different lineages of eukaryotes, the biological function of the RSC complex differs substantially in different species. Comparative functional analyses of the RSC complex among evolutionarily diverse species, therefore, provides a unique vantage point to understand its biology.



All SWI/SNF complexes, either in yeasts or humans, have a subunit with a conserved Snf5 domain. The majority of fungal species examined carry two proteins bearing a Snf5 domain (Pfam domain ID PF04855), presumably one acting as the Snf5 subunit in the SWI/SNF complex and one acting as the Sfh1 subunit in the RSC complex (Fig. 3c, Supplementary Table 6). Based on primary protein sequences, Snf5 proteins in Ascomycota separate clearly into two clades, Snf5 and Sfh1 (Fig. 3c). *C. neoformans* genome also encodes two proteins with a Snf5 domain: *SNF5* and *SFH1* (Fig. 3c). Surprisingly, both Snf5-containing proteins in *C. neoformans* and in other basidiomycetes cluster closely with the Sfh1 clade in ascomycetes (Fig. 3c). The SWI/SNF complex assemble in an ordered modular fashion and Snf5 acts as a scaffold protein<sup>5,42,43</sup>. In *S. cerevisiae*, Snf5 and Swi1 (the ARID containing protein) are likely in two different modules of the complex<sup>5,42,43</sup> given the phenotypical differences of the *snf5* and *swi1* mutants<sup>57</sup>. In *Cryptococcus*, however, mutants of Snf5 and Brf1 have nearly identical phenotypes. It is unclear if the difference, or the lack thereof, between mutations in Snf5 and the ARID domain protein in different organisms reflects the difference in their modular assembly. Interestingly, Snf5 proteins in basidiomycetes (*C. neoformans*: 1784 aa, *U. maydis*: 2080 aa) are much larger in size comparing to the Snf5 proteins in ascomycetes or Snf5 in humans (*S. cerevisiae*: 905 aa, *S. pombe*: 632aa, or humans: 385aa) (Fig. 3c). The much larger Snf5 proteins in basidiomycetes with two internal repeats near the N-terminus (Supplementary Fig. 5b) could potentially increase binding surface area and consequently help recruit and assemble the SWI/SNF complex.

The SWI/SNF family employs Snf2 as the ATPase catalytic subunit. In the ascomycetous fungi like *S. cerevisiae* and *S. pombe*, the ATPase subunit is complex-specific: the SWI/SNF and the RSC complexes use different ATPase subunits. In comparison, we showed here that the ATPase subunit Snf2 was shared between the SWI/SNF and the RSC complexes in *C.*

*neoformans*. Snf2 proteins in SWI/SNF family complexes are characterized by the presence of a HSA domain and a BROMO domain flanking the ATPase domain (the DEXDc and HELICc regions) (Supplementary Fig. 5c) <sup>4</sup>. However, a search for the HSA domain (PF07529) and the BROMO domain (PF00439) among dozens of fungal species belonging to three different major phyla in the fungal kingdom revealed that some fungi, including ascomycete *S. cerevisiae* and zygomycete *Mucor circinelloides*, have two distinct Snf2 family ATPases, presumably one for the SWI/SNF complex and one for the RSC complex. Some other fungi, including ascomycete *Aspergillus nidulans* and basidiomycete *C. neoformans*, however, have only one Snf2 ATPase, presumably shared by both the SWI/SNF complex and the RSC complex (Table 2 and Supplementary Table 7). Intriguingly, in *Drosophila melanogaster*, the BAP (SNF/SWI) complex and the PBAP (RSC) complex share the same catalytic ATPase subunit (BRM). Human BAF (mSNF/SWI) complex and PBAF (mRSC) complex can share the same ATPase BRG-1 subunit or use different ATPases (hBRM and BRG-1) <sup>4</sup>. Thus, the ATPase could be shared by or be unique to the SWI/SNF and the RSC complexes. The copy number variation of Snf2 in different organisms might have driven such divergence independent of the evolutionary distance of the species.

In conclusion, we identified and characterized the basidiomycete-specific subunit of SWI/SNF chromatin remodeling complex and revealed the major differences in the composition and biology of this complex between ascomycetes and basidiomycetes. Given the universal importance of the SWI/SNF complex in cellular differentiation in eukaryotes, our findings provide an important platform for comparative functional analyses of this complex in diverse eukaryotic lineages.

## Methods and Materials

### Strains and growth conditions

Strains used in this study were listed in Supplementary Table 8. All strains were stored in 15% glycerol at -80°C and were freshly streaked out onto YPD media (2% peptone, 1% yeast extract, 2% glucose, 2% agar, gram/liter) for each experiment. *C. neoformans* cells were cultured in YPD medium unless stated otherwise. For some assays, the defined minimal YNB medium (6.7 gram/liter nitrogen base w/o amino acids, 2% agar, 2% glucose) was used as specified in the figure legends. For mating or filamentation assays, V8 juice agar medium (1 liter medium, 50mL V8 original juice, 0.5g KH<sub>2</sub>PO<sub>4</sub>, 4% agar, pH 5.0 or 7.0) was used.

### *Agrobacterium*-mediated T-DNA insertional mutagenesis

The *Agrobacterium*-mediated cryptococcal transformation was carried out as described previously<sup>58</sup>. Briefly, engineered *Agrobacterium* cells that carry a Ti plasmid with the hygromycin resistant marker were co-incubated with the recipient *Cryptococcus* cells (P<sub>CTR4-2-mCherryZNF2-NEO</sub>, *znf2::NAT*) on the induction medium at 22°C for 2 days. The *Cryptococcus*-*Agrobacterium* cocultures were collected, diluted, and transferred onto the selection medium (with 50μM of BCS) that would induce *ZNF2* expression. Cryptococcal transformants were cultured on this selective medium for 3-5 days at 22°C in dark. Approximately 500 colonies grew on each selective plate and about 88,000 transformants were screened for smooth yeast colonies.

### Insertion site identification in the selected AMT mutants

Genomic DNA of the selected mutants was prepared with the CTAB DNA extraction protocol as described previously<sup>59</sup>. The genomic DNA for each individual strain was then

pooled together with equal-molar concentration and the pooled DNA was sent for sequencing (Illumina MiSeq, 250bp x250bp, paired end reads, BioProject accession number: PRJNA534125, SRA: SRR8943502). The insertion sites in the mutants were identified via the AIMHII program developed by Esher et.al with default parameters <sup>29</sup>.

### **Gene deletion, gene overexpression, and protein tagging**

The gene knockout constructs were constructed by fusing 5' and 3' homologous arms (each about 1kb) with dominant drug marker via overlap PCRs as previously described <sup>60</sup>. The constructs were introduced into cryptococcal cells by biolistic transformation or by TRACE (Transient CRISPR-Cas9 Coupled with Electroporation) as described previously <sup>61,62</sup>. Single guide RNAs were designed with Eukaryotic Pathogen CRISPR guide RNA/DNA Design Tool (<http://grna.ctegd.uga.edu/>) for TRACE.

To generate gene overexpression strains, the ORF amplicon with added *FseI* and *AsiSI* cutting sites was digested and ligated into the vectors where the ORF was placed downstream of the *GPD1*, the *TEF1*, or the *CTR4-2* promoter, as we described previously <sup>46</sup>. A fluorescent tag (tdTomato or mNeonGreen) or a CBP (calmodulin-binding peptide)-2xFLAG tag was placed immediately in frame downstream of the *AsiSI* cutting site, which allows in frame tagging of the protein at the C-terminus. *ZNF2* ORF was ligated into a vector where a 3xFLAG tag was downstream of the *CTR4* promoter to allow tagging at the N-terminus. The functionality of the tagged proteins was confirmed by their ability to rescue/restore the phenotypes in the corresponding gene deletion strains. All constructed plasmids used in this study are listed in Supplementary Table 9. All the primers used for constructing or confirming gene deletion, gene overexpression, or protein tagging are listed in Supplementary Table 10.

### **Phenotypic assays**

For phenotypic analyses, cells of the tested strains were cultured in YPD broth overnight at 30°C with shaking at 230rpm. Cells were collected by centrifugation, washed twice with sterile water, and then suspended with water to the same optical density at 600nm ( $OD_{600}=3$ ). Three microliters of cell suspension and 10x serial dilutions were spotted onto YPD agar medium or YPD with the supplement of Congo Red (0.3-0.5%) and were incubated at 30°C or 37°C for 1-2 days. To test carbon source utilization, glucose in the YNB medium was replaced by either sucrose or raffinose (final concentration: 2%).

To test the ability of these strains to undergo self-filamentation, 3μL of cells with  $OD_{600}=3$  were spotted onto V8 or V8+500μM  $Cu^{2+}$  medium and incubated at 22°C in dark for 2-10 days. To examine filamentation during bisexual mating, equal number of cells of compatible mating types were mixed, spotted onto V8 agar medium (pH 5 for mating assay of serotype A strains, and pH 7 for mating assay of serotype D strains) and incubated at 22°C in dark for 1-7 days.

For strains that use the *CTR4-2* inducible promoter to drive the expression of the examined genes, cells were maintained on YPD medium with 50μM  $CuSO_4$  to suppress the gene expression. To induce the gene expression, the copper chelator BCS was supplemented to the medium with the final concentration of 200μM in YPD and 50μM in V8.

### **Cell growth assay**

Cryptococcal cells from overnight culture in YPD broth were centrifuged, washed twice with water, and resuspended in water. The cell concentration was normalized to the optical density of  $OD_{600}=1$ . Fifty microliters of each strain were added to 950μL of the indicated liquid medium in 24 well plate (#353047, Falcon). The growth of the cryptococcal strains (each with 2 replicates) were monitored at  $OD_{600}$  hourly in the Cytation 5 multi-mode reader (BioTek

Instrument) with double orbit shaking (at 365 cpm) at 30°C. The reads for each well were fitted to a preloaded logistic model ( $y = \frac{A1-A2}{1+}$ ) in Origin software and the curated reads were simulated and graphed in the GraphPad Prism software.

### **Mating, genetic crosses, and cell fusion assays**

Strains of  $\alpha$  and **a** mating partners were crossed on V8 juice agar medium (pH 5 or 7) and incubated at 22°C in dark for 2-3 weeks until adequate spores were produced. Spores were micro-manipulated using a dissecting microscope. The mating type of the germinated spores was determined by successful mating with either JEC20**a** or JEC21 $\alpha$  reference strain. Genetic linkage between the presence of the drug marker and the observed mutant phenotype was established by analyzing the dissected spores as we described previously<sup>63</sup>. For each genetic linkage assay, approximately 32 viable spores were analyzed, which gave a 97% confidence level of our analysis (*confidence* = 100% –).

To analyze the genetic relationship between *Znf2* and *Brf1*, we crossed *brf1::NAT/ P<sub>TEF1</sub>-BRF1-CBP-2xFLAG-NEO* ( $\alpha$ ) with *znf2::NAT/ P<sub>CTR4-2</sub>-3xFLAG-ZNF2-NEO* (**a**) and examined the segregation of the genotypes (by diagnostic PCRs) and phenotypes in the progeny (Figure 4A).

To determine the cell-cell fusion efficiency, mutants of the mating type  $\alpha$  (*znf2::NAT*; *mat2::NAT*; *brf1::NAT*; and *snf5::NAT*) and the control strain (*prf1::NAT*) were collected and suspended in water to the same optical density (the calculated OD<sub>600</sub>=0.3 x 10). Each mutant with NAT<sup>R</sup> was mixed with the mating type **a** tester strain with NEO<sup>R</sup> marker (strain YSB133) with equal volume<sup>64</sup>. Three microliters of cell mixture were spotted onto V8 medium and incubated at 22°C in dark for 24 hours before they were collected, plated (in serial dilution) onto YPD+NEO+NAT agar medium, and incubated at 30°C for 3-5 days to select for fusion products.

## Databases and online tools

We used FungiDB (<http://fungidb.org/fungidb/>) to acquire the gene/protein sequences or the normalized FPKM data of *C. neoformans* H99 genes, *S. cerevisiae* genes and genes in other fungi. Clustal Omega (<https://www.ebi.ac.uk/Tools/msa/clustalo/>) was used for protein multiple sequence alignment and phylogenetic tree analysis. The gene tree of *BRF1* (*CNA02310*) was retrieved from the Ensembl Fungi database (<https://fungi.ensembl.org/index.html>). Simple modular architecture research tool (SMART, <http://smart.embl-heidelberg.de/>) online server was used to analyze the domain layouts for proteins. IBS online illustrator tool (<http://ibs.biocuckoo.org/online.php>) was used to illustrate all the protein domain layouts <sup>65</sup>.

## RNA extraction and RNA-seq

RNAs were extracted from cells cultured on V8 medium at 22°C in dark for 24 hours and prepared for sequencing as previously described <sup>22,23,66</sup>. HiSeq Rapid 175bp pair-end RNA sequencing was performed at the Georgia genome sequencing facility. The low-quality bases of the raw reads were trimmed with a custom perl script as published before <sup>66</sup>. Tophat2 was used to map the processed reads to the reference genome. The program HTSeq-count and DESeq2 were used to count the reads and identify the differentially expressed genes. The raw sequencing reads were deposited at NCBI with the BioProject accession number PRJNA534125, and SRA file numbers from SRR8947060 to SRR8947075.

## Co-Immunoprecipitation

Strains with tagged proteins were cultured in 15mL YPD media overnight, washed twice with cold water, flash frozen in liquid nitrogen, and lyophilized. Lyophilized cells were broken into fine powder with silica beads in a Bullet Blender Blue<sup>®</sup> (Next Advance) without buffer for 5 cycles (60s maximum blending followed by 90s chilling on ice) and then with 1mL of lysis

buffer (50mM Tris HCl pH 8.0, 150 mM NaCl, 1mM EDTA, 5mM MgCl<sub>2</sub>, 1mM DTT, 10% glycerol, 0.5mM PMSF and cocktail protease inhibitors (#A32963, ThermoFisher)) for another 5 cycles. Cell lysates were centrifuged at x500g at 4°C for 5mins. The supernatant was collected and centrifuged again at x10000g at 4°C for 20 minutes. The supernatant was then incubated with pre-washed anti-FLAG M2 agarose beads (#F2426, Sigma) at 4°C on rotator overnight. For immunoprecipitation with mCherry or mNeonGreen tagged proteins, RFP-Trap®\_MA or mNeonGreen-Trap\_MA beads from Chromotek (Germany) were used following the manufacturer's instructions.

After washing, immunoprecipitated protein samples were released from beads in the 2xSDS loading buffer (120mM Tris-HCl pH6.8, 20% Glycerol, 4% SDS, 0.04% bromophenol blue, and 10% β-mercaptoethanol) by boiling for 10 minutes. Co-IP protein samples were then loaded into pre-casted 4-12% SurePAGE™ Bis-Tris Gel (GeneScript), ran for 5minutes and visualized by Coomassie Blue staining. The total pulled down protein samples were excised from the gel and sent to the proteomics and mass spectrometry facility (<https://pams.uga.edu/>) at the University of Georgia for identification.

### **Chromatin immunoprecipitation, ChIP-qPCR, and ChIP-seq**

FLAG tagged Znf2 strains (strain JL653 and JL665) (initial OD<sub>600</sub>=0.2) were incubated in 50mL YPD+BCS broth at 30°C until the optical density reached OD<sub>600</sub>=1. Cells were then fixed in the medium with formaldehyde at 1% final concentration at 22°C for 15 minutes with occasional swirling. Glycine with the final concentration of 0.125M was added to quench the crosslinking at 22°C for 5 minutes. The cells were then washed twice with cold sterile water and lyophilized. Lyophilized cells were broken as described above for Co-IP experiment with a different lysis buffer (50mM HEPES-KOH pH 7.5, 140mM NaCl, 1mM EDTA, 1% Triton X-



100, 0.1% NaDOC, 1mM of PMSF and proteinase inhibitor cocktail). The following steps were similar to what has been described previously<sup>47,67-69</sup> and Briefly, the cell lysates were centrifuged at 8000 rpm at 4°C for 10 mins to enrich nuclei. The released nuclei were resuspended in 350uL of lysis buffer. The nuclear suspensions were sheared by sonication in a Diagenode Bioruptor™ for 25 cycles at 4°C (30s on, 30s off; cycle numbers varied). Protein-chromatin complex were recovered from the supernatant after centrifugation at 14000 rpm at 4°C for 10 mins and the volume was brought to 1mL. 50uL of each protein-chromatin suspension was saved as “Input DNA”. The rest of the sample was added to 30uL anti-FLAG M2 monoclonal antibodies on magnetic beads (#M8823, Sigma) to precipitate the FLAG tagged protein. After incubation with antibodies at 4°C overnight, the beads were washed twice with 1mL ChIP lysis buffer, once in 1mL ChIP lysis buffer containing 0.5M NaCl, once in 1mL ChIP wash buffer (10mM Tris-HCl, pH 8.0; 0.25M LiCl; 0.5% NP-40; 0.5% NaDOC; 1mM EDTA), and once in 1mL TE (10mM Tris-HCl, pH 8.0; 1mM EDTA), all at 4°C. The immunoprecipitated Znf2-3xFLAG was eluted twice by adding 200 µL of TES buffer (10mM Tris-HCl, pH 8.0; 10mM EDTA; 1% SDS) and incubated at 75°C for 15 min before the supernatant was transferred to a new tube. 20µL of 5M NaCl was added to each sample to de-crosslink at 65°C for 4 hours. 350µL of TES was added to each “Input DNA” sample before adding 20µL of 5M NaCl to reverse formaldehyde crosslinks. 1µL of RNase A (10µg/µL) was added and the sample was incubated at 37°C for 30 minutes. 4µL of Proteinase K (20µg/µL) was then added to each sample and incubated at 45°C for at least one hour to digest all the proteins. Eventually, 2µL of glycogen (molecular level, 20mg/mL) was added to chromatin DNA samples. Ethanol of 2.5 volumes was added to each sample to precipitate the glycogen tangled DNA. Precipitated DNA sample was then suspended in 80uL of nuclease free water.

For ChIP-qPCR, 3μL of 5 times diluted DNA sample and 1μL each from two primers (50μM) were mixed with 5μL of SYBR Green 2x qPCR premix reagents (Invitrogen). The qPCR reactions were carried out in a Realplex system (Eppendorf) with technical duplicates. The % Input is calculated as  $2^{-\Delta Ct [\text{normalized ChIP}]}$  where  $\Delta Ct [\text{normalized ChIP}] = Ct [\text{ChIP}] - (Ct [\text{Input}] - \log_2(\text{Input Dilution Factor}))$  as described previously<sup>69</sup>.

The same ChIP samples for qPCRs were sent for DNA sequencing at Georgia Genomics Facility (UGA) on an Illumina NextSeq500 platform. Input from ChIP-seq experiments in WT strains was used as background control for all samples. Differential peaks called from DiffBind were annotated using ChipSeeker<sup>70,71</sup>. ChIP-seq have been submitted to the GEO database. The BioProject accession number PRJNA534125.

### **ATAC-seq and data analysis**

*C. neoformans* cells were cultured in 15mL YPD liquid media at 30°C overnight or on V8 medium (pH 7) at 22°C in dark for 24 hours. Cells were collected and washed 2 times with cold sterile water. 500μL of cold lysis buffer (15mM Tris pH 7.5; 2mM EDTA; 0.5mM spermine; 80mM KCl; 20mM NaCl; 15mM (or 0.1% v/v) β-me; 0.3% TritonX-100) and 200μL (~1 PCR tube) of acid washed glass beads (0.5mm, #9831 RPI) were added to the cell pellet of about 10<sup>8</sup> cells in 1.7mL Eppendorf tubes. Cells were broken in a cell disruptor (Scientific Industries, Inc., SI-D238) at 4°C with maximum speed for 2 minutes and then spun down at x50g at 4°C for 2 minutes to remove the glass beads. Supernatant was transferred into a new Eppendorf tube and spun at x200g for another 2 minutes to remove most of the broken cells and debris. The enrichment of nuclei in the supernatant was verified by microscopic observation and the nuclei was collected for making the ATAC-seq library.

ATAC-seq libraries were generated as described previously <sup>72</sup>. Briefly, about 0.2 million nuclei were incubated with Tn5 transposase pre-loaded with Illumina sequencing adapters at 37°C for 30 minutes followed by purification of the DNA fragments by a reaction cleanup kit (Qiagen, # 28204). Libraries were PCR amplified for 10 cycles with Phusion polymerase (ThermoFisher Scientific, # F530L). Sequencing libraries were then cleaned with magnetic beads to remove free adapters and primer dimers (Beckman Coulter, #A63880). Libraries were mixed in equimolar ratios and pair-end sequenced by the Georgia Genomics Facility (UGA) on an Illumina NextSeq500 platform.

ATAC-seq reads were filtered for low-quality and short reads with Trim Galore (<https://github.com/FelixKrueger/TrimGalore>). Duplicate reads were removed using Picard MarkDuplicates tool (<http://broadinstitute.github.io/picard/>). Reads were aligned to the XL280 reference genome with HISAT2 using non-spliced alignment and a maximum fragment length of 2000 bp. Peak calling was performed with MACS2 using a q-value of 0.01, extension size of 73, and shifting reads by 37 bp to center on the insertion site. MACS2 was also used to call differential peaks <sup>73</sup>. Differential peak files were first sorted by log10 likelihood and then combined into a single file. Heatmaps were generated using deepTools with the differential peaks <sup>74</sup>. Heatmap matrices were scaled appropriately to WT cells on V8 medium to bring all samples to a comparable scale for analysis. Differential peaks from ATAC-seq were compared to genes identified as being up-regulated in WT V8 from RNA-seq analysis using BEDTools <sup>75</sup> intersect to isolate these genes from the XL280 annotation file for determining genes associated with differential peaks. ATAC-seq have been submitted to the GEO database . The BioProject accession number PRJNA534125.

## Data Accessibility

All data supporting the findings of the current study are available within the article and its Supplementary Information files or from the corresponding author upon request. All RNA-seq, ATAC-seq, ChIP-seq and DNA-seq data has been deposited in NCBI under the BioProject accession number PRJNA534125.

## Funding

This work was supported by National Institutes of Health (R01AI140719 to XL and R01GM132644 to ZL), the American Cancer Society (RSG-14-184-01-DMC to ZL), NSF GRFP (NSF# 1443117 to AF), and the University of Georgia (startup fund to XL). Dr. Lin holds an Investigator Award in the Pathogenesis of Infectious Disease from the Burroughs Wellcome Fund (1012445). The funders had no role in study design, data collection and interpretation, or the decision to submit the work for publication.

## Acknowledgement

We thank Dr. Karl Lehtreck from Department of Cellular Biology at UGA for the kind gift of the mNeonGreen plasmid, Dr. Chau-wen Chou at the UGA proteomics and mass spectrometry facility (<https://pams.uga.edu/>) for the mass spectrometry analysis of our Co-IP samples, Brigitte Hofmeister and Dr. Bob Schmitz in Department of Genetics of UGA for the generous help on ATAC-seq experiments, Dr. Fanglin Zheng from our lab for the yeast-two-hybrid experiments, and all Lin lab members for their helpful comments.

## References

- 1 Clapier, C. R., Iwasa, J., Cairns, B. R. & Peterson, C. L. Mechanisms of action and regulation of ATP-dependent chromatin-remodelling complexes. *Nat Rev Mol Cell Bio* **18**, 407-422, doi:10.1038/nrm.2017.26 (2017).

- 2 Kadoch, C. *et al.* Proteomic and bioinformatic analysis of mammalian SWI/SNF complexes identifies extensive roles in human malignancy. *Nat Genet* **45**, 592-601, doi:10.1038/ng.2628 (2013).
- 3 Mohrmann, L. & Verrijzer, C. P. Composition and functional specificity of SWI2/SNF2 class chromatin remodeling complexes. *Biochim Biophys Acta* **1681**, 59-73, doi:10.1016/j.bbaexp.2004.10.005 (2005).
- 4 Tang, L., Nogales, E. & Ciferri, C. Structure and function of SWI/SNF chromatin remodeling complexes and mechanistic implications for transcription. *Prog Biophys Mol Biol* **102**, 122-128, doi:10.1016/j.pbiomolbio.2010.05.001 (2010).
- 5 Mashtalir, N. *et al.* Modular Organization and Assembly of SWI/SNF Family Chromatin Remodeling Complexes. *Cell* **175**, 1272-1288 e1220, doi:10.1016/j.cell.2018.09.032 (2018).
- 6 Monahan, B. J. *et al.* Fission yeast SWI/SNF and RSC complexes show compositional and functional differences from budding yeast. *Nature Structural & Molecular Biology* **15**, 873-880, doi:10.1038/nsmb.1452 (2008).
- 7 Vignali, M., Hassan, A. H., Neely, K. E. & Workman, J. L. ATP-dependent chromatin-remodeling complexes. *Molecular and cellular biology* **20**, 1899-1910 (2000).
- 8 Wang, X. *et al.* Sex-induced silencing defends the genome of *Cryptococcus neoformans* via RNAi. *Genes Dev* **24**, 2566-2582, doi:10.1101/gad.1970910 (2010).
- 9 Feretzaki, M., Billmyre, R. B., Clancey, S. A., Wang, X. & Heitman, J. Gene Network Polymorphism Illuminates Loss and Retention of Novel RNAi Silencing Components in the *Cryptococcus* Pathogenic Species Complex. *PLoS genetics* **12**, e1005868, doi:10.1371/journal.pgen.1005868 (2016).

- 10 Loftus, B. J. *et al.* The genome of the basidiomycetous yeast and human pathogen *Cryptococcus neoformans*. *Science* **307**, 1321-1324, doi:10.1126/science.1103773 (2005).
- 11 Janbon, G. *et al.* Analysis of the genome and transcriptome of *Cryptococcus neoformans* var. *grubii* reveals complex RNA expression and microevolution leading to virulence attenuation. *PLoS genetics* **10**, e1004261, doi:10.1371/journal.pgen.1004261 (2014).
- 12 Catania, S. *et al.* Epigenetic maintenance of DNA methylation after evolutionary loss of the *de novo* methyltransferase. *bioRxiv*, 149385 (2017).
- 13 Zhao, Y., Lin, J., Fan, Y. & Lin, X. Life Cycle of *Cryptococcus neoformans*. *Annual review of microbiology* **73** (2019).
- 14 Velagapudi, R., Hsueh, Y. P., Geunes-Boyer, S., Wright, J. R. & Heitman, J. Spores as infectious propagules of *Cryptococcus neoformans*. *Infection and immunity* **77**, 4345-4355, doi:10.1128/IAI.00542-09 (2009).
- 15 Giles, S. S., Dagenais, T. R., Botts, M. R., Keller, N. P. & Hull, C. M. Elucidating the pathogenesis of spores from the human fungal pathogen *Cryptococcus neoformans*. *Infection and immunity* **77**, 3491-3500, doi:10.1128/IAI.00334-09 (2009).
- 16 Okagaki, L. H. & Nielsen, K. Titan cells confer protection from phagocytosis in *Cryptococcus neoformans* infections. *Eukaryotic cell* **11**, 820-826, doi:10.1128/EC.00121-12 (2012).
- 17 Zaragoza, O. & Nielsen, K. Titan cells in *Cryptococcus neoformans*: cells with a giant impact. *Current opinion in microbiology* **16**, 409-413, doi:10.1016/j.mib.2013.03.006 (2013).

- 18 Goldman, D. L., Fries, B. C., Franzot, S. P., Montella, L. & Casadevall, A. Phenotypic switching in the human pathogenic fungus *Cryptococcus neoformans* is associated with changes in virulence and pulmonary inflammatory response in rodents. *Proceedings of the National Academy of Sciences of the United States of America* **95**, 14967-14972 (1998).
- 19 Lin, X., Jackson, J. C., Feretzaki, M., Xue, C. & Heitman, J. Transcription factors Mat2 and Znf2 operate cellular circuits orchestrating opposite- and same-sex mating in *Cryptococcus neoformans*. *PLoS genetics* **6**, e1000953, doi:10.1371/journal.pgen.1000953 (2010).
- 20 Lin, J., Idnurm, A. & Lin, X. Morphology and its underlying genetic regulation impact the interaction between *Cryptococcus neoformans* and its hosts. *Med Mycol* **53**, 493-504, doi:10.1093/mmy/myv012 (2015).
- 21 Lin, X. R., Hull, C. M. & Heitman, J. Sexual reproduction between partners of the same mating type in *Cryptococcus neoformans*. *Nature* **434**, 1017-1021, doi:10.1038/nature03448 (2005).
- 22 Gyawali, R. *et al.* Pheromone independent unisexual development in *Cryptococcus neoformans*. *PLoS genetics* **13**, e1006772, doi:10.1371/journal.pgen.1006772 (2017).
- 23 Xu, X. *et al.* Glucosamine stimulates pheromone-independent dimorphic transition in *Cryptococcus neoformans* by promoting Crz1 nuclear translocation. *PLoS genetics* **13**, e1006982, doi:10.1371/journal.pgen.1006982 (2017).
- 24 Wang, L., Zhai, B. & Lin, X. The link between morphotype transition and virulence in *Cryptococcus neoformans*. *PLoS pathogens* **8**, e1002765, doi:10.1371/journal.ppat.1002765 (2012).

- 25 Neigeborn, L. & Carlson, M. Genes affecting the regulation of *SUC2* gene expression by glucose repression in *Saccharomyces cerevisiae*. *Genetics* **108**, 845-858 (1984).
- 26 Stern, M., Jensen, R. & Herskowitz, I. Five SWI genes are required for expression of the *HO* gene in yeast. *J Mol Biol* **178**, 853-868 (1984).
- 27 Chacko, N. *et al.* The lncRNA *RZE1* Controls Cryptococcal Morphological Transition. *PLoS genetics* **11**, e1005692, doi:10.1371/journal.pgen.1005692 (2015).
- 28 Walton, F. J., Idnurm, A. & Heitman, J. Novel gene functions required for melanization of the human pathogen *Cryptococcus neoformans*. *Molecular microbiology* **57**, 1381-1396, doi:10.1111/j.1365-2958.2005.04779.x (2005).
- 29 Esher, S. K., Granek, J. A. & Alspaugh, J. A. Rapid mapping of insertional mutations to probe cell wall regulation in *Cryptococcus neoformans*. *Fungal genetics and biology : FG & B* **82**, 9-21, doi:10.1016/j.fgb.2015.06.003 (2015).
- 30 Smith, R. L. & Johnson, A. D. Turning genes off by Ssn6-Tup1: a conserved system of transcriptional repression in eukaryotes. *Trends Biochem Sci* **25**, 325-330 (2000).
- 31 Mao, X. M., Cao, F., Nie, X. Y., Liu, H. P. & Chen, J. Y. The Swi/Snf chromatin remodeling complex is essential for hyphal development in *Candida albicans*. *Febs Lett* **580**, 2615-2622, doi:10.1016/j.febslet.2006.04.009 (2006).
- 32 Mao, X., Li, Y., Wang, H., Cao, F. & Chen, J. Antagonistic interplay of Swi1 and Tup1 on filamentous growth of *Candida albicans*. *FEMS microbiology letters* **285**, 233-241, doi:10.1111/j.1574-6968.2008.01236.x (2008).
- 33 Mao, X., Nie, X., Cao, F. & Chen, J. Functional analysis of ScSwi1 and CaSwi1 in invasive and pseudohyphal growth of *Saccharomyces cerevisiae*. *Acta Biochim Biophys Sin (Shanghai)* **41**, 594-602 (2009).



- 34 Ando, Y., Nakazawa, T., Oka, K., Nakahori, K. & Kamada, T. *Cc.snf5*, a gene encoding a putative component of the SWI/SNF chromatin remodeling complex, is essential for sexual development in the agaricomycete *Coprinopsis cinerea*. *Fungal genetics and biology : FG & B* **50**, 82-89, doi:10.1016/j.fgb.2012.09.010 (2013).
- 35 Nakazawa, T., Ando, Y., Hata, T. & Nakahori, K. A mutation in the *Cc.arp9* gene encoding a putative actin-related protein causes defects in fruiting initiation and asexual development in the agaricomycete *Coprinopsis cinerea*. *Current genetics* **62**, 565-574, doi:10.1007/s00294-015-0560-4 (2016).
- 36 Venkataramanan, S., Douglass, S., Galivanche, A. R. & Johnson, T. L. The chromatin remodeling complex Swi/Snf regulates splicing of meiotic transcripts in *Saccharomyces cerevisiae*. *Nucleic Acids Res* **45**, 7708-7721, doi:10.1093/nar/gkx373 (2017).
- 37 Breker, M., Gymrek, M. & Schuldiner, M. A novel single-cell screening platform reveals proteome plasticity during yeast stress responses. *J Cell Biol* **200**, 839-850, doi:10.1083/jcb.201301120 (2013).
- 38 Dallas, P. B. *et al.* The human SWI-SNF complex protein p270 is an ARID family member with non-sequence-specific DNA binding activity. *Molecular and cellular biology* **20**, 3137-3146, doi:Doi 10.1128/Mcb.20.9.3137-3146.2000 (2000).
- 39 Chandler, R. L. *et al.* ARID1a-DNA interactions are required for promoter occupancy by SWI/SNF. *Molecular and cellular biology* **33**, 265-280, doi:10.1128/MCB.01008-12 (2013).
- 40 Wilsker, D. *et al.* The DNA-binding properties of the ARID-containing subunits of yeast and mammalian SWI/SNF complexes. *Nucleic Acids Res* **32**, 1345-1353, doi:10.1093/nar/gkh277 (2004).

- 41 Kelliher, C. M., Leman, A. R., Sierra, C. S. & Haase, S. B. Investigating Conservation of the Cell-Cycle-Regulated Transcriptional Program in the Fungal Pathogen, *Cryptococcus neoformans*. *PLoS genetics* **12**, e1006453, doi:10.1371/journal.pgen.1006453 (2016).
- 42 Dutta, A. *et al.* Composition and Function of Mutant Swi/Snf Complexes. *Cell Rep* **18**, 2124-2134, doi:10.1016/j.celrep.2017.01.058 (2017).
- 43 Sen, P. *et al.* Loss of Snf5 Induces Formation of an Aberrant SWI/SNF Complex. *Cell Rep* **18**, 2135-2147, doi:10.1016/j.celrep.2017.02.017 (2017).
- 44 Cairns, B. R. *et al.* RSC, an essential, abundant chromatin-remodeling complex. *Cell* **87**, 1249-1260, doi:Doi 10.1016/S0092-8674(00)81820-6 (1996).
- 45 Cao, Y. X., Cairns, B. R., Kornberg, R. D. & Laurent, B. C. Sfh1p, a component of a novel chromatin-remodeling complex, is required for cell cycle progression. *Molecular and cellular biology* **17**, 3323-3334, doi:Doi 10.1128/Mcb.17.6.3323 (1997).
- 46 Wang, L. *et al.* Morphotype transition and sexual reproduction are genetically associated in a ubiquitous environmental pathogen. *PLoS pathogens* **10**, e1004185, doi:10.1371/journal.ppat.1004185 (2014).
- 47 Tian, X. Y. *et al.* *Cryptococcus neoformans* sexual reproduction is controlled by a quorum sensing peptide. *Nat Microbiol* **3**, 698-707, doi:10.1038/s41564-018-0160-4 (2018).
- 48 Buenrostro, J. D., Wu, B., Chang, H. Y. & Greenleaf, W. J. ATAC-seq: A Method for Assaying Chromatin Accessibility Genome-Wide. *Curr Protoc Mol Biol* **109**, 21 29 21-29, doi:10.1002/0471142727.mb2129s109 (2015).
- 49 Buenrostro, J. D., Giresi, P. G., Zaba, L. C., Chang, H. Y. & Greenleaf, W. J. Transposition of native chromatin for fast and sensitive epigenomic profiling of open

- chromatin, DNA-binding proteins and nucleosome position. *Nat Methods* **10**, 1213-1218, doi:10.1038/nmeth.2688 (2013).
- 50 Burns, L. G. & Peterson, C. L. The yeast SWI-SNF complex facilitates binding of a transcriptional activator to nucleosomal sites *in vivo*. *Molecular and cellular biology* **17**, 4811-4819 (1997).
- 51 Wallberg, A. E. *et al.* Recruitment of the SWI-SNF chromatin remodeling complex as a mechanism of gene activation by the glucocorticoid receptor tau 1 activation domain. *Molecular and cellular biology* **20**, 2004-2013, doi:Doi 10.1128/Mcb.20.6.2004-2013.2000 (2000).
- 52 Kim, J. H., Saraf, A., Florens, L., Washburn, M. & Workman, J. L. Gcn5 regulates the dissociation of SWI/SNF from chromatin by acetylation of Swi2/Snf2. *Genes Dev* **24**, 2766-2771, doi:10.1101/gad.1979710 (2010).
- 53 Neely, K. E., Hassan, A. H., Brown, C. E., Howe, L. & Workman, J. L. Transcription activator interactions with multiple SWI/SNF subunits. *Molecular and cellular biology* **22**, 1615-1625 (2002).
- 54 Lu, Y. *et al.* Efg1-mediated recruitment of NuA4 to promoters is required for hypha-specific Swi/Snf binding and activation in *Candida albicans*. *Molecular biology of the cell* **19**, 4260-4272, doi:10.1091/mbc.E08-02-0173 (2008).
- 55 Yun, M., Wu, J., Workman, J. L. & Li, B. Readers of histone modifications. *Cell Res* **21**, 564-578, doi:10.1038/cr.2011.42 (2011).
- 56 Monahan, B. J. *et al.* Fission yeast SWI/SNF and RSC complexes show compositional and functional differences from budding yeast. *Nat Struct Mol Biol* **15**, 873-880, doi:10.1038/nsmb.1452 (2008).

- 57 Giaever, G. *et al.* Functional profiling of the *Saccharomyces cerevisiae* genome. *Nature* **418**, 387-391, doi:10.1038/nature00935 (2002).
- 58 Idnurm, A., Reedy, J. L., Nussbaum, J. C. & Heitman, J. *Cryptococcus neoformans* virulence gene discovery through insertional mutagenesis. *Eukaryotic cell* **3**, 420-429 (2004).
- 59 Mondon, P. *et al.* Heteroresistance to fluconazole and voriconazole in *Cryptococcus neoformans*. *Antimicrobial agents and chemotherapy* **43**, 1856-1861 (1999).
- 60 Lin, X., Chacko, N., Wang, L. & Pavuluri, Y. Generation of stable mutants and targeted gene deletion strains in *Cryptococcus neoformans* through electroporation. *Med Mycol* **53**, 225-234, doi:10.1093/mmy/myu083 (2015).
- 61 Toffaletti, D. L., Rude, T. H., Johnston, S. A., Durack, D. T. & Perfect, J. R. Gene transfer in *Cryptococcus neoformans* by use of biolistic delivery of DNA. *Journal of bacteriology* **175**, 1405-1411 (1993).
- 62 Fan, Y. & Lin, X. Multiple Applications of a Transient CRISPR-Cas9 Coupled with Electroporation (TRACE) System in the *Cryptococcus neoformans* Species Complex. *Genetics* **208**, 1357-1372, doi:10.1534/genetics.117.300656 (2018).
- 63 Zhai, B. *et al.* Congenic strains of the filamentous form of *Cryptococcus neoformans* for studies of fungal morphogenesis and virulence. *Infection and immunity* **81**, 2626-2637, doi:10.1128/IAI.00259-13 (2013).
- 64 Bahn, Y. S., Cox, G. M., Perfect, J. R. & Heitman, J. Carbonic anhydrase and CO<sub>2</sub> sensing during *Cryptococcus neoformans* growth, differentiation, and virulence. *Curr Biol* **15**, 2013-2020, doi:10.1016/j.cub.2005.09.047 (2005).

- 65 Liu, W. *et al.* IBS: an illustrator for the presentation and visualization of biological sequences. *Bioinformatics* **31**, 3359-3361, doi:10.1093/bioinformatics/btv362 (2015).
- 66 Zhao, Y., Upadhyay, S. & Lin, X. PAS Domain Protein Pas3 Interacts with the Chromatin Modifier Bre1 in Regulating Cryptococcal Morphogenesis. *MBio* **9**, doi:10.1128/mBio.02135-18 (2018).
- 67 Dumesic, P. A. *et al.* Product binding enforces the genomic specificity of a yeast polycomb repressive complex. *Cell* **160**, 204-218, doi:10.1016/j.cell.2014.11.039 (2015).
- 68 Garcia-Santamarina, S. *et al.* Genome-wide analysis of the regulation of Cu metabolism in *Cryptococcus neoformans*. *Molecular microbiology* **108**, 473-494, doi:10.1111/mmi.13960 (2018).
- 69 Kim, T. H. & Dekker, J. ChIP-Quantitative Polymerase Chain Reaction (ChIP-qPCR). *Cold Spring Harb Protoc* **2018**, pdb prot082628, doi:10.1101/pdb.prot082628 (2018).
- 70 Yu, G., Wang, L. G. & He, Q. Y. ChIPseeker: an R/Bioconductor package for ChIP peak annotation, comparison and visualization. *Bioinformatics* **31**, 2382-2383, doi:10.1093/bioinformatics/btv145 (2015).
- 71 Stark, R. & Brown, G. DiffBind: differential binding analysis of ChIP-Seq peak data. *R package version* **100**, 4-3 (2011).
- 72 Lu, Z., Hofmeister, B. T., Vollmers, C., DuBois, R. M. & Schmitz, R. J. Combining ATAC-seq with nuclei sorting for discovery of cis-regulatory regions in plant genomes. *Nucleic Acids Res* **45**, e41, doi:10.1093/nar/gkw1179 (2017).
- 73 Zhang, Y. *et al.* Model-based analysis of ChIP-Seq (MACS). *Genome Biol* **9**, R137, doi:10.1186/gb-2008-9-9-r137 (2008).

- 74 Ramirez, F. *et al.* deepTools2: a next generation web server for deep-sequencing data analysis. *Nucleic Acids Res* **44**, W160-165, doi:10.1093/nar/gkw257 (2016).
- 75 Quinlan, A. R. & Hall, I. M. BEDTools: a flexible suite of utilities for comparing genomic features. *Bioinformatics* **26**, 841-842, doi:10.1093/bioinformatics/btq033 (2010).

## Figures and Tables

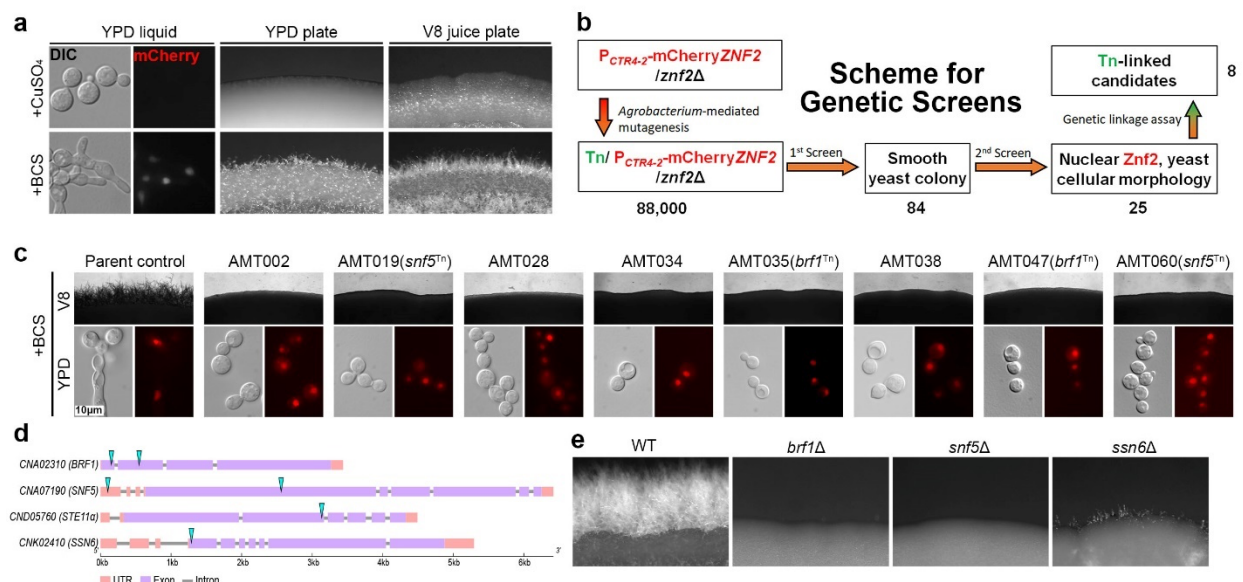


**Fig. 1. *BRF1* and *SNF5* are essential factors for filamentation.** **a.** Phenotypes of the parental reporter strain P<sub>CTR4-2</sub>-mCherry-ZNF2/*znf2*Δ used in the forward genetic screen. The reporter strain was cultured under Znf2-inducing conditions (YPD+BCS liquid overnight, YPD+BCS and V8+BCS agar medium for 2 days) or Znf2-suppressing conditions (YPD+CuSO<sub>4</sub>, V8+CuSO<sub>4</sub>). The fluorescence signal of mCherry-Znf2 was detected in the nucleus under inducing conditions. A fluffy colony edge reflects filamentous growth while a smooth edge reflects yeast growth. **b.** The scheme for the genetic screens to identify factors important for filamentation when Znf2 is produced and localized in the nucleus. **c.** The eight selected insertional mutants were cultured on V8+BCS medium for 2 days or in YPD+BCS medium overnight. **d.** The genetic loci disrupted by the T-DNA insertions with paired sequences. The cyan triangles indicate the T-DNA insertion sites. **e.** WT XL280 and the independent targeted gene deletion mutants *brf1*Δ, *snf5*Δ, and *ssn6*Δ were cultured on V8 medium for 7 days.

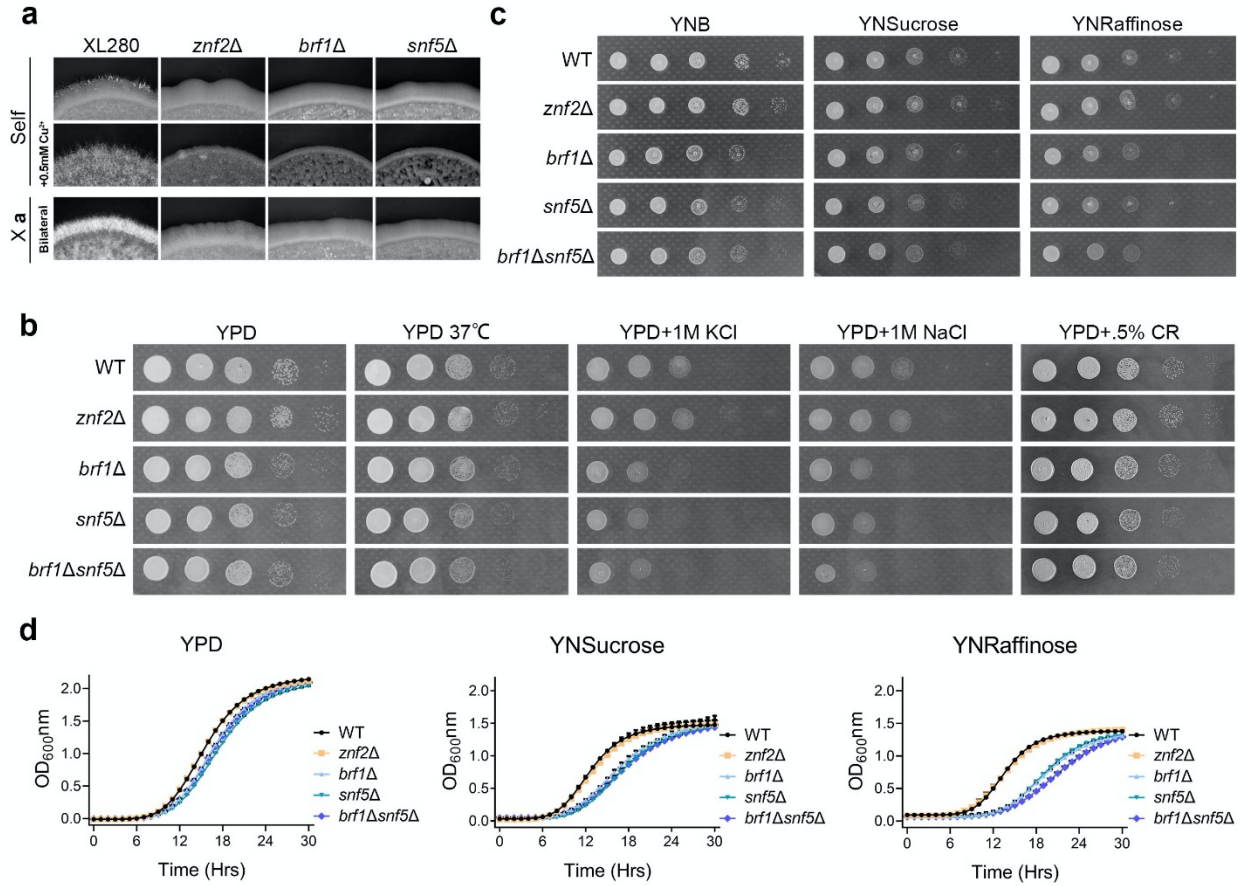


**Fig. 2. The *brf1Δ*, *snf5Δ*, and *brf1Δsnf5Δ* mutants are phenotypically identical.** **a.** WT XL280, *znf2Δ*, *brf1Δ*, and *snf5Δ* in the  $\alpha$  background were cultured on V8 or V8+500 $\mu$ M Cu<sup>2+</sup> medium (self-filamentation, upper images), or crossed with the corresponding **a** mating partners (bilateral bisexual mating, bottom images) on V8 medium in dark for 4 days. **b.** WT XL280, *znf2Δ*, *brf1Δ*, *snf5Δ*, and *brf1Δsnf5Δ* strains were cultured on YPD medium at 30°C or 37°C, or with the addition of KCl, NaCl, or Congo Red. **c.** WT XL280, *znf2Δ*, *brf1Δ*, *snf5Δ* and *brf1Δsnf5Δ* strains were cultured on minimal nitrogen base agar media with glucose, sucrose, or raffinose as the sole carbon source. **d.** WT XL280, *znf2Δ*, *brf1Δ*, *snf5Δ*, and *brf1Δsnf5Δ* strains were cultured in YPD, YNSucrose, or YNRaffinose broth at 30°C. The optical density at 600nm was plotted against the time after inoculation.



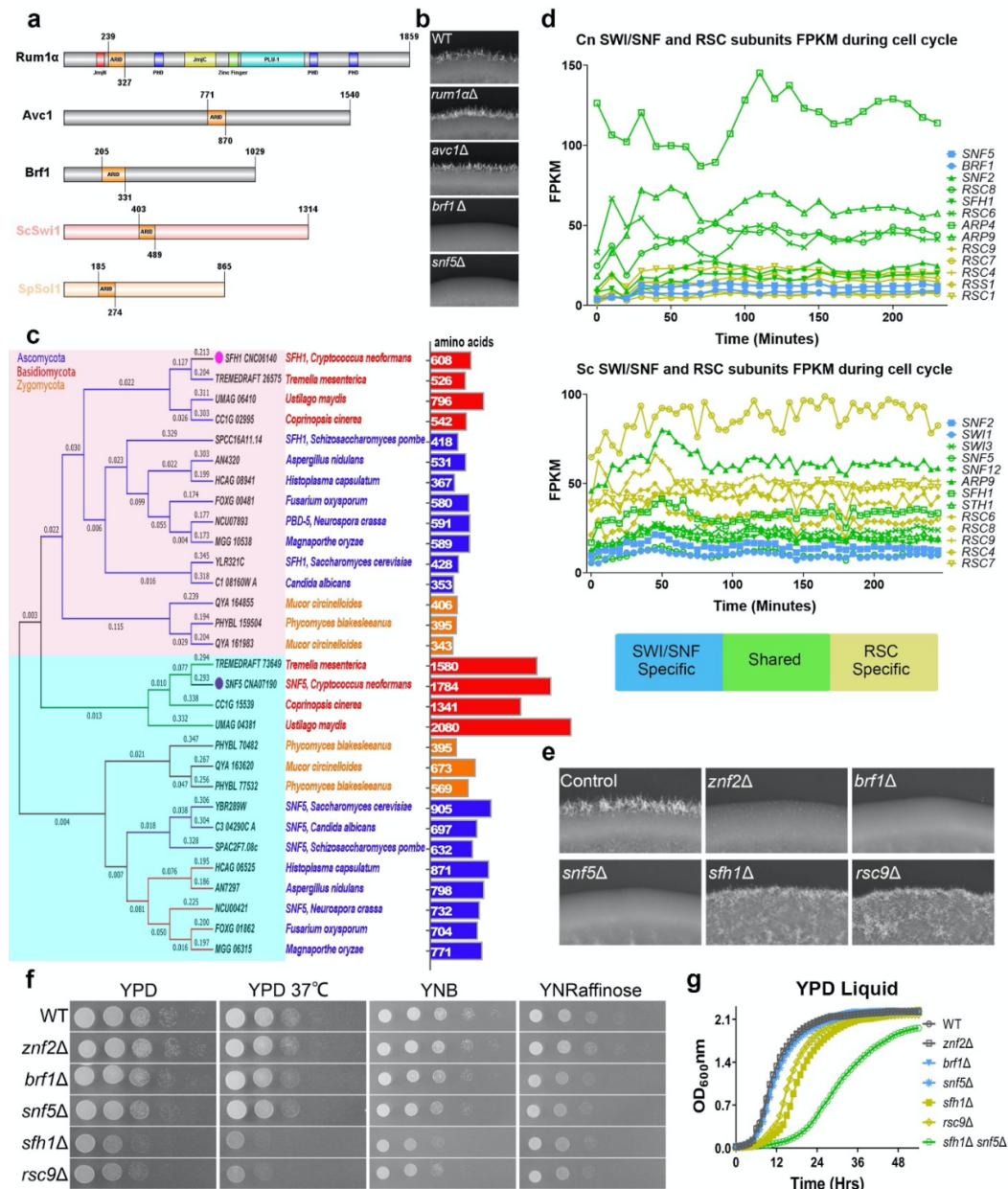


**Fig. 3. Brf1 and Snf5 are both subunits specific to the SWI/SNF complex.** **a.** Diagrams of domain organization of the three ARID-containing proteins in *C. neoformans* (Rum1 $\alpha$ , Avc1, and Brf1), and the SWI/SNF ARID-containing subunit Swi1 in *S. cerevisiae* and Sol1 in *S. pombe*. **b.** WT XL280, *snf5* $\Delta$ , *rum1* $\alpha$  $\Delta$ , *avc1* $\Delta$ , and *brf1* $\Delta$  strains were cultured on V8 agar medium at 22°C in dark for 2 days. **c.** A phylogenetic tree of Snf5-domain containing proteins in

the selected ascomycetes, basidiomycetes and zygomycetes. The number of amino acids for each protein was indicated on the right. **d.** The FPKM values for genes encoding the selected SWI/SNF and RSC subunits in *C. neoformans* and *S. cerevisiae* were plotted against the time across the cell cycle. The SWI/SNF-specific subunits are in blue, the RSC-specific subunits are in yellow, and the shared subunits are in green. **e.** WT XL280, *znf2Δ*, *brf1Δ*, *snf5Δ*, *sfh1Δ*, and *rsc9Δ* strains were cultured on V8 agar medium at 22°C in dark for 2 days. **f.** WT XL280, *znf2Δ*, *brf1Δ*, *snf5Δ*, *sfh1Δ*, and *rsc9Δ* strains were cultured on YPD agar medium at 30°C or at 37°C, YNB or YNRaffinose agar medium at 30°C. **g.** WT XL280, *znf2Δ*, *brf1Δ*, *snf5Δ*, *sfh1Δ*, *rsc9Δ*, and *snf5Δsfh1Δ* strains were cultured in YPD broth. The optical density at OD<sub>600nm</sub> was plotted against the time after inoculation. The SWI/SNF-specific subunits are in blue and the RSC-specific subunits are in yellow.

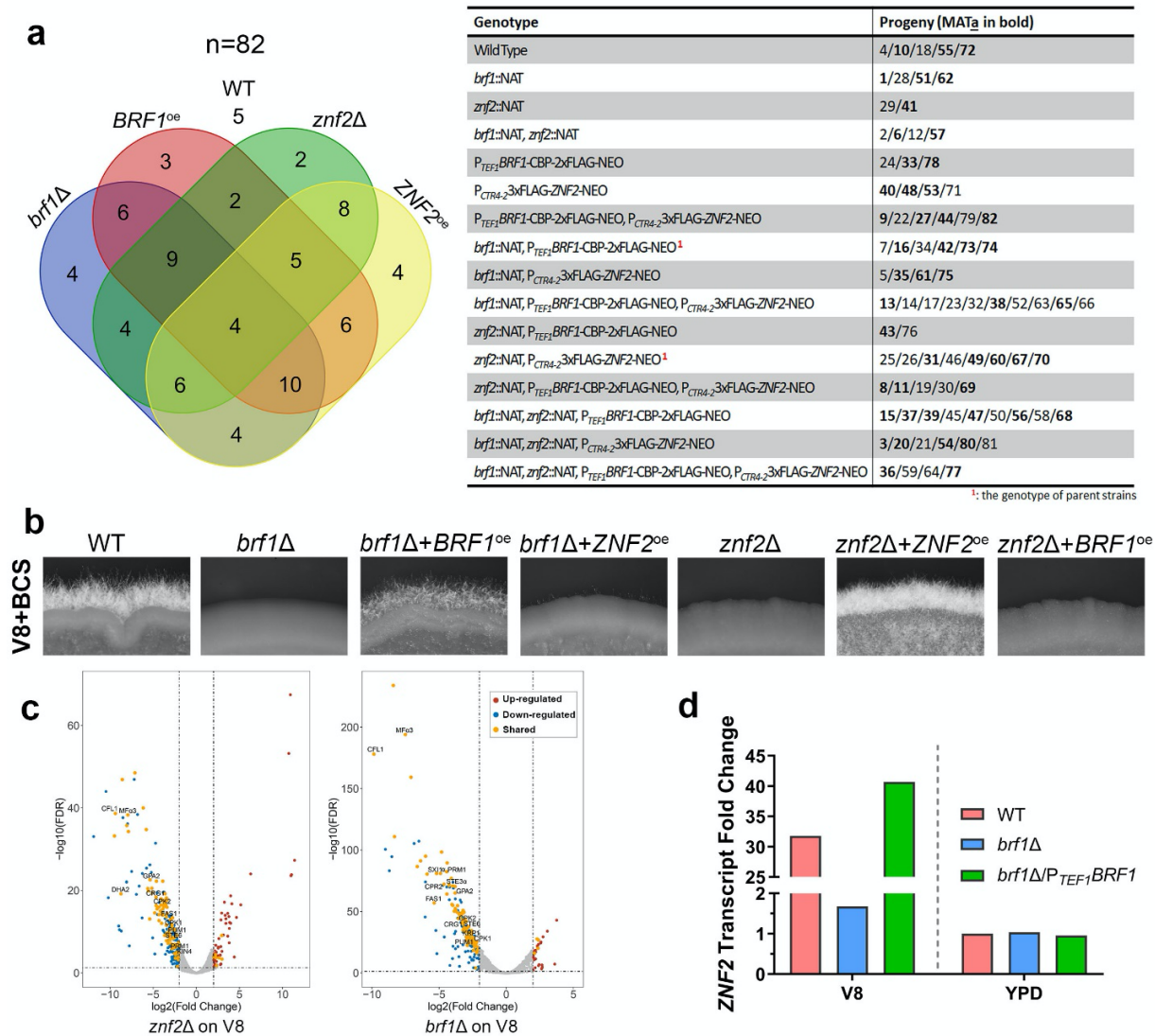


**Fig. 4. *BRF1* is required for *ZNF2* transcription induction during hyphal differentiation. a.**

The list of the genotypes of the 82 meiotic progeny dissected from a cross between *znf2* $\Delta$ /*ZNF2*<sup>oe</sup> **a** and *brf1* $\Delta$ /*BRF1*<sup>oe</sup> **a** and the Venn diagram showing the number of progeny for each genotype (progeny in the mating type **a** are bolded). **b.** WT XL280 and selected progeny of the following genotypes (*brf1* $\Delta$ , *brf1* $\Delta$ +*BRF1*<sup>oe</sup>, *brf1* $\Delta$ +*ZNF2*<sup>oe</sup>, *znf2* $\Delta$ , *znf2* $\Delta$ +*ZNF2*<sup>oe</sup>, and *znf2* $\Delta$ +*BRF1*<sup>oe</sup>) were cultured on V8+BCS medium (to induce *ZNF2*) at 22°C in dark for 5 days. **c.** Volcano plots of fold changes in transcript level in the *znf2* $\Delta$  mutant (left panel) and the *brf1* $\Delta$  mutant (right panel) compared to the wild type cultured on V8 agar medium for 24 hours. Each dot in the plots

indicates a protein-coding gene. The vertical dash lines indicate the  $|\log_2^{FC}|=2$  and the horizontal dash line shows the FDR=0.05. The differentially up-regulated genes are indicated in red and the differentially down-regulated genes are indicated in blue. The shared DEG between the *znf2Δ* and the *brf1Δ* mutants are colored in orange. **d.** The relative transcript levels of *ZNF2* in WT, *brf1Δ*, and *brf1Δ/BRF1<sup>oe</sup>* cultured on V8 agar medium and YPD medium. The *ZNF2* transcript level in WT cultured on YPD medium was used for normalization and was set as 1.

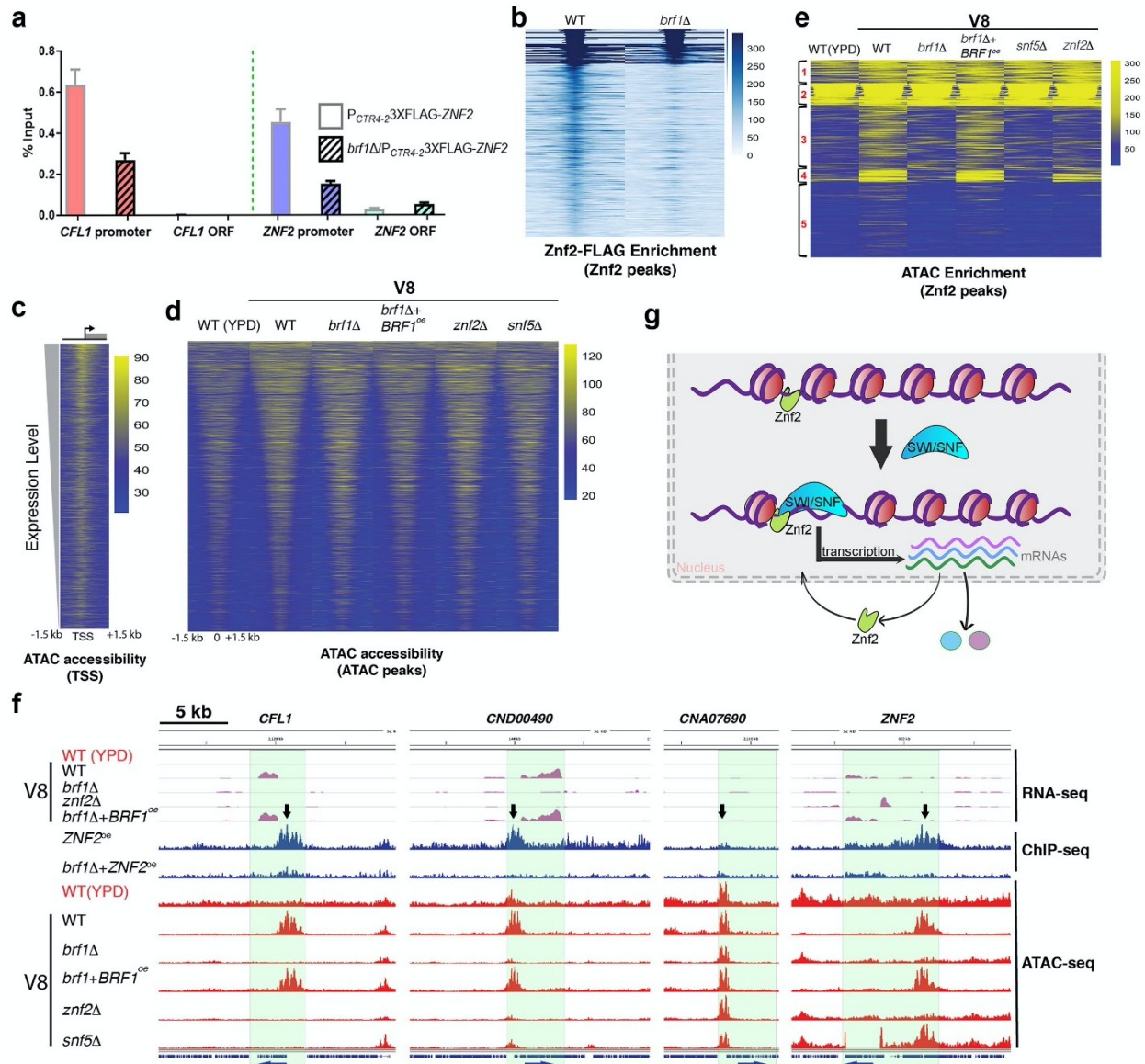


**Fig. 5. Znf2 and the SWI/SNF complex coordinate in transcription activation of filamentation genes.** **a.** ChIP-qPCR analysis of the relative abundance of DNAs associated with Znf2 in designated strains. Cells were grown in YPD+BCS media to induce the expression of Znf2. The left panel shows the %input values with or without Brf1 at the *CFL1* promoter and the ORF region; the right panel shows the %input values at the *ZNF2* promoter and the ORF region. **b.** The heatmap of the relative enrichment of Znf2-FLAG binding regions in the wild type and the *brf1Δ* background across all potential 361 Znf2 binding sites identified from ChIP-seq

(lowest  $p$  value on top and the highest  $p$  value on bottom). **c.** The heatmap depicts relative enrichment of ATAC-seq reads from a wild type strain grown on V8 medium. The peaks are centered on the transcription start sites (TSS) for all genes arranged from the highest expression level (top) to the lowest expression level (bottom). **d.** Global chromatin accessibility in the tested mutants. The relative enrichment of ATAC-seq reads for all ATAC-seq peaks from the wild type strain grown on V8 medium is shown for each indicated strain. **e.** Relative enrichment of the ATAC-seq peaks over the 361 Znf2-FLAG binding regions in WT, *brf1* $\Delta$  $\Delta$ *brf1* $\Delta$  $\Delta$ *BRF1*<sup>oe</sup>, *snf5* $\Delta$  $\Delta$  and *znf2* $\Delta$  $\Delta$  cells. **f.** Genome browser images depict relative transcript levels based on RNA-seq (purple), ChIP-seq (blue) and ATAC-seq enrichment (red) for the four indicated genetic regions of the indicated strains. Images depicting representative ATAC-seq peaks at four genetic loci that display reduced ATAC-seq enrichment in *brf1* $\Delta$  $\Delta$  *CFL1*, *CND00490*, and *ZNF2* $\Delta$  as well as one control genetic locus (*CNA07690*) that does not exhibit altered accessibility with or without Brf1. WT grown in YPD or on V8 medium is used as the negative or the positive control for filamentation. The down-arrows indicate the location of differential accessible regions. The arrows at the bottom of the plot indicate the transcription direction. **g.** A diagram of the working model depicting the coordination between Znf2 and the SWI/SNF complex in regulating gene transcription. Znf2 binds to its target sites at a low basal level. Upon culturing under filamentation-inducing condition, Znf2 recruits the SWI/SNF complex to its target sites to open chromatin and activate transcription of genes important for filamentation.

**Table 1.** The list of proteins identified from Co-IP/MS by Brf1-CBP-2xFLAG as bait.

Coding locus(D)	Coding locus(A)	Protein name	JL401 (strain 1)	JL402 (strain 2)
			# peptide spectrum matches	
CNE04020	CNAG_02134	Rsc8	12	20
CNK02030	CNAG_01863	Snf2	10	23
CNI00980	CNAG_04460	Arp9	8	9
CNA07190	CNAG_00740	Snf5	4	5
CND01230	CNAG_00995	Msc1	4	3
CNG02900	CNAG_03285	Rsc6	3	10
CNB05320	CNAG_04048	Arp4	3	4
CNE02000	CNAG_02350	Rss1	3	3
CNA02310	CNAG_00240	Brf1	2	6
CNA00820	CNAG_00091	N/A	2	2
CNK02620	CNAG_01920	Ubi4	2	2

Note: Subunits highlighted in green indicate the SWI/SNF and RSC complex shared subunits.

Subunits highlighted in blue indicates the SWI/SNF-specific subunits.



**Table 2.** The BLAST analysis of the SWI/SNF and RSC subunits in *C. neoformans*, *S. cerevisiae* (selected subunits) and *S. pombe* (selected subunits).

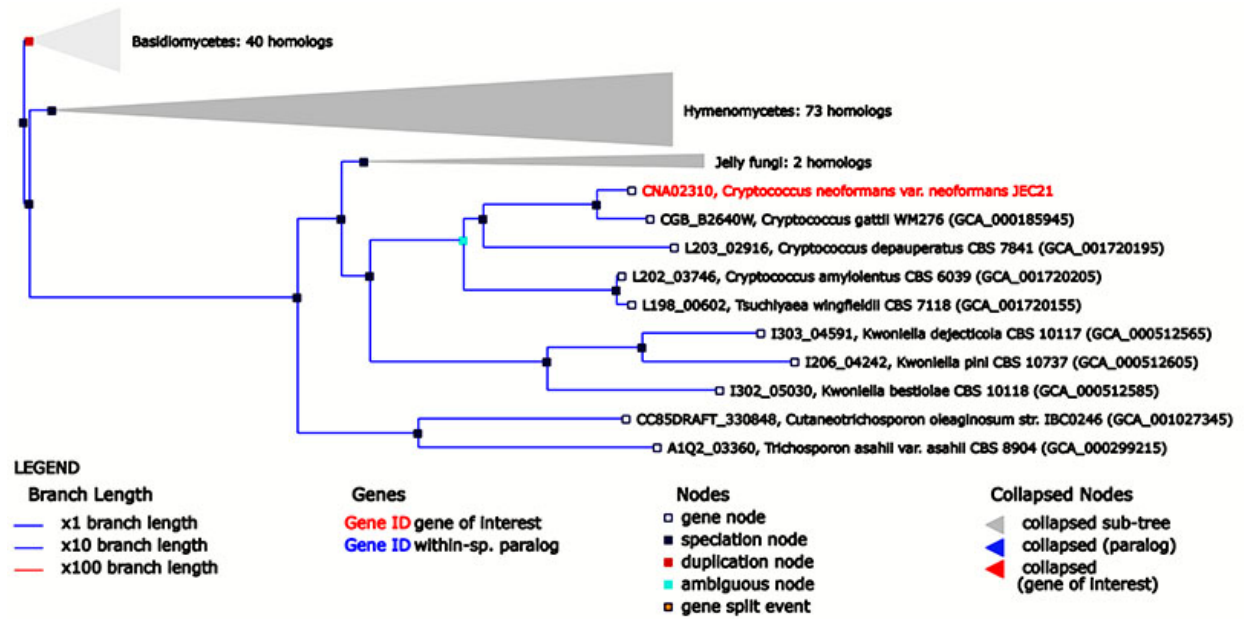
<i>C. neoformans</i>		<i>S. pombe</i>		<i>S. cerevisiae</i>	
Subunit	Deletion phenotype	Subunit	Deletion phenotype	Subunit	Deletion phenotype
Snf5	viable, nonfilamentous	Snf5	viable	Snf5	viable
		Sol1	viable	Swi1	lethal/ viable *
Brf1	viable, nonfilamentous				
Snf2	viable, reduced filament	Snf22	viable	Snf2	viable
Rsc8		Ssr1	lethal	Swi3	viable
		Ssr2	lethal		
Rsc6		Ssr3	lethal/ viable *	Snf12	viable
		Ssr4	lethal/ viable *		
Arp9		Arp9	viable	Arp9	lethal or sick
				Arp7	lethal or sick
Arp4		Arp42	viable		
Rss1					
				Rsc8	lethal
				Rsc6	lethal
Snf2	viable, reduced filament	Snf21	lethal	Sth1	lethal
Sfh1	viable, filamentous	Sfh1	lethal	Sfh1	lethal
Rsc9	viable, filamentous	Rsc9	lethal	Rsc9	lethal
Rsc7		Rsc7	lethal	Rsc7	viable
Rsc1		Rsc1	viable	Rsc1	double mutant lethal
				Rsc2	
Rsc4		Rsc4	viable	Rsc4	lethal

\* the phenotype depends on strain backgrounds.

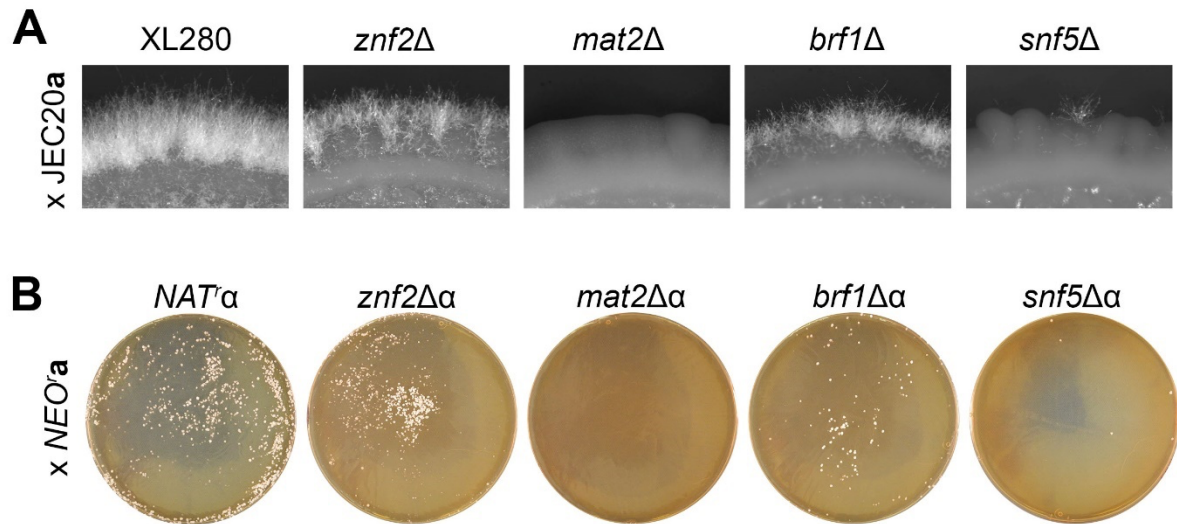
The SWI/SNF-specific subunits are highlighted in blue; the RSC-specific subunits are highlighted in yellow; and the SWI/SNF and RSC complex shared subunits are highlighted in green.



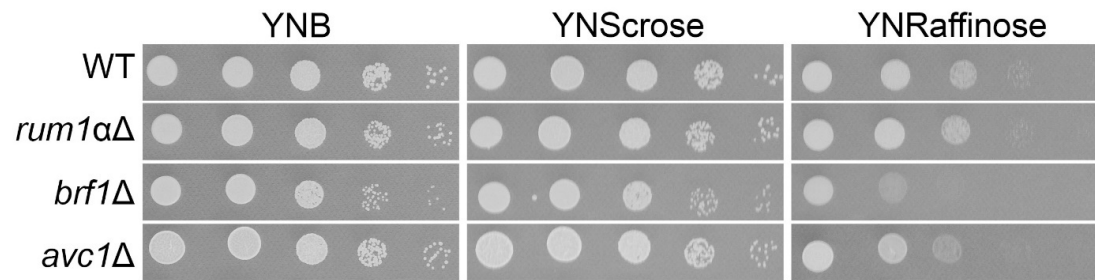




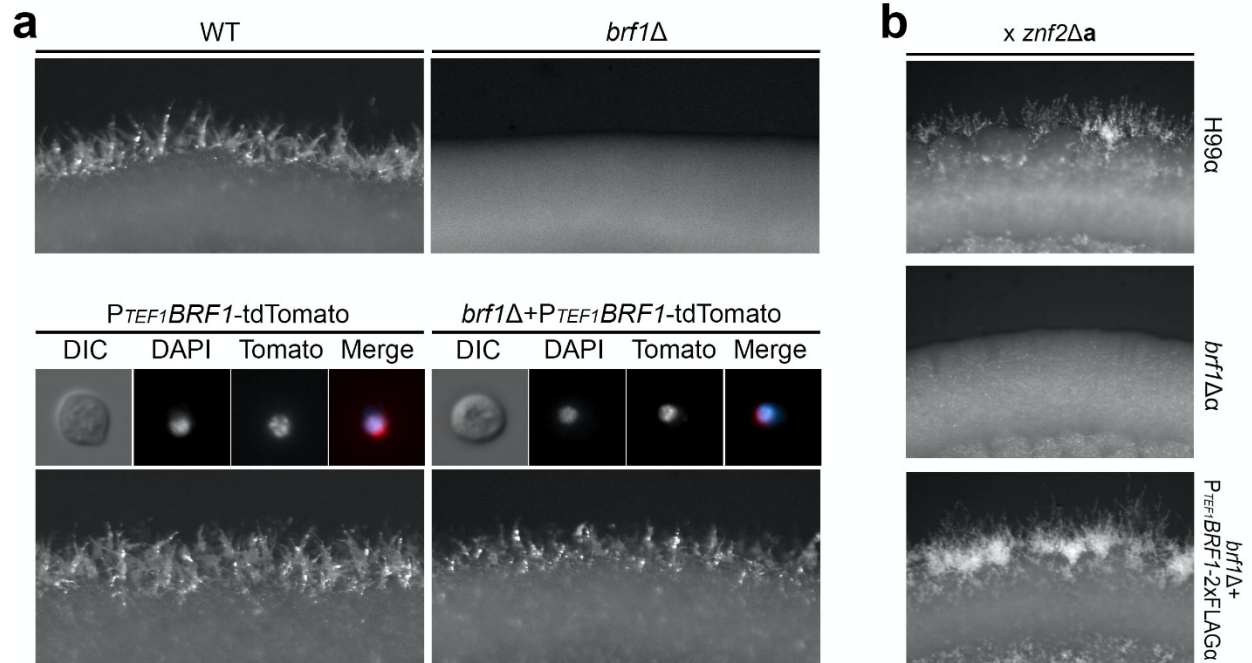
**Supplementary Fig. 1. A *BRF1* gene tree.** The gene tree was constructed on EnsemblFungi with the *BRF1* gene (gene ID *CNA02310*) as input. The gene tree was generated by the Gene Orthology/Paralogy prediction method pipeline where the maximum likelihood phylogenetic gene trees (generated by TreeBeST<sup>5</sup>) play a central role.



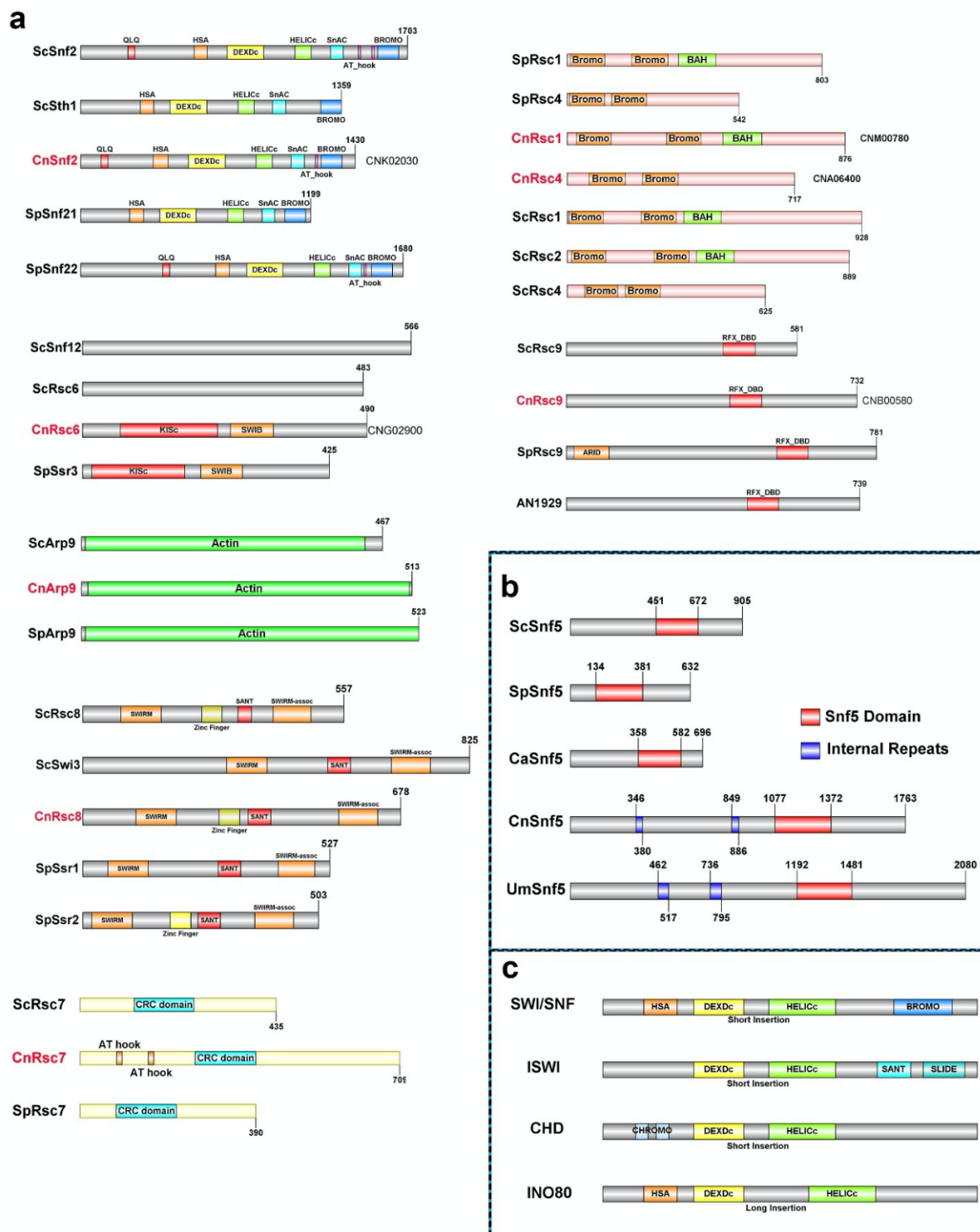
**Supplementary Fig. 2. The *brf1Δ* and *snf5Δ* strains are defective in cell fusion.** **a.** WT, *znf2Δ*, *mat2Δ*, *brf1Δ*, and *snf5Δ*  $\alpha$  strains were crossed to the wild type JEC20a reference strain on V8 medium at 22°C in dark for 4 days. JEC20a is non-filamentous by itself on V8 medium. **b.** The  $\alpha$  strains including the control XL1319, *znf2Δ*, *mat2Δ*, *brf1Δ*, and *snf5Δ* mutants with NAT<sup>R</sup> were crossed with the mating type **a** strain YSB133 with G418<sup>R</sup>. After 24 hours, the co-cultures were collected, and fusion products were selected on media supplemented with NAT and G418 drugs.



**Supplementary Fig. 3. *BRF1* is the only ARID containing gene involved in growth on raffinose medium.** The ARID containing gene deletion mutants *rum1Δ*, *avc1Δ* and *brf1Δ* along with the WT XL280 were serial diluted and spotted onto YNB, YNSucrose, and YNRaffinose media and cultured at 30°C for 1 day.

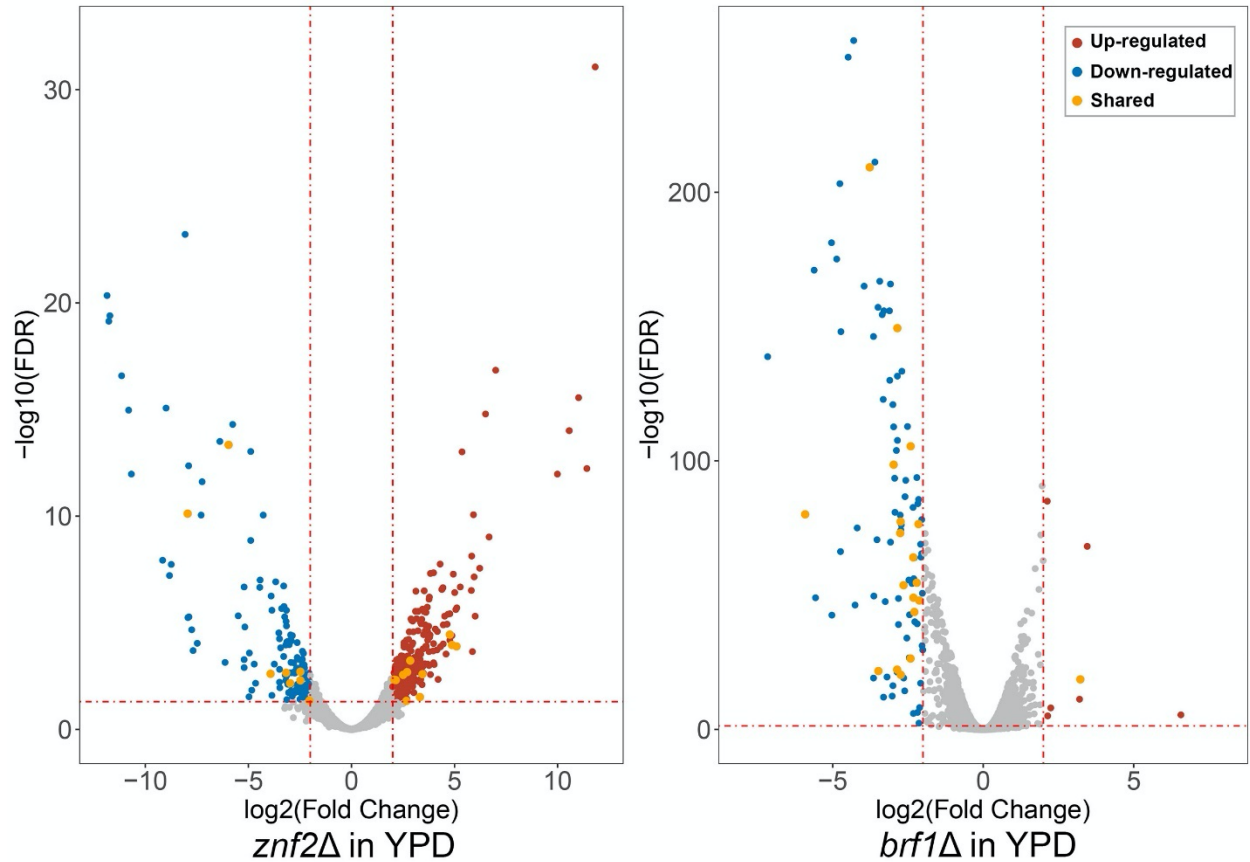


**Supplementary Fig. 4. The *BRF1* overexpression restored the defects in *brf1Δ*.** **a.** WT, *brf1Δ*, *brf1Δ+P<sub>TEF1</sub>-BRF1*-tdTomato strains was cultured on V8 medium for 2 days. The fluorescence images were from the *P<sub>TEF1</sub>-BRF1*-tdTomato cells cultured overnight in YPD liquid. **b.** WT H99, *brf1Δ* (JL131, MATα), and *brf1Δ+P<sub>TEF1</sub>-BRF1*-CBP-2xFLAG strains were crossed with a *znf2Δ* strain (strain XT110, MATa). The crosses were cultured on V8 medium for 3 days.



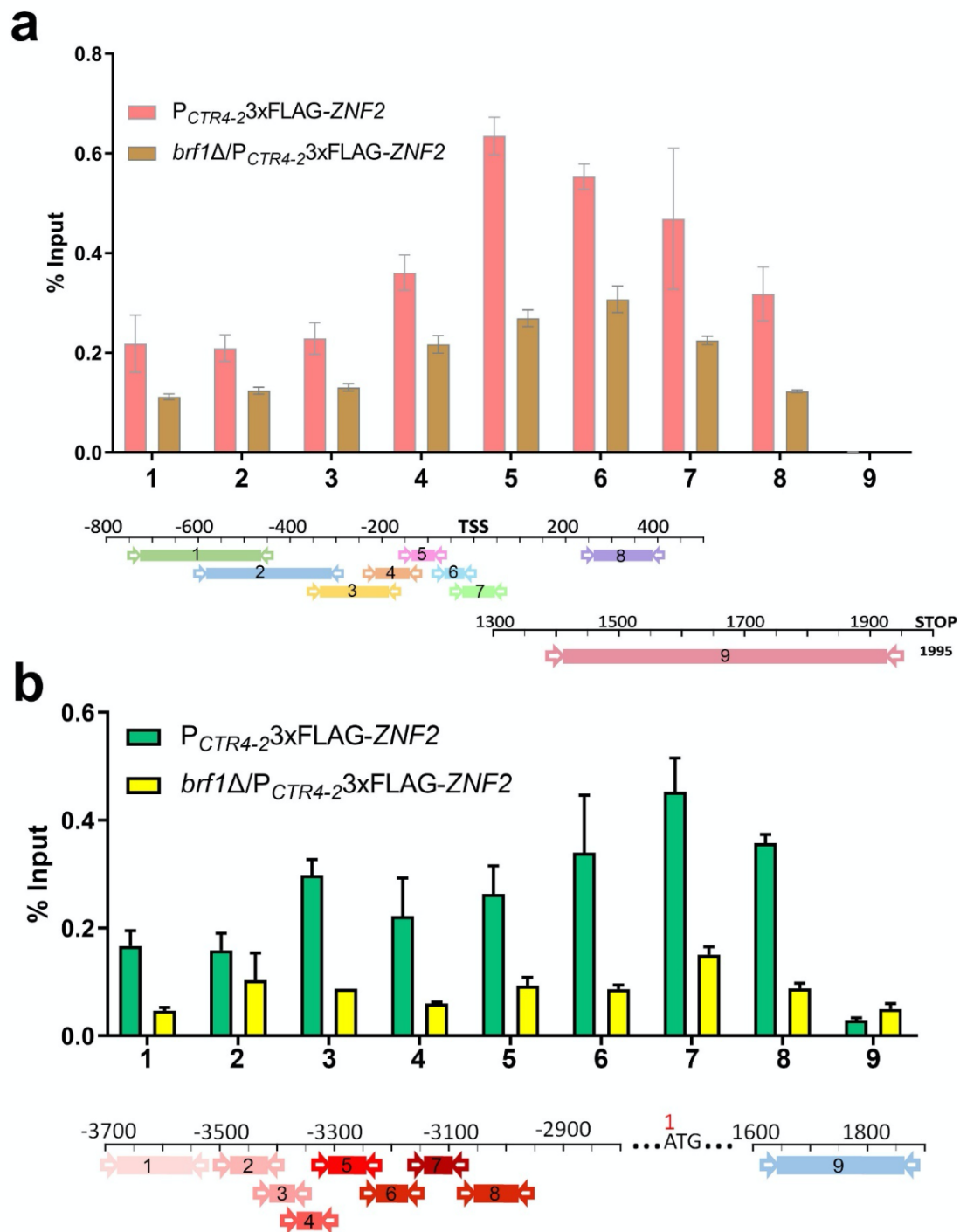
**Supplementary Fig. 5.** Diagrams of domain layout of the subunits in the SWI/SNF and RSC complex in *C. neoformans*. **a.** The domain layouts for Snf2, Rsc6, Arp9, Rsc8, Rsc7, Rsc1, Rsc4 and Rsc9 subunits in the RSC complex in *C. neoformans*, together with their homologs in *S.*

*cerevisiae* and *S. pombe*. **b.** The domain layouts for Snf5 proteins in ascomycetes (*S. cerevisiae*, *S. pombe*, and *C. albicans*) and basidiomycetes (*C. neoformans* and *Ustilago maydis*). **c.** The domain layouts for the Snf2 family ATPases in the chromatin remodeling complexes (adapted from Tang *et.al* 's review in 2010).



**Supplementary Fig. 6.** Volcano plots of fold changes in the gene transcript level in the *znf2* $\Delta$  mutant (left panel) and the *brf1* $\Delta$  mutant (right panel) compared to the wild type cultured in YPD medium for 24 hours. Each dot in the plot indicates a protein-coding gene. The vertical dash lines indicate the  $|\log_2^{FC}|=2$  and the horizontal dash line shows the FDR=0.05. The differentially up-regulated genes are colored red and the differentially down-regulated genes are colored blue. The shared DEG between *znf2* $\Delta$  and *brf1* $\Delta$  mutants are colored in orange.





**Supplementary Fig. 7.** Znf2 binds to the promoter of *ZNF2* and *CFL1*. The %input bar graph indicates the relative abundance of DNA fragments of selected regions recovered from FLAG tagged Znf2 in the presence or absence of *BRF1*. **a.** Primer pairs (from 1 to 8) spanned the

promoter region of *CFL1*, and primer pair 9 covered the open reading frame and served as a control. The primer positions are relative to the transcription start site (TSS). **b.** Primer pairs (from 1 to 8) spanned the promoter region of *ZNF2*, and primer pair 9 covered the open reading frame and served as a control. The transcription start site of *ZNF2* gene is poorly defined. The primer positions are therefore relative to the translation start ATG site.

**Supplementary Table 1.** The list of eight-four filament-defective *Agrobacterium*-mediated transformants.

**Supplementary Table 2.** The list of insertion sites from the eight linked insertional mutants.

Type of Insertion	Insertion Site in the Genome	Potential Affected Gene(s)
Paired	169nt downstream of TSS	CNA02310
Paired	656nt downstream of TSS	CNA02310
Paired	2566nt downstream of TSS	CNA07190
Paired	126nt downstream of TSS	CNA07190
Paired	3068nt downstream of TSS	CND05760
Paired	1248nt downstream of TSS	CNK02410
Singleton	At intergenic region of CNA07150 and CNA07160	CNA07150 CNA07160
Singleton	At intergenic region of CNA07230 and CNA07240	CNA07230 CNA07240

**Supplementary Table 3.** The list of proteins identified from Co-IP/MS by Sfh1-mNeonGreen as bait.

Coding Locus(D)	Coding Locus(A)	Protein name	# peptide spectrum matches
CNA03310	CNAG_00372	Rsc7	56
CNE04020	CNAG_02134	Rsc8	54

CNK02030	CNAG_01863	Snf2	50
CNC06140	CNAG_03003	Sfh1	35
CNG02900	CNAG_03285	Rsc6	29
CNM00780	CNAG_06068	Rsc1	22
CNE02000	CNAG_02350	Rss1	22
CNB00580	CNAG_06744	Rsc9	18
CNB05320	CNAG_04048	Arp4	15
CNI00980	CNAG_04460	Arp9	12

The RSC-specific subunits are highlighted in yellow, and the SWI/SNF and RSC complex shared subunits are highlighted in green.

**Supplementary Table 4.** The differentially expressed gene lists from RNA-seq.

**Supplementary Table 5.** The peaks and differential peaks from ATAC-seq.

**Supplementary Table 6.** The Snf5 domain search in fungi.

**Supplementary Table 7.** The list of Snf2 proteins in fungi identified by RBOMO and BSA domains search.

**Supplementary Table 8.** The strains used in this study.

**Supplementary Table 9.** The vectors used in this study.

<b>Vector Name</b>	<b>Genotype</b>	<b>Backbone</b>	<b>Sources</b>
pXL1	P <sub>GPD1</sub> -Fse1-Pac1-T <sub>GPD1</sub> -NEO	Topo2.1	
pXC	P <sub>CTR4-2</sub> -Fse1-Pac1-T <sub>GPD1</sub> -NEO	pXL1	
pYF5	P <sub>GPD1</sub> -PHD11-mNeonGreen- T <sub>GPD1</sub> -NEO	pUC19	This Study
pFZ3-ZNF2(D)	P <sub>CTR4-2</sub> -3X FLAG-ZNF2(D)- T <sub>GPD1</sub> -NEO	pUC19	This Study
pJL1	P <sub>TEF1</sub> -Fse1-AsiS1-CBP-2X FLAG-T <sub>GPD1</sub> -NEO	pXC	This Study
pJL2	P <sub>TEF1</sub> -BRF1-CBP-2X FLAG- T <sub>GPD1</sub> -NEO	pXL1	This Study
pJL3	P <sub>TEF1</sub> -BRF1-tdTomato- T <sub>GPD1</sub> -NEO	pXL1	This Study
pJL4	P <sub>GPD1</sub> -SFH1-mNeonGreen- T <sub>GPD1</sub> -NEO	pUC19	This Study
pJL5	P <sub>GPD1</sub> -SNF5-mNeonGreen- T <sub>GPD1</sub> -NEO	pUC19	This Study

**Supplementary Table 10.** The primers used in this study.

## APPENDIX D

### ISWI IS REQUIRED FOR NORMAL H3K27ME3 IN *NEUROSPORA CRASSA*

---

Kamei M., Ferraro A.R., Courtney A.J., Bar-Peled Y., Zhao F., Etheridge C., Lail K.,  
Ameirebrahimi M., Lipzen A., Ng V., Grigoriev I.V., Schmitz R.J., Liu Y., Lewis Z.A.  
Submitted to PNAS., 05/21/2020.

## Abstract

Polycomb Group (PcG) proteins are part of an epigenetic cell memory system that plays essential roles in multicellular development, stem cell biology, X-chromosome inactivation, and cancer. In animals, plants, and many fungi, Polycomb Repressive Complex 2 (PRC2) catalyzes trimethylation of histone H3 lysine 27 (H3K27me<sub>3</sub>) to assemble transcriptionally repressed facultative heterochromatin. PRC2 is structurally and functionally conserved in the model fungus *Neurospora crassa*, and recent work in this organism has generated insights into PRC2 control and function. To identify new components of the facultative heterochromatin pathway, we performed a targeted screen of *Neurospora* deletion strains lacking individual ATP-dependent chromatin remodeling enzymes. We found that the *Neurospora* homolog of IMITATION SWITCH (ISW) is critical for transcriptional repression and normal H3K27 methylation in facultative heterochromatin domains. A functional ISW ATPase domain was required for gene repression and H3K27 methylation. In other organisms, ISW homologs interact with accessory proteins to form multiple complexes with distinct functions. Using proteomics and molecular approaches, we identified four distinct *Neurospora* ISW-containing complexes. A triple mutant lacking three ISW-accessory factors and disrupting multiple ISW complexes led to widespread upregulation of PRC2 target genes and altered H3K27 methylation patterns, similar to an ISW-deficient strain, whereas single and double mutants lacking ISW-associated factors displayed more subtle phenotypes. Taken together, our data show that ISW is a key component of the facultative heterochromatin pathway in *Neurospora* and that distinct ISW complexes perform an apparently overlapping role to regulate chromatin structure and gene repression at PRC2-target domains.

## Significance Statement

Polycomb Repressive Complex 2 (PRC2) methylates histones to regulate multicellular development, maintenance of stem cell identity, X-chromosome inactivation, and other important processes. Given these essential roles, there is significant interest in identifying components that function with PRC2 to establish and maintain transcriptionally repressive heterochromatin. Here, we document an unexpected new role for a well-studied and conserved chromatin remodeling factor, ISWI. We found that the *Neurospora* ISWI homolog is required for normal facultative heterochromatin structure and gene repression at PRC2-target regions, and we defined requirements for ATP-dependent catalytic activity and accessory regulatory proteins. These findings provide new mechanistic insights into the formation and function of facultative heterochromatin in a model eukaryote.

## Introduction

Polycomb Group (PcG) proteins were first discovered in *Drosophila* as part of an epigenetic cell memory system (1). These proteins function to maintain repressed transcriptional states by assembling inaccessible chromatin, often referred to as facultative heterochromatin (1, 2). Polycomb Repressive Complex 2 (PRC2) catalyzes mono-, di- and tri-methylation of H3 lysine-27 (H3K27me1, -me2, -me3), and H3K27me3 is associated with transcriptionally silent genes in a diverse array of eukaryotes (3–12). PRC2 function is critical for multicellular development and for epigenetic processes such as X-chromosome inactivation in mammals and vernalization in plants (13, 14). In humans, defective regulation of H3K27me3 is associated with disease states including cancer and Weaver syndrome (15, 16).

Given the important biological roles of PRC2 and H3K27 methylation, there is significant interest in identifying new components of Polycomb-mediated repression pathways and elucidating mechanisms relevant to PRC2 control and function. Regulation of PRC2 is multifaceted. PRC2 can be recruited to specific loci by DNA binding proteins, and both recruitment and enzymatic activity can be positively and negatively regulated by local chromatin features including histone modifications, DNA methylation and RNA (17–19). For example, methyltransferase activity of mammalian PRC2 is inhibited by H3K36 methylation, and chromatin modifications found in constitutive heterochromatin antagonize H3K27 methylation in animals, plants, and some fungi (20–24). On the other hand, PRC2 methyltransferase activity is positively regulated by its enzymatic product, H3K27me3, providing a mechanism for spreading and maintenance of the H3K27-methylated state (25–27). *In vitro*, condensed chromatin substrates further stimulate activity of the mammalian PRC2 complex (28). This observation



raised the possibility that chromatin remodeling enzymes are important for PRC2 regulation *in vivo*.

Chromatin remodeling enzymes use the power of ATP hydrolysis to restructure and remodel the chromatin fiber (29, 30). These ATP-dependent enzymes are classified into four sub-families and can carry out a number of reactions, including nucleosome sliding, removal of histones or nucleosomes from chromatin, exchange of canonical core histones for histone variants, and chromatin assembly (29, 30). The activities of certain remodelers are conserved from yeast to humans. For example, homologs of *Drosophila* IMITATION SWITCH (ISWI) promote chromatin assembly and nucleosome spacing (31–35). ISWI homologs interact with diverse accessory proteins inside the cell, and these proteins regulate localization and activity of distinct ISWI-containing complexes (33, 36–38). One ISWI-containing complex, ATP-Utilizing Chromatin Assembly and Remodeling Factor (ACF; comprised of ISWI and ACF1), has been linked to gene repression in PRC2-target domains and other types of heterochromatin domains in *Drosophila*; however, genetic studies are hampered by the fact that both ACF1 and ISWI proteins are essential for development in flies and mammals (39–42). In *Arabidopsis thaliana*, a Chromodomain helicase family remodeler, PICKLE, is proposed to promote retention of nucleosomes harboring H3K27me<sub>3</sub>, raising the possibility that multiple remodeler families and mechanisms may contribute to assembly and function of heterochromatin (43). Currently, the role of chromatin remodelers in the assembly or maintenance of facultative heterochromatin is poorly understood in all experimental systems.

In this study, we asked if ATP-dependent chromatin remodeling enzymes are required for repression of PRC2 target genes and assembly of facultative heterochromatin in *Neurospora crassa*, a genetically tractable model organism with a minimal Polycomb Repression system

(44). *Neurospora* encodes a PRC2 complex that is structurally and functionally conserved, in contrast to the model yeasts *Saccharomyces cerevisiae* and *Schizosaccharomyces pombe*, which lack Polycomb repression systems (11, 44). *Neurospora* SET-7, EED, and SUZ12, are homologous to *Drosophila* Enhancer of Zeste E(z), Extra Sex Combs (Esc), and Suppressor of Zeste 12 Su(z)-12, respectively, and are essential for H3K27 methylation *in vivo* (11, 44). A fourth PRC2 subunit, CAC-3/NPF, is homologous to the *Drosophila* PRC2-associated protein Nurf55/CAF1 and contributes to PRC2 function (11, 44). In contrast to plants and animals, components of PRC1 have been lost in the fungal lineage (44). The absence of PRC1 enables straightforward genetic analyses to investigate PRC2 control and mechanisms that repress PRC2 target genes in a simple eukaryote. Approximately 7% of the *Neurospora* genome is enriched with H3K27me<sub>2/3</sub>, including domains that are adjacent to all fourteen telomeres (11, 45). Additional PRC2-target domains are located at internal sites on the chromosomes and typically span multiple genes. Recent work has uncovered at least two distinct mechanisms that regulate regional H3K27 methylation in *Neurospora*. Telomere repeats are sufficient to induce H3K27me<sub>2/3</sub>, and both CAC-3/NPF and the PRC2 Accessory Subunit (PAS) are required for H3K27 methylation adjacent to telomeres, but not at internal PRC2-target domains (11, 46, 47). Conversely, the histone variant H2A.Z is required for H3K27me<sub>3</sub> at internal domains, but not at telomeres (48). Thus, telomere-dependent and -independent mechanisms regulate PRC2 in *Neurospora*. Despite recent advances, much remains unknown about PRC2 control in fungi and in eukaryotes in general.

We took advantage of single-gene deletion strains available in the *Neurospora* gene deletion collection to investigate the role of SNF2 superfamily chromatin remodeling enzymes in facultative heterochromatin (49). We report here that a catalytically active ISWI homolog (ISW)

is required for repression of PRC2 target genes and normal patterns of H3K27 methylation in *Neurospora*. In addition, we identified multiple ISW-containing complexes and provide genetic evidence that ISW complexes function redundantly at PRC2 target genes. Together, our data suggest that ISW activity is critical for structure and function of facultative heterochromatin domains.

## Results

### ***The Neurospora ISWI homolog is required for repression of PRC2 target genes***

To determine if SNF2 family chromatin remodeling enzymes are important for gene repression within PRC2-dependent facultative heterochromatin domains, we carried out a targeted RNA-seq screen of selected strains available in the *Neurospora* gene deletion collection (49). RNA was isolated and sequenced from wild type and  $\Delta set-7$  control strains, as well as from nine deletion strains lacking individual SNF2 family enzymes. Two strains were determined to be heterokaryons, harboring a mixture of deletion and wild-type nuclei, but both were included in this analysis to test for possible gene dosage effects ( $\Delta crf3-1^{het}$  and  $\Delta crf8-1^{het}$ ). The single ASH-1 H3K36 di-methyltransferase is known to repress a subset of PRC2-target domains in *Neurospora* (50). We also compared our RNA-sequencing data to published data from the *ash1*(Y888F) mutant strain encoding a catalytically inactive version of the essential ASH1 protein (50). We first plotted the average gene expression level of transcriptionally silent genes within H3K27me2/3 enriched regions (n=642 genes; hereafter referred to as PRC2 target genes). As expected, we observed upregulation of PRC2 target genes in the  $\Delta set-7$  and *ash-1*<sup>Y888F</sup> control strains. In addition, we observed a marked increase in PRC2-target gene expression in the  $\Delta isw$  strain (also called  $\Delta crf4-1$ ; (51), which lacks the sole *Neurospora* homolog of ISWI (Figures 1A and S1A,B). All three strains displayed an increased average expression level of PRC2 target

genes that was at least two-fold higher than in wild type, with the highest expression level observed in the  $\Delta isw$  strain (Figure 1A;  $\Delta set-7 = 2.2$ -fold;  $ash-1^{Y888F} = 4.16$ -fold;  $\Delta isw = 15.72$ -fold), whereas other strains exhibited modest or no induction of this gene set. Biological replicate samples yielded highly reproducible results (Figure S1A,B).

We next examined expression of PRC2 target genes at the individual gene level. We constructed a heat map to plot relative expression levels of PRC2 target genes in wild-type and mutant backgrounds (Figure 1B). Of all mutants tested, the  $\Delta isw$  strain displayed increased expression of the highest number of genes. We therefore decided to focus on ISW for this study.

### ***ISW is required for normal H3K27me2/3***

We next asked whether ISW was required for normal facultative heterochromatin structure in *Neurospora*. We performed ChIP-seq in the  $\Delta isw$  mutant to examine the distribution of H3K27 methylation. Independent ChIP-seq experiments were performed using two previously validated antibodies that recognize H3K27me2/3 and H3K27me3, respectively. In both cases, the  $\Delta isw$  mutant displayed a striking defect in H3K27 methylation (Figure 1C and S1C). Inspection of H3K27me2/3 enrichment data in a genome browser revealed that reduction or complete loss of H3K27me2/3 at most internal domains, whereas telomere-adjacent domains displayed normal or modestly increased enrichment of H3K27me2/3. Control ChIP-seq experiments to examine H3K9me3, a mark for constitutive heterochromatin, revealed no changes in the  $\Delta isw$  mutant, demonstrating that the phenotype was specific for facultative heterochromatin (Fig S1D). Previous peak calling of H3K27me2/3 in wild type revealed 309 domains comprising 6% of the *Neurospora* genome (48). To quantify the change in H3K27me2/3 patterns, we identified H3K27me2/3-enriched peaks in the  $\Delta isw$  mutant and compared these to previously identified H3K27me2/3-enriched peaks in the wild-type strain (Table S1; a cut-off of 4-fold enrichment

over background and a false-discovery rate of  $<0.001$  was applied). More than 30% of wild type regions were not identified in the  $\Delta isw$  strain (102/309 H3K27me<sub>2/3</sub> peaks). We used HOMER to quantify H3K27me<sub>2/3</sub> enrichment across all previously identified wild type peaks and found that 130 wild type peaks had a normalized enrichment value reduced by  $>50\%$  compared to the wild type strain (Table S1). We found 30 peaks that exhibited higher normalized enrichment in the  $\Delta isw$  mutant, all adjacent to telomeres. By comparing H3K27me<sub>2/3</sub>-enriched peaks identified in  $\Delta isw$  to wild type peaks, we identified 132 peaks that were present in the  $\Delta isw$  strain, but not in wild type (Table S1). These regions were characterized by low levels of enrichment and were short, averaging 2.2 kilobase pairs compared to an average size of 7.9 kilobase pairs for H3K27me<sub>2/3</sub> peaks in wild type. Inspection in a genome browser revealed that  $\Delta isw$ -specific peaks of H3K27me<sub>2/3</sub> were typically near telomeres and adjacent to wild type PRC2-target domains, suggesting that low levels of H3K27me<sub>2/3</sub> may spread into regions that are adjacent to typical PRC2-target domains. We next visualized global H3K27me<sub>2/3</sub> enrichment by plotting relative H3K27me<sub>2/3</sub> levels across the left boundaries of all previously identified H3K27me<sub>2/3</sub> domains (Fig 1D and S1D). These data confirm that  $\Delta isw$  exhibits global defects in H3K27me<sub>2/3</sub>, including widespread losses of H3K27me<sub>2/3</sub> as well as local hypermethylation near telomeres.

### ***ISW catalytic activity is required for normal H3K27 methylation and gene repression***

Since ISWI homologs are required for maintaining genome stability in yeast and animals, our findings raised the possibility that a second site mutation in the  $\Delta isw$  strain could be responsible for the observed phenotype. To confirm that defective H3K27me<sub>2/3</sub> and derepression of PRC2 target genes was indeed due to loss of ISW, we introduced an *isw-ha* construct into the  $\Delta isw$  strain and tested for complementation. In addition to chromatin

remodeling activity, yeast ISW1 acts in an RNA quality control pathway in an ATPase-independent manner (52). We therefore simultaneously tested if ISW catalytic activity is required for gene repression and H3K27me2/3 by constructing and introducing an ATPase-defective *isw* mutant allele. The engineered allele encodes an ISW protein with an arginine in place of conserved lysine residue 214 in the conserved GTK motif required for catalysis (*isw*<sup>K214R</sup>; Figure 2A) (33). Both the ISW-3xHA and the ISW<sup>K214R</sup>-3xHA fusion proteins were expressed at similar levels (Fig 2B). We found that the *isw-ha* construct rescued the slow growth rate and the DNA damage hypersensitivity phenotype of the  $\Delta isw$  strain whereas the *isw*<sup>K214R</sup> construct did not rescue either phenotype (Fig2C-D). Furthermore, introduction of *isw-ha* into the  $\Delta isw$  strain restored repression of four PRC2 target genes analyzed by RT-qPCR (Fig 2E,G), and H3K27me2/3 was re-established at these loci, though not quite to the wild-type level (Fig2F). In contrast, the *isw*<sup>K214R</sup>-3xha construct failed to restore gene repression or H3K27me2/3 levels when introduced into the  $\Delta isw$  mutant (Fig 2F-G). These data confirm that ISW is required for gene repression and normal H3K27me2/3 in facultative heterochromatin and show that this function depends on ISW catalytic activity.

### ***ISW is present in multiple complexes***

ISWI homologs in other organisms interact with multiple accessory subunits to form distinct complexes, and these various accessory subunits are required to regulate the localization and catalytic activity of ISWI complexes (36, 39, 41, 53–55). To identify ISW-associated proteins in *Neurospora*, we purified ISW complexes from *Neurospora* cells and performed proteomic analysis. We first engineered a 3xFLAG-tagged ISW fusion protein, which was expressed from the endogenous *isw* locus under control of the native promoter. The ISW-3xFLAG protein supported wild-type growth and displayed normal patterns of H3K27me2/3,

suggesting the fusion protein was fully functional (Figure S2). We performed ChIP-seq experiments using anti-FLAG antibodies and found no enrichment of ISW-3xFLAG, suggesting that ISW interacts only transiently with chromatin (Figure S2). We next purified the ISW-3xFLAG protein and identified interacting proteins by LC-MS/MS (Figure 3A; Table S2). We removed proteins that are commonly identified in *Neurospora* FLAG pull-down experiments as probable background hits (56). This revealed several specific interacting proteins including NCU00164, a protein with similarity to known ISWI-interacting protein ACF1; the best reciprocal DELTA-BLAST hits for NCU00164 from yeast and mouse, respectively, were Itc1p and ACF1/BAZ1A (57). We hereafter refer to this protein as *Neurospora* ACF1 and the gene as *acf-1*. The conserved CHRAC complex - first identified in *Drosophila* - is composed of ISWI, ACF1, and two histone fold proteins named CHRAC14 and CHRAC16 (CHRAC15/17 in mammals)(58, 59) . Two histone-fold containing proteins co-purified with *Neurospora* ISW, encoded by uncharacterized genes NCU03073 and NCU06623. Since histone fold proteins often participate in several complexes, we refer to these proteins as Histone Fold Protein-1 and -2 (HFP-1 and HFP-2), and the genes as *hfp-1* and *hfp-2*. Several mammalian ISWI-interacting proteins contain a characteristic WHIM1 (WSTF, HB1, Itc1p, MBD9) motif, which is present in mammalian ISWI-interacting proteins ACF1, Williams Syndrome Transcription Factor (WSTF), and Remodeling and Spacing Factor 1 (RSF1) (60). We identified a second WHIM1 domain-containing protein, NCU00412, which was poorly conserved even within the ascomycete fungi. The best reciprocal DELTA-BLAST hits for NCU00412 in mouse corresponds to the WHIM1 motif of RSF1. The best reciprocal DELTA-BLAST hit in yeast was the yeast ISWI-interacting protein Ioc3, though amino acid similarity between NCU0412 and Ioc3 was restricted to only part of the WHIM1 domain. Finally, we identified NCU09388, a fungal-specific protein

containing a Plant Homeodomain (PHD) motif (61). NCU09388 did not produce a reciprocal best hit in yeast, *Drosophila*, mouse, or humans using DELTA-BLAST. Since these proteins have not been characterized in *Neurospora*, we refer to NCU00412 as ISW Accessory Factor-1 (IAF-1) and NCU09388 as IAF-2, encoded by *iaf-1* and -2, respectively.

To validate these putative interactions, we constructed strains expressing 3xFLAG-tagged versions of *Neurospora* ACF-1, IAF-1, and IAF-2, and we crossed them to a strain expressing an ISW-3xHA fusion protein integrated into the endogenous ISW locus. We then performed reciprocal co-immunoprecipitation experiments using anti-FLAG and anti-HA antibodies (Figure 3B-D). Co-IP experiments confirmed that ISW interacts with *Neurospora* ACF, IAF-1, and IAF-2 in vivo. To determine if *Neurospora* formed multiple ISW complexes, we carried out additional immunoprecipitation experiments using 3xFLAG-tagged versions of ACF, IAF-1, and IAF-2 followed by LC-MS/MS to identify interacting proteins (Table S2; interactions summarized in Figure 3E). Purification of ACF identified ISW, HFP-1, and HFP-2, suggesting that ACF and CHRAC complexes exist in *Neurospora*, as in other systems. Purification of IAF-1 identified ISW, but not other ISW-interacting proteins, suggesting that ISW and IAF-1 form a distinct complex. Similarly, purification of IAF-2 identified ISW but not other ISW interactors, suggesting that ISWI and IAF-2 comprise another discrete complex. Together, these data suggest that ISW forms multiple complexes in *Neurospora* through interactions with distinct accessory subunits.

### ***Partially redundant ISW complexes maintain gene repression in facultative heterochromatin***

To determine if any individual ISW accessory subunits are required for normal facultative heterochromatin structure, we examined H3K27me<sub>2/3</sub> in gene deletion strains lacking ACF, IAF-1, or IAF-2. Gene deletions of *iaf-1* and *iaf-2* were available in the *Neurospora*



deletion strain collection, and we constructed a *acf-1* deletion strain by replacing the ACF-1 coding sequence with a hygromycin resistance cassette. Surprisingly, all three mutants retained near wild-type patterns of H3K27me<sub>2/3</sub>, though a subtle reduction in H3K27me<sub>2/3</sub> was observed in the  $\Delta acf-1$  strain (Fig 4A,B).

We next ask if any of the individual ISWI-containing complexes are critical for repressing PRC2 target genes. We performed RNA-seq in each of the single deletion strains, and we plotted gene expression levels for all 642 PRC2 target genes (Fig 4C). This revealed that only the  $\Delta acf-1$  mutant displayed increased expression of PRC2 target genes, though the level of expression and the number of induced genes were substantially less than observed for the  $\Delta isw$  mutant.

We considered the possibility that individual ISW complexes may compensate for one another. To test this, we constructed all double and triple mutant combinations of ISW-interacting proteins and performed ChIP-seq for H3K27me<sub>2/3</sub>. Individual double mutants displayed subtle reductions in H3K27me<sub>2/3</sub> but did not resemble the reduction observed in the  $\Delta isw$  deletion strain. In contrast, a triple mutant lacking ACF1, IAF-1, and IAF-2 displayed significant defects in H3K27me<sub>2/3</sub> similar to the  $\Delta isw$  single mutant (Fig 4D,E). Similarly, analyses of gene expression by RNA-seq revealed that PRC2 target genes were significantly upregulated in the triple mutant (Fig 4F). Thus, the gene expression phenotype closely matched the  $\Delta isw$  single mutant. Taken together, these data demonstrate that *Neurospora* ISW and multiple ISW-accessory proteins are critical regulators of gene expression and chromatin structure in facultative heterochromatin.

## Discussion

We report for the first time in any system that an ISWI homolog is broadly required for the repression of PRC2 target genes. The biochemical and biophysical properties of ISWI chromatin remodeling complexes have been studied extensively, but information about their physiological roles is still limited, partly because ISWI and some ISWI accessory proteins are essential for development in animal models (39, 40). As a result, genetic studies in many experimental systems are limited to early stages of embryonic development or certain cell types such as embryonic stem cells (35, 39, 41). We took advantage of *Neurospora*, an experimental system with powerful genetics and biochemistry to investigate the role of ATP-dependent chromatin remodeling enzymes in gene repression mediated by H3K27me<sub>3</sub>-dependent facultative heterochromatin. Of the nine SNF2 family enzymes screened here, we found that *Neurospora* ISW was uniquely required for repression of PRC2 target genes. We found that *Neurospora* ISW is required for normal patterns of H3K27 methylation in the *Neurospora* genome, and that its absence makes strains hypersensitive to genotoxic stress. ISWI proteins are ATP-driven remodelers that create ordered arrays of nucleosomes *in vitro* and *in vivo* (31–35). Alternatively, yeast ISW1 performs an ATPase-independent function in RNA quality control (52). We found that a functional ATPase domain is required for repression of PRC2 target genes and for normal H3K27 methylation, suggesting that ISW controls gene expression and chromatin structure via its nucleosome remodeling activity. Biochemical analysis of PRC2 revealed higher activity on dense chromatin substrates (28). It is possible that ISW activity is needed to create an optimal chromatin substrate for stimulating PRC2, and therefore may be critical for spreading or maintenance of H3K27me<sub>2/3</sub>. Our finding that ATPase activity is required to establish or maintain normal H3K27me<sub>2/3</sub> patterns in *Neurospora* is consistent with this possibility.

Alternatively, transcriptional upregulation in the absence of ISW may indirectly interfere with PRC2 activity. Future studies will distinguish between these two hypotheses.

We provide genetic evidence that ISWI-containing complexes act redundantly to repress PRC2 target genes. Our findings expand on previous work in *Drosophila* (42), raising the possibility that regulation of gene repression and chromatin structure within PRC2-target domains is a conserved function of ISWI complexes. Artificial tethering of the ISWI accessory factor ACF1 was sufficient to repress nearby reporter genes, but only when the reporter construct was integrated in repressive environments such as those marked by H3K27me3 (42). Moreover, *Drosophila* ACF1-null mutants displayed increased expression of a small number of genes residing in repressive chromatin environments. The relatively subtle transcriptional phenotypes reported for *Drosophila* ACF1-null mutants may be explained by redundant activities of ISWI complexes, as supported by our data for *Neurospora*. Indeed, we observed subtle activation of PRC2 target genes in the *Neurospora*  $\Delta acf-1$  strain, similar to the situation in *Drosophila*. In contrast, generation of a triple mutant lacking three *Neurospora* ISW accessory proteins displayed broad activation of PRC2 target genes and H3K27 methylation defects, similar to the  $\Delta isw$  deletion strain.

Together, our data suggest that ISW performs a general role in assembly or maintenance of repressed chromatin states, and that this role can be fulfilled redundantly by various ISW complexes containing distinct accessory proteins. ISWI complexes are proposed to sample chromatin through transient binding events that rarely lead to nucleosome translocation (62). It is therefore possible that multiple ISW complexes function globally in addition to performing sequence-directed remodeling mediated by individual accessory subunits. *Drosophila* CHRAC/ACF complexes may function to maintain a repressive chromatin “ground state” (42).

Our data extend this model to include additional ISW-containing complexes that function together to maintain transcriptionally repressed states. Taken together, our findings support a new, and unexpected, role for eukaryotic ISWI complexes in maintaining gene repression and chromatin structure at facultative heterochromatin domains.

## **Materials and Methods**

### ***Strains and Growth Media***

All strains and primers used in this study are listed in Table S3 and S4, respectively. Available knock-out strains were generated by the Neurospora gene knockout consortium and obtained from the Fungal Genetics Stock Center (49, 63). We constructed an  $\Delta acf::hph+$  deletion cassette by first amplifying the 5' and 3' flank regions using the indicated primers (Table S4) and then performing overlapping PCR using plasmid pCSN44 to introduce the selectable *hph+* cassette. Transformations, crosses, and maintenance of *Neurospora* cultures was performed as described by (64). For RNA sequencing, *Neurospora* cultures were grown in 150mm Petri plates containing 25mL liquid medium (1X Vogel's plus 1.5% glucose) in constant light for ~24 hours. Mycelial plugs were isolated using a 10mm cork borer and transferred to a 50 mL flask containing Vogel's minimal media (VMM) with 2% sucrose and grown for 24 hours at 30°C under constant light. To identify ISW-interacting proteins, transgenic strains expressing FLAG-tagged proteins were grown in 1L of liquid Vogel's minimal media with 1.5% sucrose at 32°C for 16 hours. Strains were genotyped by PCR and genotypes were confirmed using Illumina sequencing data. To test for hypersensitivity to methyl methanesulfonate (MMS), 10-fold serial dilutions of conidial suspensions ( $10^6$ - $10^3$  conidia) were inoculated on VMM plates with 2% sorbose supplemented with MMS. Knock-in constructs to create epitope-tagged strains

(3xFLAG, 3xHA, GFP) strains were made with indicated primers (Table S4) using plasmids and protocols described by Honda and Selker (65).

### ***Protein purification***

To purify protein complexes for analysis by LC-MS/MS, nuclei from 1L cultures were enriched using an established nuclear extraction protocol (66). After the final centrifugation to pellet nuclei, the nuclear pellet was resuspended in 10 mL of FLAG-purification buffer (10mM HEPES pH 7.5, 200 mM NaCl, 1mM EDTA, and cCOMPLETE, protease inhibitor tablets; Roche cat #11836170001). We performed a FLAG- affinity purification by adding 200 ul of M2 FLAG affinity gel (cat # A2220; Sigma-Aldrich) and incubating at 4°C for 4 hours. The beads were washed three times in 10 mL of FLAG purification buffer and three times in 1 mL FLAG purification buffer. Proteins were eluted twice in 300 uL of FLAG purification buffer containing 200 µg/mL of 3X FLAG peptide (Sigma-Aldrich, cat # F4799). Elution fractions were combined and proteins were precipitated with ice cold TCA, resuspended in 1X SDS loading buffer and run on pre-cast 4-12% acrylamide gel for 4 min at constant 200V. Proteins were stained with SYPRO RUBY for 3 hours. Purified proteins in a single gel slice were excised, subjected to in-gel trypsin digestion, and analyzed by LC-MS/MS using a Thermo Orbitrap instrument at the University of Georgia Proteomics core. Western blotting, and Co-immunoprecipitation (Co-IP) were performed as previously described (67).

### ***Nucleic acid and computational analysis.***

RNA isolation was performed as described (68). For reverse transcription/quantitative real-time PCR (RT-qPCR), 500 ng of total RNA was analyzed using iTaq One step reagents (cat #1725150; BioRad). A minimum of three independent biological replicates and two technical replicates were performed for RT-qPCR experiments. RNA-sequencing library preparation and

sequencing was performed at the Joint Genome Institute or the Georgia Genomics and Bioinformatics Core. At JGI, Illumina RNASeq w/PolyA Selection, Plates: Plate-based RNA sample prep was performed on the PerkinElmer Sciclone NGS robotic liquid handling system using Illumina TruSeq Stranded mRNA HT sample prep kit utilizing poly-A selection of mRNA following the protocol outlined by Illumina in their user guide (cat# 20020595) and with the following conditions: total RNA starting material was 1 ug per sample and 8 cycles of PCR was used for library amplification. The prepared libraries were quantified using KAPA Biosystem's next-generation sequencing library qPCR kit and run on a Roche LightCycler 480 real-time PCR instrument. The libraries were then multiplexed and sequencing was performed on the Illumina NovaSeq sequencer using NovaSeq XP V1 reagent kits, S4 flow cell, and following a 2x150 indexed run recipe. At UGA, libraries were constructed using the Illumina TruSeq mRNA stranded Library Kit (cat. # RS-122-2101) according to manufacturer instructions. For RNA-seq data, short reads (<20 bp) and adaptor sequences were removed using TrimGalore (version 0.4.4), cutadapt version 1.14 , and Python 2.7.8, with fastqc command (version 0.11.3) (69). Trimmed Illumina single-end reads were mapped to the current *Neurospora* NC12 genome assembly 12 (Genbank accession #: GCA\_000182925.2) using the Hierarchical Indexing for Spliced Alignment of Transcripts 2 (HISAT2: version 2.1.0) with parameters –RNA-strandness R then sorted and indexed using SAMtools (version 1.9) (69, 70). FeatureCounts from Subread (version 1.6.2) was used to generate gene level counts for all RNA bam files (71). Raw counts were imported into R and differential gene expression analysis was conducted using Bioconductor: DeSeq2 (72). Table S5 contains TPM count data for PRC2 target genes in all strains. Normalized counts were plotted in R using ggplot2 and pheatmap packages. PRC2 target genes are listed in Table S5, and were identified using bedtools intersect to identify genes that

overlap a wild type H3K27me<sub>2/3</sub> domain (listed in Table S1) by at least 70%. Genes with wild type TPM values greater than 5 were classified as expressed genes and were removed from the list. The heat map depicting relative expression of PRC2 genes was constructed using pheatmap. Only genes with detectable expression in at least one strain were plotted.

Chromatin immunoprecipitation (ChIP) was performed and analyzed by qPCR or Illumina sequencing as described using antibodies that recognize H3K9me<sub>3</sub> (cat# 39161; Active Motif) and H3K27me<sub>2/3</sub> (cat# 39535; Active Motif), or H3K27me<sub>3</sub> (cat# 9733; Cell Signalling) (73, 74). Primers used for ChIP-quantitative real-time PCR (ChIP-qPCR) are listed in Table S4. qPCR was performed using iTaq Universal SYBR green Supermix (cat# 172-5122; Bio-Rad) and an iCycler IQ instrument. For Illumina sequencing, libraries were prepared as described (74). DNA sequencing was performed using an Illumina NextSeq 500 instrument at the University of Georgia genomics core. Short reads (<20 bp) and adaptor sequences were removed using TrimGalore (version 0.4.4), cutadapt version 1.14, and Python 2.7.8, with fastqc command (version 0.11.3) (69). Trimmed Illumina reads were aligned to the current *Neurospora* NC12 genome assembly available from NCBI (accession # GCA\_000182925.2) using the BWA (version 0.7.15) mem algorithm, which randomly assigns multi-mapped reads to a single location (75). Files were sorted and indexed using SAMtools (version 1.9) (70). To plot the relative distribution of mapped reads, read counts were determined for each 25 bp window across the genome using IGV tools and data were displayed using the Integrated Genome Viewer (76). The Hypergeometric Optimization of Motif EnRichment (HOMER) software package (version 4.8) was used to identify H3K27me<sub>3</sub> peaks using “findPeaks.pl” with the following parameters: -style histone (77) . For peak calling, a cutoff of 4-fold enrichment and a false discovery rate

value of <0.001 were used. Bedtools (version 2.27.1) “intersect” (version 2.26.0) was used to determine the number of peaks that intersect with other peak files.

**Data Availability.** Sequencing data generated at UGA have been deposited to the NCBI GEO database with project series accession #**GSE150758** (reviewer access token: spgvceqqjdwtxsf). Accession numbers of samples generated at JGI and previously published data sets analyzed in this study are included in Table S6.

### Acknowledgements

This work was supported by grants from the American Cancer Society (RSG-14-184-01-DMC) and the NIH (R01GM132644) to Z.A.L and the National Science Foundation Graduate Research Fellowship Program Grant (DGE-1443117) to A.R.F. and A.J.C. The work conducted by the U.S. Department of Energy Joint Genome Institute, a DOE Office of Science User Facility, is supported by the Office of Science of the U.S. Department of Energy under Contract No. DE-AC02-05CH11231. We are grateful to Michael Freitag and Kristina Smith for constructive comments on this manuscript.

### References

1. B. Schuettengruber, H.-M. Bourbon, L. Di Croce, G. Cavalli, Genome Regulation by Polycomb and Trithorax: 70 Years and Counting. *Cell* **171**, 34–57 (2017).
2. R. Margueron, D. Reinberg, The Polycomb complex PRC2 and its mark in life. *Nature* **469**, 343–349 (2011).
3. R. Cao, *et al.*, Role of histone H3 lysine 27 methylation in Polycomb-group silencing. *Science* **298**, 1039–1043 (2002).
4. B. Czermin, *et al.*, Drosophila enhancer of Zeste/ESC complexes have a histone H3 methyltransferase activity that marks chromosomal Polycomb sites. *Cell* **111**, 185–196 (2002).
5. A. Kuzmichev, K. Nishioka, H. Erdjument-Bromage, P. Tempst, D. Reinberg, Histone methyltransferase activity associated with a human multiprotein complex containing the Enhancer of Zeste protein. *Genes Dev.* **16**, 2893–2905 (2002).



6. J. Müller, *et al.*, Histone methyltransferase activity of a Drosophila Polycomb group repressor complex. *Cell* **111**, 197–208 (2002).
7. L. Jiao, X. Liu, Structural basis of histone H3K27 trimethylation by an active polycomb repressive complex 2. *Science* **350**, aac4383 (2015).
8. G. Makarevich, *et al.*, Different Polycomb group complexes regulate common target genes in Arabidopsis. *EMBO Rep.* **7**, 947–952 (2006).
9. X. Zhang, *et al.*, Whole-genome analysis of histone H3 lysine 27 trimethylation in Arabidopsis. *PLoS Biol.* **5**, e129 (2007).
10. T. S. Mikkelsen, *et al.*, Genome-wide maps of chromatin state in pluripotent and lineage-committed cells. *Nature* **448**, 553–560 (2007).
11. K. Jamieson, M. R. Rountree, Z. A. Lewis, J. E. Stajich, E. U. Selker, Regional control of histone H3 lysine 27 methylation in Neurospora. *Proc. Natl. Acad. Sci. U. S. A.* **110**, 6027–6032 (2013).
12. P. A. Dumesic, *et al.*, Product binding enforces the genomic specificity of a yeast polycomb repressive complex. *Cell* **160**, 204–218 (2015).
13. R. Bastow, *et al.*, Vernalization requires epigenetic silencing of FLC by histone methylation. *Nature* **427**, 164–167 (2004).
14. K. Plath, *et al.*, Role of histone H3 lysine 27 methylation in X inactivation. *Science* **300**, 131–135 (2003).
15. A. Laugesen, J. W. Højfeldt, K. Helin, Role of the Polycomb Repressive Complex 2 (PRC2) in Transcriptional Regulation and Cancer. *Cold Spring Harb. Perspect. Med.* **6** (2016).
16. O. Deevy, A. P. Bracken, PRC2 functions in development and congenital disorders. *Development* **146** (2019).
17. R. J. Klose, S. Cooper, A. M. Farcas, N. P. Blackledge, N. Brockdorff, Chromatin sampling--an emerging perspective on targeting polycomb repressor proteins. *PLoS Genet.* **9**, e1003717 (2013).
18. J.-R. Yu, C.-H. Lee, O. Oksuz, J. M. Stafford, D. Reinberg, PRC2 is high maintenance. *Genes Dev.* **33**, 903–935 (2019).
19. A. Laugesen, J. W. Højfeldt, K. Helin, Molecular Mechanisms Directing PRC2 Recruitment and H3K27 Methylation. *Mol. Cell* **74**, 8–18 (2019).
20. W. Yuan, *et al.*, H3K36 methylation antagonizes PRC2-mediated H3K27 methylation. *J. Biol. Chem.* **286**, 7983–7989 (2011).

21. F. W. Schmitges, *et al.*, Histone methylation by PRC2 is inhibited by active chromatin marks. *Mol. Cell* **42**, 330–341 (2011).
22. L. J. Gaydos, A. Rechtsteiner, T. A. Egelhofer, C. R. Carroll, S. Strome, Antagonism between MES-4 and Polycomb repressive complex 2 promotes appropriate gene expression in *C. elegans* germ cells. *Cell Rep.* **2**, 1169–1177 (2012).
23. A. Deleris, *et al.*, Loss of the DNA methyltransferase MET1 Induces H3K9 hypermethylation at PcG target genes and redistribution of H3K27 trimethylation to transposons in *Arabidopsis thaliana*. *PLoS Genet.* **8**, e1003062 (2012).
24. E. T. Wiles, E. U. Selker, H3K27 methylation: a promiscuous repressive chromatin mark. *Curr. Opin. Genet. Dev.* **43**, 31–37 (2017).
25. K. H. Hansen, *et al.*, A model for transmission of the H3K27me3 epigenetic mark. *Nat. Cell Biol.* **10**, 1291–1300 (2008).
26. R. Margueron, *et al.*, Role of the polycomb protein EED in the propagation of repressive histone marks. *Nature* **461**, 762–767 (2009).
27. C. Xu, *et al.*, Binding of different histone marks differentially regulates the activity and specificity of polycomb repressive complex 2 (PRC2). *Proceedings of the National Academy of Sciences* **107**, 19266–19271 (2010).
28. W. Yuan, *et al.*, Dense chromatin activates Polycomb repressive complex 2 to regulate H3 lysine 27 methylation. *Science* **337**, 971–975 (2012).
29. C. R. Clapier, B. R. Cairns, The biology of chromatin remodeling complexes. *Annu. Rev. Biochem.* **78**, 273–304 (2009).
30. C. R. Clapier, J. Iwasa, B. R. Cairns, C. L. Peterson, Mechanisms of action and regulation of ATP-dependent chromatin-remodelling complexes. *Nat. Rev. Mol. Cell Biol.* **18**, 407–422 (2017).
31. T. Ito, M. Bulger, M. J. Pazin, R. Kobayashi, J. T. Kadonaga, ACF, an ISWI-Containing and ATP-Utilizing Chromatin Assembly and Remodeling Factor. *Cell* **90**, 145–155 (1997).
32. D. F. V. Corona, *et al.*, ISWI Is an ATP-Dependent Nucleosome Remodeling Factor. *Mol. Cell* **3**, 239–245 (1999).
33. T. Tsukiyama, J. Palmer, C. C. Landel, J. Shiloach, C. Wu, Characterization of the imitation switch subfamily of ATP-dependent chromatin-remodeling factors in *Saccharomyces cerevisiae*. *Genes Dev.* **13**, 686–697 (1999).
34. S. Baldi, S. Krebs, H. Blum, P. B. Becker, Genome-wide measurement of local nucleosome array regularity and spacing by nanopore sequencing. *Nat. Struct. Mol. Biol.* **25**, 894–901 (2018).

35. D. Barisic, M. B. Stadler, M. Iurlaro, D. Schübeler, Mammalian ISWI and SWI/SNF selectively mediate binding of distinct transcription factors. *Nature* **569**, 136–140 (2019).
36. J. C. Vary Jr, *et al.*, Yeast Isw1p forms two separable complexes in vivo. *Mol. Cell. Biol.* **23**, 80–91 (2003).
37. X. He, H.-Y. Fan, J. D. Garlick, R. E. Kingston, Diverse regulation of SNF2h chromatin remodeling by noncatalytic subunits. *Biochemistry* **47**, 7025–7033 (2008).
38. M. Oppikofer, *et al.*, Expansion of the ISWI chromatin remodeler family with new active complexes. *EMBO Rep.* **18**, 1697–1706 (2017).
39. R. Deuring, *et al.*, The ISWI Chromatin-Remodeling Protein Is Required for Gene Expression and the Maintenance of Higher Order Chromatin Structure In Vivo. *Mol. Cell* **5**, 355–365 (2000).
40. T. Stopka, A. I. Skoultschi, The ISWI ATPase Snf2h is required for early mouse development. *Proc. Natl. Acad. Sci. U. S. A.* **100**, 14097–14102 (2003).
41. D. V. Fyodorov, M. D. Blower, G. H. Karpen, J. T. Kadonaga, Acf1 confers unique activities to ACF/CHRAC and promotes the formation rather than disruption of chromatin in vivo. *Genes Dev.* **18**, 170–183 (2004).
42. A. Scacchetti, *et al.*, CHRAC/ACF contribute to the repressive ground state of chromatin. *Life Sci Alliance* **1**, e201800024 (2018).
43. B. Carter, *et al.*, The Chromatin Remodelers PKL and PIE1 Act in an Epigenetic Pathway That Determines H3K27me3 Homeostasis in Arabidopsis. *Plant Cell* **30**, 1337–1352 (2018).
44. Z. A. Lewis, Polycomb Group Systems in Fungi: New Models for Understanding Polycomb Repressive Complex 2. *Trends Genet.* **33**, 220–231 (2017).
45. K. M. Smith, *et al.*, The fungus *Neurospora crassa* displays telomeric silencing mediated by multiple sirtuins and by methylation of histone H3 lysine 9. *Epigenetics Chromatin* **1**, 5 (2008).
46. K. J. McNaught, E. T. Wiles, E. U. Selker, Identification of a PRC2 accessory subunit required for subtelomeric H3K27 methylation in *Neurospora*. *Mol. Cell. Biol.* (2020) <https://doi.org/10.1128/MCB.00003-20>.
47. K. Jamieson, *et al.*, Telomere repeats induce domains of H3K27 methylation in *Neurospora*. *Elife* **7** (2018).
48. A. J. Courtney, *et al.*, The histone variant H2A.Z is required to establish normal patterns of H3K27 methylation in *Neurospora crassa*. *bioRxiv*, 127 (2020).
49. H. V. Colot, *et al.*, A high-throughput gene knockout procedure for *Neurospora* reveals

- functions for multiple transcription factors. *Proc. Natl. Acad. Sci. U. S. A.* **103**, 10352–10357 (2006).
50. V. T. Bicocca, T. Ormsby, K. K. Adhvaryu, S. Honda, E. U. Selker, ASH1-catalyzed H3K36 methylation drives gene repression and marks H3K27me2/3-competent chromatin. *Elife* **7** (2018).
  51. K. A. Borkovich, *et al.*, Lessons from the genome sequence of *Neurospora crassa*: tracing the path from genomic blueprint to multicellular organism. *Microbiol. Mol. Biol. Rev.* **68**, 1–108 (2004).
  52. A. Babour, *et al.*, The Chromatin Remodeler ISW1 Is a Quality Control Factor that Surveys Nuclear mRNP Biogenesis. *Cell* **167**, 1201–1214.e15 (2016).
  53. A. Eberharther, *et al.*, Acf1, the largest subunit of CHRAC, regulates ISWI-induced nucleosome remodelling. *EMBO J.* **20**, 3781–3788 (2001).
  54. R. Strohner, *et al.*, NoRC--a novel member of mammalian ISWI-containing chromatin remodeling machines. *EMBO J.* **20**, 4892–4900 (2001).
  55. I. Kukimoto, S. Elderkin, M. Grimaldi, T. Oelgeschläger, P. D. Varga-Weisz, The Histone-Fold Protein Complex CHRAC-15/17 Enhances Nucleosome Sliding and Assembly Mediated by ACF. *Mol. Cell* **13**, 265–277 (2004).
  56. E. Y. Basenko, M. Kamei, L. Ji, R. J. Schmitz, Z. A. Lewis, The LSH/DDM1 Homolog MUS-30 Is Required for Genome Stability, but Not for DNA Methylation in *Neurospora crassa*. *PLoS Genet.* **12**, e1005790 (2016).
  57. G. M. Boratyn, *et al.*, Domain enhanced lookup time accelerated BLAST. *Biol. Direct* **7**, 12 (2012).
  58. D. F. Corona, *et al.*, Two histone fold proteins, CHRAC-14 and CHRAC-16, are developmentally regulated subunits of chromatin accessibility complex (CHRAC). *EMBO J.* **19**, 3049–3059 (2000).
  59. P. D. Varga-Weisz, *et al.*, Chromatin-remodelling factor CHRAC contains the ATPases ISWI and topoisomerase II. *Nature* **388**, 598–602 (1997).
  60. L. Aravind, L. M. Iyer, *The HARE-HTH and associated domains: novel modules in the coordination of epigenetic DNA and protein modifications.* *Cell Cycle* **11**, 119–131 (2012).
  61. X. Shi, *et al.*, Proteome-wide analysis in *Saccharomyces cerevisiae* identifies several PHD fingers as novel direct and selective binding modules of histone H3 methylated at either lysine 4 or lysine 36. *J. Biol. Chem.* **282**, 2450–2455 (2007).
  62. F. Erdel, K. Rippe, Quantifying transient binding of ISWI chromatin remodelers in living cells by pixel-wise photobleaching profile evolution analysis. *Proc. Natl. Acad. Sci. U. S. A.* **109**, E3221–30 (2012).

63. K. McCluskey, The Fungal Genetics Stock Center: from molds to molecules. *Adv. Appl. Microbiol.* **52**, 245–262 (2003).
64. R. H. Davis, F. J. De Serres, “[4] Genetic and microbiological research techniques for *Neurospora crassa*” in *Methods in Enzymology*, (Academic Press, 1970), pp. 79–143.
65. S. Honda, E. U. Selker, Tools for fungal proteomics: multifunctional neurospora vectors for gene replacement, protein expression and protein purification. *Genetics* **182**, 11–23 (2009).
66. J. Cha, M. Zhou, Y. Liu, Methods to study molecular mechanisms of the *Neurospora* circadian clock. *Methods Enzymol.* **551**, 137–151 (2015).
67. Z. A. Lewis, *et al.*, DNA methylation and normal chromosome behavior in *Neurospora* depend on five components of a histone methyltransferase complex, DCDC. *PLoS Genet.* **6**, e1001196 (2010).
68. Z. Zhou, Y. Dang, M. Zhou, H. Yuan, Y. Liu, Codon usage biases co-evolve with transcription termination machinery to suppress premature cleavage and polyadenylation. *Elife* **7** (2018).
69. M. Martin, Cutadapt removes adapter sequences from high-throughput sequencing reads. *EMBnet.journal* **17**, 10–12 (2011).
70. H. Li, *et al.*, The Sequence Alignment/Map format and SAMtools. *Bioinformatics* **25**, 2078–2079 (2009).
71. Y. Liao, G. K. Smyth, W. Shi, featureCounts: an efficient general purpose program for assigning sequence reads to genomic features. *Bioinformatics* **30**, 923–930 (2014).
72. M. I. Love, W. Huber, S. Anders, Moderated estimation of fold change and dispersion for RNA-seq data with DESeq2. *Genome Biol.* **15**, 550 (2014).
73. T. Sasaki, *et al.*, Heterochromatin controls  $\gamma$ H2A localization in *Neurospora crassa*. *Eukaryot. Cell* **13**, 990–1000 (2014).
74. A. R. Ferraro, Z. A. Lewis, ChIP-Seq Analysis in *Neurospora crassa*. *Methods Mol. Biol.* **1775**, 241–250 (2018).
75. H. Li, R. Durbin, Fast and accurate long-read alignment with Burrows-Wheeler transform. *Bioinformatics* **26**, 589–595 (2010).
76. H. Thorvaldsdóttir, J. T. Robinson, J. P. Mesirov, Integrative Genomics Viewer (IGV): high-performance genomics data visualization and exploration. *Brief. Bioinform.* **14**, 178–192 (2013).
77. S. Heinz, *et al.*, Simple combinations of lineage-determining transcription factors prime cis-regulatory elements required for macrophage and B cell identities. *Mol. Cell* **38**, 576–589 (2010).

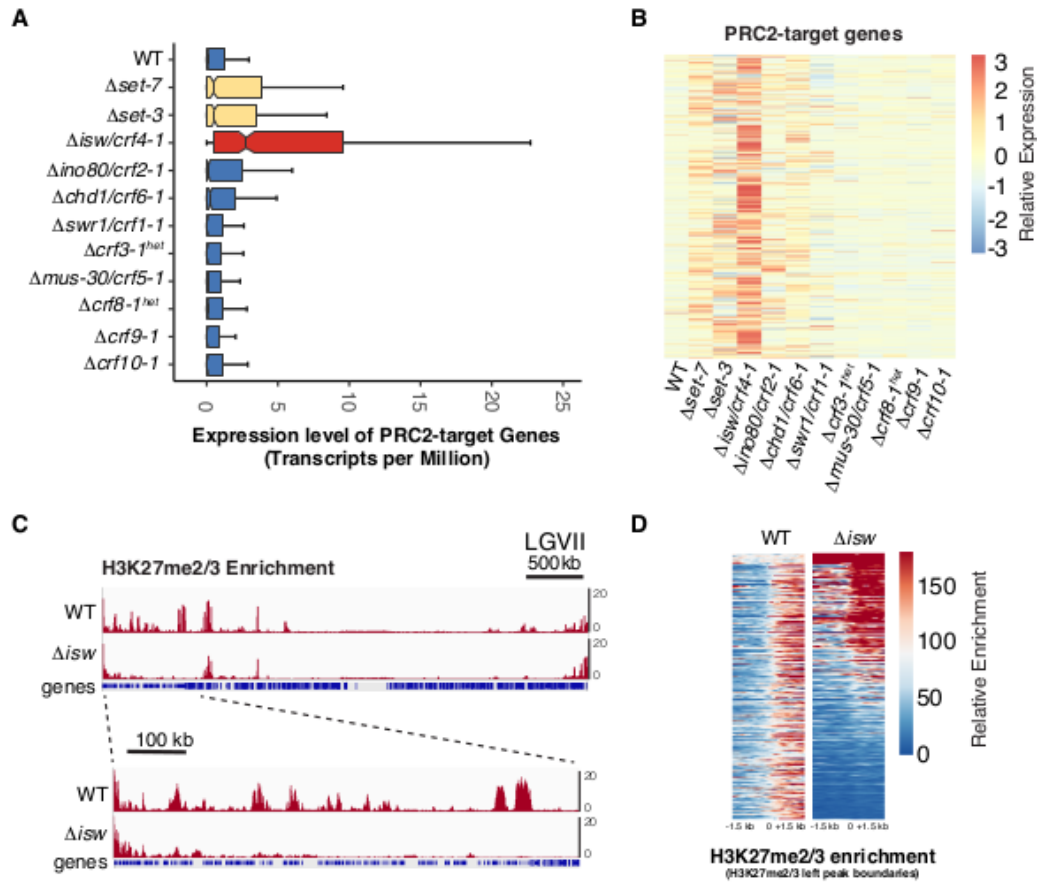


**Figure 1. ISW is required for repression of PRC2 target genes.** **A)** The box plot depicts average expression level (TPM) and the interquartile range for PRC2 target genes for each of the indicated strains. **B)** The heatmap shows relative expression levels of PRC2 target genes sorted by chromosomal position (rows) in the indicated deletion strain (columns). **C)** ISW is required for normal patterns of H3K27me2/3. H3K27me2/3 enrichment determined by ChIP-seq was plotted using the Integrated Genome Viewer for the indicated strains across one chromosome (Linkage Group VII). The bottom graph shows a magnified view of the left end of LGVII. **D)** The heat map depicts H3K27me2/3 across all 309 H3K27me2/3-enriched domains in the *Neurospora* genome. Each heat map row depicts a 3 kb window centered at the left boundary of an H3K27me2/3-enriched peak identified in WT cells.

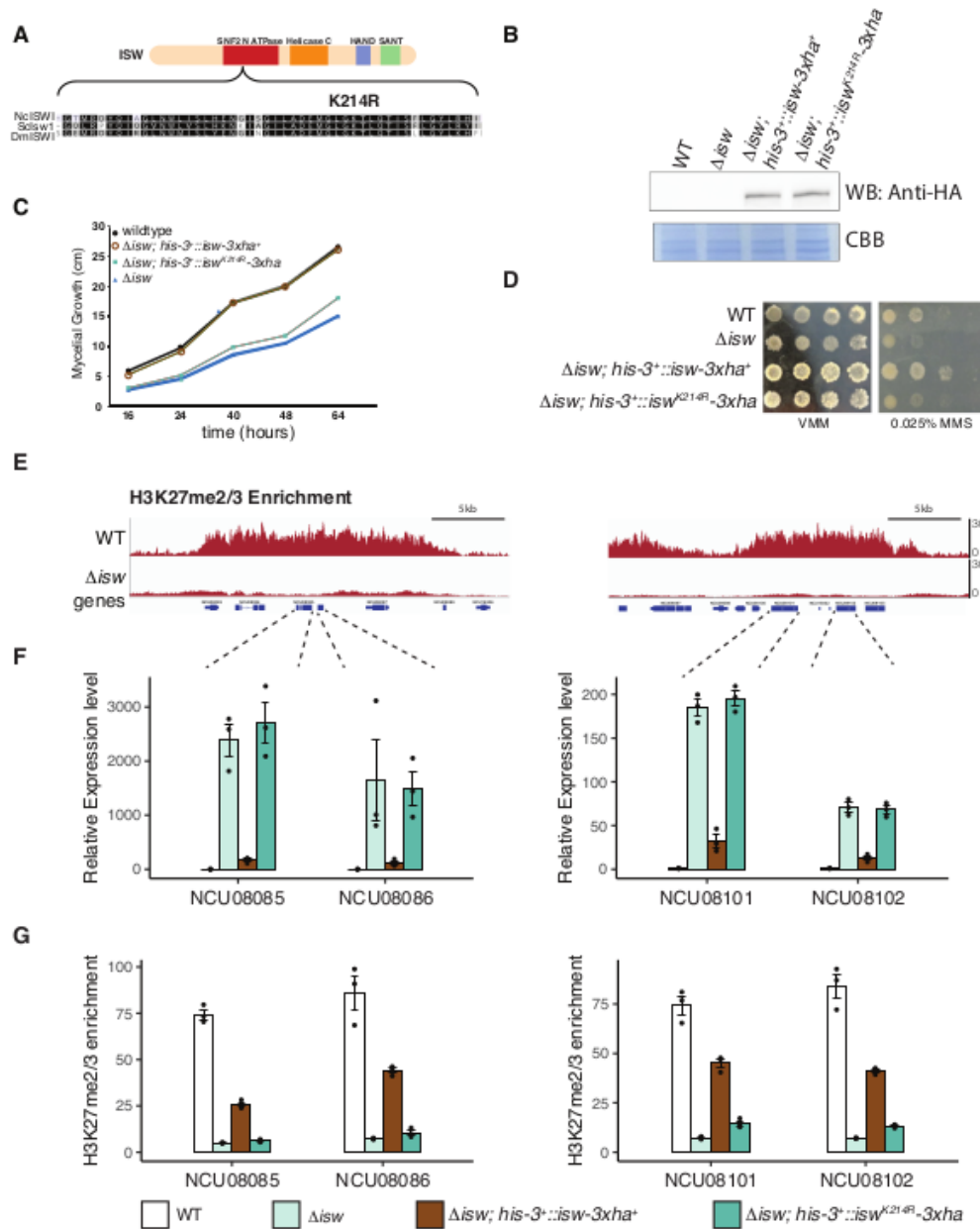


**Figure 2. ISW catalytic activity is required for repression and H3K27me2/3.** **A)** The schematic illustrates the predicted protein domains in the *Neurospora* ISW sequence. The sequence alignment indicates the amino acid conservation between the ATPase domain of *Neurospora* ISW, *S. cerevisiae* ISW-1, and *D. melanogaster* ISWI. The location of the conserved lysine residue mutated to arginine in this study is indicated. **B)** Both wild type ISW-3xHA and the ISW<sup>K214R</sup>-3xHA fusion proteins are expressed at similar levels. Total protein extracts were

analyzed by Western blotting using an anti-HA antibody or by staining with Coomassie Brilliant Blue as a loading control for the indicated strains. **C)** The graph depicts the linear growth rates of the indicated strains measured using “race tubes”. **D)** For the indicated strains, serial dilutions of fungal cells (conidia;  $10^6$ - $10^3$  from left to right) were spotted on Vogel’s Minimal Medium (VMM) with or without the genotoxic agent methyl methanesulfonate (0.025%; MMS). **E)** The IGV genome browser image depicts H3K27me<sub>2/3</sub> enrichment determined by ChIP-seq for the indicated strains. The location of four genes analyzed by RT-qPCR and ChIP-qPCR are indicated with dashed lines. **F)** Relative gene expression data are shown for the four genes, NCU08085, NCU08086, NCU08101, and NCU08102 for the strains indicated at the bottom of panel G. Expression is relative to the constitutive *vma-2* transcript and normalized to wild type. **G)** Enrichment of H3K27me<sub>2/3</sub> across the four genes shown in panels E and F was examined by ChIP-qPCR for the indicated strains. ChIP-enrichment at the indicated locus was normalized to enrichment at the euchromatic *hH4* gene locus.



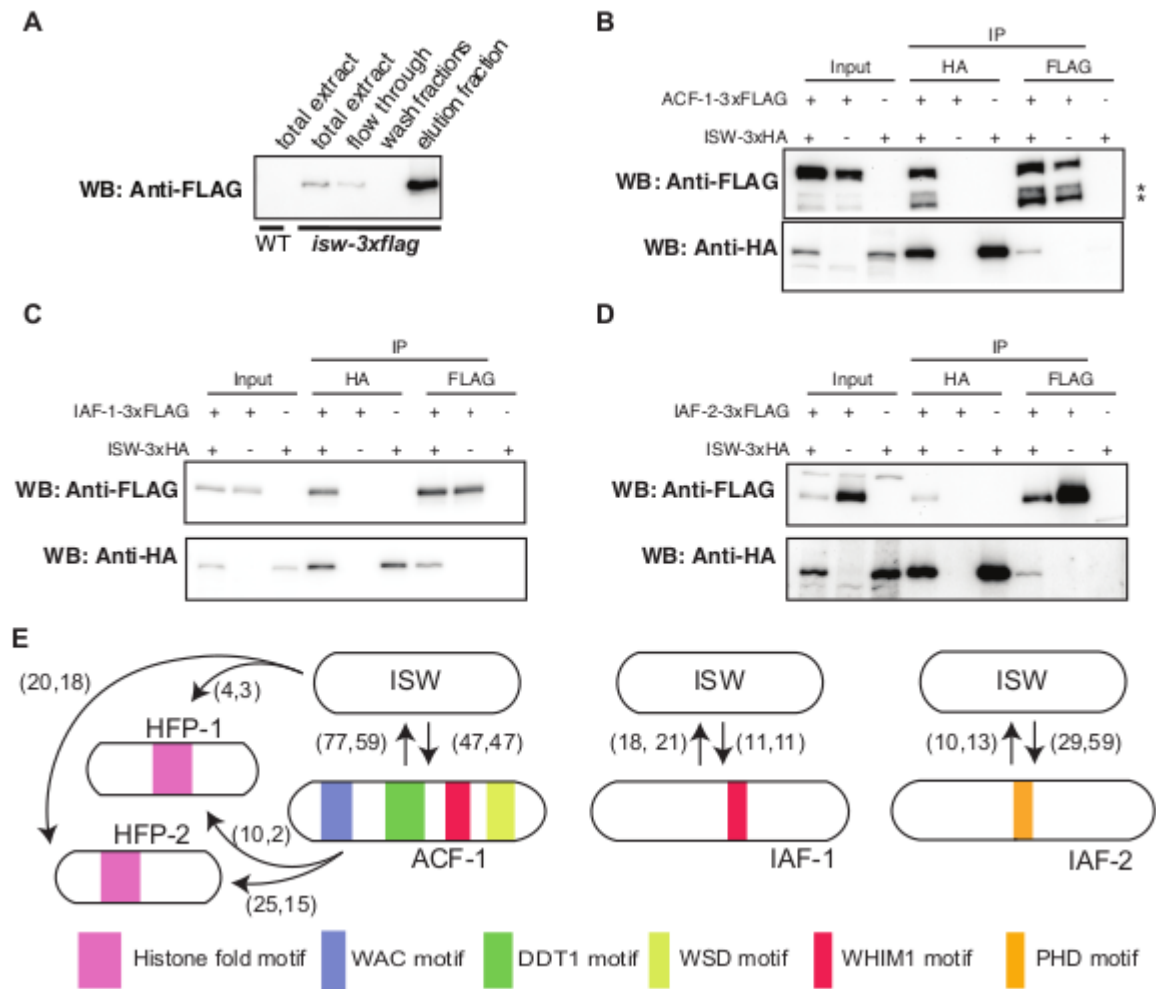


**Figure 3. *Neurospora* ISW is present in at least three distinct complexes.** A) Enrichment of ISW-3xFLAG was validated by Western blotting. Total protein extracts were analyzed from a wild type control strain (WT) and for the *isw-3xflag* strain, ISW-3xFLAG was examined in total extracts, the unbound fraction following incubation with an M2-anti-FLAG affinity resin (flow through), an aliquot of 6 combined wash fractions, and the final elution fraction containing purified ISW-3xFLAG. B-D) Immunoprecipitation experiments were performed using extracts from strains expressing ACF1-3xFLAG, IAF1-3xFLAG, IAF2-3xFLAG, and ISW-3xHA as indicated by (+) or (-). The input fraction, the -FLAG immunoprecipitate (IP:FLAG), and the -HA immunoprecipitate (IP:HA) were subject to western blotting and probed with the anti-FLAG

or anti-HA antibodies as indicated (WB). The asterisk indicates presumed ACF degradation products. E) The schematic summarizes the results of protein identification by LC-MS/MS for independent, reciprocal protein purification experiments using ISW-3xFLAG, ACF1-3xFLAG, IAF-1-3xFLAG, and IAF-2-3xFLAG (2 replicates each). The arrows extend from the purified protein and point to the captured prey protein. The numbers in parentheses indicate the number of unique peptides corresponding to the identified prey protein for two independent replicate purification and LC-MS/MS experiments.

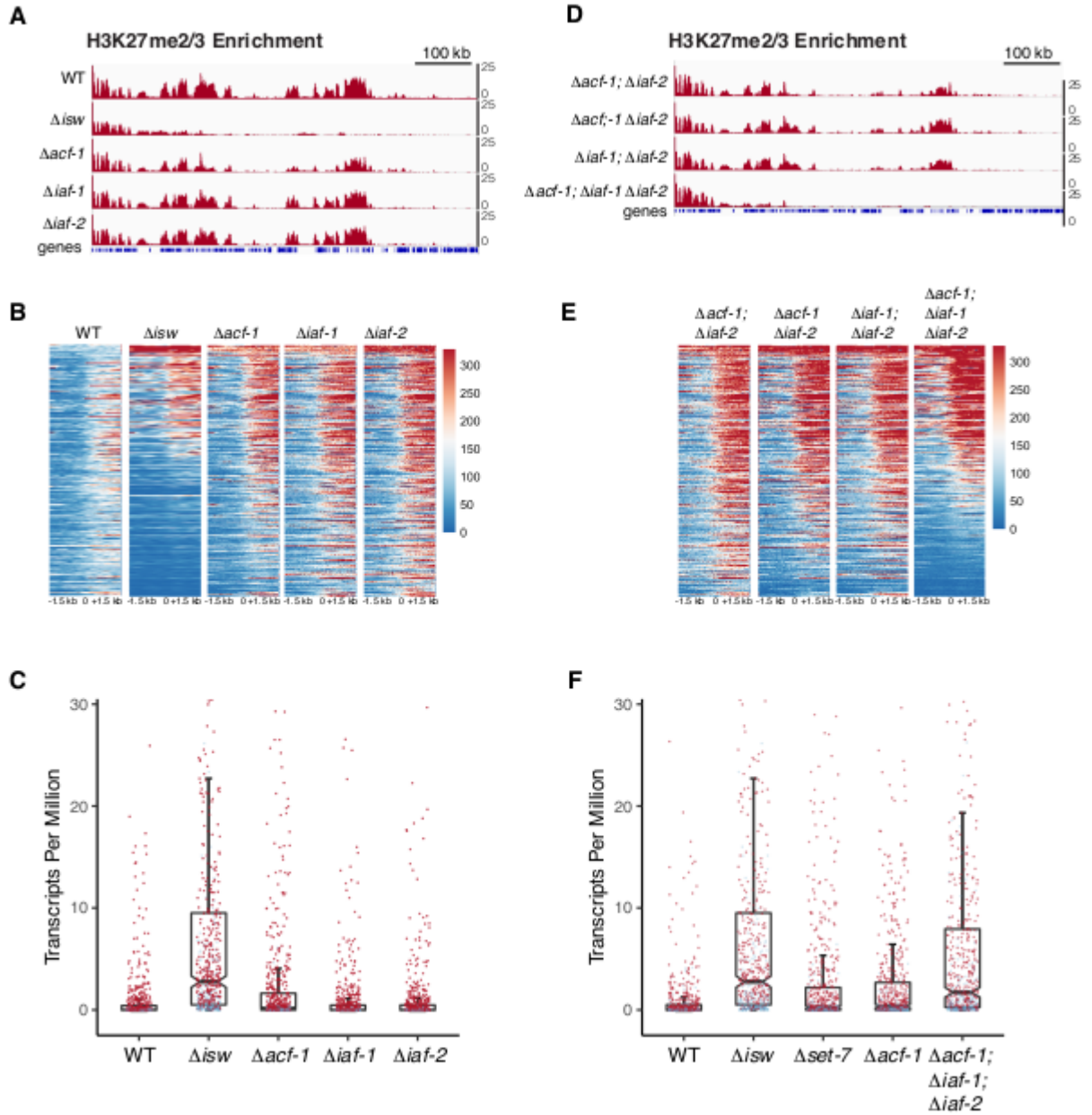


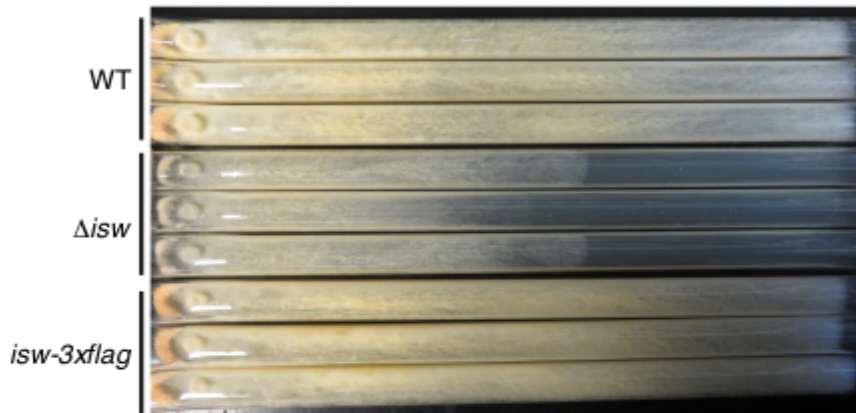
**Figure 4. ISW complexes partially compensate for one another.** A) H3K27me2/3 enrichment determined by ChIP-seq was plotted using the Integrated Genome Viewer for the indicated strains across the left end of Linkage Group VI. The scale bar on the top right corresponds to 100 kb. B) The heat maps depict H3K27me2/3 across all wild type H3K27me2/3-enriched domains in the *Neurospora* genome for the indicated strains. Each heat map row depicts a 3 kb window centered at the left boundary of an H3K27me2/3-enriched peak identified in WT cells. C) The

box plot depicts average expression level (transcripts per million) and the interquartile range for 642 PRC2 target genes for the indicated strains. Each dot represents the expression level of a PRC2-target gene colored by statistical significance (Red dots = adjusted p-value  $<0.05$ ; grey dots = adjusted p-value  $>0.05$ ). D-E) Same as panels A-C.

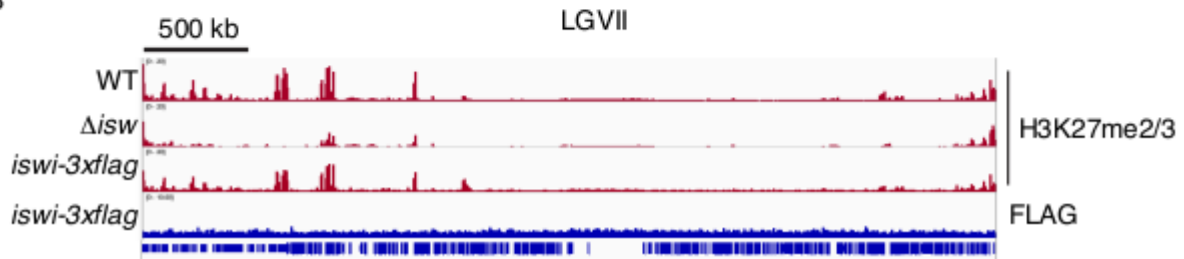


indicated strains and replicates. D) Heat maps depict H3K27me2/3 enrichment across the 5' boundary of all 309 PRC2-target domains for individual replicate samples, as indicated.

A



B



**Supplemental Figure 2. ISW-3xFLAG is fully functional and does not exhibit region-specific enrichment in ChIP-seq experiments.** A) The *iswi-3xflag* “knock-in” strain displays WT growth. B) ISW-3xFLAG supports normal H3K27me2/3. ChIP-seq was performed using antibodies to H3K27me2/3 or FLAG for the indicated strains.

Table S1. Table of called H3K27me2/3 peaks.

Table S2. Table of LC-MS/MS data.

Table S3. Strains.

Table S4. Oligos.

Table S5. RNA-seq values for individual replicates of silent PRC2-target genes.

Table S6. NCBI Short-read Archive of JGI-generated RNA-sequencing samples.